UNIVERSITÀ DEGLI STUDI DI MILANO

PhD in Chemistry – XXXVI cycle

Department of Chemistry

PhD thesis

Toward a better cleaning and selectivity in electroanalysis: TiO_2-based sensors and enantioselective materials.

SSD: CHIM/01

PhD candidate: Silvia Comis

Tutor: prof. Luigi Falciola

PhD School Coordinator: prof. Daniele Passarella

A.A. 2022-2023

"Le incredibili scoperte
della chimica esprimono
con forza la magia della
natura"

Johann Wolfgang Goethe

Table of contents.

Extended abstract.

In the latest years the concern on environmental issues has grown dramatically. One of the major problems of environmental chemistry are emerging contaminants (ECs), which are not commonly monitored in the environment. They can cause undesirable effects on ecosystems and human health. This group of substances includes pharmaceutical and personal care products (PPCPs), endocrine disrupting chemicals, hormones, pesticides, plasticizers, flame retardants and so on. Some of these emerging contaminants have been added to the list of priority substances and corresponding individual environmental quality standards have been set. These substances include pharmaceuticals (macrolide antibiotics, estrogenic hormones, carbamazepine, diclofenac, ibuprofen), industrial chemicals (bisphenol A), metals (silver) and pesticides (triclosan, nicosulfuron, glyphosate, neonicotinoids, pyrethroids).

Modern analytical techniques can easily detect emerging contaminants in the environment, but they are expensive and time consuming. In this context, electrochemical sensors could overcome these problems since they are easy to use, they can be portable, disposable and they can be adapted to every necessity.Thanks to their properties and characteristics, such as high active surface, increased surface/volume ratio, increased selectivity, nanomaterials are broadly used in a wide range of applications, like energy, catalysis and electroanalysis.

One of the most valued characteristics for modern sensors are self-cleaning properties, *i.e.* the possibility to use the sensor more than once and to detect analytes in complex matrices, remotely without the need to clean and restore them for long time.

Starting from the aforementioned points, the aim of this PhD thesis is the study of different materials to enhance the selectivity and the cleaning properties of electrochemical sensors. In particular, titanium dioxide was studied for its photocatalytic activity to give photo-renewable properties to electrochemical sensors using different supports (fluorine-doped tin oxide glass electrodes and gold disk microelectrodes) in the detection of different emerging contaminants. Its properties were also studied for the photoelectrochemical detection of ciprofloxacin, a fluoroquinolone antibiotic. Titanium dioxide was coupled with gold nanoparticles (AuNPs) to enhance its signal and with mesoporous silica to increase the selectivity of the devices.

At first, the focus was on the study of the aging time of the titanium dioxide sol and how it influences the electrochemical and photoelectrochemical

performances on the final structures. The starting device, an FTO glass, was covered with titanium dioxide and it was electrochemically characterised by cyclic voltammetry (CV), electrochemical impedance spectroscopy (EIS), atomic force microscopy (AFM) and transient photocurrent analysis. Once the study of the aging time of the sol was over, AuNPs were added to the device to form a heterojunction. This device was used for the detection of different emerging contaminants and the photocatalytic properties of TiO_2 were used to photo-renew the surface of the sensor.

Then this device was used for the photoelectrochemical detection of ciprofloxacin with different light sources. In particular, a low-power light source was used for this purpose, an UV LED. The determination of ciprofloxacin was also possible at low applied potential (+0.1 V vs SCE) and with good detection limits and good sensitivity. The analysis of possible interferences showed that the device was sensible to the presence of humic acids at high concentrations. For this reason, vertically aligned mesoporous silica was added to the device, in order to use its porosity to load gold nanoparticles and to use the charge- and size-exclusion properties of the material. The device was electrochemically characterised with CV, EIS, transmission electron microscopy (TEM) and transient photocurrent analysis. Then ciprofloxacin was detected with this device, obtaining good analytical parameters. Moreover, possible interferents were analysed and, in this case, even high concentrations of humic acids did not interfere with the determination of ciprofloxacin.

The photo-renewable properties of titanium dioxide were also studied using a gold disk microelectrode in the presence of dopamine, a molecule known for its soiling problems. The titanium dioxide layer was deposited onto the microelectrode surface through a pseudo-calcination process and its behaviour was studied after the use of the sensor for the detection of dopamine. It has been seen that it is possible to restore the initial properties of the electrode even after its soiling.

In last part of this PhD thesis, the enantioselective properties of oligo-BT_2T_4 enantiopure films and the electrocatalytic properties of multi-walled carbon nanotubes (MWCNTs) were studied together on the same device at the same time. At first the electrochemical properties of the materials were studied using a non-chiral probe in CV and EIS. Then the enantioselectivity of the oligo-BT_2T_4 enantiopure films was tested using a chiral probe in cyclic voltammetry. The surface of the device was also analysed using scanning electron microscopy (SEM). The presence of MWCNTs allows the detection of the

chiral probe at lower potentials than would have happened only with the enantiopure film, thus having a catalytic effect.

In conclusion, several materials are here investigated starting from their physico-chemical and electrochemical characterizations. Their application as electroanalytical sensors is explored, evidencing the presence of synergistic effects in the hybrid systems with respect to the single components, assuring enhanced properties and superior performances.

1. Introduction

A chemical sensor is defined by IUPAC [1] as "*a device that converts chemical data, ranging from the concentration of a single sample component to complete composition analysis, into an analytically usable signal*".

A chemical sensor is constituted of two essential functional units: a receptor and a physicochemical transducer. The receptors are variable and can range from activated or doped surfaces to complex (macro)molecules that create highly specific interactions with the analyte (Figure 1.1).

The sensor is called "bio-sensor" if the receptor has a biological origin (such as DNA, antibodies, or enzymes). The recognition event is transformed into a preset output signal by the receptor's interaction with the analyte. Maintaining a high level of specificity for the target analyte in the presence of possibly interfering chemical species is one of the fundamental requirements for sensors to prevent false-positive results. The transducer, which transforms the signal produced by the receptor-analyte interaction into a readable value, is another essential part of sensors. Consequently, catalytic or affinity-based devices can be used to categorize chemical and biosensors. While affinity-based devices rely on highly specific interactions between the receptor and analyte, such as using the specific affinity of nucleic acids (such as ssDNA and aptamers), antibodies–antigens, or host–guest interactions, catalytic sensors use catalytic activity to generate the signal, as in the case of enzymatic, DNAzyme, or functionalized surfaces that can perform redox reactions under certain conditions. Depending on the transducer type being used, a variety of techniques (such as optical, gravimetric, or electrochemical) can be used to monitor the recognition events [2].
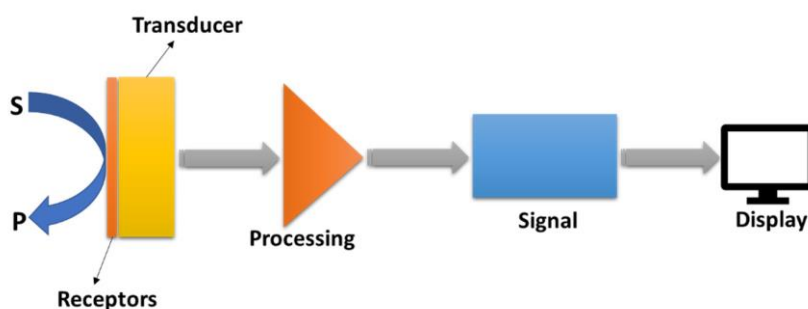

Figure 1.1 - A schematic diagram illustrating the main components of a standard sensor (taken from [3]).

Due to their advantages, which include low detection limits as low as picomoles, rapidity, and inexpensive sensing equipment, electrochemical sensors are by far the most widely used form of sensors.

There are several different form factors for electrochemical sensors, from top-bench to completely integrated wearable devices [3].

A chemical sensor's use is to provide precise, up-to-date information about the chemical makeup of its environment. Such a device would ideally be able to react continuously and reversibly without affecting the sample. These devices have a transduction element coated with a biological or chemical identifying layer. The electrical signal generated by the target analyte's contact with the recognition layer is where electrochemical sensors obtain their analytical information. Depending on the criteria for sensitivity or selectivity, the sample matrix's composition, and the kind of analyte, a variety of electrochemical devices can be used for environmental monitoring. Depending on the type of device, the majority of these devices can be classified as electrochemical sensors, such as amperometric and potentiometric [4, 5]. Amperometric sensors are used to identify electroactive substances engaged in chemical or biological identification.

1.1. Types of electrochemical sensors.

Electrochemical sensors can be classified into several categories including amperometric, potentiometric, impedimetric, photoelectrochemical, and electrogenerated chemiluminescence.

When no current is permitted to flow in the system, a local Nernstian equilibrium is produced at the sensor interface for potentiometric sensors, providing information on the analyte's concentration. This is the result of particular interactions between the sensor and the analyte. According to the Cottrell equation, amperometric sensors use a voltage applied between a reference and working electrode to start electrochemical oxidation or reduction. They then measure the current that results as a quantitative indicator of the analyte's concentration.

$$i = \frac{nFAc_1^0 \sqrt{D_j}}{\sqrt{\pi t}} \qquad\qquad \text{Eq. 1.1}$$

where:

i = current (in ampere);

n = number of electrons;

F = Faraday constant (96,485 C/mol);

A = area of the (planar) electrode in cm^2;

c^0_j = initial concentration of the reducible analyte in mol/cm^3;

D_j = diffusion coefficient for species in cm^2/s;

t = time in seconds.

On the other hand, conductometric sensors, also known as impedimetric sensors, use surface impedance changes to identify and measure analyte-specific recognition events on the electrode.

1.1.1. Potentiometric sensors.

Potentiometric sensors have been the most widely used practical sensors since the early 1930s because of their affordability and ease of use. Three categories can be used to group potentiometric devices:

- Ion-selective electrodes (ISEs);
- Coated-wire electrodes (CWEs);
- Field-effect transistors (FETs).

When building an electrode that is selective to a single species, the kind and composition of the membrane material are important considerations. An almost limitless number of analytes can now be used in a range of applications thanks to research in this field; the only constraints are related to the dopant and ionophore composition of the membrane matrix.

Depending on the kind of membrane, ISEs can be divided into three groups: glass electrodes, liquid electrodes and solid electrodes. Using response membrane electrodes made especially for this purpose, over two dozen ISEs are commercially available from companies like Corning, Orion, Radiometer, Beckman, and Hitachi. These ISEs are widely used for the analysis of organic ions and anionic or cationic species in a variety of effluents, in the oil industry, and in the manufacturing process and drug monitoring [6-8].

Sweat analysis in combination with wearable device technology and potentiometric ion sensors, which are based on an all-solid state principle,

shows considerable promise for assessing physical status during athletic performance as well as clinical care [9].

For many years, pH electrodes have been the most widely used potentiometric device overall and for a number of decades prior to that. The most popular kind of electrodes are glass electrodes, which come in a range of shapes and sizes and are made from a thin, ion-sensitive glass membrane. However, in addition to those mentioned above, there are other kinds of potentiometric sensors that can be used to measure pH. These sensors use redox-active chemicals (such quinones and ferrocenes) or organic polymers (like polymethylene blue). Furthermore, it has been reported that glass electrodes can be used for monovalent cations, including lithium, sodium and potassium sensors [10-12].

Although it has shown to be quite effective, the use of glass membrane electrodes for pH solution determination is currently limited to aqueous measurements. When calculating the concentration of hydrogen ions in nonaqueous liquids, adjustments must be made [13].

1.1.2. Amperometric sensors.

Amperometric measurements are widely employed as a very sensitive and accurate analytical technique in which the applied voltage acts as a catalyst for electrocatalytic redox processes, which produce electrical currents proportional to the analyte's concentration. The basic instrumentation consists of a controlled-potential system, and the electrochemical cell consists of two electrodes immersed in a suitable electrolyte. Using a three-electrode cell, where one electrode serves as a reference electrode, is a more advanced and popular design [14]. A reference electrode, such as Ag/AgCl/KCl or $Hg/Hg_2Cl_2/KCl$ is described as the electrode that maintains a constant potential in comparison to a working electrode, whereas a working electrode is the electrode where the reaction of interest happens [15]. An inert conducting material, such as platinum or graphite, is frequently used as counter/auxiliary electrode. A supporting electrolyte is required in controlled-potential investigations to minimize the resistance of the solution, stop electromigration effects, and keep the ionic strength constant. Both practical methods and theoretical considerations have been thoroughly discussed in literature [16, 17].

1.1.3. Impedimetric sensors.

Conductometric sensors are used to measure the tendency of a medium or the electrolyte solution to allow electrical current to pass through between working electrode and counter electrodes or reference electrode. Capacitance variations are analysed using the conductometric sensing approach [18]. Impedance spectroscopy examines the impedance of the electrochemical cell surface, which is proportional to and dependent upon the analyte concentration and sensor application.

Capacitance measurement methods are regularly reviewed, and an integrated approach known as electrochemical spectroscopy is being explored [19]. The typical resistance value is all that a DC current can sense. In impedimetric sensing, AC current is typically used to obtain changes in the electrode's capacitance value [20].

In Table 1, examples of electrochemical transducers that are often employed for measurements (*i.e.*, potentiometric, impedimetric and amperometric) are reported as well as instances of analytes that have been measured [21].

Table 1.1 - different types of electrodes and their possible analytes

Measurement category	Transducer	Transducer analyte	Reference
Potentiometric	Ion-selective electrode (ISE), glass electrode, gas electrode, metal electrode	K^+, Cl^-, Ca^{2+}, F^-, H^+, Na^+, CO_2, NH_3 redox species	[22]
Amperometric	Carbon electrode, chemically modified electrodes (CMEs)	O_2, sugars, alcohols, phenols, oligonucleotides	[23]
Conductometric	Interdigitated electrodes, metal electrode	Urea, charged species, oligonucleotides	[24]

1.1.4. Electrochemical sensors applications.

For the study of biological, environmental, industrial, and pharmaceutical species, electrochemical sensors have long been sought after due to their low cost, speed and ease of downsizing, as well as their high sensitivity, precision and long-term reliability. To improve analytical performance, a variety of nanomaterials with remarkable properties, including metals, conductive polymers, metal oxides, and metal–organic and carbon–based nanomaterial frameworks, have been included into electrochemical tests for more than twenty years. With the use of recognition molecules like enzymes, antibodies and aptamers as well as bioinspired receptors that can precisely and efficiently capture targets, this modification makes it possible to increase the loading capacity and, consequently, the specificity of the electrochemical sensors. Strong electrocatalytic activity for specific electrochemical processes is intimately related to this goal. Furthermore, it is feasible to increase surface area and electrical conductivity by changing the form and structure of the surface, which should improve the sensitivity of these tests.

Due to new applications including wearables, point-of-care diagnostics, in vivo analysis, and single-molecule sensing, electrochemical sensors have become more and more popular recently [25].

Numerous benefits come with electrochemical sensors: low LODs and LOQs, high sensitivity; quick analytical response for flow analysis and alert systems; almost infinite geometries, electrode materials, and configurations due to their simplicity; and ease of use (low-cost, basic equipment, ability to be integrated as a detection module in a variety of analytical systems).

Because they offer the following further benefits, biosensors are intriguing analytical tools for biological and environmental research:

1. quick data collection;
2. detection of the important substrate is frequently accomplished without previous separation;
3. a LOD that can reach ng/mL;
4. good selectivity and, occasionally, even specificity;
5. a high benefit/cost ratio and easy usage [26-28].

1.2.   Diffusion at the surface of the electrode.

Diffusion phenomena have firstly been treated and studied in depth by the pioneering work of Adolf Fick, more than 150 years ago [29]. Diffusion is a phenomenon occurring when a concentration gradient is present. In more details, diffusion of a particular species toward an object is established from a zone of higher concentration to a one of lower concentration. It is possible to talk about a diffusive flux, at any point, described by Fick's first Law (Eq. 1.2):

$$j = -D\frac{\partial c}{\partial x}$$

Eq. 1.2

where j is the flux (in mol cm^{-2} s^{-1}), describing the number of moles that pass through unit area in unit time, $\partial c/\partial x$ is the local concentration gradient at the x point and D (in cm^2 s^{-1}) is the diffusion coefficient, typical of the molecule that is under investigation and that it is diffusing in the environment. The minus sign is implying that the flux is on the opposite direction than the concentration gradient. It is worthwhile noticing that in a common voltammetric experiment, where the electrolyte solution is not particularly viscous, like some ionic liquids,[30] the values of D are commonly in the range of 10^{-6} to 10^{-5} cm^2 s^{-1}, and they are dependent from the temperature, often following an Arrhenius-type relationship. Moreover, following Eq. 1.1, it is evident that the flux is driven only by concentration differences in solution and no gradients of electrical potential is taken into consideration. This is correct in case of uncharged diffusing species, but in the case of ions (charged species), the electrical potential has a significant effect. By the way, it is common practice in a voltammetric experiment to work with sufficient quantities and concentrations of background electrolytes (supporting electrolytes) that eliminate the presence of significant electric fields in the solution except the one very close to the electrode surface. In this way, it is possible to assume that, in a conventional experiment, the materials in solution are brought towards the electrode only by diffusion (in a quiescent environment, at constant temperature, also the convection mechanism is suppressed). But how is the concentration changing with time? The answer to this question is given by the Fick's second law (Eq. 1.3), in one dimension:

$$\frac{\partial c}{\partial t} = D\frac{d^2 c}{dx^2}$$

Eq. 1.3

Now that the equation for the flux are given, it is interesting to introduce them in a practical voltammetric experiment, where, in general, a potential is applied

to an electrode and the resulting current is measured, as a function of time. In more details, it follows the Eq. 1.4:

$$I = nFAj \qquad \qquad Eq.\ 1.4$$

where n is the number of electrons that are involved in the electrode reaction and F is the Faraday's constant, A is the electrode area and finally j is the flux. By substituting the flux as expressed by the Fick's First law, it follows the Cottrell Equation (Eq. 1.5):

$$I = \frac{nFA\sqrt{D}c^*}{\sqrt{\pi t}} \qquad \qquad Eq.\ 1.5$$

from which it is easily to understand that the current of a reaction at an electrode, resulting from a potential step, decay to zero with an inversely proportional dependence to the square root of time. This equation is valid in the case of a planar macro-electrode. When dealing with spherical or hemispherical electrode, the equation that regulates the flux toward the surface is the following (Eq. 1.6), where re represents the radius of the electrode:

$$j = Dc^* \left[\frac{1}{\sqrt{D\pi t}} + \frac{1}{r_e} \right] \qquad \qquad Eq.\ 1.6$$

In this case, it is evident that the flux, and so the current, are dependent both from the time and from the radius of the electrode (r_e). The first term is the "time-dependent" term, while the second one represents the "steady-state" condition, in which effectively the current is independent from the time and stay fixed at a certain value. In a "short time" limit, when $\sqrt{D\pi t} \ll r_e$, the second term of Eq. 1.5 is negligible and the flux is now described by Eq. 1.7, while in the "long-time" limit, when $\sqrt{D\pi t} \gg r_e$, the flux is descripted by Eq. 1.8:

$$j = \frac{c^*\sqrt{D}}{\sqrt{\pi t}} \qquad \qquad Eq.\ 1.7$$

$$j = D\frac{c^*}{r_e} \qquad \qquad Eq.\ 1.8$$

So, in the first case, an almost linear diffusion (or planar) is expected, meaning that the current lines are behaving like they are perpendicular to the surface of the electrode and parallel one to the other. In the second case, on the contrary, convergent diffusion (or radial) is established, where the current lines come to

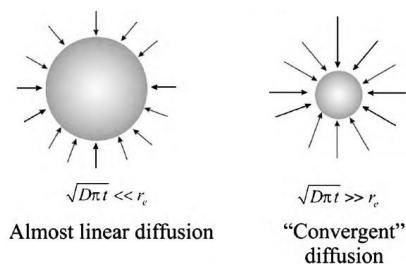the electrode from every direction, and they are not parallel one to the other (see Figure 1.2).

$$\sqrt{D\pi t} \ll r_e \qquad\qquad \sqrt{D\pi t} \gg r_e$$

Almost linear diffusion   "Convergent" diffusion

Figure 1.2 - Schematical representation of two different diffusion mechanisms at a spherical electrode (taken from [31]).

In the "long time" limit, the diffusion layer thickness is high, and it is higher than the time-scale of the performed voltammetry. In this case, a steady-state current is normally reached, resulting in a step-shaped voltammetric signal. Figure 1.3 shows the relationship between the size of the electrode, with respect to the diffusion layer thickness, and the contribution of convergent diffusion to the observed voltammetry. It is evident how the convergent diffusion is responsible for a different shape of the voltammetric signal, but also for an enhancement of the current intensity values. The magnitude of the flux under steady-state conditions is proportional to the size of the electrode: the smaller the electrode, the greater the current density and the faster the material diffuses to (and from) the electrode surface.
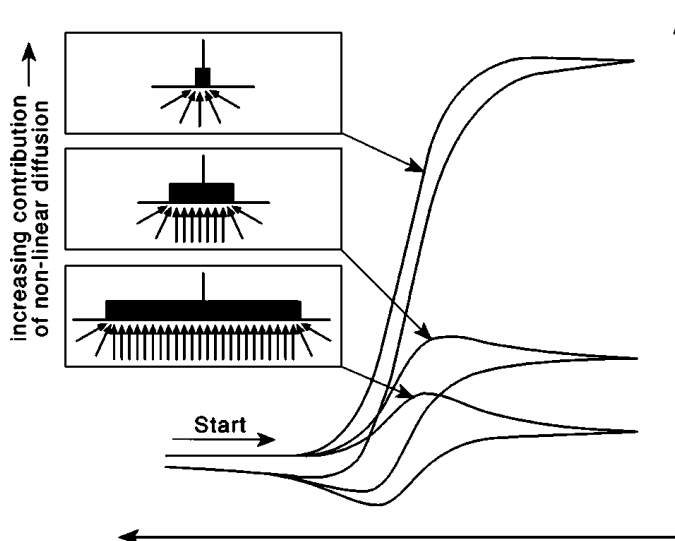

Figure 1.3 - Schematic diagram showing the relationship between the size of the electrode (with respect to the diffusion layer thickness) and the contribution of convergent diffusion to the observed voltammetry (taken from [31]).

It is almost clear now that it is possible to have different diffusional mechanisms by changing the experimental conditions and the type of the electrode. In this context, the differences in the type of the electrode platforms, intended in their size and shape, is of particular interest. In fact, a macro electrode is completely different from a micro or a nano-electrode, starting from the diffusional mechanism that are involved at their surfaces. In more details, smaller electrodes lead to:

a. Non planar diffusion: microelectrodes favour faster rates of mass transport, leading to current lines that approach the electrode in a radial way and from every direction, with a diffusion layer thickness higher than the size of the electrodes itself.
b. Reduced Capacitance: The capacitance of the double layer is related to the electroactive area of the electrode. The reduction of the electrode area reduces the capacitance.
c. Reduced Ohmic Drop: The ohmic drop is proportional to the total passed current. Dealing with smaller electrodes, this current decreases.

The advantages in the use of microelectrodes are again enhanced if more than one electrode is involved in the experiment. In this case, it is created a so-called microelectrodes' array. This definition refers to systems in which hundreds or even thousands of microdisc electrode wires are in parallel. They can be produced in several ways, from lithography to random assembly. The peculiarity of these systems is that they can provide a voltammetric response of similar magnitude to their macro counterparts, but with a considerably less background capacitive current [45]. For what concerns the redox reaction of a probe toward such electrodes, different situations can be imagined. In fact, in the case of an array of microdisc electrodes separated by an insulating material, individual diffusion layers will develop and grow during the experiment. Depending on the size and the reciprocal distance between the microelectrodes, the diffusive layers will overlap or not in different ways, resulting in different diffusional mechanisms of the redox reaction. A schematic representation is shown in Figure 1.4. In the first category (Figure 1.4, 1), the microelectrodes are so far apart that their diffusion layers do not interact, and they are fully independent since the timescale of the voltammetry is short (fast scan rate). In this case, a planar diffusion to the electrode is expected, with a peak-shaped peak. In the second case (Figure 1.4, 2), the electrodes are sufficiently spaced like the situation 1, but now the timescale is longer, and the diffusional mechanism is radial (convergent), resulting in a step-shaped curve. In the third case (Figure 1.4, 3), the microelectrodes are closer, and the diffusional layers

are partially overlapped. This situation is a mixed one, with voltammetric properties that are not perfectly categorized. In the last category (Figure 1.4, 4), the microelectrodes are so close that there is a complete overlapping of the diffusional fields leading to a situation in which the array is behaving like a macroelectrode (peak-shaped curves and peak current scaling with the square root of the voltage scan rate).

Considering all these facts on the diffusional mechanism and the size of the electrodes, it is possible to explain how the current intensity varies in the case of a macroelectrode and in the case of a spherical (or hemispherical) microelectrode.
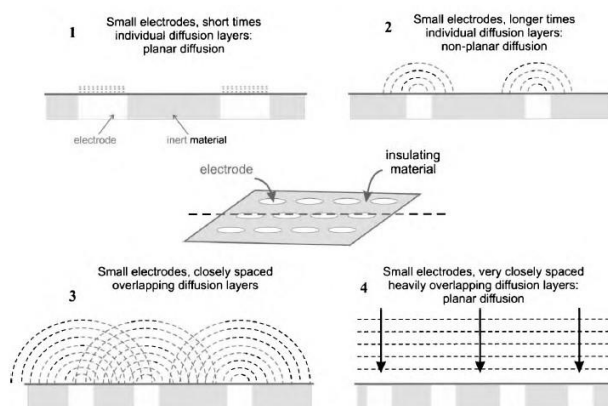
Figure 1.4 - Different diffusion profile that can be present at an array of microelectrodes (taken from [45]).

For a macro-electrode, the current is governed by the Randles-Sevcik equation (Eq. 1.9):

$$I_{peak} = 2.69 \cdot 10^{-5} n^{3/2} D^{1/2} c_{bulk} v^{1/2} A \qquad Eq. \ 1.9$$

where I_{peak} is the peak current, n is the number of electrons transferred in the rate determining step, D is the diffusion coefficient, c_{bulk} is the bulk concentration of active species in solution, v is the scan rate and A is the electrode surface area.

In the case of a hemispherical electrode, the limiting current (steady state) is explained by the equation 1.10:

$$I_{lim} = 2\pi n F c_{bulk} D r \qquad Eq. \ 1.10$$

where r is the radius of the electrode. In the case of an array of microelectrodes, where their shape is a hemispherical one, it is considered that one electrode

should be distant for at least a value equal to $10r$ to its nearest neighbour to be diffusionally independent. In this way, the total current for a particular area A of the nanoparticle array is:

$$I_{total} = I_{lim}A(10r)^{-2} \qquad \qquad Eq.\ 1.11$$

Taking typical values for the parameters of $n=1$, $D=1\ 10^{-5}\ cm^2\ s^{-1}$, $c_{bulk}=1\cdot10^{-6}$ mol cm^{-3}, $v=1\cdot10^{-2}\ V\ s^{-1}$ and $A=1\ cm^2$, the peak current for different electrodes can be estimated as follow:

Macroelectrode: $I = 85\cdot10^{-6}$ A

Nanoparticles array ($r = 1$ μm, 10 r spacing): $I = 6\cdot10^{-4}$ A

($r = 100$ nm, 10 r spacing): $I = 6\cdot10^{-3}$ A

This calculation illustrates a potentially great advantage of reducing the size of the nanoparticles in an array in theory. [32, 33]

1.3. Environmental applications.

Environmental protection could take a radical turn thanks to electroanalytical chemistry. Particularly alluring for on-site monitoring of priority pollutants and other environmental criteria are electrochemical sensors and detectors. Many of the requirements for on-site environmental analysis may be satisfied by such technologies. Decentralized clinical analysis has already benefited greatly from such capabilities. Despite its enormous potential for environmental monitoring, electrochemical sensors for pollution management are still in the early stages of development [34].

Inorganic ions, metal cations, organic chemicals and biomolecules can be analysed using trace analytical methods like electrochemical stripping analysis (ESA). The target analytes are preconcentrated on a working electrode, then released through a scan potential. This method has been acknowledged to be one of the best methods for the determination of metal traces [35-40]. Thanks to the possibility of miniaturization of electrochemical devices, it is possible to perform online and on-site analyses on environmental matrices.

In the sensor industry, nanotechnology has become increasingly popular in recent years. The use of materials at the nanoscale and the use of such technologies are thought to improve sensor performances. It has been found that nanomaterials provide a range of distinctive and fascinating physical and

chemical properties [41, 42]. Low-dimensional nanometer-sized materials and systems have opened up a new area of research in condensed-matter physics in recent decades. Apart from the above specified material groups, a diverse range of materials can be employed to fabricate nano sensors.

The fact that carbon can be used for so many different things makes it a unique element. There are many different forms of carbon, such as graphite, diamond, fullerenes and graphene. Carbon is an interesting element. Previous studies [43-47] have covered some of the most notable and recent developments made possible using carbon-based nanostructures in nanotechnology for the manufacture of chemical and biological sensors as well as their usage in the pharmaceutical and biomedical areas.

1.4. Emerging contaminants.

Emerging contaminants (ECs) are synthetic or naturally occurring chemicals or any microorganisms that are not commonly monitored in the environment but have the potential to enter the environment and cause known or suspected adverse ecological or human health effects [48]. In nature, most of these contaminants are organic in nature and typically occur in traces in the range of parts per trillion (ppt or ng/L) to parts per billion (ppb or µg/L) [49].

It is important to remember that most emerging contaminants are not brand-new or have only recently entered the environment. Still, the majority of newly found contaminants are already well-known pollutants with a recently identified mode of action (MOA) or adverse impact. As a result, the word "emerging" refers to both the contamination and the growing concern that it poses a problem. Thus, emerging contaminants are frequently referred to as "chemicals of emerging concern" or "contaminants of emerging concern" (CECs) [50, 51]. A growing number of scientists, engineers and members of the public are becoming concerned about contaminants of emerging concern that have been found throughout the hydrological cycle, including surface and groundwater, wastewater treatment plant effluents, and surface waterways. These contaminants have a detrimental effect on both terrestrial and aquatic life forms as well as human health. Such chemical compounds have long existed in environmental media; they date back to 2000 years ago, when lead, the oldest worldwide contaminant, appeared because of Roman and Greek overexploitation of lead mines [52]. From then, the trend gradually moves from traditional contaminants to contemporary nanomaterials, medications, personal care products, and so forth. Recent research has discovered many

chemical pollutants in both surface and groundwater. Other industrial chemicals that have been detected in the ng/L–g/L range include hormones and pharmaceuticals, insecticides, illegal narcotics, artificial sweeteners, personal care products, disinfection byproducts, perfluorinated compounds, and UV filters [53]. Emerging contaminants (ECs), which include medicines, X-ray contrast media, cosmetics, and personal hygiene items, have been discovered in wastewater, groundwater, and surface waters [54-71].

These pollutants enter the groundwater, pass through wastewater treatment plants, and eventually leak into receiving rivers after entering the environment through leaking sewage pipelines and septic systems. Different pathways allow ECs to enter the aquatic environment: surface runoff from urban or agricultural areas where treated sludge/wastewater or manure Refuse is applied for irrigation; direct discharge of treated or raw wastewater from municipal, industrial wastewater treatment plants (WWTPs), hospitals; sewer overflow/leakage; and landfill leachate. Due to the widespread use of these substances and the dearth of suitable removal techniques, such as adsorption, ozonation, and their mixtures, several ECs are frequently linked to discharges from WWTPs [72].

The truth is that WWTPs are not specifically meant to get rid of many of these compounds because they are not currently covered by the wastewater treatment laws that are in place (Directive 2000/60/EC, Directive 2008/56/EC, and Directive 2013/39/EU). Consequently, research has demonstrated that WWTPs only eliminate <25% of several ECs, including diclofenac and carbamazepine. Continuous discharges support a variety of aquatic habitats at sublethal concentrations that could lead to several CEC reaching chronic levels (low g/L range) [73-75].

Other environmental contaminants (ECs) include leftovers from recreational drug use and their metabolites, as well as agricultural chemicals that are not frequently monitored, such as various herbicides, insecticides,and medications used in animal husbandry [76-80].

A schematic illustration of the routes via which ECs enter the environment is presented in Figure 1.5.
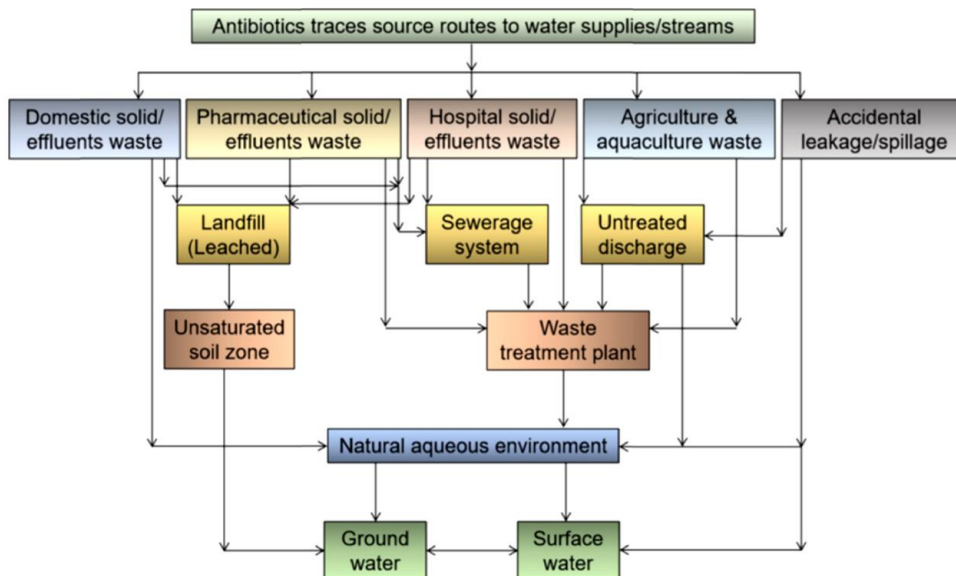
Figure 1.5 - Diagram showing pathways of emerging pollutants from sources to environment (taken from [81]).

ECs are often bioaccumulative and bioactive. Both a broad occurrence and a long-lasting presence are feasible. Global population growth is expected to increase the concentration of ECs in the environment and the number of contaminated ecosystems, especially in high-density areas. Since there is no regulation and a vast amount of ECs are present, it is essential to regularly monitor, examine, and report on the likelihood that ECs exist in water supplies and wastewater discharges as well as any possible toxicity. Because of the low concentration levels required, the complexity of the samples, and the difficulties in separating these compounds, it is difficult to contaminate the environment (water, soils, wastewater, and river sediments) with these pollutants [82].

Long-term exposure to these chemicals can be detrimental, even though EC values in aquatic sources have been shown to range from ng/L to g/L [83-85]. The adoption of the best treatment practices for guaranteeing the use of water that is safe for the general population to drink requires knowledge of the identification of emerging pollutants in water and technological developments for their removal.

A particular class of EC that has received much attention recently is known as disruptive endocrine chemicals (EDCs). The Endocrine Society defines EDCs as follows: "*an exogenous (non-natural) chemical, or a mixture of chemicals,*

18

that interferes with any aspect of hormone action." By acting as hormone antagonists, imitating hormones, influencing the development of hormone receptors, altering hormone binding, or disrupting hormone production, these substances have a variety of effects on the body's hormonal balance. Pharmaceuticals and personal care products (PPCPs), synthetic chemicals used as industrial solvents/lubricants and their byproducts, plastics (bisphenol A (BPA), polybrominated biphenyls (PBBs), dioxins, and plasticizers (phthalates)) are among the many molecules that are considered endocrine disruptors [86]. EDCs have demonstrated physiological activity at concentrations as low as a few nanograms per litre of solution. As seen in Figure 1.6, EDCs accumulate into the environment, particularly waterways, through a variety of routes. These pathways can be point-sources (like landfills, industrial wastewaters, and municipal sewage) or non-point sources (such agricultural runoff subterranean contamination).
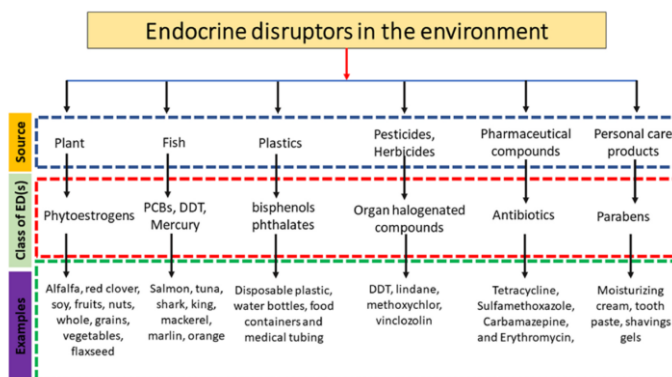
Figure 1.6 – Various sources of endocrine disruptor compounds (EDCs) (taken from [87]).

These manufactured or natural compounds mimic biological hormones, which have been linked to significant alterations in the natural processes of several species, such as fish and animals [88, 89]. The scientific community is paying more and more attention to pharmaceutical and personal care products (PPCPs), which are part of the expanding category of contaminants. Among them are analgesics, antiseptics, antibiotics, and a variety of other substances. It is more difficult to identify and eliminate polar functional groups from this class of pollutants because they are more prevalent [90].

According to a study by Jiang *et al.* [91], ECs are identified in the environments of 14 countries and are investigated for their presence, destiny, and migration. Jiang *et al.*'s data [91] show that over 80 different types of PCPs, EDCs, and pharmaceuticals were detected in treated and untreated sewage, streams, lakes, oceans, sediments, and even tap water. ECs have been found in wastewater,

groundwater, and surface water. Only a small number have been found in the environment, though. When directly detected at the outflow of wastewater and sewage treatment plants, their concentration is usually increased because of processes such volatilization, photolysis, biodegradation, sorption or a combination of these.

However, because of photolysis, biodegradation, volatilization, sorption or a combination of these activities, it is usually lower when measured in surface waters [92, 93]. However, the main place where wastewater treatment plant effluents end up is in surface waters. The magnitude and concentration levels recorded in surface waters are generally larger than in groundwaters because surface water residence times are shorter than groundwater residence times [94]. Groundwater ECs have been found in the environment most frequently in the following substances: ibuprofen, sulfamethoxazole, caffeine, bisphenol A, diclofenac, and carbamazepine [95]. The properties of the material presents are influenced by the source of the ECs. Environmental factors and physicochemical traits, such as water solubility, temperature, polarity, volatility, organic matter content, pH, precipitation, altitude, and latitude, also affect the transit and conversion of ECs. When estimating an EC's life expectancy in the environment, these considerations need to be taken into account. There are many different types and quantities of ECs sources. There are two categories of pollution sources: point and diffuse [96].

These include manufactured items in the home, human and animal waste, drugs that shouldn't be flushed, landfills, industrial facilities, mining operations, and food processing facilities. Processed municipal and industrial wastewater from wastewater treatment plants in the urban, industrial, and agricultural sectors, as well as other areas, is the main source of pollution [97-102]. Synthetic steroids and natural hormones (PPCPs) are major point sources of numerous environmental pollutants. According to current estimations, over 30% of medications sold in Germany and 25% of pharmaceuticals sold in Austria are disposed of as expired or unused drugs [103-105]. Hospital wastewater contains some very persistent chemicals, such as diatrizoate, iopamidol and iopromide, which have been detected in both groundwater and surface water [106-109]. Due to their toxicity, landfill sites are also a major source of ECs, or polychlorinated compounds, which are especially common in groundwater. Numerous countries, such as Denmark [110], the United States [111], and Croatia [111, 112], have documented pharmaceutical compounds contaminating groundwater in their waste areas [113]. It is well recognized that farms with animal production are point sources of estrogenic compounds in the

surrounding water. Steroid hormones and veterinary medications are among the numerous physiologically active substances that are both sourced and sunk by soils and river sediments.

Compared to concentrated sources, diffuse sources—such as stormwater runoff, terrestrial runoff from roads, cities, highways and agricultural land—typically release smaller amounts of contaminants into the environment [114]. Most people agree that one of the biggest causes of pollution in agriculture is pesticide use. In the German lakes of Tegel and Wannsee, herbicides (mecocrop and bentazone) and pesticides (two DDT metabolites) were found, along with flame-retardant substances (Tris(2-chloroethyl)-phosphate and Tris (2-chloroisopropyl)-9-phosphate), which were employed to artificially replenish the local aquifer [115]. Groundwater sources may be impacted by chemical pollutants (ECs) present in biosolids from wastewater treatment facilities that are applied to land [116-118].

1.4.1. Impact of ECs on ecosystems and human health.

Emerging pollutants' effects on animals are extensively documented. However, research on the direct effects on people is still ongoing. As seen in Figure 1.7, even minute quantities of ECs present a serious risk to human health. The major way that humans are exposed to endocrine-disrupting chemicals (EDCs) is through the consumption of food and drink items that have been tainted by microorganisms, contaminated soil, water, plants or animals. For animals at the top of the food chain in particular, this can take the form of biomagnification and bioaccumulation. The toxicity and effects of heavy metal ions and EDCs, such as bisphenol-A (BPA), which is mostly present in WWTPs, landfills, surface runoff and seepage, are not well understood, though [119, 120]. Numerous investigations into the long-term effects of ECs compounds have shown a significant impact. For instance, a six-week study on female *Danio rerio* subjected to a pharmacological cocktail (carbamazepine, acetaminophen, gemfibrozil, and venlafaxine) revealed a significant reduction in embryo development [121].
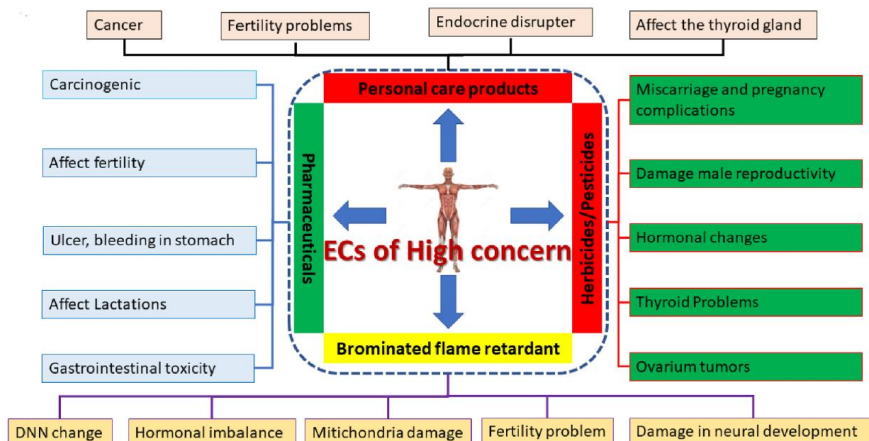
Figure 1.7 - Major impacts and harmful effects on human health of emerging contaminants (taken from [87]).

Because medications are water-soluble, it is impossible to separate them significantly in an aqueous solution. Pharmaceuticals can cross biological barriers and stay stable in the human body because they are made to perform a variety of physiological and biochemical tasks. The potential for pharmacologically active chemicals to accumulate and to harm species other than those for which they are intended for usage raises serious concerns. Exposure to these compounds causes harm to an animal's physiology. Studies were conducted on the ecotoxic effects of pharmacological orthologs (human) on sixteen distinct animals. It was revealed that zebrafish, daphnids, and a green alga contained 86%, 61%, and 35% of the orthologs [122]. Antibiotics that are used as growth promoters, medicines, prophylactics or in food (milk, meat, eggs, fruits, vegetables, and fish) might be harmful to your health. Aquatic items have been found to contain thiam-phenicol, erythromycin, sarafloxacin and oxytetracycline.

The quantities of ciprofloxacin and enrofloxacin in vegetables were found to range from 2.5–27.5 mg/kg and 2.0–32.3 mg/kg, respectively [123].

Antibiotics have also been demonstrated to go from a plant's root to its stem and leaf. Due to their high solubility, pesticides can be absorbed by biological organisms in a variety of ways. Some of these chemicals may function as endocrine disruptors, changing hormone levels, as the US Environmental Protection Agency has previously stated in a document [124, 125].

Buzea *et al.* [126] claim that a number of variables, such as exposure, size, shape, chemistry, electromagnetic properties and aggregation state of the NPs, as well as pre-existing diseases and genetics, influence how harmful nanoparticles are to human health. There is a clear link between respiratory and

cardiovascular disorders and particle air pollution, according to recent epidemiological studies. Particulate air pollution levels, malignancies, deaths and respiratory and cardiovascular illnesses are strongly correlated, according to recent epidemiological study. Numerous nanomaterials have the ability to cause in vitro cytotoxicity and reactive oxygen species. Additionally, they are able to pass through biological barriers such blood-brain barriers and cell membranes [127-130].

1.5.   Aim of this PhD thesis.

Considering all the above-mentioned features, the great advantages in the use of electrochemical sensors in analytical chemistry is the reason of the interest of many scientists in such a field. The number of works about electrochemical sensors is growing drastically over time and the potentialities of these devices are dramatically expanding.

The focus of this PhD thesis will be the study of different new and smart materials for electrochemical sensing. At first titanium dioxide based electrochemical sensors will be studied. TiO_2 properties and the effect of sol aging on the electrochemical sensor performances will be studied in Chapter 2. In Chapter 3, the photoelectrochemical properties will be studied in hybrid systems made of titanium dioxide and gold nanoparticles. In Chapter 4, this system will be implemented with a layer of mesoporous silica, to also have charge and size exclusion effects. In Chapter 5, the titanium dioxide layer will be deposited on a microelectrode, to study its photo-renewable property. Finally, in Chapter 6, a system composed of multi-walled carbon nanotubes (MWCNTs) and oligo-BT_2T_4 (an inherently chiral polymer) will be studied for the first time for its catalytic and enantioselective properties.

All these systems will be applied for the detection of different analytes, in particular for emerging contaminants.

1.6. Bibliography.

[1] Hulanicki, A.; Glab, S.; Ingman, F. Chemical sensors: Definitions and classification. *Pure Appl. Chem.* **1991**, 63, 1247–1250.

[2] Miri, P.S.; Khosroshahi, N.; Darabi Goudarzi, M.; Safarifard, V. MOF-biomolecule nanocomposites for electrosensing. *Nanochem. Res.* **2021**, 6, 213–222.

[3] Shetti, N.P.; Nayak, D.S.; Reddy, K.R.; Aminabhvi, T.M. Graphene–Clay-Based Hybrid Nanostructures for Electrochemical Sensors and Biosensors. In Graphene-Based Electrochemical Sensors for Biomolecules; *Elsevier*, **2019**; pp. 235–274.

[4] Meti, M.D.; Abbar, J.C.; Lin, J.; Han, Q.; Zheng, Y.; Wang, Y.; Huang, J.; Xu, X.; Hu, Z.; Xu, H. Nanostructured Au-graphene modified electrode for electrosensing of chlorzoxazone and its biomedical applications. *Mater. Chem. Phys.* **2021**, 266.

[5] Neiva, E.G.C.; Bergamini, M.F.; Oliveira, M.M.; Marcolino, L.H.; Zarbin, A.J.G. PVP-capped nickel nanoparticles: Synthesis, characterisation and utilization as a glycerol electrosensor. *Sens. Actuators B Chem.* **2014**, 196, 574–581.

[6] Yoshinobu, T.; Schöning, M.J. Light-addressable potentiometric sensors for cell monitoring and biosensing. *Curr. Opin. Electrochem.* **2021**, 28, 100727.

[7] Isildak, Ö.; Özbek, O. Application of Potentiometric Sensors in Real Samples. *Crit. Rev. Anal. Chem.* **2020**, 51, 218–231.

[8] ElDin, N.B.; El-Rahman, M.K.A.; Zaazaa, H.E.; Moustafa, A.A.; Hassan, S.A. Microfabricated potentiometric sensor for personalized methacholine challenge tests during the COVID-19 pandemic. *Biosens. Bioelectron.* **2021**, 190, 113439.

[9] Cuartero, M.; Parrilla, M.; Crespo, G. Wearable Potentiometric Sensors for Medical Applications. *Sensors* **2019**, 19, 363.

[10] Bohnke, C.; Duroy, H.; Fourquet, J.L. pH sensors with lithium lanthanum titanate sensitive material: Applications in food industry. *Sens. Actuators B Chem.* **2003**, 89, 240–247.

[11] Yuskina, E.; Tugashov, K.; Shur, V.B.; Tikhonova, I.A.; Babain, V.; Kirsanov, D. Cross-Sensitive Potentiometric Sensors Based on Anti-Crown

(C_6HgF_4)$_3$. In Proceedings of the 1st International Electronic Conference on Chemical Sensors and Analytical Chemistry, Online, 1–15 July 2021.

[12] Trujillo, R.M.; Barraza, D.E.; Zamora, M.L.; Cattani-Scholz, A.; Madrid, R.E. Nanostructures in Hydrogen Peroxide Sensing. *Sensors* **2021**, 21, 2204.

[13] Cho, G.; Azzouzi, S.; Zucchi, G.; Lebental, B. Electrical and Electrochemical Sensors Based on Carbon Nanotubes for the Monitoring of Chemicals in Water—A Review. *Sensors* **2021**, 22, 218.

[14] Hu, J.; Sang, G.; Zeng, N.; Lv, C.; Xu, C. Amperometric sensor for the detection of hydrogen stable isotopes based on Pt nanoparticles confined within single-walled carbon nanotubes (SWNTs). *Sens. Actuators B Chem.* **2022**, 356, 131344.

[15] Stasyuk, N.Y.; Gayda, G.Z.; Zakalskiy, A.E.; Fayura, L.R.; Zakalska, O.M.; Sibirny, A.A.; Nisnevitch, M.; Gonchar, M.V. Amperometric biosensors for L-arginine and creatinine assay based on recombinant deiminases and ammonium-sensitive Cu/Zn(Hg)S nanoparticles. *Talanta* **2022**, 238, 122996.

[16] Matthews, C.J.; Andrews, E.S.V.; Patrick,W.M. Enzyme-based amperometric biosensors for malic acid—A review. *Anal. Chim. Acta* **2021**, 1156, 338218.

[17] Emir, G.; Dilgin, Y.; Ramanaviciene, A.; Ramanavicius, A. Amperometric nonenzymatic glucose biosensor based on graphite rod electrode modified by Ni-nanoparticle/polypyrrole composite. *Microchem. J.* **2021**, 161, 105751.

[18] Grieshaber D, MacKenzie R, Voeroes J, Reimhult E. Electrochemical biosensors-sensor principles and architectures. *Sensors* **2008**; 8(3):1400-58.

[19] Yilong Z, Dean Z, Daoliang L. Electrochemical and other methods for detection and determination of dissolved nitrite: A review. *Int. J. Electrochem. Sci.* **2015** Feb 1;10:1144-68.

[20] Stradiotto NR, Yamanaka H, Zanoni MV. Electrochemical sensors: a powerful tool in analytical chemistry. *Journal of the Brazilian Chemical Society* **2003** Apr;14(2):159-73.

[21] Thévenot, D.R.; Toth, K.; Durst, R.A.; Wilson, G.S. Electrochemical biosensors: Recommended definitions and classification 1 International Union of Pure and Applied Chemistry: Physical Chemistry Division, Commission I.7 (Biophysical Chemistry); Analytical Chemistry Division, Commission V.5 (Electroanalytical Chemistry) 1. *Biosens. Bioelectron.* **2001**, 16, 121–131.

[22] Fatibello-Filho, O. Potentiometric Biosensors. In Tools and Trends in Bioanalytical Chemistry; *Springer International Publishing: Cham, Switzerland*, **2022**; pp. 265–272.

[23] Haritha, V.S.; Kumar, S.R.S.; Rakhi, R.B. Amperometric cholesterol biosensor based on cholesterol oxidase and Pt-Au/ MWNTs modified glassy carbon electrode. *Mater. Today Proc.* **2022**, 50, 34–39.

[24] Soldatkin, O.O.; Soldatkina, O.V.; Piliponskiy, I.I.; Rieznichenko, L.S.; Gruzina, T.G.; Dybkova, S.M.; Dzyadevych, S.V.; Soldatkin, A.P. Correction to: Application of gold nanoparticles for improvement of analytical characteristics of conductometric enzyme biosensors. *Appl. Nanosci.* **2021**, 12, 1005.

[25] Zhou, Y.; Kubota, L.T. Trends in Electrochemical Sensing. *ChemElectroChem* **2020**, 7, 3684–3685.

[26] Castillo, J.; Gáspár, S.; Leth, S.; Niculescu, M.; Mortari, A.; Bontidean, I.; Soukharev, V.; Dorneanu, S.A.; Ryabov, A.D.; Csöregi, E. Biosensors for life quality. *Sens. Actuators B Chem.* **2004**, 102, 179–194.

[27] Chaubey, A.; Malhotra, B.D. Mediated biosensors. *Biosens. Bioelectron.* **2002**, 17, 441–456.

[28] Llorent-Martínez, E.J.; Ortega-Barrales, P.; Fernández-de Córdova, M.L.; Ruiz-Medina, A. Trends in flow-based analytical methods applied to pesticide detection: A review. *Anal. Chim. Acta* **2011**, 684, 30–39.

[29] Fick, A. Uber Diffusion. *Poggendorff's Annel. Phys.* **1855**, 94, 59.

[30] Buzzeo, M. C.; Evans, R. G.; Compton, R. G. Non-Haloaluminate Room-Temperature Ionic Liquids in Electrochemistry - A Review. *ChemPhysChem* **2004**, 5 (8), 1106–1120.

[31] Compton, R. G.; Banks, C. E. Understanding Voltammetry; *Imperial College Press*, London, **2001**.

[32] Welch, C. M.; Compton, R. G. The Use of Nanoparticles in Electroanalysis: A Review. *Anal. Bioanal. Chem.* **2006**, 384, 601–619.

[33] Campbell, F. W.; Compton, R. G. The Use of Nanoparticles in Electroanalysis: An Updated Review. *Anal. Bioanal. Chem.* **2010**, 396 (1), 241–259.

[34] Moro, G.; De Wael, K.; Moretto, L.M. Challenges in the electrochemical (bio)sensing of nonelectroactive food and environmental contaminants. *Curr. Opin. Electrochem.* **2019**, 16, 57–65.

[35] Rahman, M.; Kumar, P.; Park, D.-S.; Shim, Y.-B. Electrochemical Sensors Based on Organic Conjugated Polymers. *Sensors* **2008**, 8, 118–141.

[36] Ariño, C.; Banks, C.E.; Bobrowski, A.; Crapnell, R.D.; Economou, A.; Królicka, A.; Pérez-Ràfols, C.; Soulis, D.; Wang, J. Electrochemical stripping analysis. *Nat. Rev. Methods Prim.* **2022**, 2, 63.

[37] Lin, X.-Y.; Zhou, Q.-W.; Huo, X.-L.; Bao, N. Copper tape to improve analytical performance of disposable carbon electrodes in stripping analysis. *Microchem. J.* **2022**, 179, 107428.

[38] Liu, Q.; Liu, L.; Perdicakis, M.; Walcarius, A. Electrochemical stripping analysis from micro-counter electrode. *Electrochim. Acta* **2021**, 393, 139095

[39] Mohamad Nor, N.; Arivalakan, S.; Zakaria, N.D.; Nilamani, N.; Lockman, Z.; Abdul Razak, K. Self-Assembled Iron Oxide Nanoparticle-Modified APTES-ITO Electrode for Simultaneous Stripping Analysis of Cd(II) and Pb(II) Ions. *ACS Omega* **2022**, 7, 3823–3833.

[40] Jovanovski, V.; Xhanari, K.; Finšgar, M. Editorial: Recent advances of metal-film electrodes for trace electrochemical analysis. *Front. Chem.* **2022**, 10, 973672.

[41] Senocak, A.; Sanko, V.; Tümay, S.O.; Orooji, Y.; Demirbas, E.; Yoon, Y.; Khataee, A. Ultrasensitive electrochemical sensor for detection of rutin antioxidant by layered $Ti_3Al_{0.5}Cu_{0.5}C_2$ MAX phase. *Food Chem. Toxicol.* **2022**, 164, 113016.

[42] Kurbanoglu, S.; Ozkan, S.A. Electrochemical carbon based nanosensors: A promising tool in pharmaceutical and biomedical analysis. *J. Pharm. Biomed. Anal.* **2018**, 147, 439–457.

[43] Sanchez, F.; Sobolev, K. Nanotechnology in concrete—A review. *Constr. Build. Mater.* **2010**, 24, 2060–2071.

[44] Bhushan, B. Springer Handbook of Nanotechnology; *Springer*: Berlin/Heidelberg, Germany, **2007**.

[45] Pérez-López, B.; Merkoçi, A. Nanomaterials based biosensors for food analysis applications. *Trends Food Sci. Technol.* **2011**, 22, 625–639.

[46] Pandey, P.; Datta, M.; Malhotra, B.D. Prospects of Nanomaterials in *Biosensors. Anal. Lett.* **2008**, 41, 159–209.

[47] Petrie, A.A.; van der Ven, A.M.; Honek, J.F. Nanomaterial-based biosensors. In Biosensors and Their Applications in Healthcare; *Future Science Group: London*, *UK*, **2013**; pp. 68–82.

[48] T. Smital, in: D. Barcelò, M. Petrovic (Eds.), Acute and Chronic Effects of Emerging Contaminants BT - Emerging Contaminants from Industrial and Municipal Waste: Occurrence, Analysis and Effects, *Springer Berlin Heidelberg, Berlin, Heidelberg*, **2008**, pp. 105–142.

[49] O.M. Rodriguez-Narvaez, J.M. Peralta-Hernandez, A. Goonetilleke, E.R. Bandala, Treatment technologies for emerging contaminants in water: a review, *Chem. Eng. J.* **2017**, 323, 361–380.

[50] P.E. Rosenfeld, L.G.H. Feng, B.T.-R., Emerging Contaminants, *William Andrew Publishing, Boston*, **2011**, pp. 215–222.

[51] A. Gogoi, P. Mazumder, V.K. Tyagi, G.G. Tushara Chaminda, A.K. An, M. Kumar, Occurrence and fate of emerging contaminants in water environment: a review, *Groundw. Sustain. Dev.* **2018**, 6, 169–180.

[52] S. Sauvé, M. Desrosiers, A review of what is an emerging contaminant, *Chem. Cent. J.*, **2014**, 8.

[53] F. Riva, S. Castiglioni, E. Fattore, A. Manenti, E. Davoli, E. Zuccato, Monitoring emerging contaminants in the drinking water of Milan and assessment of the human risk, *Int. J. Hyg Environ. Health* **2018**, 221, 451–457.

[54] C.H. Swartz, S. Reddy, M.J. Benotti, H. Yin, L.B. Barber, B.J. Brownawell, R. A. Rudel, Steroid estrogens, nonylphenol ethoxylate metabolites, and other wastewater contaminants in groundwater affected by a residential septic system on cape cod, MA, *Environ. Sci. Technol.* **2006**, 40, 4894–4902.

[55] D.S. Aga (Ed.), Fate of Pharmaceuticals in the Environment and in Water Treatment Systems, 1st Edition, *CRC press*, Boca Raton, **2007**.

[56] Y. Cabeza, L. Candela, D. Ronen, G. Teijon, Monitoring the occurrence of emerging contaminants in treated wastewater and groundwater between 2008 and 2010. The Baix Llobregat (Barcelona, Spain), *J. Hazard Mater.* **2012,** 239–240.

[57] R. Lòpez-Serna, A. Jurado, E. Vàzquez-Suñé, J. Carrera, M. Petrovic, D. Barcelò, Occurrence of 95 pharmaceuticals and transformation products in urban, *J. Envpol.* **2013** 305–315.

[58] R. Meffe, C. Kohfahl, E. Hamann, J. Greskowiak, G. Massmann, U. Dünnbier, A. Pekdeger, Fate of para-toluenesulfonamide (p-TSA) in groundwater under anoxic conditions: modelling results from a field site in Berlin (Germany), *Environ. Sci. Pollut. Res.* **2014**, 21, 568–583.

[59] D. Gao, Z. Li, Z. Wen, N. Ren, Occurrence and fate of phthalate esters in full-scale domestic wastewater treatment plants and their impact on receiving waters along the Songhua River in China, *Chemosphere* **2014**, 95, 24–32.

[60] J.O. Tijani, O.O. Fatoba, L.F. Petrik, A review of pharmaceuticals and endocrinedisrupting compounds: sources, effects, removal, and detections, *Water, Air, Soil Pollut.* **2013**, 224, 1770.

[61] S. Keerthanan, C. Jayasinghe, J.K. Biswas, M. Vithanage, Pharmaceutical and Personal Care Products (PPCPs) in the environment: plant uptake, translocation, bioaccumulation, and human health risks, *Crit. Rev. Environ. Sci. Technol.* **2021**, 51, 1221–1258.

[62] N.A. Khan, V. Vambol, S. Vambol, B. Bolibrukh, M. Sillanpaa, F. Changani, A. Esrafili, M. Yousefi, Hospital effluent guidelines and legislation scenario around the globe: a critical review, *J. Environ. Chem. Eng.* **2021**, 9, 105874.

[63] P.R. Rout, T.C. Zhang, P. Bhunia, R.Y. Surampalli, Treatment technologies for emerging contaminants in wastewater treatment plants: a review, *Sci. Total Environ.* **2021**, 753, 141990.

[64] E. Godfrey, W.W. Woessner, M.J. Benotti, Pharmaceuticals in on-site sewage effluent and ground water, Western Montana, *Ground Water* **2007**, 45, 263–271.

[65] K.K. Barnes, D.W. Kolpin, E.T. Furlong, S.D. Zaugg, M.T. Meyer, L.B. Barber, A national reconnaissance of pharmaceuticals and other organic wastewater contaminants in the United States — I) Groundwater, *Sci. Total Environ.* **2008**, 402, 192–200.

[66] M. Fürhacker, The Water Framework Directive – can we reach the target? *Water Sci. Technol.* **2008**, 57, 9–17.

[67] R. Loos, B.M. Gawlik, G. Locoro, E. Rimaviciute, S. Contini, G. Bidoglio, EU-wide survey of polar organic persistent pollutants in European river waters, *Environ. Pollut.* **2009**, 157, 561–568.

[68] S. Pérez, M. Köck, L. Tong, A. Ginebreda, R. Lòpez-Serna, C. Postigo, R. Brix, M. L. de Alda, M. Petrovic, Y. Wang, *et al.*, Wastewater Reuse in the Mediterranean Area of Catalonia, Spain: Case Study of Reuse of Tertiary Effluent from a Wastewater Treatment Plant at el Prat de Llobregat (Barcelona) BT - Waste Water Treatment and Reuse in the Mediterranean Region, *Springer Berlin Heidelberg, Berlin, Heidelberg*, **2011**, pp. 249–294.

[69] G. Teijon, L. Candela, K. Tamoh, A. Molina-Díaz, A.R. Fernàndez-Alba, Occurrence of emerging contaminants, priority substances (2008/105/CE) and heavy metals in treated wastewater and groundwater at Depurbaix facility (Barcelona, Spain), *Sci. Total Environ.* **2010**, 408, 3584–3595.

[70] B.F. da Silva, A. Jelic, R. Lòpez-Serna, A.A. Mozeto, M. Petrovic, D. Barcelò, Occurrence and distribution of pharmaceuticals in surface water, suspended solids and sediments of the Ebro River basin, Spain, *Chemosphere* **2011**, 85, 1331–1339.

[71] Y. Valcàrcel, S. Gonzàlez Alonso, J.L. Rodríguez-Gil, A. Gil, M. Català, Detection of pharmaceutically active compounds in the rivers and tap water of the Madrid Region (Spain) and potential ecotoxicological risk, *Chemosphere* **2011**, 84, 1336–1348.

[72] N.H. Tran, M. Reinhard, K.Y.-H. Gin, Occurrence and fate of emerging contaminants in municipal wastewater treatment plants from different geographical regions-a review, *Water Res.* **2018**, 133, 182–207.

[73] C. Prasse, D. Stalter, U. Schulte-Oehlmann, J. Oehlmann, T.A. Ternes, Spoilt for choice: a critical review on the chemical and biological assessment of current wastewater treatment technologies, *Water Res.* **2015**, 87, 237–270.

[74] D. Montes-Grajales, M. Fennix-Agudelo, W. Miranda-Castro, Occurrence of personal care products as emerging chemicals of concern in water resources: a review, *Sci. Total Environ.* **2017**, 595, 601–614.

[75] L.C. Pereira, A.O. de Souza, M.F.F. Bernardes, M. Pazin, M.J. Tasso, P.H. Pereira, D.J. Dorta, A perspective on the potential risks of emerging contaminants to human and environmental health, *Environ. Sci. Pollut. Res.* **2015**, 22.

[76] E.J. Rosi-Marshall, D. Snow, S.L. Bartelt-Hunt, A. Paspalof, J.L. Tank, A review of ecological effects and environmental fate of illicit drugs in aquatic ecosystems, *J. Hazard Mater.* **2015**, 282, 18–25

[77] J. Wilkinson, P.S. Hooda, J. Barker, S. Barton, J. Swinden, Occurrence, fate and transformation of emerging contaminants in water: an overarching review of the field, *Environ. Pollut.* **2017**, 231, 954–970.

[78] M. Patel, R. Kumar, K. Kishor, T. Mlsna, C.U. Pittman, D. Mohan, Pharmaceuticals of emerging concern in aquatic systems: chemistry, occurrence, effects, and removal methods, *Chem. Rev.* **2019**, 119, 3510–3673.

[79] B.S. Rathi, P.S. Kumar, P.-L. Show, A review on effective removal of emerging contaminants from aquatic systems: current trends and scope for further research, *J. Hazard Mater.* **2021**, 409, 124413.

[80] B.S. Rathi, P.S. Kumar, Application of adsorption process for effective removal of emerging contaminants from water and wastewater, *Environ. Pollut.* **2021**, 280, 116995.

[81] M. Bilal, S.S. Ashraf, D. Barcelò, H.M.N. Iqbal, Biocatalytic degradation/redefining "removal" fate of pharmaceutically active compounds and antibiotics in the aquatic environment, *Sci. Total Environ.* **2019**, 691, 1190–1211.

[82] D.D. Snow, D.A. Cassada, S. Biswas, A. Malakar, M. D'Alessio, L.J. Carter, R. D. Johnson, J.B. Sallach, Detection, occurrence, and fate of emerging contaminants in agricultural environments, *Water Environ. Res.* **2019**, 91, 1103–1113.

[83] P.R. Rout, T.C. Zhang, P. Bhunia, R.Y. Surampalli, Treatment technologies for emerging contaminants in wastewater treatment plants: a review, *Sci. Total Environ.* **2021**, 753, 141990.

[84] S. Gheorghe, J. Petre, I. Lucaciu, C. Stoica, M. Nita-Lazar, Risk screening of pharmaceutical compounds in Romanian aquatic environment, *Environ. Monit. Assess.* **2016**, 188, 379.

[85] N. Liu, X. Jin, C. Feng, Z. Wang, F. Wu, A.C. Johnson, H. Xiao, H. Hollert, J. P. Giesy, Ecological risk assessment of fifty pharmaceuticals and personal care products (PPCPs) in Chinese surface waters: a proposed multiple-level system, *Environ. Int.* **2020**, 136, 105454.

[86] E. Diamanti-Kandarakis, J.-P. Bourguignon, L.C. Giudice, R. Hauser, G.S. Prins, A. M. Soto, R.T. Zoeller, A.C. Gore, Endocrine-disrupting chemicals: an endocrine society scientific statement, *Endocr. Rev.* **2009**, 30, 293–342.

[87] Rohitashw Kumar, Mahrukh Qureshi, Dinesh Kumar Vishwakarma, Nadhir Al-Ansari, Alban Kuriqi, Ahmed Elbeltagi, Anuj Saraswat, A review on emerging water contaminants and the application of sustainable removal technologies, *Case Studies in Chemical and Environmental Engineering* **2022**, 6, 100219.

[88] O. Braga, G.A. Smythe, A.I. Schäfer, A.J. Feitz, Fate of steroid oestrogens in Australian inland and coastal wastewater treatment plants, *Environ. Sci. Technol.* **2005**, 39, 3351–3358.

[89] K.D. Brown, J. Kulis, B. Thomson, T.H. Chapman, D.B. Mawhinney, Occurrence of antibiotics in hospital, residential, and dairy effluent, municipal wastewater, and the Rio Grande in New Mexico, *Sci. Total Environ.* **2006**, 366, 772–783.

[90] M. Wilson, M. Aqeel-Ashraf, Study of fate and transport of emergent contaminants at wastewater treatment plant, *Environ. Contam. Rev.* **2018**, 1, 1–12.

[91] [J.-Q. Jiang, Z. Zhou, V.K. Sharma, Occurrence, transportation, monitoring and treatment of emerging micro-pollutants in wastewater — a review from global views, Microchem. J. 110 (2013) 292–300, https://doi.org/10.1016/j.microc.2013.04.014

[92] C.J. Gurr, M. Reinhard, Harnessing natural attenuation of pharmaceuticals and hormones in rivers, Environ. Sci. Technol. 40 (2006) 2872–2876, https://doi.org/10.1021/es062677d.

[93] A. Pal, K.Y.-H. Gin, A.Y.-C. Lin, M. Reinhard, Impacts of emerging organic contaminants on freshwater resources: review of recent occurrences, sources, fate and effects, Sci. Total Environ. 408 (2010) 6062–6069, https://doi.org/10.1016/j.scitotenv.2010.09.026.

[94] [K.K. Barnes, D.W. Kolpin, E.T. Furlong, S.D. Zaugg, M.T. Meyer, L.B. Barber, A national reconnaissance of pharmaceuticals and other organic wastewater contaminants in the United States — I) Groundwater, Sci. Total Environ. 402 (2008) 192–200, https://doi.org/10.1016/j.scitotenv.2008.04.028.

[95] [D.J. Lapworth, N. Baran, M.E. Stuart, R.S. Ward, Emerging organic contaminants in groundwater: a review of sources, fate and occurrence, Environ. Pollut. 163 (2012) 287–303, https://doi.org/10.1016/j.envpol.2011.12.034]

[96] [D.J. Lapworth, N. Baran, M.E. Stuart, R.S. Ward, Emerging organic contaminants in groundwater: a review of sources, fate and occurrence, Environ. Pollut. 163 (2012) 287–303, https://doi.org/10.1016/j.envpol.2011.12.034

[97] A. Pal, K.Y.-H. Gin, A.Y.-C. Lin, M. Reinhard, Impacts of emerging organic contaminants on freshwater resources: review of recent occurrences, sources, fate and effects, Sci. Total Environ. 408 (2010) 6062–6069, https://doi.org/10.1016/j.scitotenv.2010.09.026.

[98] D.J. Lapworth, N. Baran, M.E. Stuart, R.S. Ward, Emerging organic contaminants in groundwater: a review of sources, fate and occurrence, Environ. Pollut. 163 (2012) 287–303, https://doi.org/10.1016/j.envpol.2011.12.034.

[99] S.T. Glassmeyer, E.T. Furlong, D.W. Kolpin, J.D. Cahill, S.D. Zaugg, S.L. Werner, M.T. Meyer, D.D. Kryak, Transport of chemical and microbial compounds from known wastewater discharges: potential for use as indicators of human fecal contamination, Environ. Sci. Technol. 39 (2005) 5157–5169, https://doi.org/10.1021/es048120k.

[100] R.O. Carey, K.W. Migliaccio, Contribution of wastewater treatment plant effluents to nutrient dynamics in aquatic systems: a review, *Environ. Manag.* **2009**, 44, 205–217.

[101] E. Iloms, O.O. Ololade, H.J.O. Ogola, R. Selvarajan, Investigating industrial effluent impact on municipal wastewater treatment plant in vaal, South Africa, *Int. J. Environ. Res. Publ. Health* **2020**, 17.

[102] W. Zielinski, E. Korzeniewska, M. Harnisz, J. Drzymała, E. Felis, S. Bajkacz, Wastewater treatment plants as a reservoir of integrase and antibiotic resistance genes – an epidemiological threat to workers and environment, *Environ. Int.* **2021**, 156, 106641.

[103] K. Kümmerer, in: K. Kümmerer (Ed.), Pharmaceuticals in the Environment – A Brief Summary - Pharmaceuticals in the Environment: Sources, Fate, Effects and Risks, *Springer Berlin Heidelberg, Berlin, Heidelberg*, **2008**, ISBN 978-3-540- 74664-5, pp. 3–21.

[104] K. Kümmerer, Pharmaceuticals in the Environment: Sources, Fate, Effects and Risks, *Springer Science & Business Media*, **2008**, ISBN 3540746641.

[105] K. Kümmerer, The presence of pharmaceuticals in the environment due to human use – present knowledge and future challenges, *J. Environ. Manag.* **2009**, 90, 2354–2366.

[106] R. Hirsch, T.A. Ternes, A. Lindart, K. Haberer, R.-D. Wilken, A sensitive method for the determination of iodine containing diagnostic agents in aqueous matrices using LC-electrospray-tandem-MS detection, *Fresenius' J. Anal. Chem.* **2000**, 366, 835–841.

[107] T.A. Ternes, R. Hirsch, Occurrence and behavior of X-ray contrast media in sewage facilities and the aquatic environment, *Environ. Sci. Technol.* **2000**, 34, 2741–2748.

[108] F. Sacher, F.T. Lange, H.-J. Brauch, I. Blankenhorn, Pharmaceuticals in groundwaters: analytical methods and results of a monitoring program in Baden- Württemberg, Germany, *J. Chromatogr. A* **2001**, 938, 199–210.

[109] M. Schulz, D. Löffler, M. Wagner, T.A. Ternes, Transformation of the X-ray contrast medium iopromide in soil and biological wastewater treatment, *Environ. Sci. Technol.* **2008**, 42, 7207–7217.

[110] J.V. Holm, K. Ruegge, P.L. Bjerg, T.H. Christensen, Occurrence and distribution of pharmaceutical organic compounds in the groundwater downgradient of a landfill (Grindsted, Denmark), *Environ. Sci. Technol.* **1995**, 29, 1415–1420.

[111] M. Ahel, N. Mikac, B. Cosovic, E. Prohic, V. Soukup, The impact of contamination from a municipal solid waste landfill (Zagreb, Croatia) on underlying soil, *Water Sci. Technol.* **1998**, 37, 203–210.

[112] N. Mikac, B. Cosovic, M. Ahel, S. Andreis, Z. Toncic, Assessment of groundwater contamination in the vicinity of a municipal solid waste landfill (Zagreb, Croatia), *Water Sci. Technol.* **1998**, 37, 37–44.

[113] P.M. Buszka, D.J. Yeskis, D.W. Kolpin, E.T. Furlong, S.D. Zaugg, M.T. Meyer, Waste-indicator and pharmaceutical compounds in landfill-leachate-affected ground water near Elkhart, Indiana, 2000-2002, *Bull. Environ. Contam. Toxicol.* **2009**, 82, 653–659.

[114] D.J. Lapworth, N. Baran, M.E. Stuart, R.S. Ward, Emerging organic contaminants in groundwater: a review of sources, fate and occurrence, *Environ. Pollut.* **2012**, 163, 287–303.

[115] T. Heberer, A. Mechlinski, B. Fanck, A. Knappe, G. Massmann, A. Pekdeger, B. Fritz, Field studies on the fate and transport of pharmaceutical residues in bank filtration, *Ground Water Monit. Remed.* **2004**, 24, 70–77.

[116] E. Topp, S.C. Monteiro, A. Beck, B.B. Coelho, A.B.A. Boxall, P.W. Duenk, S. Kleywegt, D.R. Lapen, M. Payne, L. Sabourin, *et al.*, Runoff of pharmaceuticals and personal care products following application of biosolids to an agricultural field, *Sci. Total Environ.* **2008**, 396, 52–59.

[117] L. Sabourin, A. Beck, P.W. Duenk, S. Kleywegt, D.R. Lapen, H. Li, C.D. Metcalfe, M. Payne, E. Topp, Runoff of pharmaceuticals and personal care products following application of dewatered municipal biosolids to an agricultural field, *Sci. Total Environ.* **2009**, 407, 4596–4604.

[118] B.O. Clarke, S.R. Smith, Review of 'emerging' organic contaminants in biosolids and assessment of international research priorities for the agricultural use of biosolids, *Environ. Int.* **2011**, 37, 226–247.

[119] K.E. Murray, S.M. Thomas, A.A. Bodour, Prioritizing research for trace pollutants and emerging contaminants in the freshwater environment, *Environ. Pollut.* **2010**, 158, 3462–3471.

[120] K.V. Thomas, M.J. Hilton, The occurrence of selected human pharmaceutical compounds in UK estuaries, *Mar. Pollut. Bull.* **2004**, 49, 436–444.

[121] M. Galus, J. Jeyaranjaan, E. Smith, H. Li, C. Metcalfe, J.Y. Wilson, Chronic effects of exposure to a pharmaceutical mixture and municipal wastewater in zebrafish, *Aquat. Toxicol.* **2013**, 132–133, 212–222.

[122] J. Roberts, A. Kumar, J. Du, C. Hepplewhite, D.J. Ellis, A.G. Christy, S.G. Beavis, Pharmaceuticals and personal care products (PPCPs) in Australia's largest inland sewage treatment plant, and its contribution to a major Australian river during high and low flow, *Sci. Total Environ.* **2016**, 541, 1625–1637.

[123] X.-W. Li, Y.-F. Xie, C.-L. Li, H.-N. Zhao, H. Zhao, N. Wang, J.-F. Wang, Investigation of residual fluoroquinolones in a soil–vegetable system in an intensive vegetable cultivation area in Northern China, *Sci. Total Environ.* **2014**, 468–469, 258–264.

[124] USEPA, Triazine Cumulative Risk Assessment, United States Environ. Prot. Agency, **2006**.

[125] F. Ji, L. Zhao, W. Yan, Q. Feng, J.-M. Lin, Determination of triazine herbicides in fruits and vegetables using dispersive solid-phase extraction coupled with LC–MS, *J. Separ. Sci.* **2008**, 31, 961–968.

[126] C. Buzea, I.I. Pacheco, K. Robbie, Nanomaterials and nanoparticles: sources and toxicity, *Biointerphases* **2007**, 2.

[127] T. Xia, M. Kovochich, J. Brant, M. Hotze, J. Sempf, T. Oberley, C. Sioutas, J.I. Yeh, M.R. Wiesner, A.E. Nel, Comparison of the abilities of ambient and manufactured paradigm, *Nano Lett.* **2006**, 6, 1794–1807.

[128] S. Foley, C. Crowley, M. Smaihi, C. Bonfils, B.F. Erlanger, P. Seta, C. Larroque, Cellular localisation of a water-soluble fullerene derivative, *Biochem. Biophys. Res. Commun.* **2002**, 294, 116–119.

[129] K. Shosaku, Distribution of nanoparticles in the see-through medaka (Oryzias latipes), *Environ. Health Perspect.* **2006**, 114, 1697–1702.

[130] J.S. Kim, T.-J. Yoon, K.N. Yu, B.G. Kim, S.J. Park, H.W. Kim, K.H. Lee, S.B. Park, J.-K. Lee, M.H. Cho, Toxicity and tissue distribution of magnetic nanoparticles in mice, *Toxicol. Sci.* **2006**, 89, 338–347.

2. Study of the sol aging.

2.1. Introduction.

As previously explained, one of the great advantages of electrochemical sensors is the possibility of modifying them with different materials, such as nanomaterials, semiconductors, enzymes, polymers.

Nanomaterials are chemicals ranging in at least one size from 1 to 100 nm. Nanomaterials occur in nature (such as pollen particles), produced unintentionally by human activities (for example by combustion) or are artificially produced (such as titanium dioxide). Nanomaterials are currently used in many sectors: engineering, technology information and communication, medicine, pharmaceuticals, textiles, chemicals, cosmetics, food. The European Commission has adopted the following definition of nanomaterial "*... By nanomaterial we mean a natural, derived or manufactured material containing particles in the free state, aggregated or agglomerated, and in which, for at least 50% of the particles in the numerical size distribution, one or more external dimensions are between 1 nm and 100 nm...* "[1].

Nanotechnology is one of the most promising technologies of the 21st century. It can convert nanoscience theory into useful applications by observing, measuring, manipulating, assembling, controlling, and producing matter at the nanoscale. There are two conditions for having the presence of nanotechnology: nanoscale and it should create novelty. There is a difference between nanoscience and nanotechnology. Nanoscience is a materials science concerned with manipulating materials at the atomic level and molecular scales; while nanotechnology is the ability to observe, measure, manipulate, assemble, control, and produce matter at the nanoscale [2].

Two possible approaches have been developed to describe the different possibilities of synthesis of nanostructures: top-down and bottom-up.

The bottom-up approach builds nanostructures from the bottom up: atom by atom or molecule by molecule with physical and chemical methods that are in nanoscale range (1 nm to 100 nm) using the controlled manipulation of the self-assembly of atoms and molecules. That is, we start from small particles (atoms) up to larger particles, *i.e.*, the structures are organized in an orderly way through chemical-physical interactions. The top-down approach is the decomposition of the bulk material to obtain particles of nanometric size. This can be achieved using advanced techniques such as precision engineering and lithography.
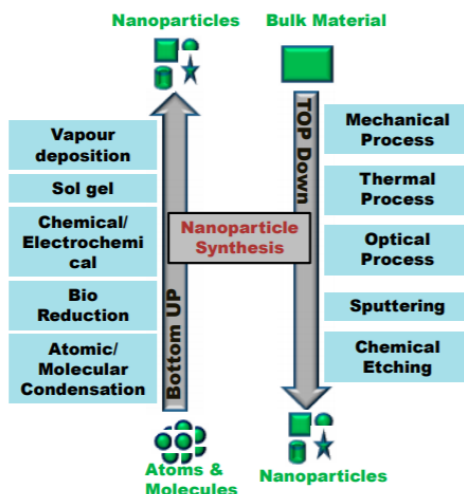
Figure 2.8 - The concept of top down and bottom-up technology: different methods for nanoparticle synthesis (taken from [2]).

2.1.1. Synthesis of gold nanoparticles (AuNPs).

In recent years, researchers have become increasingly interested in the synthesis of gold nanoparticles (AuNPs), due to their unique physical and chemical properties in broad areas such as catalysis, biomarking, non-linear optical devices and in the field of drug delivery [3]. AuNPs have exceptional optical properties because of surface plasmon resonance (SPR). Itis an optical phenomenon that occurs from the interaction between an electromagnetic wave and the conduction of electrons in a metal. This property makes AuNPs very useful in the fields of bioimaging and biomedical therapies and as biodiagnostic tools [4].

A variety of techniques have been introduced so far, by chemical, thermal, electrochemical routes. In general, the preparation of AuNPs by the chemical reduction method comprises two main parts: reduction by agents, such as borohydrides, aminoboranes, hydrazine, polyols, citric and oxalic acids, sulfites, acetylene and reducing agents; stabilization of agents, *e.g.*, thiolates, phosphorus binders, oxygen binders, nitrogen-based binders, polymers, and surfactants (CTAB). To avoid particle aggregation, some kind of stabilizing agent is usually added [5].

One of the best-known techniques for the synthesis of AuNPs is the one devised by Turkevich, based on the reduction of $HAuCl_4$ by citrate in water. In this method, the $HAuCl_4$ solution is boiled and the trisodium citrate dihydrate

is added rapidly to the boiling solution under vigorous stirring. After a few minutes the colour of the solution changes from light yellow to wine red. This method produces AuNPs that measure approximately 20 nm in diameter. Hence, citrate ions play a double role, both as stabilizing agents and as reducing agents [6, 7].
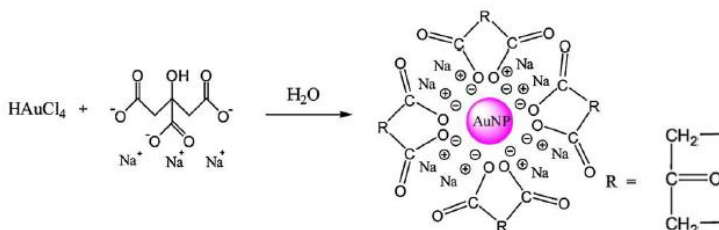
Figure 2.9 - AuNPs synthesis using the Turkevich method (taken from [7]).

Over time, scientists modified Turkevich's synthesis to better control the size and dimensional distribution of particles. For example, the citrate was replaced with sodium borohydride (reducing agent) allowing the reaction to be carried out at room temperature. Both syntheses are so-called "*in situ*" because nucleation and growth occur in the same process. Other methods involve a "seed growth" method in which particles are enlarged step by step, with more control over size and shape. With this technique it is possible to obtain not only spherical nanoparticles but also nano-hexapods, nano-bars and anisotropic AuNPs [8, 9].

AuNPs are often used in electrochemistry since they have several main advantages compared to the bulk material:

- they have a greater surface area thus leading to a better signal-to-noise ratio;
- the small dimensions cause a convergent diffusion, consequently there is also a higher speed of mass transport to the electrode surface;
- they have a catalytic effect, leading to a decrease in potential, which gives a better peaks separation and a better selectivity of the analysis;
- Multilayers of conductive nanoparticles give rise to a porous, high surface-area electrode, where the local microenvironment of the metallic nanoparticles can be controlled by the crosslinking elements and may lead to specific and selective interactions with substrates;
- the basic material is quite cheap.

The main disadvantage compared to the use of nanoparticles is the possible oxidation of the electrode area [10].

2.1.2. Titanium dioxide (TiO₂).

TiO_2 in nature is present in the form of three polymorphs: rutile (tetragonal system), anatase (tetragonal) and brookite (orthorombic). Only the first two play a significant role in industrial applications, while experimental data on brookite are limited due to its rarity and difficult preparation [11].

Titania is a semiconductor material that has long-term stability, it is non-toxic and has substantially low costs, to the point that it is currently also used for photovoltaic applications. Titania also has hydrophobic, hydrophilic, photocatalytic and antibacterial properties. It is applied for air and water purification, on fabrics and on glass, it has antibacterial and self-cleaning effects [12].

Rutile in ambient conditions is the thermodynamically most stable form. It has a tetragonal structure in which each Ti atom is coordinated by six O atoms to form a slightly distorted octahedron by means of four equatorial and two apical bonds longer. Anatase has a tetragonal structure and coordination of Ti and O atoms like that of rutile. The distortion of the TiO_6 octahedron, on the other hand, is greater with the four short bonds and there is a contraction of the c axis which involves a volume contraction of about 9%. For this reason, the rutile turns out to be denser than anatase. Brookite has a formed orthorhombic structure from octahedra that share three sides with neighbours. Pure brookite is very difficult to synthesize and so it is studying its properties [13].
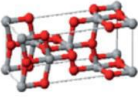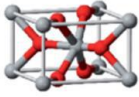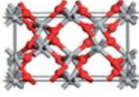
Property	Anatase	Rutile	Brookite	Ref.
	Tetragonal	Tetragonal	Orthorhombic	
Crystal bulk structure				18 and 19
Atoms per unit cell (Z)	4	2	8	20
Crystal size (nm)	<11	>35	11–35	17
Lattice parameters (nm)	$a = b = 0.3785, c = 0.9514$	$a = b = 0.4594, c = 0.2959$	$a = c = 0.5436, b = 0.9166$	19 and 21

Figure 2.10 - Properties of anatase, rutile, and brookite (taken from [14]).

2.1.3. Preparation and deposition of TiO₂.

The sol-gel process includes four steps.

1. Preparation of the sol: a colloidal suspension is formed from the dispersion of nanometric particles, derived from a precursor material, inside a solvent.
2. Transition from sol to gel: reaction of hydrolysis and condensation occur, the latter catalysed by the addition of an acid or a base, which initiates the polymerization by forming an interconnected chain structure.
3. Gel aging: the gel is aged in its stock solution to increase its mechanical strength.
4. Gel drying: the solvent is removed from the pores [15]. When exposed to UV or solar radiation, titanium dioxide nanoparticles perform photocatalytic activity, *i.e.*, they can modify the speed of some chemical reactions. In the presence of light, humidity and oxygen contained in the air, a strong oxidative process is activated, and it can decompose various organic and inorganic substances. The application of titanium dioxide film allows to modify the wettability characteristics of the treated surfaces making them super-hydrophilic, which is why the water that is deposited on the treated surface tends to form a continuous thin film rather than drops. This leads to an increase in the self-cleaning properties, also favouring the washing away of degraded molecules resulting from the photocatalytic activity [16].

2.1.4. Aim of this work.

The aim of this part of PhD thesis is the development and optimization of an electroanalytical hybrid device to detect emerging contaminants preventing and solving fouling problems. The hybrid device consists of a conductive glass, FTO, on which the gold nanoparticles are deposited so that emerging pollutants can be detected, and then covered with a titanium dioxide layer. This hybrid device combines the unique properties of AuNPs with the photochemical properties of TiO₂ to have a photo-renewable surface and a photo-electrochemical sensor for the detection of emerging contaminants (see also Chapter 3).

The study of titanium dioxide sol aging has been performed using different techniques: Dynamic Light Scattering (DLS) and UV-vis spectrophotometry (directly on the sol), Cyclic Voltammetry (CV), Electrochemical Impedance

Spectroscopy (EIS), Atomic Force Microscopy (AFM) and transient photocurrent (on the electrode material). Once the device has been prepared, different analytes were tested: diclofenac, paracetamol, flurbiprofen, ciprofloxacin and arsenic.

2.2. Materials and methods.

The reagents used, with repetitive use, their CAS number and brand are reported in Table 2.1; Table 2.2 reports the tools and materials used.

Table 2.1 - description of all reagents used in this work.

Name	Use	CAS number	Brand
Titanium(IV) isopropoxide	Titania synthesis	546-68-9	Sigma-Aldrich
Hydrocloric acid 37%	Titania synthesis	7647-01-0	Sigma-Aldrich
LUTENSOL ON70	Titania synthesis	-	-
Ethanol absolute ≥ 99.8%	Titania synthesis, electrode assembly	64-17-5	Sigma-Aldrich
Acetone	Electrode assembly	67-64-1	Sigma-Aldrich
2-propanol	Electrode assembly	67-63-0	Carlo Erba
Sulfuric acid, 95.0-97.0%	Electrode assembly	7664-93-9	Sigma-Aldrich
Toluene anhydrous 99.8%	Electrode assembly	108-88-3	Sigma-Aldrich
(3-Mercaptopropyl)trimethoxysilane (MPTMS)	Electrode assembly	4420-74-0	Sigma-Aldrich
(3-Aminopropyl)triethoxysilane (APTES)	Electrode assembly	919-30-2	Sigma-Aldrich
Diclofenac sodium salt	Analyte	15307-79-6	Sigma-Aldrich
4-acetamidophenol	Analyte	103-90-2	Sigma-Aldrich
Ciprofloxacin HCl	Analyte	86393-32-0	Sigma-Aldrich
Flurbiprofen	Analyte	5104-49-4	Millipore
As_2O_3	Analyte	1327-53-3	Fluka

Sodium phosphate dibasic	Electrolyte preparation (PBS)	7558-79-4	Sigma-Aldrich
Potassium phosphate monobasic	Electrolyte preparation (PBS)	7778-77-0	Fluka
Sodium perchlorate hydrate	Electrolyte	207683-20-3	Sigma-Aldrich
Potassium ferrocyanide $K_4[Fe(CN)_6] \cdot H_2O$	Probe molecule	14459-95-1	Fluka
Sodium hydroxide NaOH	Solvent for As_2O_3	1310-73-2	Fluka

Table 2.2 - description of the materials and tools used.

Name	Brand
FTO	Sigma-Aldrich
Potentiostat Galvanostat [PGSTAT30]	MetrOhm
Micropipettes	Gilson
Oven	Forno MAB
UV-vis spectrophotometer [model UV-2600; 240V]	Shimadzu
N_2 [air liquid 6.0]	Alphagz 2.0a
Analytical scale [crystal 100 cal]	Gibertini
pHmeter [model 338]	AMEL instruments
DLS [Zetasizer Nano ZS]	Malvern
AFM [Nanoscope Multimode IIId system]	Bruker
UV lamp [HG 500]	Jelosil

2.2.1. Preparation of solutions.

$NaClO_4$ 0.1 M was prepared by dissolving 12.12 g of $NaClO_4$ salt in 1 dm^3 of MilliQ water. The solution was prepared and kept at room temperature.

Phosphate-buffered saline (PBS) was prepared by dissolving 5.4124 g of Na_2HPO_3 and 1.1722 g of KH_2PO_3 in 1 dm^3 of milliQ water. The solution has been kept in the refrigerator at 4 °C. The solution thus obtained is at pH 7.4,

but in most tests, it has been used at pH 4; to adjust the pH at 4, HCl 37% has been added dropwise and the resulting pH has been measured with a pHmeter.

NaOH 0.1 M was prepared by dissolving 2.0 g of NaOH in tablets in 500 cm^3 of milliQ water under stirring. The solution was kept at room temperature.

To prepare the solution of the ferrocyanide probe, 10.66 g of K$_4$[Fe(CN)$_6$]·3H$_2$O were weighed on an analytical balance and transferred quantitatively into a 500 cm^3 flask and made up to volume with milliQ water. After mixing the solution, the flask has been stored in the refrigerator. The solution thus prepared was used to make the additions to the electrolytic solution (PBS or NaClO$_4$) so that the solution had a concentration of Fe (III) 1, 2, 3 mM; consequently, to a solution of 20 cm^3 of 0.1 M electrolyte, 400 mm^3 of the iron probe were added.

2.2.2. Synthesis of the titanium dioxide sol.

The sol was synthesised following a known procedure: 14.2 g of Ti(OC$_3$H$_7$)$_4$ were placed in 50 cm^3 of ethanol in a three-necked flask and subsequently 0.45 cm^3 of HCl 37% were added to the solution under stirring. In a beaker 0.235 g of LUTENSOL ON70 (a non-ionic surfactant) were dissolved in 50 cm^3 of ethanol, once mixed, and then added to the flask. The three necks of the flask are sealed, and the suspension is left under stirring at room temperature for one hour [17].

The titania sol prepared in this way was stored in five glass bottles, sealed with parafilm, and placed in a desiccator. This procedure was used to try to minimize the contact of the sol with the humidity of the air which, if absorbed, leads to the destabilization of the suspension itself, leading to the formation of a precipitate of increasing size. For the same reason it was necessary to wash and put all the glassware back in the stove before using it, so that it was perfectly dry.

2.2.3. Device assembly: electrodes with deposition of titania sol.

The procedure for assembling the electrodes consists of the following steps.

1. Preparation and cleaning of the FTO substrate. First, the FTO plate is cut by making a rectangle of 3x2 cm. The non-conductive part is marked, and the device is sonicated for ten minutes in a 1:1:1 solution

of water, acetone, and 2-propanol. Subsequently, the washed slide is irradiated under UV light for one hour. Often this procedure was performed the day before the preparation of the complete device.

2. Pretreatment of the slide. The conductive slide is immersed in sulfuric acid 95-97% for approximately 90 seconds. This operation allows the further cleaning of the glass, and the creations of some -OH groups on its surface that will be used for the connection of the linkers. Subsequently the substrate is rinsed with milliQ water and then dried under nitrogen flow, to avoid impurities.

3. Deposition of the titania layer and calcination. The functionalized slide is immersed in the TiO_2 sol for 60 seconds. The slide is positioned in the reactor so that the conductive face is upwards, in direct contact with the nitrogen flow. Nitrogen is flushed for one minute to eliminate the oxygen present in the reactor. At this point the reactor is placed in the oven to perform calcination for 1 hour at 400 °C with a nitrogen flow of 200 $cm^3 \cdot min^{-1}$. This phase is necessary for the mineralisation of the organic part and to promote the growth of the crystalline anatase phase of titanium dioxide.

Since titania is photosensitive, it is better storing the prepared electrodes in the dark, in a box covered with aluminium foil to avoid direct contact with light.

2.2.4. CV characterisation.

At the beginning of this work, it was decided to perform a study on the sol of titania as, through previous studies, it was noted that there was a variation in the voltametric curves as the sol ages. Then, once the titanium dioxide sol had been synthesised, the study of the scan rate was performed on treated FTO electrodes on which only the deposition of titania was performed by drop casting and subsequently calcined at different days to study the possible change of shape and of signal strength.

The study of the scan rate was performed on 9 different electrodes, as triple the quantities for titanium dioxide were synthesized to divide the sol into 5 small bottles. It was thought to do this because in previous works it was noted that with humidity there was the precipitation of aggregates on the bottom of the bottle, and therefore it was thought to see if there was a difference between electrodes synthesized at different days of life of the sol always using the same sol (therefore more and more in contact with the air and therefore also

humidity) and electrodes synthesized on the same days but with a bottle of sol opened the same morning of the synthesis.

For the study of the scan rate, cyclovoltammetries were performed and the parameters were:

- Apply potential: 0 V
- Start potential: 0 V
- Upper potential: 1.5 V
- Lower potential: -0.5 V
- Stop potential: 0 V
- Number of scans: 1
- Scan rates: 0.01; 0.02; 0.05; 0.1; 0.2; 0.5; 0.75 V s^{-1}
- Step: 0.008 V

In a 50 cm^3 beaker positioned above a magnetic stirrer, 20 cm^3 of $NaClO_4$ 0.1M, and a magnetic bar, are inserted and the 3 electrodes are connected (in a triangle geometry) to the instrument. Specifically, the calcined electrode with titania alone is used as working electrode (WE), saturated calomel electrode (SCE) as reference electrode (RE) and a platinum wire as counter electrode (CE). Before carrying out any study of the scan rate, 5 scans between -0.5 V and 1.5 V are carried out to stabilize the electrode.

The study of the scan rate was performed for all 9 calcined electrodes, on the $NaClO_4$ 0.1 M electrolyte solution alone (background) and then with 3 successive additions of 400 mm^3 of the ferrocyanide probe so that the resulting solutions were 1, 2, 3 mM. Figure 2.4 shows the studies of the scan rate for electrode 1, that is, that electrode calcined with the sol synthesized on the same day, on the zero day of life of the sol.

48
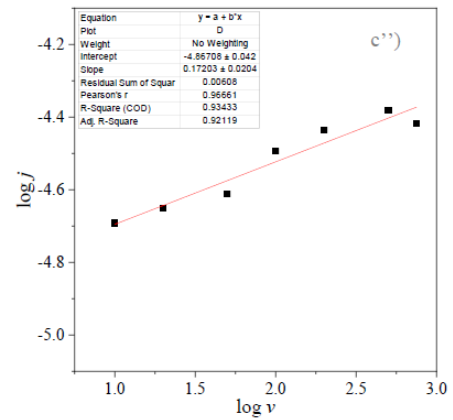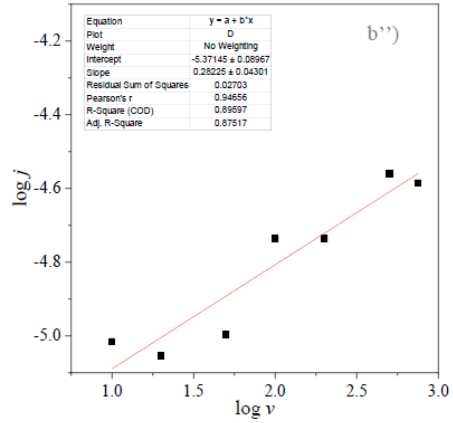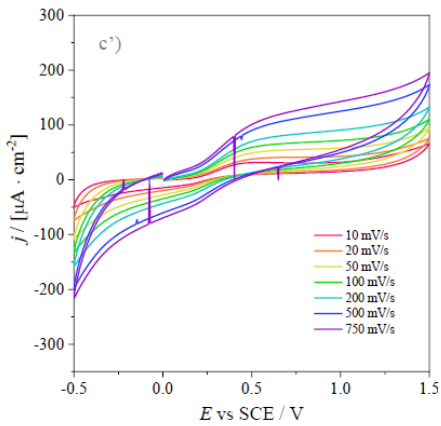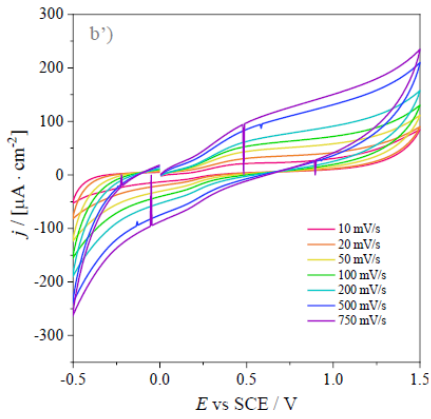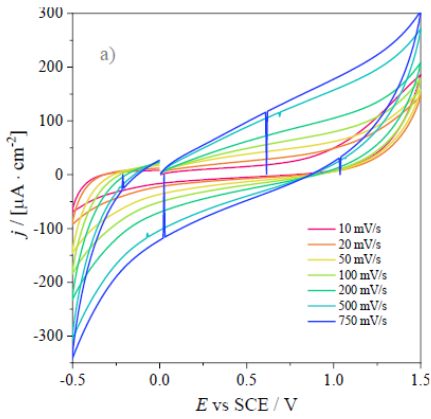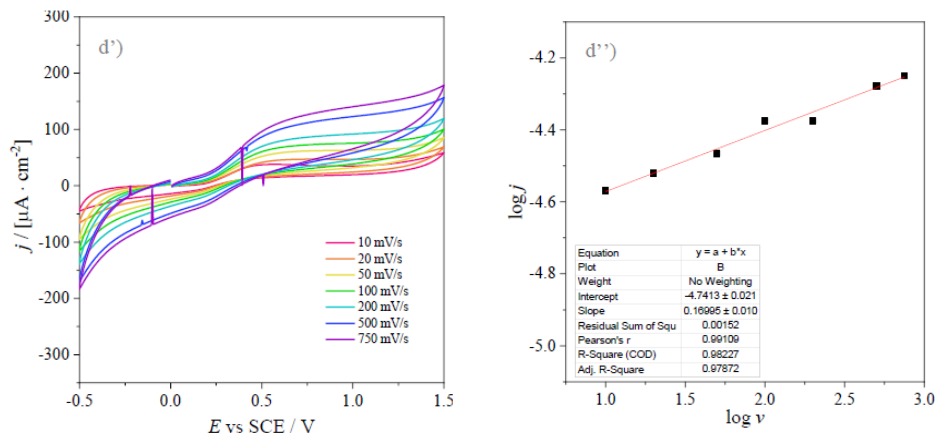
Figure 2.4 - a') is the graph of the cyclovoltammetries on the background study of the scan rate (NaClO₄); b') is the graph of the cyclovoltammetries on the study of the scan rate of the 1 mM ferrocyanide probe (NaClO₄), where b'') is the respective calibration line; c') is the graph of the cyclovoltammetries on the study of the scan rate of the 2 mM ferrocyanide probe (NaClO₄), where c') is the respective calibration line; d') is the graph of the cyclovoltammetries on the study of the scan rate of the 3 mM ferrocyanide probe (NaClO₄), where d'') is the respective calibration line.

For brevity, only the graphs of the 3 mM Fe probe for all electrodes and their calibration lines will be reported in this part.

Electrode 2_sol 2_day 2

j / [$\mu A \cdot cm^{-2}$]

E vs SCE / V

- 10 mV/s
- 20 mV/s
- 50 mV/s
- 100 mV/s
- 200 mV/s
- 500 mV/s
- 750 mV/s

$\log j$

$\log v$

Equation	y = a + b*x
Plot	D
Weight	No Weighting
Intercept	-4.61063 ± 0.04604
Slope	0.224 ± 0.02208
Residual Sum of Squares	0.00713
Pearson's r	0.97655
R-Square (COD)	0.95365
Adj. R-Square	0.94438

Electrode 3_sol 1_day 2

j / [$\mu A \cdot cm^{-2}$]

E vs SCE / V

- 10 mV/s
- 20 mV/s
- 50 mV/s
- 100 mV/s
- 200 mV/s
- 500 mV/s
- 750 mV/s

$\log j$

$\log v$

Equation	y = a + b*x
Plot	D
Weight	No Weighting
Intercept	-4.62206 ± 0.0160
Slope	0.22172 ± 0.0077
Residual Sum of Square	8.66553E-4
Pearson's r	0.997
R-Square (COD)	0.994
Adj. R-Square	0.9928

Electrode 4_sol 3_day 6

j / [$\mu A \cdot cm^{-2}$]

E vs SCE / V

- 10 mV/s
- 20 mV/s
- 50 mV/s
- 100 mV/s
- 200 mV/s
- 500 mV/s
- 750 mV/s

$\log j$

$\log v$

Equation	y = a + b*x
Plot	B
Weight	No Weighting
Intercept	-4.76494 ± 0.04447
Slope	0.31464 ± 0.02133
Residual Sum of Squares	0.00665
Pearson's r	0.9887
R-Square (COD)	0.97763
Adj. R-Square	0.97304

Electrode 5_sol 1_day 6

Equation	y = a + b*x
Plot	B
Weight	No Weighting
Intercept	-4.65257 ± 0.03463
Slope	0.26914 ± 0.01661
Residual Sum of Squares	0.00403
Pearson's r	0.99051
R-Square (COD)	0.98131
Adj. R-Square	0.97757

Electrode 6_sol 4_day 8

Equation	y = a + b*x
Plot	B
Weight	No Weighting
Intercept	-4.60809 ± 0.05947
Slope	0.24117 ± 0.02853
Residual Sum of Squares	0.01189
Pearson's r	0.96676
R-Square (COD)	0.93462
Adj. R-Square	0.92155

Electrode 7_sol 1_day 8

Equation	y = a + b*x
Plot	B
Weight	No Weighting
Intercept	-4.59889 ± 0.0344
Slope	0.23332 ± 0.0165
Residual Sum of Squares	0.00396
Pearson's r	0.98773
R-Square (COD)	0.97561
Adj. R-Square	0.97073

51

Electrode 8_sol 5_day 15

10 mV/s
20 mV/s
50 mV/s
100 mV/s
200 mV/s
500 mV/s
750 mV/s

Equation	y = a + b*x
Plot	B
Weight	No Weighting
Intercept	-4.6358 ± 0.04003
Slope	0.22194 ± 0.0192
Residual Sum of Squares	0.00539
Pearson's r	0.9818
R-Square (COD)	0.96393
Adj. R-Square	0.95671

Electrode 9_sol 1_day 15

10 mV/s
20 mV/s
50 mV/s
100 mV/s
200 mV/s
500 mV/s
750 mV/s

Equation	y = a + b*x
Plot	B
Weight	No Weighting
Intercept	-4.64476 ± 0.03955
Slope	0.21651 ± 0.01897
Residual Sum of Squares	0.00526
Pearson's r	0.98135
R-Square (COD)	0.96304
Adj. R-Square	0.95565

Figure 2.5 - the cyclovoltammetries of all nine electrodes of FTO are shown on the left with the calcination of the titanium dioxide at different days of life relative to the 3 mM of the iron probe, while on the right are shown the respective calibration lines.

Table 2.3 - definition of the slopes of the calibration curves relative to 3 mM Fe probe for all 9 electrodes, referred to Figure 2.5.

Electrode	Slope*
Electrode 1	(0.170 ± 0.010)
Electrode 2	(0.224 ± 0.022)
Electrode 3	(0.222 ± 0.008)
Electrode 4	(0.315 ± 0.021)
Electrode 5	(0.269 ± 0.017)
Electrode 6	(0.241 ± 0.028)
Electrode 7	(0.233 ± 0.165)
Electrode 8	(0.222 ± 0.192)
Electrode 9	(0.216 ± 0.019)

*The slope is relative to the straight line obtained from Log j (current density) vs Log v (scan rate).

From Table 2.3, it can be seen that the slopes of the straight lines obtained from the study of the scan rate (Log *j* vs Log *v*) are always lower than 0.5, varying from 0.170 to 0.320. Comparing these data with those from the literature [18], it is possible to deduce that the diffusion is of a convergent radial type (see also Chapter 1.2).

Therefore, based on Compton's studies and based on the first results concerning the slopes of the lines Log *j* vs *t* we could hypothesize to be in case 3. To be able to have more certain answers, it was decided to continue with the electrochemical studies.

Considering these results, a variation in the shape of the signal was noted, to be sure it was decided to superimpose the CVs performed on the electrodes used the day after calcination, differentiating the type of sol used (on the graph on the left there are systems with sol 1, therefore the one open several times, while on the right there are the electrodes immersed in the sol just opened).
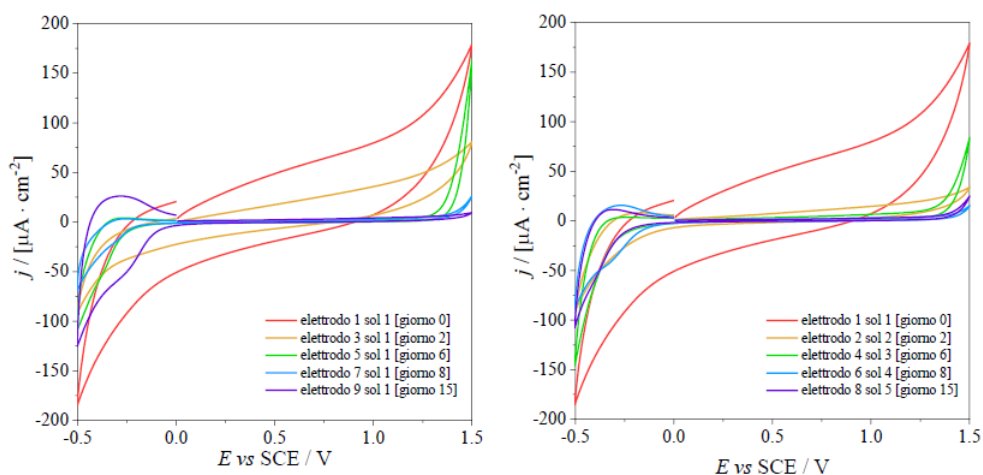
Figure 2.6 - On the left are the cyclovoltammetries on the backgrounds (NaClO₄) of the calcined electrodes using the sol 1 opened several times (specifically, electrode 1 was calcined with a sol at day 0 of life, electrode 3 with a sol at 2 days of life, electrode 5 with a sol at 6 days of life, electrode 7 with a sol at 8 days old and electrode 9 with a sol at 15 days old), while on the right there are the cyclovoltammetries of the calcined electrodes using sol flasks opened for the first time (specifically, electrode 1 was calcined with a sol at day 0 of life, electrode 2 with a sol at 2 days of life, electrode 4 with a sol at 6 days of life, electrode 6 with a sol at 8 days old and the 8 electrode with a sol at 15 days old).
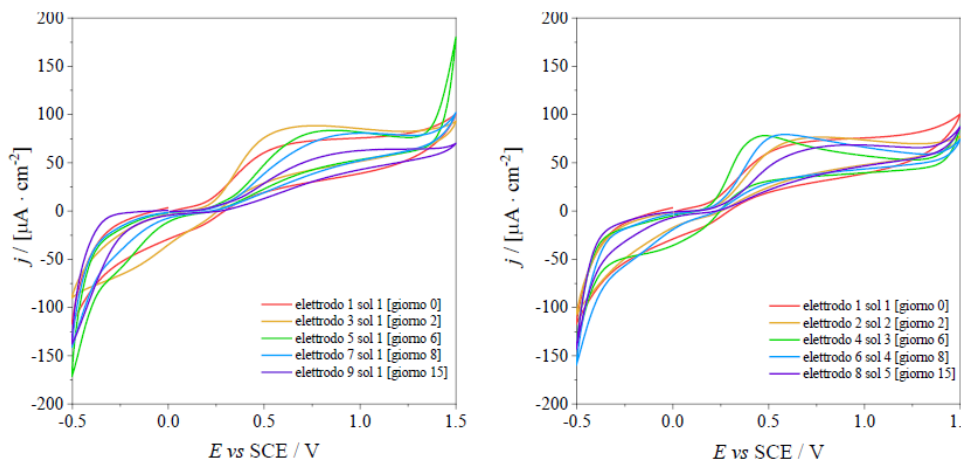
Figure 2.7 - On the left the cyclovoltammetries on the 3 mM ferrocyanide probe (in NaClO₄) of the calcined electrodes using the sol 1 opened several times (specifically, electrode 1 was calcined with a sol at day 0 of life, electrode 3 with a sol at 2 days of life, electrode 5 with a sol at 6 days of life, electrode 7 with a sol at 8 days old and electrode 9 with a sol at 15 days old), while on the right there are the cyclovoltammetries of the calcined electrodes using sol flasks opened for the first time (specifically, electrode 1 was calcined with a sol at day 0 of life, electrode 2 with a sol at 2 days of life, electrode 4 with a sol at 6 days of life, electrode 6 with a sol at 8 days old and the 8 electrode with a sol at 15 days old).

As it can be seen from these superimpositions, the signal tends to change its shape, and it passes from a pseudo step on the electrodes calcined with the sol at day 0 and at day 2, to a pseudo peak for the electrodes calcined with the sol on days 6 and 8, to then have a distortion of the peak for the electrodes calcined with the sol on day 15.

However, in our specific case, observing the Table 3 with the slopes of the lines Log j vs Log v and comparing the results with the data in the literature, we can say that we are in case 3 because in the end there is a dependence on the scan rate with the intensity and therefore the current density but there is no law that describes it exactly (as it would be for a peak or for a step). In fact, we do not get perfect peaks or steps, but they are pseudo steps that turn into pseudo peaks.

2.2.5. EIS characterisation.

Simultaneously with the study of the scan rate, the electrochemical impedance spectroscopy analyses were performed, for all 9 electrodes, for the background (20 cm³ of NaClO₄) and for $K_4[Fe(CN)_6]$ 1 mM, 2 mM, 3 mM, with an applied potential at -0.1V, 0.1V and 0.25V.

The parameters used for the EIS analyses were:

- First applied frequency: 65000 Hz
- Last applied frequency: 0.1 Hz
- Number of frequencies: 50
- Frequency step type: Logarithmic
- Amplitude: 0.01 V$_{RMS}$

Since the graphs obtained for each sample are many, only the superimpositions relating to the background and of K$_4$[Fe(CN)$_6$] 3 mM of the impedances performed at an applied potential of 0.25 V are shown below.
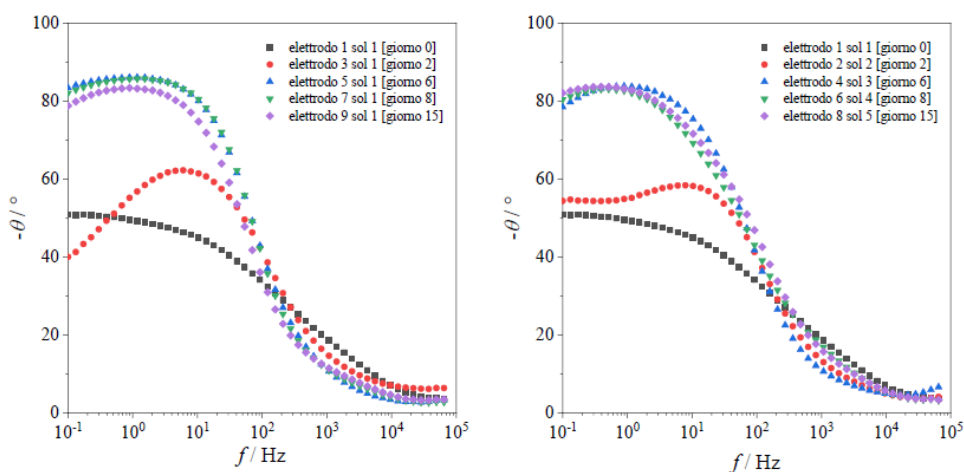
Figure 2.8 - Bode plots on the background (NaClO$_4$), on the left it refers to the electrodes calcined with sol 1 (specifically, electrode 1 was calcined with a sol at day 0 of life, electrode 3 with a sol at 2 days of life, electrode 5 with a sol at 6 days of life, electrode 7 with a sol at 8 days old and electrode 9 with a sol at 15 days of life), on the right the electrodes calcined with the sol open only once (specifically, electrode 1 was calcined with a sol at day 0 of life, electrode 2 with a sol at 2 days of life, electrode 4 with a sol at 6 days of life, electrode 6 with a sol at 8 days old and electrode 8 with a sol at 15 days of life).

In Figure 2.8, where the Bode plots of the background are represented, as there is no type of probe inside the electrolytic solution, there is information inherent only to the material. In the specific case it can be noted that the trend for both graphs, both on the right (electrodes calcined with the sol opened several times) and on the left (electrodes calcined with the sol opened for the first time), the calcined electrodes are very different to the day of life of the sol 0 and 2. The fact of opening the bottle of the sol several times influences slightly more in the first days of the life of the sol, but then have no influence from day 6

onwards. Even without calculating the equivalent circuit of the electrodes, it is noted that those calcined at day zero of the life of the sol have a totally different trend compared to those calcined at the days of life of sol 2, 6, 8, 15.

On the other hand, the electrodes calcined at day 6, 8, 15 have a more capacitive behaviour, that is, they can behave as if they were the plates of a capacitor, as we speak of a pure capacitor when the $-\theta$ is 100°, in the case specific we have a $-\theta$ of about 80° so they have a good capacity. This suggests that these electrodes have a more ordered arrangement of the particles on the surface, while the electrodes calcined at day 0 and day 2 of the life of the sol, have lower values of $-\theta$ therefore pure capacities cannot be defined, probably for an unordered surface or a sol not yet stable.
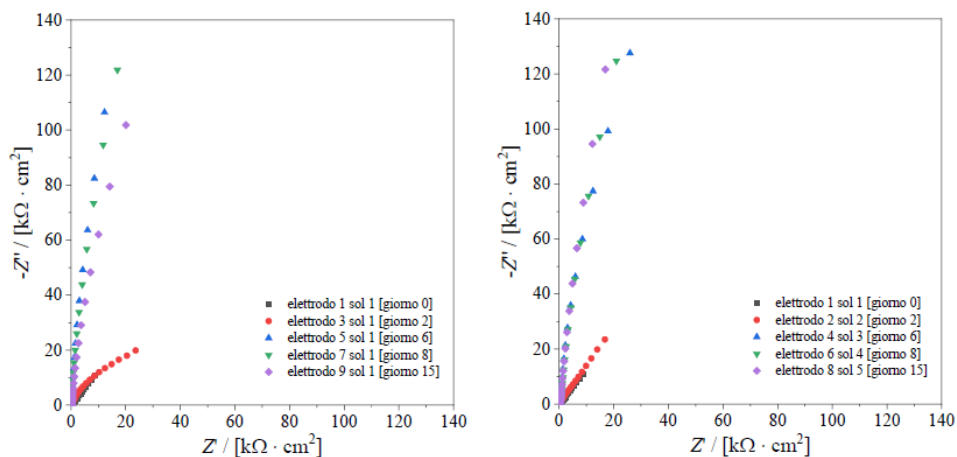
Figure 2.9 - Nyquist plots on the background (NaClO₄), on the left it refers to the electrodes calcined with sol 1 (specifically, electrode 1 was calcined with a sol at day 0 of life, electrode 3 with a sol at 2 days of life, electrode 5 with a sol at 6 days of life, electrode 7 with a sol at 8 days old and electrode 9 with a sol at 15 days of life), on the right the electrodes calcined with the sol opened only once (specifically, electrode 1 was calcined with a sol at day 0 of life, electrode 2 with a sol at 2 days of life, electrode 4 with a sol at 6 days of life, electrode 6 with a sol at 8 days old and electrode 8 with a sol at 15 days of life).

Observing the Nyquist graphs of the background it would seem that there is a clear variation between the trend of electrode 1 (day 0 of life of the sol) compared to electrode 2/3 (day 2 of life of the sol) and the subsequent electrodes. Specifically, it would seem that it goes from an unstable electrode at day 0, to an electrode that begins to stabilize but which in any case has a chaotic surface arrangement as for the calcined electrodes at day 2 of the life of the sol, to then have much more stable electrodes from day 6 onwards,

probably because the first electrodes have too many small and fine pores. The latter hypothesis cannot be confirmed without carrying out SEM images to understand how thick the deposited layer is and consequently how deep the pores are.
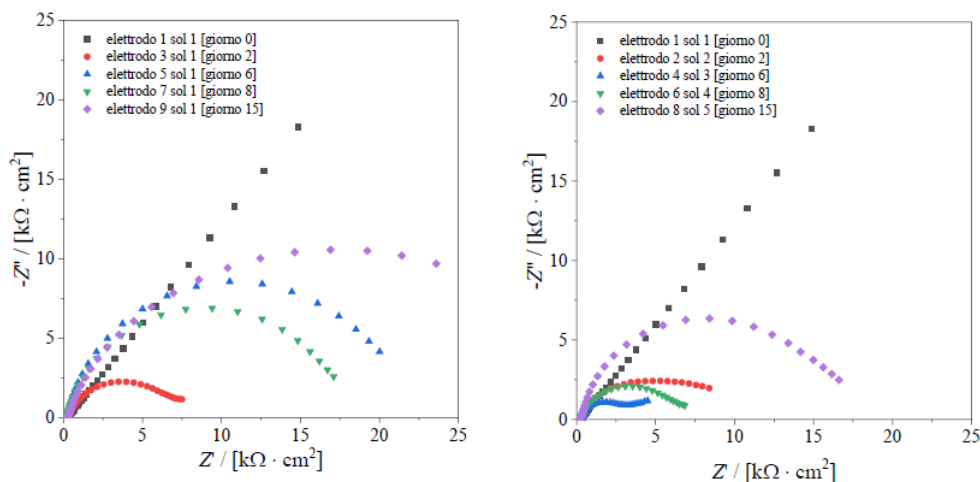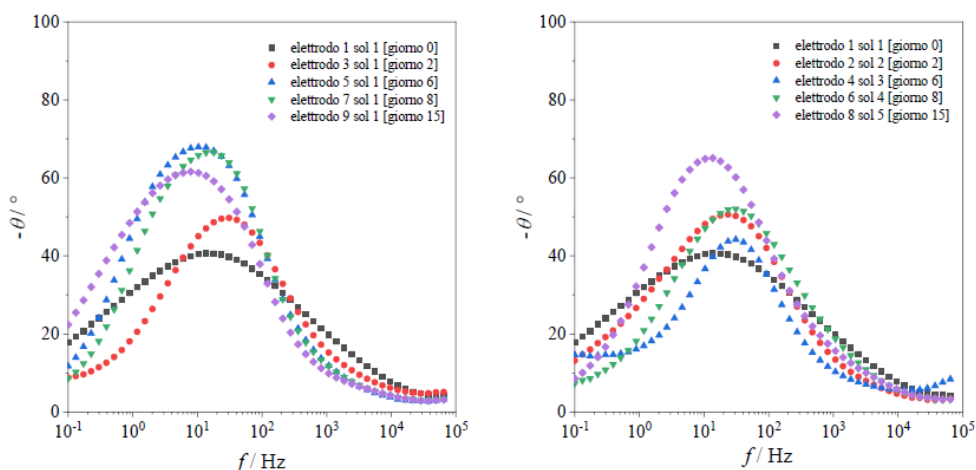

Figure 2.10 - Nyquist plots on NaClO₄ + 3 mM ferrocyanide probe, on the left it refers to the electrodes calcined with sol 1 (specifically, electrode 1 was calcined with a sol at day 0 of life, electrode 3 with a sol at 2 days of life, electrode 5 with a sol at 6 days of life, electrode 7 with a sol at 8 days old and electrode 9 with a sol at 15 days of life), on the right the electrodes calcined with the sol opened only once (specifically, electrode 1 was calcined with a sol at day 0 of life, electrode 2 with a sol at 2 days of life, electrode 4 with a sol at 6 days of life, electrode 6 with a sol at 8 days old and electrode 8 with a sol at 15 days of life).

Observing the Nyquist diagram of the electrolyte with the presence of the iron probe (which is an inner sphere probe), it can be seen that this also leads to rearrangements as well as to have charge transfers. But, looking at the Figure 2.10, we immediately notice that the electrode at day 0 does not have a semicircle, and therefore does not have a resistance to charge transfer, but only has a resistance to mass transfer, in fact it is a straight line at about 45°, as if it was the Warburg line, and therefore the resistance only generated by the passage of molecules. This is because, for the Fe (II) → Fe (III) + e⁻ reaction to occur, the probe must reach the surface of the FTO, so it must move, leading to resistance to mass transfer. For electrode 1, therefore, there seems to be no problems related to charge transfer; if the pores on the electrode were small and even shallow, there would be a pure convergent diffusion, but this cannot be certain until SEM studies are carried out. If this were the case, the mass transfer would be faster, as iron would be easier to release electrons.

The calcined electrodes on day 2 of the life of the sol begin to have a semicircle; therefore, in addition to having resistance to mass transfer, they have resistance to charge transfer. However, between electrode 2 and electrode 3 (electrodes synthesized on day 2, but respectively with the sol open the first time and the sol previously open) have a similar height, but the opening and therefore the contact of the titanium dioxide sol with oxygen and the humidity of the air seems to be good for the sol itself.

In general, from the electrodes on day 2 to the electrodes on day 15, the electrodes synthesized with the sol opened several times have a lower height, which means that there is a lower resistance to charge transfer, so the electrode transfer is more facilitated. For all electrodes, excluding electrode 1, there is no information on mass transfer since they do not have the Warburg line, probably because, depending on the range of frequencies analysed, there is no time to observe this resistance since the titania it is an insulating layer; in fact the graphs are in the order of $k\Omega$ and therefore only the resistance to charge transfer is seen, the resistance to mass transfer is not observed which consequently cannot be commented on but is certainly present.

The electrodes synthesized at day 6, 8, 15 of the life of the titania sol show a similar trend both for what concerns the electrodes calcined with the sol opened several times and for those calcined with the sol opened for the first time. The heights and amplitudes of the semicircles are different, but there is certainly a worsening of the electronic transfer with the aging of the days of life of the sol. Another thing that changes with the passing of the days is the shape of the semicircle, which tends to become more and more semi-oval with time. The electrodes on day 2, 6, and 8 are more of a semicircle shape, which means that these electrodes are fairly uniform with the interactions with the probe. While the electrodes synthesized on day 15 lose this uniformity, and it becomes a semi-oval.

There is a general increase in charge transfer with increasing days of aging of the sol because there is a tendency to lose the convergent diffusion (both for the sol opened for the first time and for the sol opened several times). Probably this is because over time a thicker layer of titania is created on the electrode (information to be confirmed with SEM) and a larger pore (the latter information is confirmed with the AFM study, which is reported below, where there is an increase in roughness, therefore, tends to increase the pore width) increase linear diffusion. This is because in contact with FTO there is not only a molecule of Fe (II) that releases the electrons, but once the first one manages to carry out the oxidation reaction, the others that were behind it is able to

release the electron as a result. The problem is that with linear diffusion there are fewer molecules that can enter the pore, there is a higher resistance to charge transfer which will be slower. In addition to being hindered by the titania layer, the oxidation reaction is also hindered by solvent molecules and water molecules.

Globally, electrodes synthesized with sol 1, and therefore calcined electrodes with sol opened several times, have a more semi-circular Nyquist plot, compared to electrodes synthesized with sol opened for the first time which instead have a more a semi-oval; therefore, all this suggests that oxygen and humidity in the air help titanium dioxide to stabilize. Also, the electrodes synthesized with sol 1 have a lower resistance to charge transfer, as if humidity accelerated the sol aging.

Figure 2.11 – Bode plots on NaClO4 + 3mM ferrocyanide probe, on the left it refers to the electrodes calcined with sol 1 (specifically, electrode 1 was calcined with a sol at day 0 of life, electrode 3 with a sol at 2 days of life, electrode 5 with a sol at 6 days of life, electrode 7 with a sol at 8 days old and electrode 9 with a sol at 15 days of life), on the right the electrodes calcined with the sol open only once (specifically, electrode 1 was calcined with a sol at day 0 of life, electrode 2 with a sol at 2 days of life, electrode 4 with a sol at 6 days of life, electrode 6 with a sol at 8 days old and electrode 8 with a sol at 15 days of life).

With the Bode graph referred to the electrodes analysed with $NaClO_4$ and $K_4[Fe(CN)_6]$ 3 mM, it is noted that aging slows down for the electrodes synthesized with the sol open for the first time. Observing the electrodes synthesized on day 2, electrode 3 (the one synthesized with the sol opened several times) has a thinner and slightly lower signal than electrode 2 (synthesized with the sol opened for the first time) which instead has a wider signal and therefore has a less homogeneous, more inhomogeneous surface.

For electrodes 5, 7, and 9 (synthesized with sol 1) they have the maximum at about the same value as the frequencies whose value is lower than electrode 3 (day 2), which means that the charge transfer is slower.

Electrode 1, on the other hand, has a maximum of about 40°, a little less than 45° which occurs for the Warburg graph, in fact in the respective Nyquist plot this electrode is in the form of a straight line, with no component on the charge transfer.

Simultaneously with the study of the scan rate on the electrodes 1-9, it was decided to simultaneously perform studies on the aging of the sol using the DLS and UV.

2.2.6. UV characterisation.

To obtain further information, it was decided to carry out the UV spectra on the various sols, using UV spectrophotometer. 10 mm^3 of sol and 2490 mm^3 of pure ethanol are inserted into a quartz cuvette. The UV spectra were performed on the same day as the velocity study, which means the day after the electrodes were calcined. Then the sol 1 which was opened several times and the sol 2_5 which were opened only the day before were analysed at the same time to dip the FTO slide by dip coating and then carry out the calcination. UV spectra were acquired between 185 nm and 800 nm.
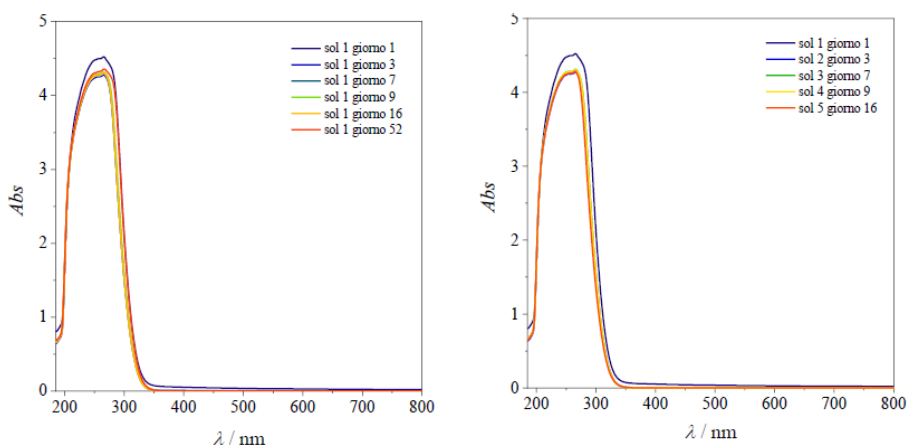
Figure 2.12 - superposition of the UV spectra of titanium dioxide, distinguishing on the right the sols opened the first time while on the left sol 1 (opened several times).

For all these graphs the absorption maximum oscillates between 264 and 266 nm.

All these tests were performed using ethanol as a solvent, but thus it is not possible to define it as blank, consequently, to confirm, two spectra of sol 5 were performed (at day 52) using only ethanol as the solvent (as done for all the tests mentioned above), the spectrum of which was compared with that obtained having the real white as solvent, that is, in addition to ethanol, also Lutensol and HCl at 37%.
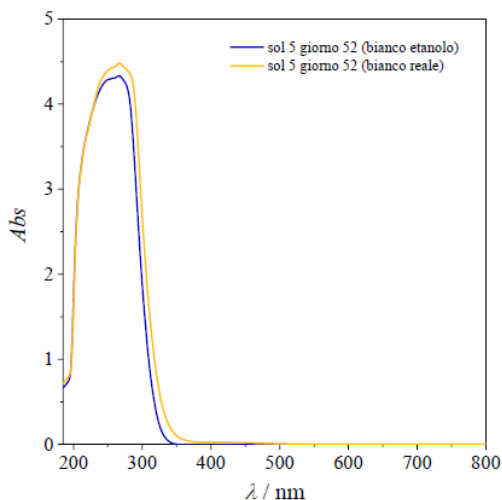
Figure 2.13 - Superimposition of the spectrum of sol 5 to day 51 of the sol using the real blank (blue) for the dilution of the sol (ethanol, Lutensol and HCl), and the ethanol (yellow).

Also, in this case the maximum falls to 266 nm for the real blank and 265 nm for the ethanol, therefore the analyses were not replicated again using the actual blank, because in any case it would not have changed the result obtained.

As it can be seen from the superimpositions in Figure 2.12, the absorption maximum remains the same for all sols, around 265 nm, and therefore, it would seem not to vary with the openings of the bottles of sol and therefore the humidity does not affect this value. Taking these results into consideration, many doubts have arisen, above all because in the literature the typical absorption values of the titania sol, where titanium dioxide is in the form of anatase, oscillate between about 385 and 410 nm depending on the size of the particles [19].

At this point it was decided to perform the spectrum of the so-called blank, that is the solution containing titanium (IV) isopropoxide and ethanol. Specifically, 0.7227 g of titanium (IV) isopropoxide have been quantitatively transferred to the flask containing pure ethanol, then the flask was shaken. To run the UV

spectrum of the precursor tale of the sol of titania, 10 mm^3 of the solution have been transferred to a quartz cuvette, to which have been added 2490 mm^3 of pure ethanol. The resulting spectrum was depicted in Figure 2.14 where the spectrum of sol 1 at day 1 of life was also superimposed.
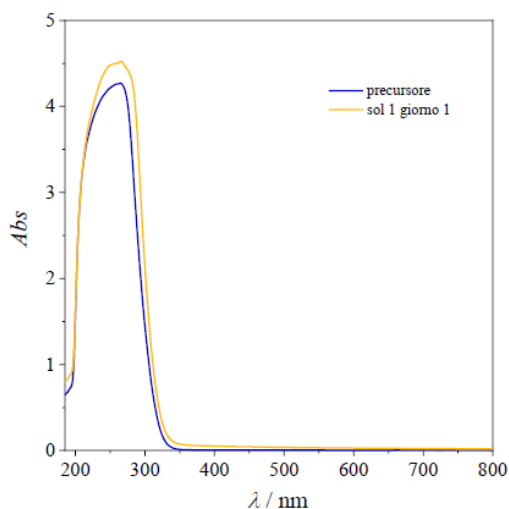
Figure 2.14 - UV spectra superimposition of the precursor of the sol and of the titania sol.

From Figure 2.14 it is immediately evident that the absorption maximum always remained at about 265 nm, which suggests that all the previous tests performed with the UV spectrophotometer were not related to the sol, but to the precursor, or the so-called blank, or some other species obtained in the reaction. This, therefore, makes it clear that for our purpose, UV is not a useful technique.

2.2.7. DLS characterisation.

In previous works, in addition to characterizing the titania with the DLS, the Z-potential was performed, showing a positive surface charge. This was probably due to the presence of vacancies and Ti^{3+} and Ti^{4+} ions on the TiO$_2$ surface due to the lack of the exact number of bonds.

During the day of the calcination of the electrodes, the DLS analysis was performed as a further technique to try to understand the variation in the size of the sol with its aging. In these analyses, the sol was never diluted, it was directly taken (about 1 cm^3 of aliquot) from the small bottles by means of a Pasteur pipette and inserted into the plastic cuvette which in turn was placed

in the sample holder of the DLS. Also, in this case the aim was to test the variation of the particle size of the titanium dioxide sol, simultaneously analysing sol 1, and the other sols, to understand if aging affected the particle size and especially if the latter was influenced by the humidity of the air.

The instrument used for the measurements was a Zeta-Sizer Nano ZS Instrument equipped with a solid-state He-Ne laser ($\lambda = 633$ nm). The detector of the instrument is placed at $\theta = 173°$ to detect the backscattered light. For the analysis, a disposable translucent plastic cuvette is used, where about 1 cm^3 of solution is inserted, working at 298 K. Each hydrodynamic diameter was calculated by repeating 3 repetitions of 10 scans.

The figures below show the graphs obtained at the DLS for sol 1 at day 0 of life, that is, the day of synthesis of the sol relating respectively to the intensity, volume, and size of the particles.
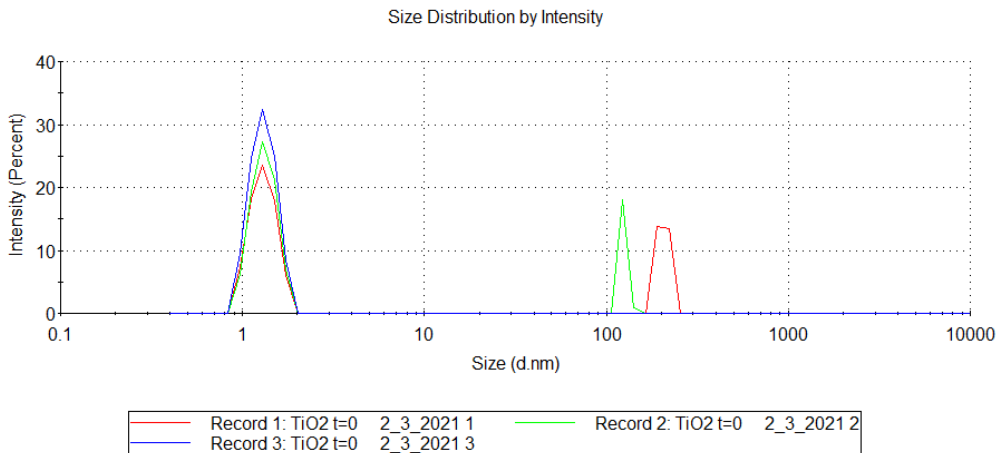
Figure 2.15 - Graph obtained from the DLS of the intensity of the particles of the sol of titania at day zero of life.
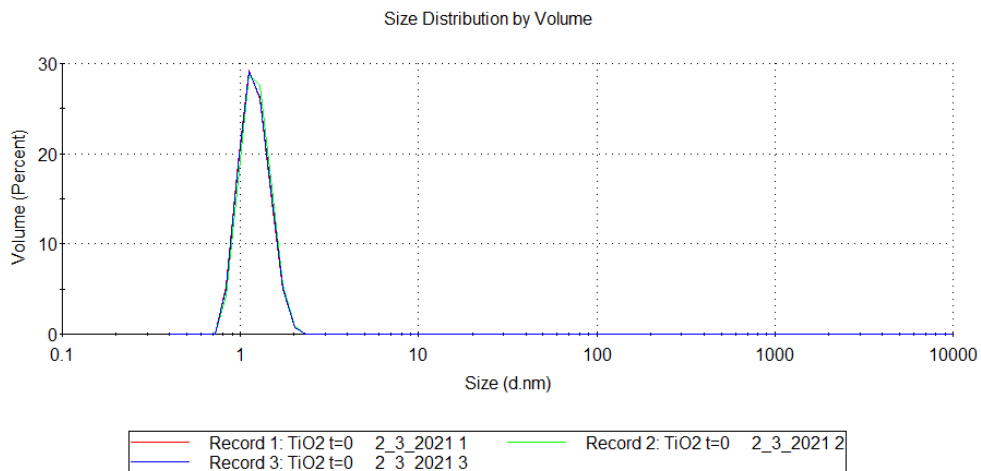
Figure 2.16 - Graph obtained from the DLS of the volume of the particles of the sol of titania at day zero of life.

From these two above graphs, it can be seen that at around 1 nm there is a population of particles, and it would seem that even around 100 nm there is another one, but the latter has such a small volume, that it is not detectable. The number of particles with a size of about 100 nm is very small, so it might not be considered, and therefore it can be said that sol 1 is characterized by particles of about 1 nm in diameter.
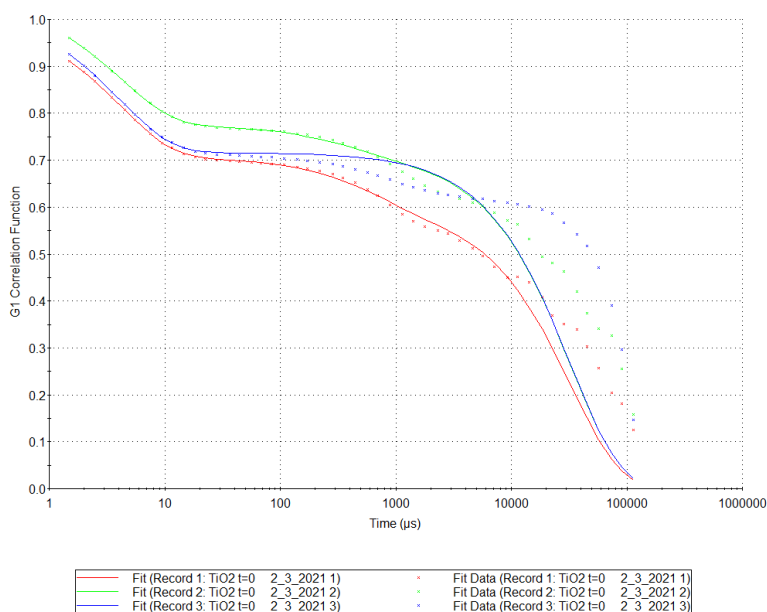
Figure 2.17 - Graph obtained directly from the DLS instrument relating to the correlation functions of the three repetitions of the analysis performed on sol 1 at day of zero life.

The problem, however, arose by observing from the instrument the correlation function of the three repetitions performed on sol 1 at day 0 of life. As, observing Figure 2.17, it can be seen that the data, represented with dots, cannot be fitted well, above all the correlation is lost over a longer period. So, to be able to understand if the results obtained were realistic, it was decided to manually perform the correlation function using Origin, using as a correlation function:

$$y = 0.35 \, (A_1 \cdot e^{D_1 \cdot 727.1 \cdot x}) + (A_2 \cdot e^{D_2 \cdot 727.1 \cdot x}) + (A_3 \cdot e^{D_3 \cdot 727.1 \cdot x})]^2$$
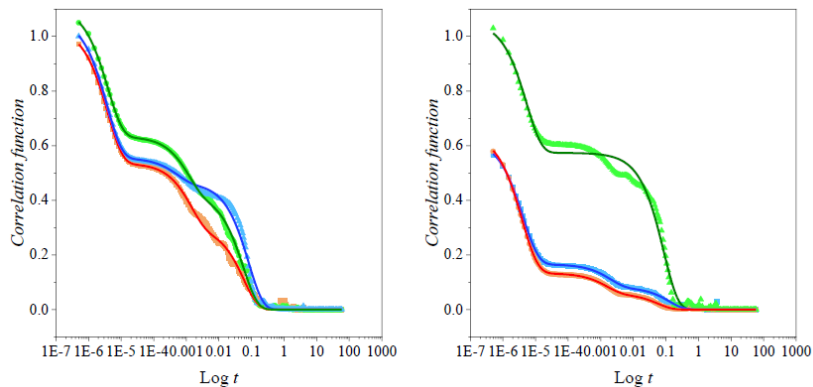
Figure 2.18 - Origin graph obtained relating to the correlation functions of the three repetitions of the analysis performed on sol 1 at day of life zero (on the left), on sol 5 at day aging 15 (on the right).

From these correlation functions the values of A_1, A_2, A_3, D_1, D_2, D_3 were obtained. Once these values were known, it was possible to exploit an inverse relationship of the Stoke-Einstein law to be able to determine the value of the particle radius.

From the elaboration, for each analysis performed on the sol, 3 particle size distributions are obtained, but by carrying out the ratio between these three populations, a much more abundant one is obtained, as already shown by the DLS with the spectrum on the number of particles.

Figure 2.18 shows the correlation functions of only two sols analysed because it was noted that the dimensions obtained from Origin did not shift significantly compared to the dimensions obtained directly from the DLS. As for the graph on the right, the dimensions obtained by Origin were: 1.35 nm, 1.34 nm, and 1.29 nm, consequently their average is 1.33 nm, while the average obtained by the instrument was 1.310 nm, definable values equal. In the case of the graph on the right, the dimensions obtained by Origin were: 1.61 nm,

1.60 nm, 1.83 nm, consequently their average is 1.68 nm, while the average obtained by the instrument was 1.501 nm. Since the values do not change much, below, only the averages of the average particle sizes obtained directly from the DLS have been reported in Table 2.4:

Table 2.4 - Average particle size.

Sol used in the analysis	Day of aging	Average particle size / nm	Sol used in the analysis	Day of aging	Average particle size / nm
Sol 1	0	1.310	Sol 1	0	1.310
Sol 1	2	1.373	Sol 2	2	1.300
Sol 1	6	1.286	Sol 3	6	1.300
Sol 1	8	1.335	Sol 4	8	1.396
Sol 1	15	1.168	Sol 5	15	1.501

It was expected that with the increase of the aging time of the sol, the size of the particles would increase. However, from the values in Table 6, it can be seen that there aren't such high variations. This raised the question that what is seen at DLS was not titanium dioxide but its precursor, titanium (IV) isopropoxide. So, the DLS spectrum of the precursor was executed, obtaining Figure 2.19 and 2.20:
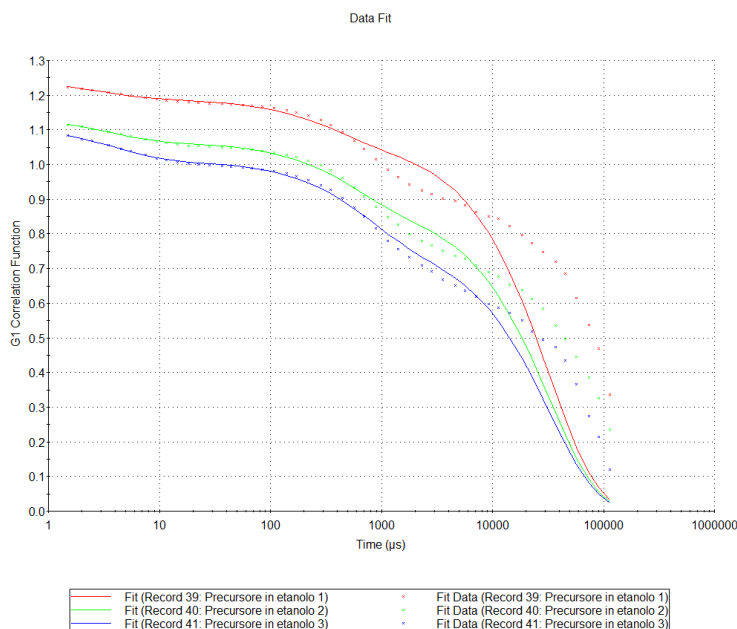
Figure 2.19 - Correlation function of the precursor for the three repetitions.
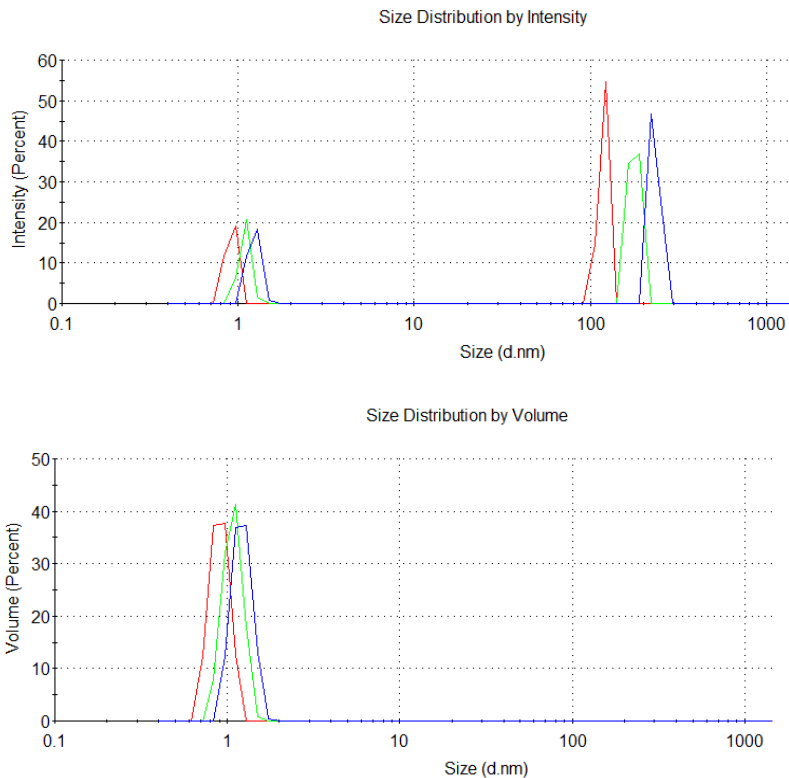
Figure 2.20 - the graph relating to the correlation between intensity and particle size of the precursor is shown at the top, while at the bottom it is correlated to the volume.

The first graph shows that the particles have two populations, one around 1 nm, and the other around 100 nm. But the population of the former is the most abundant to such an extent that the population at 100 nm does not appear in the volume vs size graph.

From these analyses it appears that the size of the precursor is (1.08 ± 0.05) nm, so probably what was seen in the previous DLS tests for titanium dioxide was the precursor itself or possibly of the other products.

To be sure, the size calculation of the titanium (IV) isopropoxide was performed by *Chemdraw*, the diameter of which was found to be 1.2 nm, which confirmed the thinking from the results. That is, what was seen with the DLS analyses was not titania, but titanium isopropoxide (precursor) or otherwise unreacted species.

All this made it clear that in addition to UV also DLS is not an optimal technique for observing the particle size of the titanium dioxide sol. In fact, it was subsequently decided to directly analyse the electrodes synthesized at

several days of life with a surface study technique (AFM) to observe the variation in roughness.

2.2.8. AFM characterisation.

Considering all the previous results, where the UV and DLS analysis failed to demonstrate what seen through the study of the scan rate of the nine electrodes, it was decided to carry out AFM analyses in order to try to obtain a correlation of the previous results through the roughness of the electrodes.

Specifically, 5 different electrodes were brought to be analysed:

- "Bianco", FTO electrode dipped for dip coating to a solution prepared with the same procedure as the titania sol but without inserting the titanium (IV) isopropoxide;
- Electrode 2, prepared using sol 2 which had 2 days of aging;
- Electrode 6, prepared using sol 4 which had 8 days of aging;
- Electrode 8, prepared using sol 5 which had 15 days of aging;
- T1 electrode, prepared using sol 1 (but not of the same synthesis as the previous sols) which had 31 days of aging.

To perform the AFM analyses it was necessary to cut the electrodes at 1x1 cm, so that it could enter the sample port of the instrument, using a cutter with a diamond point.

These electrodes were chosen because they were electrodes synthesized from a sol opened for the first time for the dip coating immersion of the slide just before calcination. Not all the electrodes were analysed but those that showed a greater variation in the shape of the signal, to understand if this variation was really linked to a different roughness of the device and therefore to a different diffusion.
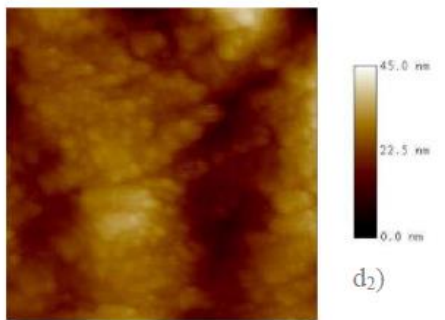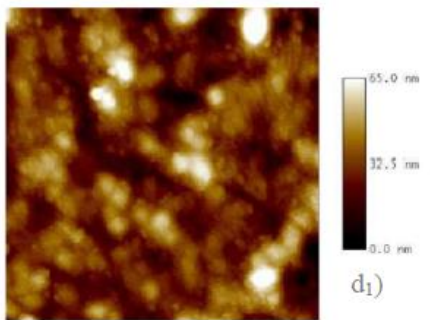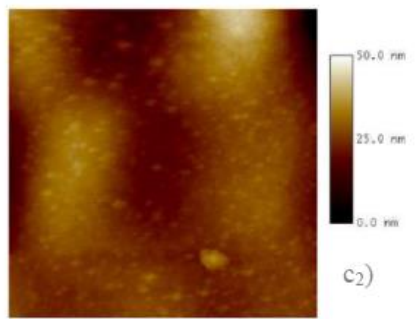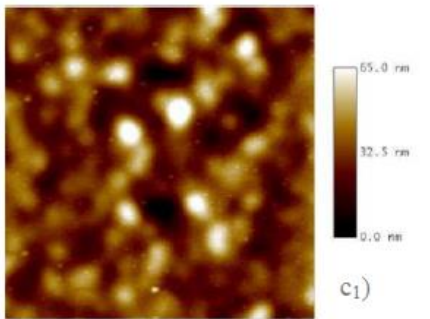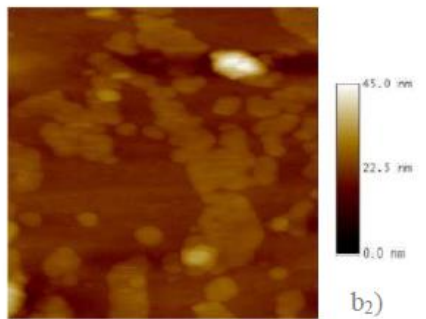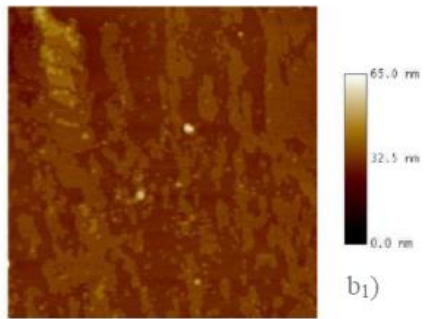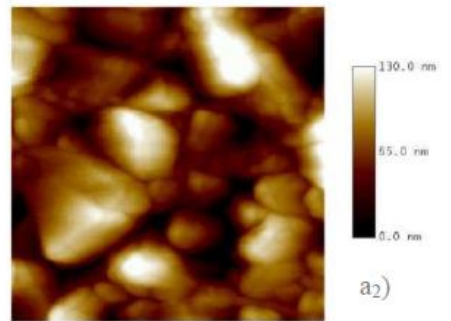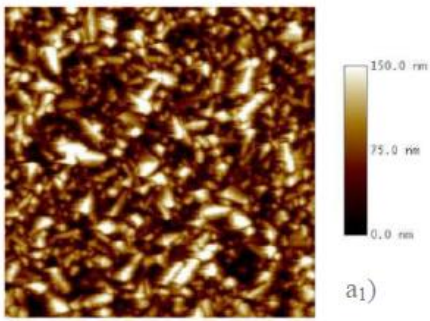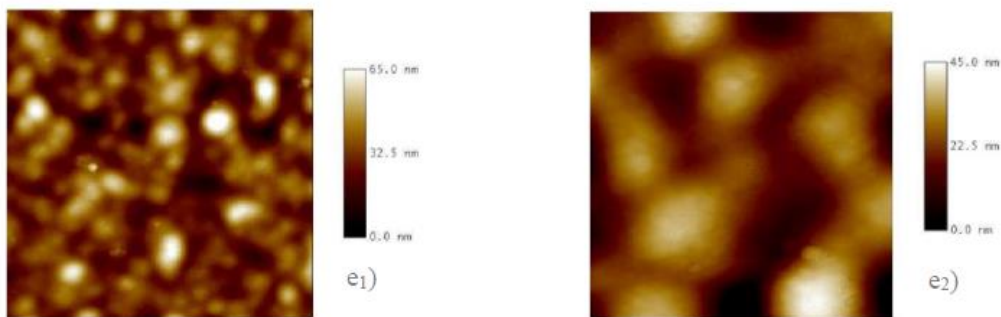
Figure 2.21 - the images on the left represent scans with dimension 5x5 μm² while the images on the left represent scans of dimension 1x1 μm²; a1) and a2) represent AFM images of an FTO electrode coated with ethanol, Lutensol and HCl 37% and subsequently calcined; b1) and b2) represent AFM images of an FTO electrode covered by the titania sol aged 2 days and subsequently calcined; c1) and c2) represent AFM images of an FTO electrode covered by the titania sol aged 8 days and subsequently calcined; d1) and d2) represent AFM images of an FTO electrode covered by the titania sol aged 15 days and subsequently calcined; e1) and e2) represent AFM images of an FTO electrode covered with titania sol aged 31 days and subsequently calcined.

Table 2.5 - Description of the roughness of the 5 electrodes analysed at the AFM.

Electrode	Roughness/ nm
Blank	(29.5 ± 3.6)
2 sol 2 [day 2]	(1.9 ± 0.3)
6 sol 4 [day 8]	(7.7 ± 1.1)
8 sol 5 [day 15]	(8.6 ± 0.9)
T1 sol 1 [day 31]	(10.7 ± 1.4)
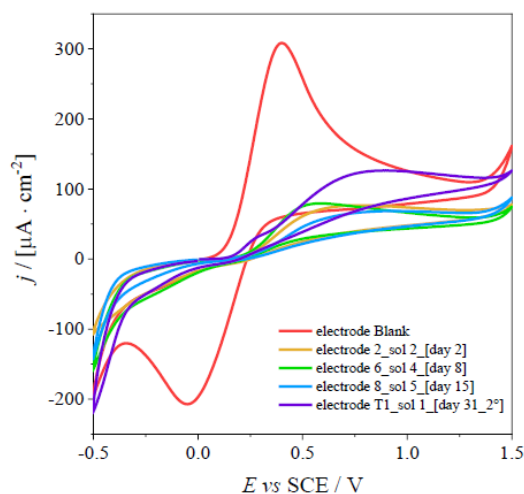
Figure 2.22 - Superimposition of the cyclovoltammetries of the 3 mM Fe probe in an electrolytic solution of $NaClO_4$ of the 5 electrodes which were subsequently analysed with AFM.

The "blank" electrode, which does not have the titanium (IV) isopropoxide has a much higher roughness, probably because FTO is already a rough material. As for the electrodes immersed in the sol of titania, and subsequently calcined, they have an increasing roughness, where the greatest growth occurs between

electrode 2 and 4, in which, in the study of the scan rate we had a true and own modification of the signal shape, from pseudo step to pseudo peak.

As seen previously in the literature, narrow or shallow pores exhibit convergent diffusion, while distant or very deep pores have linear diffusion. Technically, this is what is observed through the shape of the signals in the CVs of the various electrodes since we pass from a pseudo step to a pseudo peak and then have a distortion of the latter. But the shape of the signals in this case are never perfect, so we are in case 3 where the diffusion is of the radial convergent type.

2.2.9. Transient photocurrent characterisation.

In a transient photocurrent analysis, the current between WE and CE is measured when the system is illuminated. The current tends to decrease up to a plateau condition due to the hole-electron recombination, no longer being able to close the circuit. In the dark, there is a decrease in current. By studying the decay over time, it is possible to obtain information on the hole-electron recombination since $D = \frac{I(t)-I(st)}{I(in)-I(st)}$ and $D = e^{-\frac{t}{\tau}}$, therefore, calculating D we obtain τ, representing transient time constant.

Therefore, usually the photocurrent is a technique used to define the hole-electron recombination time, and consequently to obtain information on the energy gap. In this specific case it did not help us, as this value is already known for the titanium dioxide, in the form of anatase, about 3.1 eV. The reason why this study was started was to understand if with our devices we could also use the transient photocurrent as a technique to perform analytical determination, as has been found in the literature for the determination of the ciprofloxacin, as for the work of Ling Cao *et al* [20].
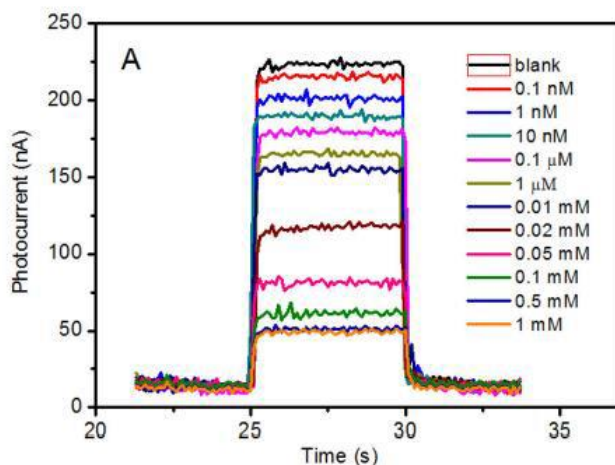
Figure 2.23 - Photocurrent response as a function of concentration for ciprofloxacin detection at the two-layer 5 nm AuNPs modified photoelectrode.

As it can be seen from this graph taken from the work of Ling Cao, the additions of ciprofloxacin decrease the photocurrent of the ITO electrode with the gold nanoparticles. This work therefore makes it clear that the photocurrent is a technique beyond for the study of the material, once it is known, it can be used for the electroanalytical determination [20].

For the following work, the transient photocurrents of all 9 electrodes calcined with the titania sol (on which the study of the scan rate was previously carried out) were performed. The parameters set for the chronoamperometry were:

- OCP -0.128 V
    - Maximum time: 120 s
    - dE/dt limit: $1 \cdot 10^{-6}$ V·s^{-1}
- Apply potential 0.1 V$_{OCP}$
- Cell on
- Record signal
    - Duration: 4500 s
    - Interval time: 1 s
- Cell off
- OCP -0.011 V
    - Maximum time: 120 s
    - dE/dt limit: $1 \cdot 10^{-6}$ V·s^{-1}

During the 4500 s, 600 s of darkness were performed initially, and then 10 light and dark cycles were repeated each for 200 s and 100 s, respectively.

Before performing chronoamperometry, 5 CV cycles were always performed to stabilize the electrodes. Also, for these tests the electrolyte used was $NaClO_4$ (20 cm³), and the electrodes were always the same, such as CE the platinum wire, RE the saturated calomel and the respective 9 electrodes as WE. These 3 electrodes have always been positioned in a triangle, but in such a way that the WE had the conductive face towards the UV lamp, and the distance between the WE and the lamp is 15 cm.

By superimposing the graphs for the 9 electrodes, Figure 2.24 has been obtained, in which can be seen that the first 3 electrodes have the same trend, from the fourth the current density is always higher up to electrode 6 which has the maximum value of j, which then gradually decreases from electrode 7 to 9. This trend made us think of a possible correlation we had with the study of the scan rate of these same electrodes, since from electrode 1 to electrode 6 there was a progressive variation of the shape of the signal from pseudo step to pseudo peak, to then, from electrode 6 onwards, obtain further distortions of the peak.
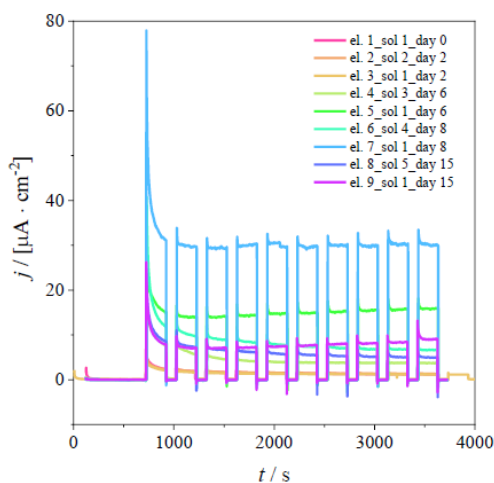
Figure 2.24 - Superimposition of the transient photocurrents of the 9 electrodes with the titania.

From Figure 2.24 it can be seen that as the days increase, there is an increase in the current density, specifically, the electrode 1, 2, 3 are superimposed, and have the lowest value of j, then from electrode 4 to electrode 6 there is a progressive increase in j, to then have a decrease from electrode 7 to 9. It is as if this trend were comparable to the variation in the shape of the signal in CVs as a function of the aging of the sol.

Specifically, to understand this trend, the averages of the j in the moments of light (stationary trend) were made for the repetitions from 2 to 10, and these averages were made a function of the days of aging of the sol (see Figure 2.25).
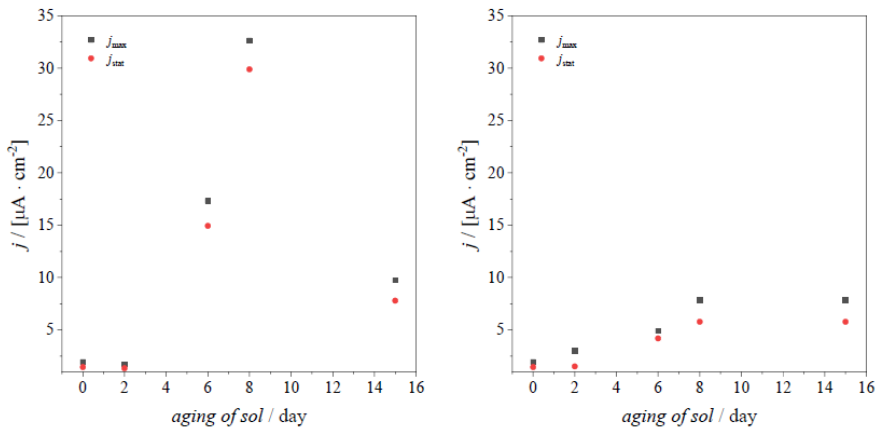
Figure 2.25 - graphs representing the trend of the current density of the maximum peak and of the stationary current, on the left relative to sol 1 (opened several times), on the right relative to the different sols, therefore electrodes from 1 to 5, calcined at the first opening day of the titanium dioxide sol bottle.

The electrodes are very different from day 6 to day 15 of aging of the sol probably because the opening of the bottle of the sol, and therefore the contact of the sol with the air and humidity, tends to increase the current density, even if this difference is high for the electrodes calcined at day 6 and 8 of aging of the sol, while for the others there is no clear variation. Globally there is a sort of bell-shaped trend, there is an increase in the value of *j* from day 0 to day 8, and then there is a decrease, as it can be seen for CVs, where the step turns to peak and then becomes a pseudo peak, as from day 15 the ideality of the peak is totally lost.

According to the work of D. Tafalla and P. Salvador [21] by plotting ln *D* vs *t*, a linear trend for n-TiO_2 electrodes is not obtained; this behaviour is apparently in contradiction with the existence of a recombination of the surface process, which should follow a first order kinetics; consequently, the linear section was taken into consideration to calculate the τ.

This deviation was also noted in the work of L. Lo Presti *et al.* [22] in which the recombination time for titania was calculated using both a mono-exponential and a biexponential fitting. The mono-exponential fitting perfectly correlates the data obtained for a titania system with polymorphs of anatase

and brookite, while the bi-exponential fits well the points of the photocurrent obtained for the anatase.

Given these studies in the literature, it was decided to obtain the τ using all three methods, *i.e.*, the first 50 s of light starting from the second repetition were taken into consideration, and on these the values of D for each point were obtained using the formula $D = \frac{I(t)-I(st)}{I(in)-I(st)}$, from where it was obtained ln D, plotted with the time (t) expressed in seconds. These values were fitted through a straight line (taking into consideration the points that were straighter to each other), through a mono-exponential fitting of equation $y = A_1 \cdot e^{-\frac{x}{t_1}} + y_0$ and a bi-exponential $y = A_1 \cdot e^{-\frac{x}{t_1}} + A_2 \cdot e^{-\frac{x}{t_2}} + y_0$.

Table 2.6 - Tabulation of the τ calculated using the linear fitting.

	τ_{medio} (**retta**)	σ_{medio}	R^2-**adj**$_{medio}$
Elettrodo 1	11.71	1.44	0.95
Elettrodo 2	7.95	0.77	0.94
Elettrodo 3	5.23	0.75	0.94
Elettrodo 4	15.54	3.92	0.97
Elettrodo 5	7.45	0.91	0.99
Elettrodo 6	10.91	1.99	0.97
Elettrodo 7	6.48	2.76	0.96
Elettrodo 8	12.38	1.86	0.97
Elettrodo 9	7.59	2.94	0.98

Table 2.7 - Tabulation of the τ calculated using the monoexponential fitting.

	T_{avg} (**monoexp**)	σ_{avg}	R^2-**adj**$_{avg}$
Elettrodo 1	6.44	0.31	0.98
Elettrodo 2	3.66	0.73	0.95
Elettrodo 3	2.07	0.20	0.98
Elettrodo 4	12.03	3.12	0.96
Elettrodo 5	8.20	1.17	0.98
Elettrodo 6	9.27	0.51	0.98
Elettrodo 7	6.80	3.49	0.94
Elettrodo 8	10.29	2.19	0.99
Elettrodo 9	6.64	1.51	0.96

	τ_{1avg} (biexp)	σ_{1avg}	τ_{2avg}(biexp)	σ_{2avg}	R^2-adj$_{avg}$
Elettrodo 1	2.08	0.38	12.64	2.10	0.998
Elettrodo 2	1.33	0.24	11.28	1.63	0.999
Elettrodo 3	0.96	0.18	4.56	1.39	0.996
Elettrodo 4	6.98	6.42	16.90	9.55	0.96
Elettrodo 5	3.66	2.08	13.23	5.30	0.990
Elettrodo 6	2.98	0.55	19.09	4.70	0.993
Elettrodo 7	2.94	1.26	13.61	13.43	0.95
Elettrodo 8	3.29	0.77	16.46	3.82	0.998
Elettrodo 9	1.92	0.54	13.61	2.21	0.993

Electrode 4 and electrode 7 were the electrodes with the greatest irregularity among the data obtained, and very often the monoexponential and biexponential fitting were overlapped to such an extent that the τ values were almost identical. Since a lot of data had to be eliminated, averages were performed on only about 4 values for these two electrodes. In general, the averages were not performed on all the values obtained experimentally, but only on those that made sense (therefore the negative values were discarded) and on those that did not show total irregularities on their trend.

Taking into consideration Table 2.8, the electrodes calcined with the sol opened several times (electrode 3, electrode 5, electrode 7, electrode 9) tend to have a lower τ value than the electrodes calcined using the dioxide bottle just opened titanium (electrode 2, electrode 6, electrode 8). Probably this is generated by the fact that by opening the bottle, the sol has greater contact with the air and humidity; therefore, more defects are generated on the electrode and therefore there is a more efficient and faster electron-hole recombination. This is also confirmed by the results showed in paragraph 2.2.5, where it is possible to see a worsening of the electronic transfer with the aging of the days of life of the sol, due to the formation of surface defect sites that are responsible for the occurrence of charge recombination processes, that decrease the connectivity of the TiO_2 film.

Furthermore, from Table 2.8, it is also noted that, excluding electrode 1 (day 0 of life of the sol), the others have an increase in τ with the aging of the sol, reaching a plateau condition for the electrodes synthesized from day 8 of aging

onwards. All this, therefore, confirms what has been previously seen with both CVs and AFM, since the τ, being the hole-electron recombination time, depends on the path that the electron follows, therefore on the morphology of the material, as well as voltammetry and roughness. Basically, the values of τ confirm the variation in diffusion from day 0 (convergent diffusion) to day 7 (linear diffusion) to then have a radial convergent diffusion, an intermediate situation between the two.

2.2.10.   Gold nanoparticle (AuNPs).

2.2.10.1.   Synthesis of the AuNPs.

0.015 g of $AuCl_3$, 0.022 g of trisodium citrate dihydrate and 0.01375 g of PVP10 were dissolved separately in 50 cm3 of milliQ water. They were then poured into a three-necked round-bottomed flask with a mechanical stirrer. Then, 0.001875 g of $NaBH_4$ was dissolved in 1.25 cm^3 of milliQ water and added dropwise to the flask with stirring. The solution immediately turns to intense red and is left under stirring for fifteen minutes. After that, the colloidal gold solution is placed in a clean bottle and left, at first, at room temperature in the dark for a few hours and then stored in the refrigerator.

In this thesis the synthesis of gold nanoparticles was not carried out, using AuNPs previously synthesized. Before use, a DLS analysis was carried out to ensure if the dimensions were still the same or if the nanoparticles had created aggregations.

From the DLS analysis this graph was obtained:
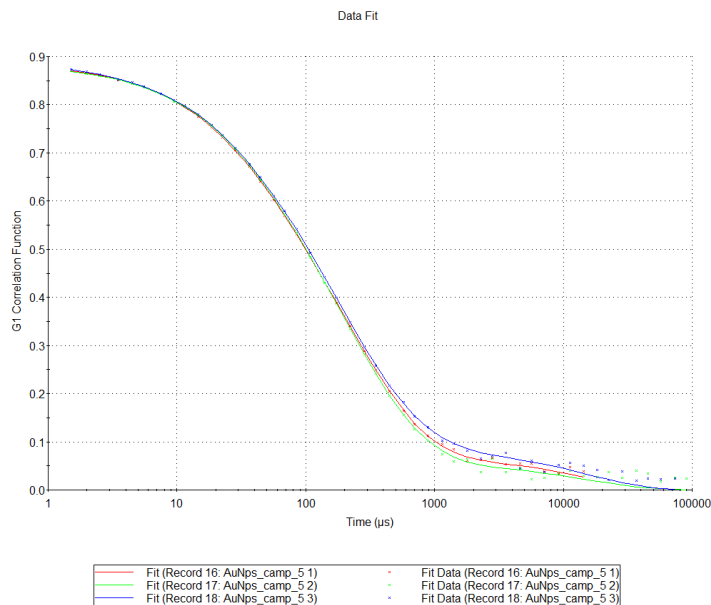
Figure 2.26 - Superimposition of three repetitions of the correlogram of the nanoparticle solution.

Since in this case the correlation curve fits the experimental points well, it was decided to report only the data obtained directly from the DLS, without performing elaborations on *Origin*.

			Size (d.nm):	% Intensity:	St Dev (d.nm):
Z-Average (d.nm):	41.78	Peak 1:	102.7	81.7	80.79
PdI:	0.845	Peak 2:	8.993	13.0	2.867
Intercept:	0.882	Peak 3:	4610	5.3	827.2
Result quality :	Refer to quality report				
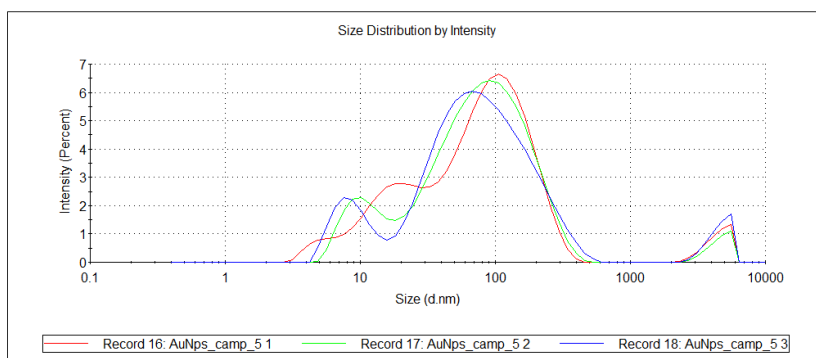
Figure 2.27 - Superimposition of three repetitions of the trend of signal intensities as a function of particle size.

		Size (d.nm):	% Volume:	St Dev (d.n...
Z-Average (d.nm): 41.78	**Peak 1:**	8.032	99.3	8.417
PdI: 0.845	**Peak 2:**	4908	0.7	899.5
Intercept: 0.882	**Peak 3:**	0.000	0.0	0.000
Result quality : **Refer to quality report**				
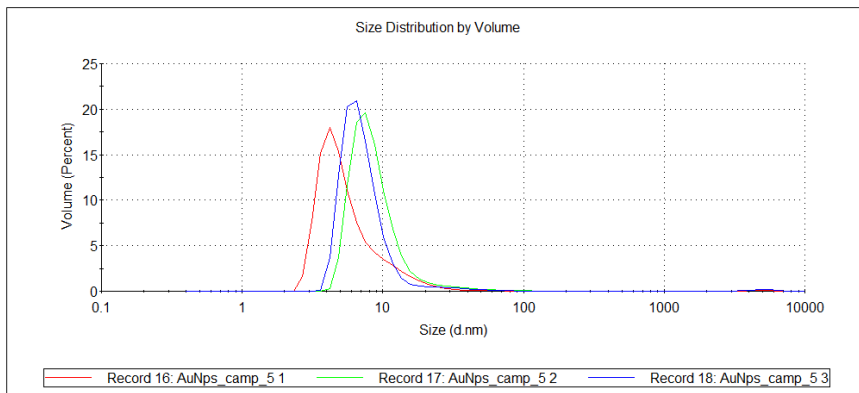
Figure 2.28 – Superimposition of three repetitions of the trend of signal volume as a function of particle size.

From Figure 2.27 it was noted the presence of three populations of particles, respectively with dimensions of about 10 nm, 100 nm, and 1000 nm, but, from Figure 2.28 it can be defined that the only prevailing population is the one having 10 nm in diameter. This then showed that the gold nanoparticles remained stable over time, and that their size remained around 10 nm, specifically, through the three repetitions at the DLS the average size of the AuNPs is (11.97±1.43) nm.

To confirm this result, it was also decided to perform a UV-vis spectrum of the nanoparticle solution to define the position of the plasmon band and thus confirm the particle size. Specifically, 250 mm^3 of gold nanoparticle solution was inserted into a quartz cuvette and then brought to volume (1250 mm^3) with milliQ water. The UV spectrum was obtained between 250 nm and 800 nm as shown in Figure 2.29:
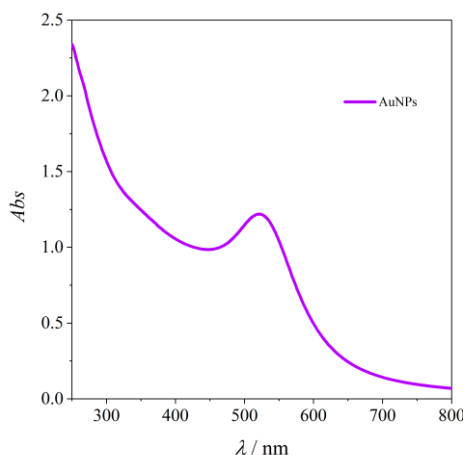
Figure 2.29 - UV-vis spectrum of AuNPs.

The maximum absorption is at 521 nm, which confirms what was obtained by the DLS, as, the plasmon band of gold nanoparticles with a size of 10 nm is about 520 nm.

2.2.11. Device assembly: electrodes with deposition of gold nanoparticles.

The procedure for assembling the slides consists of the following steps:

1. Preparation and cleaning of the FTO substrate. First, the FTO plate is cut by making a rectangle of 3x2 cm. The non-conductive part is marked, and the device is sonicated for ten minutes in a 1:1:1 solution of water, acetone, and 2-propanol. Subsequently, the washed slide is irradiated under UV light for one hour. Often this procedure was performed the day before the assembly of the complete device.

2. Pretreatment of the slide. The conductive slide is immersed in a 95-97% sulfuric acid solution for appro 90 seconds. This operation allows to further clean the glass, and to create on its surface some -OH groups that will be used for the connection of the linkers. Subsequently the substrate is rinsed with milliQ water and then dried underneath nitrogen flow, to avoid impurities.

3. Preconditioning. The conductive part of the FTO is placed upwards, placing everything inside a cell created ad hoc (Figure 2.30). Subsequently 18 cm^3 of anhydrous toluene are added. Finally, the cell is carefully sealed with parafilm and degassed with nitrogen for a couple of minutes, to remove most of the oxygen present inside the cell.

80

At this point the reactor is placed on a petri dish inside a crystallizer previously heated to 70 °C.

4. Adding linkers. After one hour at 70 °C, 36 mm^3 of MPTMS and 4 mm^3 of APTES in 2 cm^3 of anhydrous toluene are dissolved in a flat bottom tube, which are subsequently added to the cell. The reactor is then left at 70 °C for three hours.

5. Cleaning the device. After three hours, the modified slide is removed from the cell and sequentially sonicated in toluene, ethanol and milliQ water for three minutes each. This step is performed to remove all silanes not anchored on the FTO and to promote the creation of a single monolayer.

6. Deposition of gold nanoparticles. The device is placed on a petri dish, with the conductive part upwards and the solution of AuNPs is deposited by drop casting on the surface using a Pasteur pipette. The petri dish is closed, to prevent dust or dirt from settling, and the system is left like this for an hour. At this point, the slide functionalized with gold nanoparticles is washed with milliQ water and dried under nitrogen flow.

7. The electrode is positioned in the reactor so that the conductive face is upwards, in direct contact with the nitrogen flow. Nitrogen is flushed for one minute to eliminate the oxygen present in the reactor. At this point the reactor is placed in the oven in order to perform a quick calcination for 1 hour conducted at 400 °C with a nitrogen flow of 200 cm^3·min^{-1}.

Figure 2.30 - the image on the left is the cell created ad hoc, on the right there is the global system to perform the synthesis of the slides, at the centre is the deposition of gold nanoparticles on the electrodes.

To be able to understand if there were differences between the use of the device prepared with only the deposition of the gold nanoparticles without carrying out the calcination, and an electrode instead prepared with the gold and calcined nanoparticles, the characterizations were performed on the two respective ones, then, the studies of the scan rate in NaClO₄ and the respective additions of the iron probe with the cyclovoltammetries and subsequently the impedances at -0.1 V, +0.1 V and +0.25 V.

2.2.12.   CV characterisation.

As just mentioned, studies of the scan rate were carried out on the two electrodes, and then subsequent cyclovoltammetries were performed with these operating parameters:

- Apply potential: 0 V
- Start potential: 0 V
- Upper potential: 0.8 V
- Lower potential: -0.05 V
- Stop potential: 0 V
- Number of scans: 1
- Scan rates: 0.1; 0.01; 0.02; 0.05; 0.1; 0.2; 0.5; 0.75; 0.1 V·s⁻¹
- Step: 0.005 V

Figure 2.31 shows only the cyclovoltammetries referred to the 3 mM of the two electrodes with their respective calibration lines:
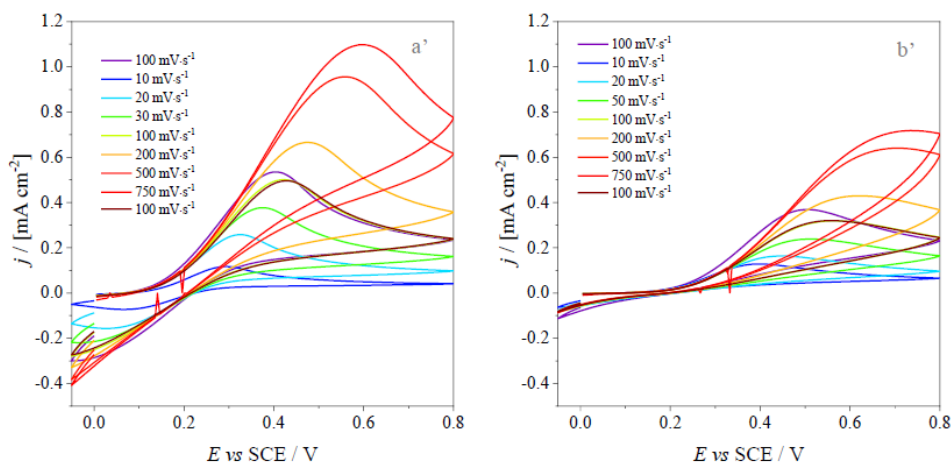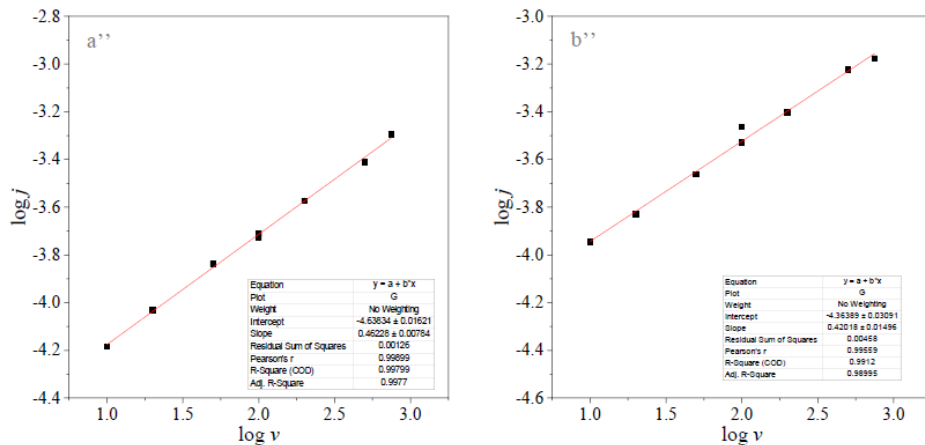
Figure 2.31 - In graph a' and b' the superimpositions of the cyclovoltammetries performed in 20 cm³ of NaClO₄ with 3 mM of Fe probe respectively with the non-calcined electrode and the calcined electrode have been reported. While a" and b" are the respective calibration lines, so the one on the left relates to the non-calcined electrode while the one on the right relates to the calcined electrode.

From Figure 2.31 it can be seen that the peak is more evident for the non-calcined electrode, which also has a higher slope, specifically, the non-calcined electrode with AuNPs has a slope of (0.462 ± 0.008) A·cm^{-2}·M^{-1}, while the calcined electrode with gold nanoparticles has a slope of (0.42 ± 0.01) A·cm^{-2}·M^{-1}. It must also be said that observing the electrodes after these tests, they showed a clear sign, the part immersed in the electrolytic solution and therefore that worked, was of a much less intense colour, a much more faded pink, as if gold had been lost in solution. This clear variation was much more pronounced for the non-calcined electrode than for the calcined one since the latter has nanoparticles more anchored to the electrode support.
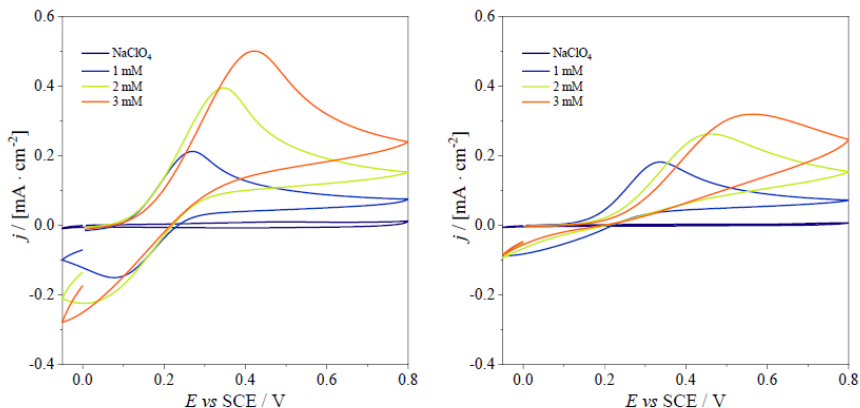
Figure 2.32 - Superposition of the cyclovoltammetries of: background (NaClO₄), 1 mM, 2 mM, 3 mM of the iron probe, to the left of the non-calcined electrode with the gold nanoparticles, to the right of the calcined electrode with the gold nanoparticles.

To be able to observe the variation of the behaviour of the calcined electrode from the non-calcined one, the cyclovoltammetries of the background (NaClO₄) and of the 3 additions of $K_4[Fe(CN)_6]$ (1 mM, 2 mM, 3 mM) of the non-calcined electrode were superimposed on the left; on the right those of the non-calcined. From Figure 2.32 it can be seen that in both cases with the additions there is a shift of the peak at higher potentials, but the shift is higher for the calcined electrode which also has lower peak heights (lower current density).

At this point, it was assumed that the high use of the two devices had created problems inherent in the responses of the electrodes, especially as regards the electrode with non-calcined gold nanoparticles. To understand if the use had led to shifts in the peak potential, it was decided to synthesize two other electrodes and perform a superimposition of the cyclovoltammetries in Figure 2.33.
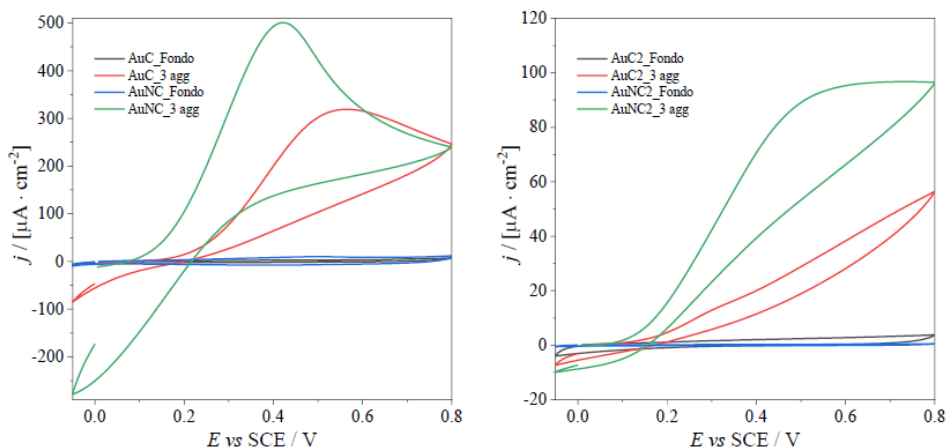
Figure 2.33 - Superimpositions of the cyclovoltammetries of the calcined and non-calcined electrodes with the respective background (NaClO₄) and 3 mM of the iron probe. On the left there is the superimposition of the electrodes which were already used for the study of the scan rate; on the right there is the superimposition of the electrodes synthesized and used a few days after calcination without performing studies of the scan rate.

Observing these two superimpositions, it can be immediately noted that the stabilization of the electrode (*i.e.*, not using the electrode for few days and letting it "rest") is necessary, since, especially for the calcined electrode with nanoparticles, the first use does not even show the net peak at about +0.5 V.

2.2.13. EIS characterisation.

Characterization by EIS was also performed on the same electrodes, to understand how much the calcination changed in the response. For this technique, 20 cm³ of NaClO₄ were taken and the impedances for the background were carried out, for the addition of the 1 mM, 2 mM, and 3 mM of iron probe. The spectra were performed with the same parameters as the previous impedances, with an accumulation potential of -0.1 V, +0.1 V, +0.25 V.

Once all the impedances were collected, superimpositions were made in Figure 2.34, where there are the spectra with an accumulation potential of +0.25 V in the background and 3 mM for both the electrode with the calcined and non-calcined nanoparticles.
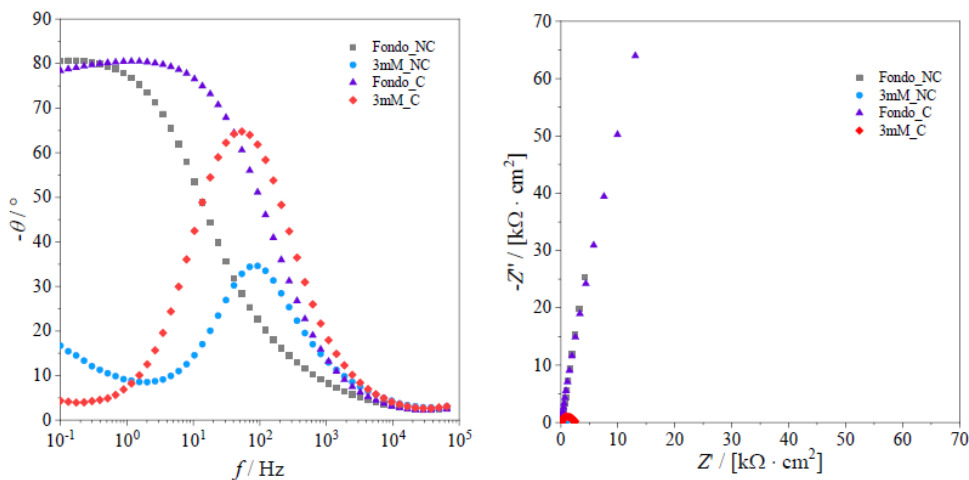
Figure 2.34 - Superimposition of the Bode plot of the calcined and non-calcined electrodes of the background and of the 3 mM of the iron probe have been reported on the left, while on the right the superimposition of the Nyquist graph of the calcined and non-calcined electrodes have been reported.

From the Bode graph it is possible to see immediately that the calcined electrode has a higher -θ, in the case of the background it is hardly visible while in the case of the 3 mM probe the difference is much more pronounced. In addition to having a variation of the -θ, there is also a variation of the frequencies, but the presence of the probe causes the maximum to shift to higher f values, so we imagine that the electrode transfer is faster. Both for the calcined electrode and for the non-calcined electrode, the background has similar -θ values, in both cases it is about 80°, so it is a good capacitor, while, for both electrodes the probe decreases this value and therefore no longer makes the electrode a good capacitor due to the presence of the iron probe.

The superimposition of the Nyquist plot is not so obvious, so it was decided to separate the graphs for the calcined electrode on the right and the non-calcined electrode on the left in Figure 2.35:
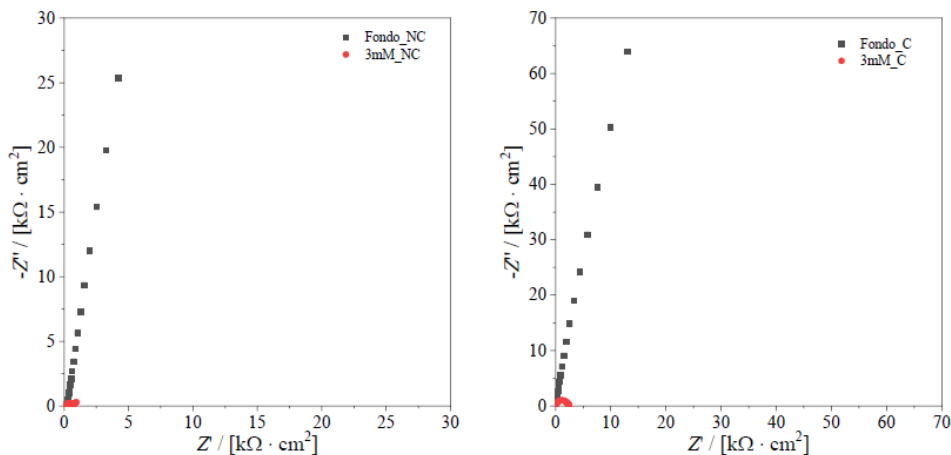
Figure 2.35 - On the left the superimposition of the Nyquist plots of the non-calcined electrode (background + 3 mM probe), while on the right the superimpositions of the Nyquist plots of the calcined electrode (background + 3 mM probe).

From these two Nyquist plots it can be seen that for both cases the presence of the iron probe influences the charge transfer, as the non-calcined electrode has a semicircle with a smaller amplitude, which means a simpler charge transfer, but in addition to the semicircle there is a beginning of the Warburg line and therefore problems also related to mass transfer. While in the case of the calcined electrode there is a wider semicircle for the 3 mM probe and therefore more problems related to charge transfer, but there is no information on mass transfer.

2.2.14. Device assembly: electrodes with deposition of AuNPs and titanium dioxide.

The procedure for assembling the slides consists of the following seven steps:

1. Preparation and cleaning of the FTO substrate. First, the FTO plate is cut by making a rectangle of 3x2 cm. The non-conductive part is marked, and the device is sonicated for ten minutes in a 1:1:1 solution of water, acetone, and 2-propanol. Subsequently, the washed slide is irradiated under UV light for one hour. Often this procedure was performed the day before the summary of the complete device.

2. Pretreatment of the slide. The conductive slide is immersed in a 95-97% sulfuric acid solution for 90 seconds. This operation allows to further clean the glass, and to create on its surface some -OH groups that will be used for the connection of the linkers. Subsequently the

substrate is rinsed with milliQ water and then dried underneath nitrogen flow, to avoid impurities.

3. Preconditioning. The conductive part of the FTO is placed upwards, placing everything inside a cell created ad hoc (Figure 2.30). Subsequently 18 cm^3 of anhydrous toluene are added. Finally, the cell is carefully sealed with parafilm and degassed with nitrogen for a couple of minutes, to remove most of the oxygen present inside the cell. At this point the reactor is placed on a petri dish inside a crystallizer previously heated to 70 °C.

4. Adding linkers. After one hour that the cell has been at 70 °C, 36 mm^3 of MPTMS and 4 mm^3 of APTES in 2 cm^3 of anhydrous toluene are dissolved in a flat bottom tube, which are subsequently added to the cell. The reactor is then left at 70 °C for three hours.

5. Cleaning the device. After three hours, the modified slide is removed from the cell and sequentially sonicated in toluene, ethanol and milliQ water for three minutes each. This step is performed to remove all silanes not anchored on the FTO and to promote the creation of a single monolayer.

6. Deposition of gold nanoparticles. The device is placed on a petri dish, with the conductive part upwards and the solution of AuNPs is deposited on the surface using a Pasteur pipette. The petri dish is closed, to prevent dust or dirt from settling, and the system is left like this for an hour. At this point, the slide functionalized with gold nanoparticles is washed with milliQ water and dried under nitrogen flow.

7. Deposition of the titania layer and calcination. The functionalized slide is immersed in the TiO$_2$ sol for 60 seconds. The slide is positioned in the reactor so that the conductive face is upwards, in direct contact with the nitrogen flow. Nitrogen is flushed for one minute to eliminate the oxygen present in the reactor. At this point the reactor is placed in the oven to perform a quick calcination for 1 hour conducted at 400 °C with a nitrogen flow of 200 cm^3·min^{-1}. This phase serves to mineralize the organic part and to promote the growth of the crystalline anatase phase of titanium dioxide.

The presence of gold nanoparticles generates a reddish surface, but being subsequently covered by a layer of titania, there is also some greyish part as well as the typical iridescence of titania. The presence of TiO$_2$ can be observed by the "rainbow" due to titania and the persistence of transparency. Since

titania is a photosensitive, it would be better storing the electrode in the dark, in a box covered with aluminium foil, to avoid direct contact with light.

2.2.15. CV characterisation.

The first thing that was noticed between the use of devices obtained by calcination with titanium dioxide only, compared to those that also contain gold nanoparticles, is that in the first case the stabilization of the electrode did not require a long time to stabilize, while in the second case the stabilization required a few days of use after calcination before carrying out the tests, so that the excess gold nanoparticles were taken away from the electrode surface or that in any case the electrode response began to be as reproducible as possible.
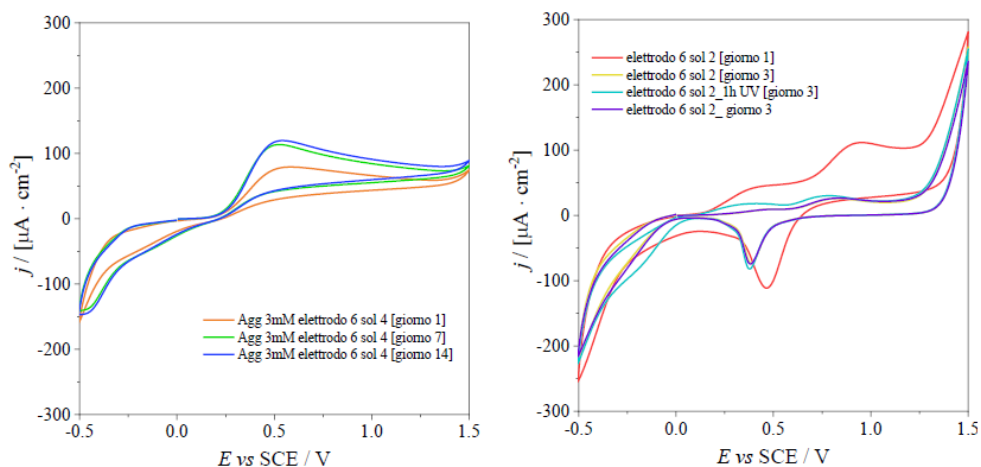
Figure 2.36 – CV stabilisation comparison.

In both cases, waiting few days allows to have a much more reproducible signal in current density. However, the biggest difference lies in the fact that for the electrode with the titania alone there is no variation in the shape of the signal. While in the case of the electrode with also AuNPs, there is a clear decrease in the intensity of the signal linked to the oxidation of gold, and a small variation in its position.

At this point, once the electrodes were stabilized, studies of the scan rate were performed on the electrodes synthesized on day 1, day 7 and day 14 of the titanium dioxide sol life. Furthermore, these studies of the scan rate were performed using two different electrolytes, $NaClO_4$ and PBS at a pH of approximately 4.

The parameters used in the cyclovoltammetries were:

PBS:
- Apply potential: 0 V
- Start potential: 0 V
- Upper potential: 1.0 V
- Lower potential: -0.3 V
- Stop potential: 0 V
- Number of scans: 1
- Scan rates: 0.1; 0.01; 0.02; 0.05; 0.1; 0.2; 0.5; 0.75; 0.1 $V \cdot s^{-1}$
- Step: 0.008 V

NaClO$_4$:
- Apply potential: 0 V
- Start potential: 0 V
- Upper potential: 0.8 V
- Lower potential: -0.3 V
- Stop potential: 0 V
- Number of scans: 1
- Scan rates: 0.1; 0.01; 0.02; 0.05; 0.1; 0.2; 0.5; 0.75; 0.1 $V \cdot s^{-1}$
- Step: 0.005 V

Since in subsequent studies the electrodes calcined on the seventh day of the sol's life were used (also based on the previous study performed on the aging of the sol, which presented as a response the more defined peak than the others), only these are reported:
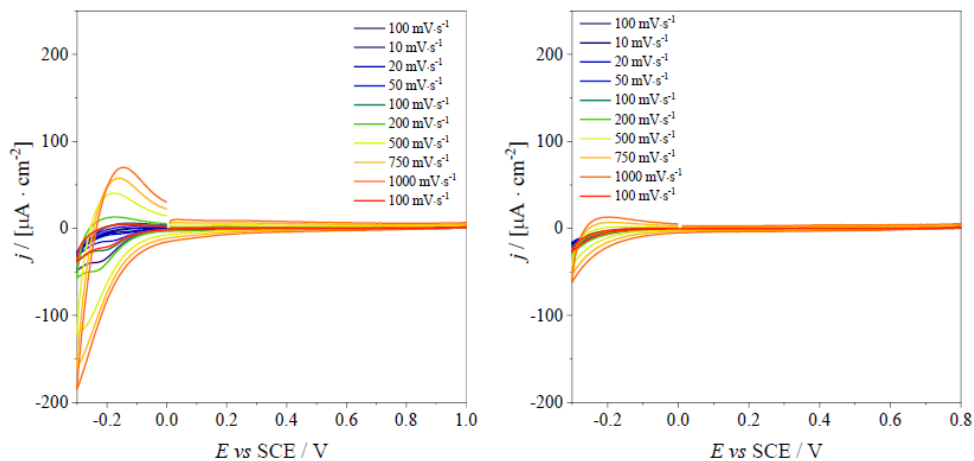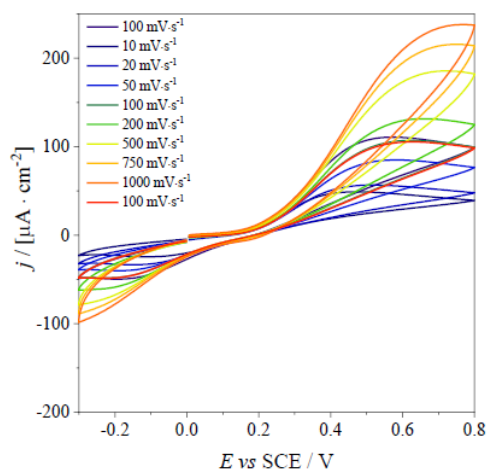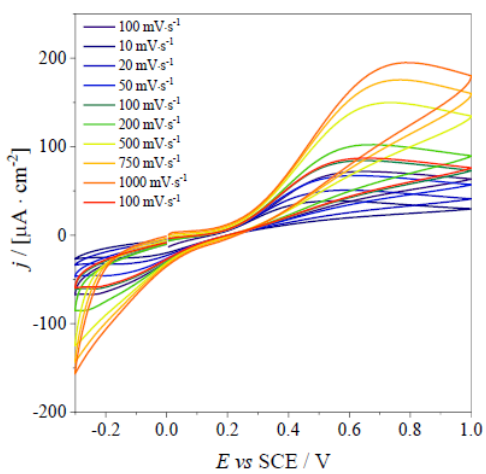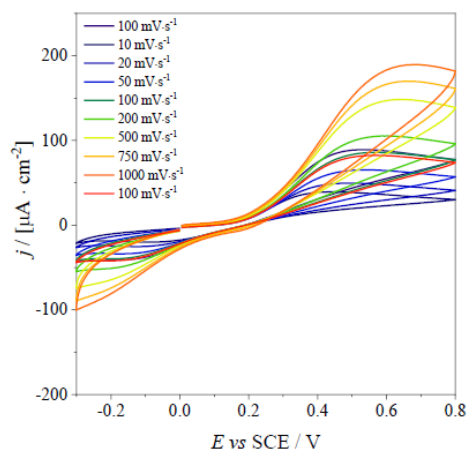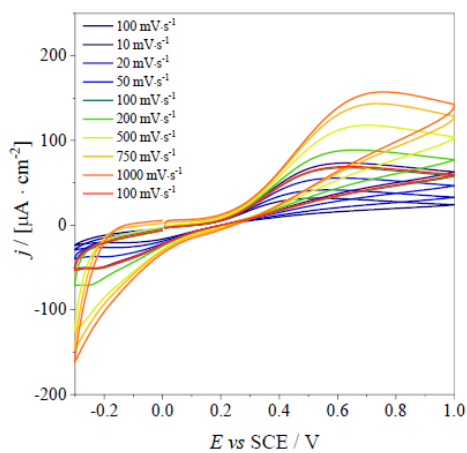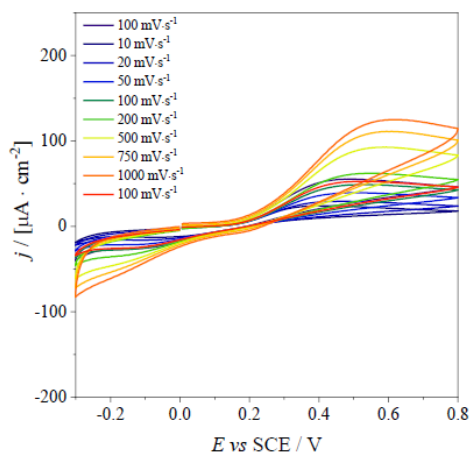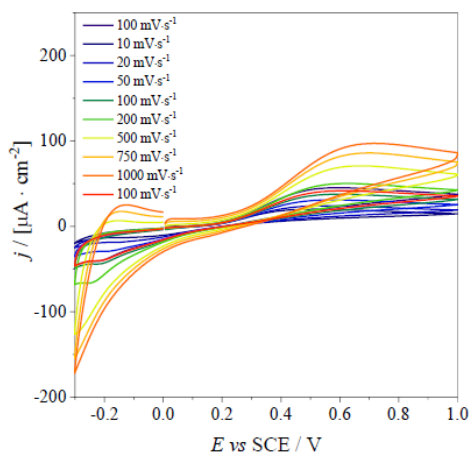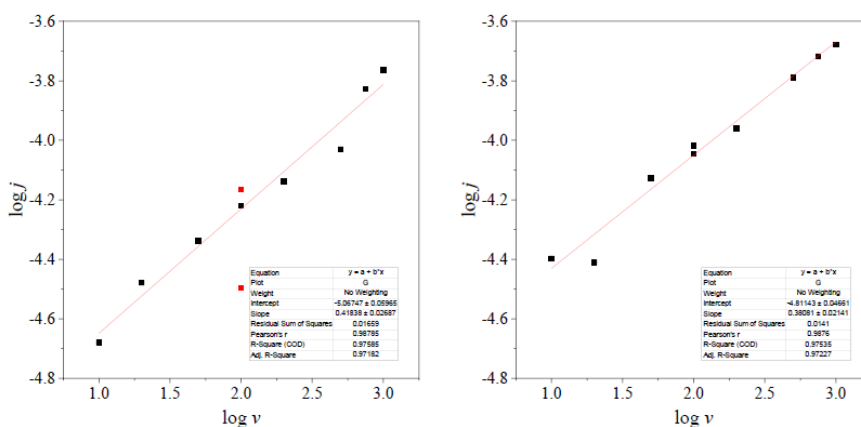
Figure 2.37 - on the right the cyclovoltammetries of electrode 6 have been represented with both AuNPs and titanium dioxide using NaClO$_4$ as electrolyte, while on the left PBS with a pH of about 4 as electrolyte. From the top: the first graph is of the background, from the second to the fourth are respectively 1 mM, 2 mM, 3 mM (of the ferrocyanide probe). The fifth graphs are the calibration lines of the respective 3 mM.

The different slope of the two lines and, consequently, the interaction between the probe molecule and the electrode in the two electrolytes considered can be explained by the fact that, ss it will be further explained in chapter 2.3.5., titanium dioxide is positively charged at pH values lower than the point of zero charge (pzc), which is approximately 6.2. Potassium ferrocyanide is a negatively charged probe and it has a better interaction with a positively charged surface, like the one of TiO$_2$ when working at low pH values.

When working in NaClO$_4$, the surface is partially positive, so the probe molecule has a slightly worse interaction with the electrode, thus resulting in a lower slope.

2.2.16.   EIS characterisation.

Also in this case the parameters used to carry out the impedances are the same as those described previously. In the specific case, EIS was performed on electrodes calcined with gold nanoparticles and titania, using both NaClO$_4$ and PBS as electrolyte. Figure 2.38 shows the superimposition of the backgrounds and the 3 mM of the iron probe performed at +0.25 V.
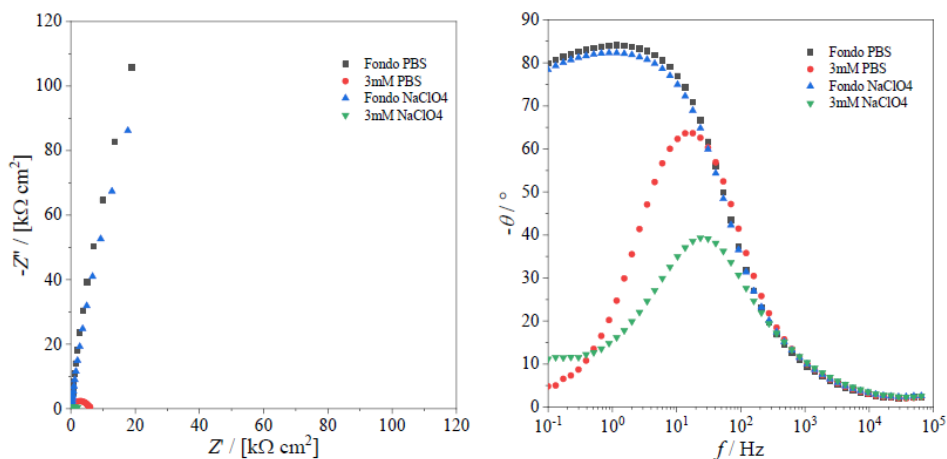
Figure 2.38 - EIS of the FTO electrodes calcined with AuNPs and titania with two different electrolytes, NaClO₄ and PBS, with ferrocyanide 3 mM. On the left are the Nyquist plots while on the right the Bode plots.

From Figure 2.38 it is possible to see the differences of the resistances for different electrolytes. Specifically, from the Bode plot, it can be seen that, in the case of the background, the trend is very similar for the two electrolytic solutions, and both are good capacitors having a $-\theta$ at about 85°, the presence of the probe instead, in addition to shifting the maximum of the peak to higher frequencies presents a higher peak for the 3 mM of the PBS, while for NaClO₄ the peak is lower. Therefore, there are different charge transports, specifically, also observing the Nyquist plot, the resistance to the electrode transfer is higher for the PBS.

At this point it was decided to make a comparison between the three electrodes calcinated and analysed in NaClO₄, that is the electrode with the titania, the electrode with the gold nanoparticles and the electrode with both the gold nanoparticles and with the titania.
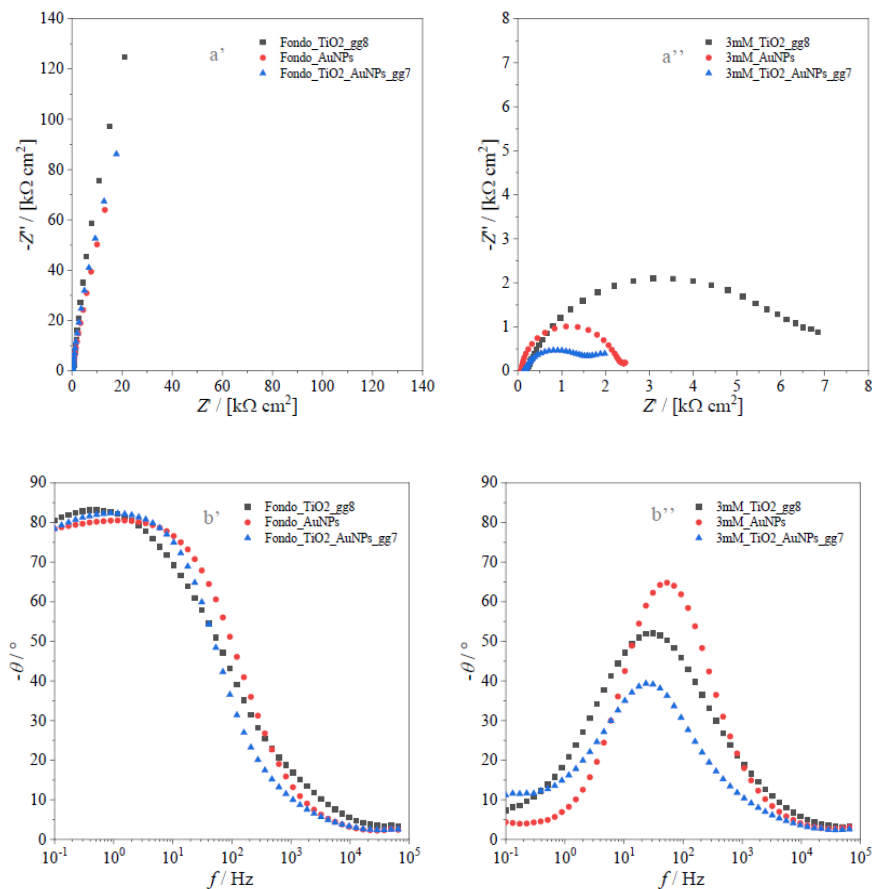
Figure 2.39 - The graphs a' and a" depict the Nyquist plots respectively of the background and the 3 mM of the probe, while the graphs b' and b" represent the Bode plots of the background and the 3 mM of the probe respectively.

From the Bode plot in Figure 2.39 it can be seen that the presence of the probe decreases the value of $-\theta$, in fact, it passes from about 85° for the background (excellent capacitor) to lower values for the presence of ferrocyanide, and above all the probe differentiates the three electrodes, specifically the best capacitor is the electrode with only the nanoparticles, probably because titania is an insulating material and therefore decreases the capacitive properties.

From the Nyquist plot in Figure 2.39 it can be seen that the presence of the probe distinguishes more the electrodes analysed in that range of frequencies. Specifically, there is greater resistance to electronic transfer for the electrode with only titania, which decreases for the electrode with only gold nanoparticles and decreases even more due to the presence of both gold nanoparticles and titania. Furthermore, the presence of gold nanoparticles makes the Nyquist graph increasingly resemble the electron transfer graph at

the interphase with control of both charge and matter transfer, i.e., the contribution of the diffusion of the reagents to the electrode (i.e., the Warburg line).

2.3. Results and discussion.

This chapter shows the results of the electroanalytical determinations of the following analytes, possible emerging contaminants: diclofenac, flurbiprofen, paracetamol, ciprofloxacin and arsenic. For all analyses, the following setup was used: a platinum wire as CE, saturated calomel as RE and the FTO electrode calcined with gold nanoparticles and titanium dioxide as WE. Inside a 50 cm^3 beaker, 20 cm^3 of electrolyte solution (PBS at different pH according to the tests performed) were always inserted.

2.3.1. Diclofenac.

For the first analysis it was thought to analyse diclofenac, because, from previous studies, it had been seen that it can be analysed with these modified electrodes, and therefore we tried to continue this path. First, we performed cyclovoltammetries to understand the electrochemical behaviour of the analyte. A $1.0 \cdot 10^{-3}$ M solution of diclofenac was prepared by weighing 0.0159 g of salt, transferred quantitatively into a 50 cm^3 flask and made up to volume with milliQ water. In an electrolytic solution of PBS at pH 4 (20 cm^3), 3 additions of the solution thus prepared (1.5 cm^3) were carried out. The CVs performed had these parameters:

- Apply potential: 0.3 V
- Start potential: 0.3 V
- Upper potential: 1.2 V
- Lower potential: 0.292 V
- Stop potential: 0.3 V
- Number scan: 1
- Scan rate: 0.1 V·s^{-1}
- Step: 0.008 V
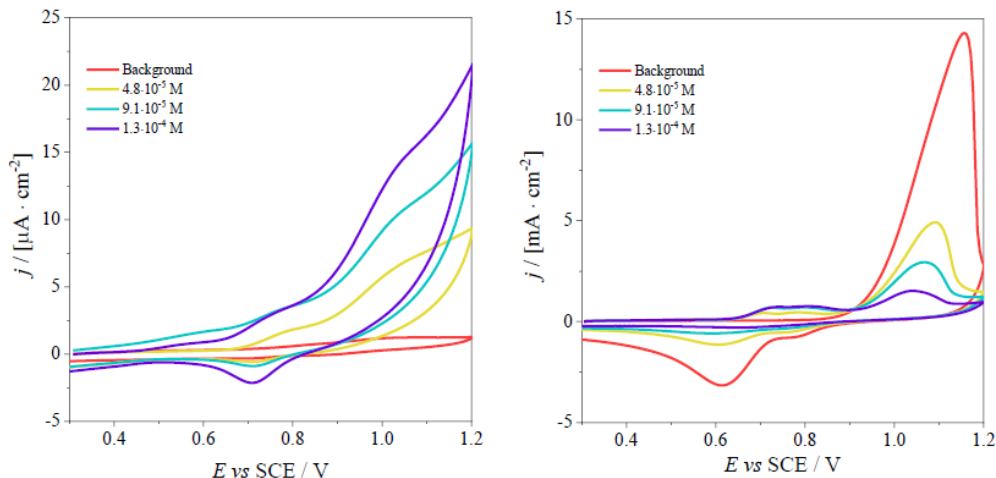
Figure 2.40 - on the left the CVs performed with the FTO electrode modified with gold nanoparticles and titania as WE, while on the right the CVs are related to a bare gold wire electrode as WE. In both cases, the overlaps are relative to the background (20 cm³ of PBS at pH 4), and to three consecutive 1.5 cm³ additions of the stock solution 1.0·10⁻³ M.

As it can be seen from Figure 2.40, the bare gold wire is drastically soiled by diclofenac, because from the background to the third addition of the analyte, there is a clear decrease of intensity of the signal at 1.1 V (gold oxidation peak), however, there is an increase in the signal at 0.7 V (which would almost look like a double peak), but between the second and third addition there is no longer this increase, probably because the electrode has been fouled from the previous additions. In the case of the modified FTO electrode, on the other hand, the gold oxidation signal is not present in the background, which however appears with the additions, as well as the step at 0.7 V, which also in this case seems to reach the saturation between the second and third addition.

At this point we tried to study the fouling of the FTO electrode, at first by cleaning it only with milliQ water, and then also exploiting an hour of irradiation with the UV lamp. The operating parameters used for this test were the same as in the previous test:
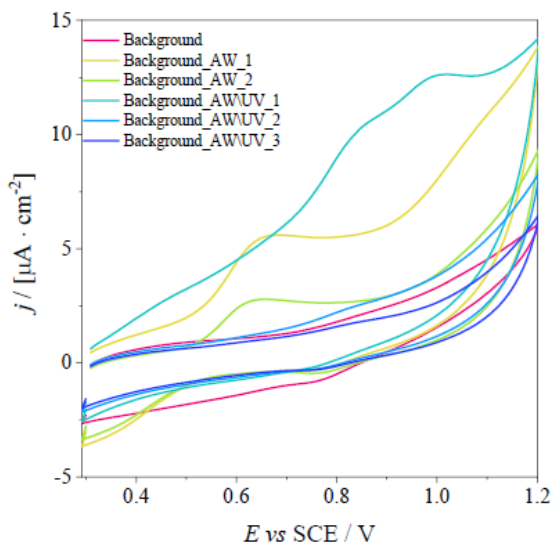
Figure 2.41 - Superimposition of the background (PBS at approximately pH of 4) in LSVs, of the three aliquots of diclofenac and the subsequent cleaning of the electrode with milliQ water (AW) and also by UV irradiation (AW\UV).

At this point, a pulsed technique has been used, in order to increase the sensitivity of the technique, specifically two pulsed techniques were used: normal pulse voltammetry (NPV) and (differential normal pulse voltammetry) DNPV, with the same operating parameters:

NPV:
- Apply potential: 0.3 V
- Start potential: 0.3 V
- Stop potential: 1.5 V
- Base potential: 0 V
- Step: 0.005 V
- Normal pulse time: 0.07 s
- Interval time: 0.5 s

DNPV:
- Apply potential: 0.3 V
- Start potential: 0.3 V
- Stop potential: 1.7 V
- Base potential: 0 V
- Step: 0.005 V
- Modulation time: 0.025 s
- Normal pulse time: 0.025 s
- Interval time: 0.5 s

For these tests the aliquots were not taken from the 10^{-3} M stock solution, but a dilution was performed from the latter. That is, from the solution $9.9 \cdot 10^{-4}$ M 200 mm^3 were taken and transferred quantitatively to a 25 cm^3 flask making up to volume with milliQ water.
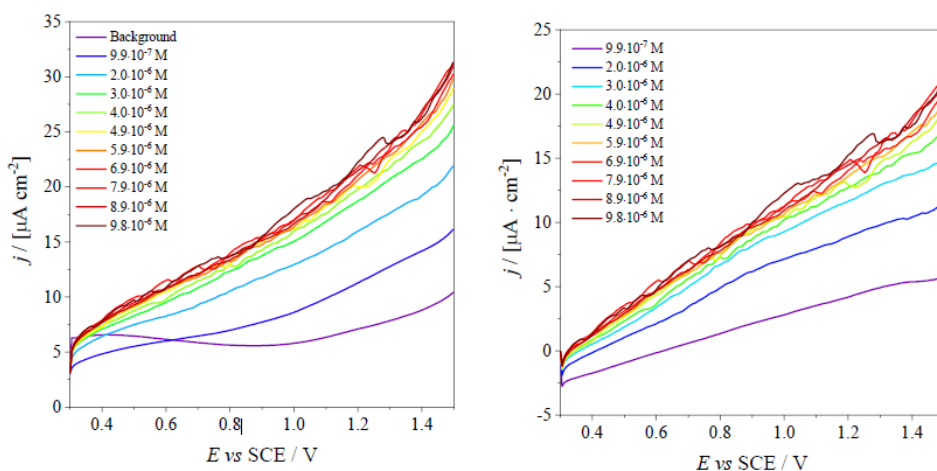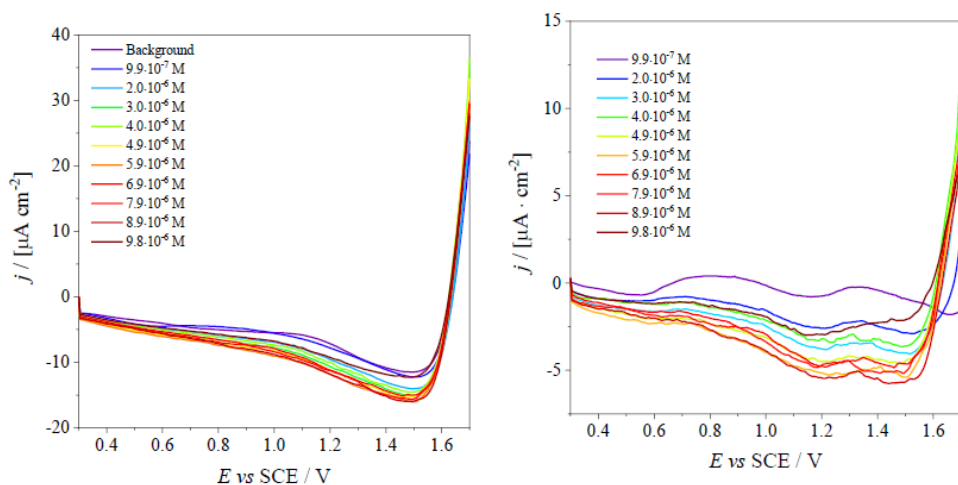
Figure 2.42 - NPVs performed on the background (20 cm³ of PBS at pH about 4) and then after 10 consecutive additions of 200 mm³ of diclofenac 9.9·10⁻⁵M. On the left the NPVs with the presence of the background were reported, while on the right the subtraction of the background was performed to try to understand if it was possible to see the diclofenac peak.

From Figure 2.42, it was not possible to obtain a calibration straight line, as there is no peak relative to diclofenac, in addition to the fact that by increasing the concentration the curves are very noisy and not with a constant increase. Increasing the concentration of the drug increases the trend of the curve, but not in a constant way and without the vision of peaks or steps related to the analyte.

Figure 2.43 - DNPVs performed on the background (20 cm³ of PBS at pH about 4) and then after 10 consecutive additions of 200 mm³ of diclofenac 9.9·10⁻⁵M. On the left the DNPVs with the presence of the background were reported, while on the right the subtraction of the background was performed to try to understand if it was possible to see the peak of diclofenac.

It can be seen from Figure 2.43 that the baseline tends to drop with the additions and it is very noisy, so even if there seems to be two peaks, one at about 0.8 V probably related to diclofenac oxidation, and one at about 1.4 V probably related to the oxidation of gold, however, despite the subtraction of the background the peaks are not defined and therefore it was not possible to obtain a calibration line.

Considering these results, it was decided to change the analyte as it seemed that 10 minutes of irradiation are not enough to clean the electrode, and that perhaps the only way would have been the use of amperometric techniques with UV lighting.

2.3.2. Flurbiprofen.

Given the unsatisfactory results of the test performed with diclofenac, it was decided to analyse a molecule like it on a pharmacological level, so it was decided to analyse flurbiprofen, which is an NSAID with anti-inflammatory functionality as well as diclofenac.

Flurbiprofen was prepared not only in aqueous solution but with the addition of alcohol because this drug has a low solubility (8 mg·dm^{-3}). 0.0121 g of flurbiprofen were weighed, transferred quantitatively to a 50 cm^3 flask, to which 5 cm^3 of 2-propanol was added and then made up to volume with milliQ water. The solution has been sonicated and placed in the refrigerator, and it has a concentration of $9.9 \cdot 10^{-4}$ M.

As first test, linear sweep voltammetries (LSVs) were performed with the same parameters (so that it was clear if this molecule could be determined with these electrodes):

- Apply potential: 0 V
- Start potential: 0 V
- Stop potential: 1.2 V
- Scan rate: 0.1 V·s^{-1}
- Step: 0.008 V

To obtain Figure 2.44, 20 cm^3 of PBS at approximately pH 4 were added to which three aliquots of 1 cm^3 of the previously prepared $9.9 \cdot 10^{-4}$ M solution were subsequently added.
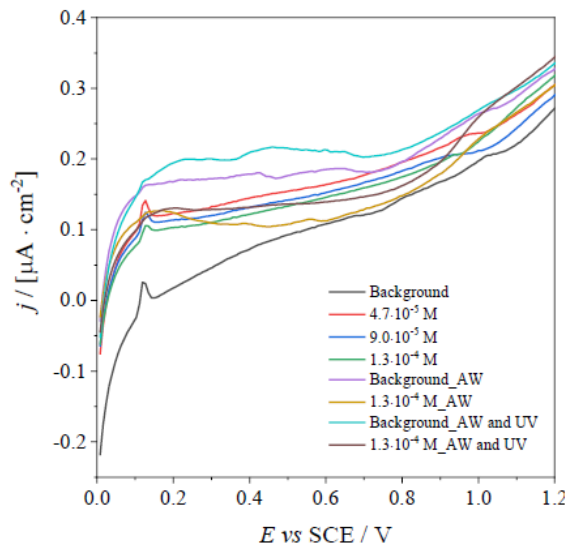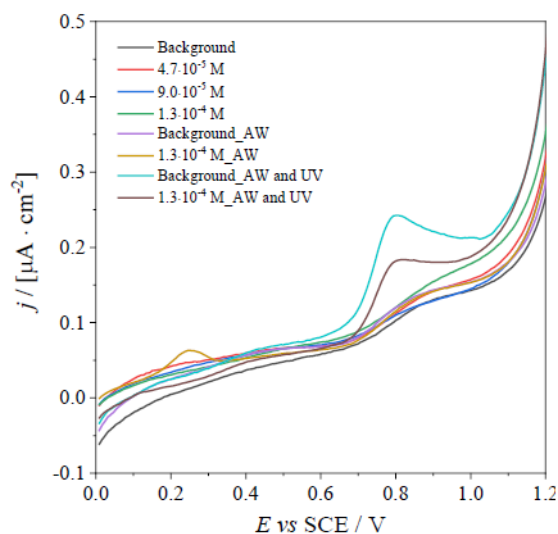
Figure 2.44 - superimposition of the LSVs of the background (PBS at approximately pH of 4), of the three aliquots of flurbiprofen and the subsequent cleaning of the electrode with milliQ water and by UV irradiation.

To obtain Figure 2.45, 20 cm^3 of PBS at pH 4 were added, to which three aliquots of 1 cm^3 of the previously prepared 9.9·10^{-4} M solution were subsequently added.

Figure 2.45 - Superimposition of the background (PBS at approximately pH of 4) LSVs, of the three aliquots of flurbiproben and the subsequent cleaning of the electrode with milliQ water and by UV irradiation.

To understand if it was a problem related to classical voltammetries, it was decided to use NPV as a determination technique, which is much more sensitive than CV, and it was decided to analyse a lower concentration range to understand if for the analyses it may have been a problem of too high a concentration.

The electrolyte used was always PBS at pH 7.4, to which 10 aliquots of 20 mm^2 of the previously analysed $9.9 \cdot 10^{-4}$ M flurbiprofen solution were added. The operating parameters used are the following:

- Apply potential: 0.3 V
- Start potential: 0.3 V
- Stop potential: 1.5 V
- Base potential: 0 V
- Step: 0.005 V
- Normal pulse time: 0.07 s
- Interval time: 0.5 s
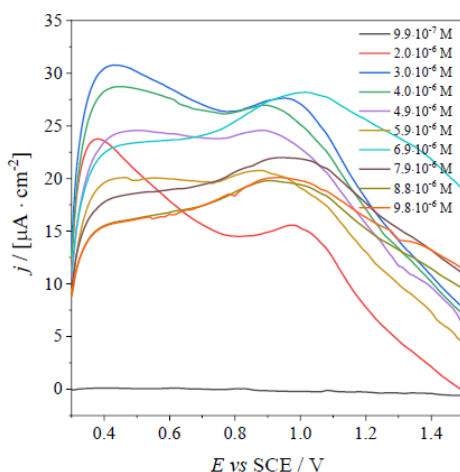
Figure 2.46 - NPVs superposition of the 10 20 mm³ aliquots of the $9.9 \cdot 10^{-4}$ M flurbiprofen solution, obtained by background subtraction (PBS) with Nova.

It can be seen from figures 2.44, 2.45 and 2.46 that flurbiprofen is not a good candidate to be detected with this electrode, since there is not any linearity between the addition of flurbiprofen and the electrochemical signal.

2.3.3. Paracetamol.

Given the unconvincing results regarding the determination of two NSAIDs, it was decided to change the type of drug, and move on to the class of analgesics-antipyretics, specifically, paracetamol. This is because, in addition to being

important for the treatment of COVID-19, and in general used by children to elderly people, it is a drug that has been studied very much at an environmental level and very often with analytical techniques, such as using GCE modified through DPV techniques, or modified gold electrodes using cyclovoltammetries, and many other systems.

To understand if the FTO electrodes modified with gold nanoparticles and titania were sensitive to the determination of paracetamol, we started by running LSV between 0 and 1.5 V, and to understand if this analyte dirty the electrodes. Specifically, these operating parameters were used:

- Apply potential: 0 V
- Start potential: 0 V
- Stop potential: 1.5 V
- Scan rate: 0.1 V·s^{-1}
- Step: 0.008 V

A solution of paracetamol 10^{-3} M was prepared, weighing 0.0154 g of drug, transported quantitatively in a 100 cm^3 flask making up to volume with milliQ water (effective concentration 1.02·10^{-3}M).

The background LSVs (20 cm^3 of PBS at pH 4) were performed, and subsequently three consecutive additions of 1 mL of 1.02·10^{-3} M solution. To understand the possible fouling of the electrode, the latter was rinsed with milliQ water, and both the background and the third addition were retested; they were retested even after cleaning the electrode with both milliQ water and an hour exposure to the UV lamp.
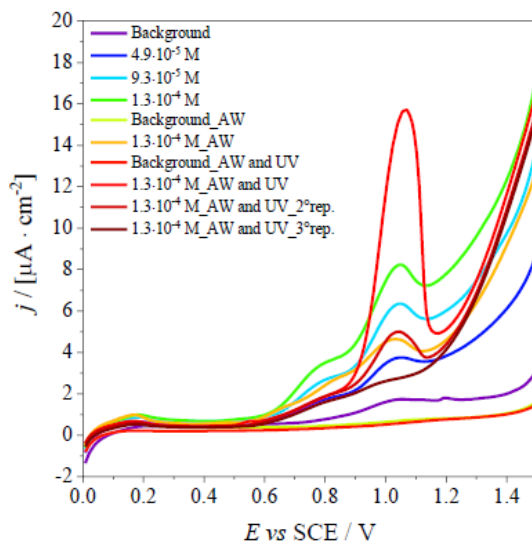
Figure 2.47 - superposition of the cyclic voltammetries performed in PBS at pH 4 respectively of the background, of the subsequent additions of the 10^{-3} M paracetamol solution, which were also tested after washing with water and after UV irradiation.

As it can be seen from Figure 2.47, compared to the background, paracetamol is seen as an increase in the signal at about 1.0 V, that is the oxidation peak of gold, and, with a step at about 0.7 V, probably just for paracetamol as there is no signal on the background. However, that signal fails to disappear either for the background after the electrode has been washed with milliQ water, or when it has been irradiated with the UV lamp.

Surely the irradiation can clean the gold better, but the signal immediately loses its intensity after performing several repetitions of the same LSV.

At this point, to try to understand how much paracetamol could foul the electrode, it was decided to perform the same aliquots as before, but between each addition, the electrode was irradiated with the UV lamp for an hour.
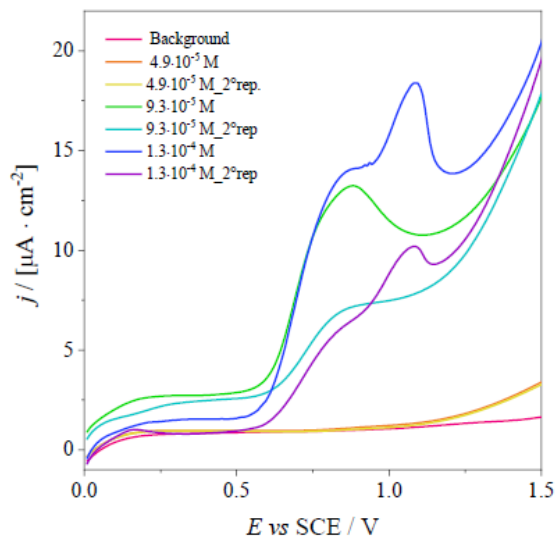
Figure 2.48 - Superimposition of the LSVs performed in the same way: background, 1 addition of paracetamol, irradiation of one hour, second addition of paracetamol, irradiation of one hour, third addition of paracetamol.

As it can be seen from Figure 2.48, the first addition of paracetamol is not distinguished from the background, However, the other additions, made just after UV irradiation, are seen through a step at about 0.6 V, while with the third addition the gold signal again appears at about 1.0 V. These results lead to think that it was probably necessary to clean the electrode continuously before one addition and the other.

For this reason, it was decided to perform a DPV (as it is the most used technique for this analyte according to the bibliographic searches carried out) of 10 successive aliquots of 20 mm^3 (taken from the $1.02 \cdot 10^{-3}$ M solution of paracetamol) and between each addition, irradiate the electrode immersed in the solution under stirring with ultraviolet light for 10 minutes. The operating parameters used were:

- Apply potential: 0 V
- Start potential: -0.5 V
- Stop potential: 1.5 V
- Step: 0.02 V
- Modulation amplitude: 0.05 V
- Modulation time: 0.1 s
- Interval time: 0.2 s
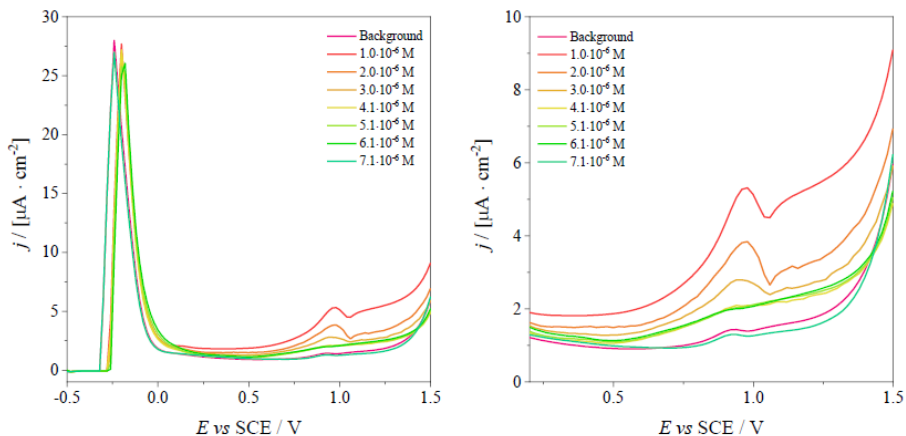
Figure 2.49 - DPV superimposition of the background and of the 7 consecutive additions, on the left the graph for the analysed potential range was shown, while on the right the same spectrum in the 0.2 - 1.5 V potential range was shown in order to enlarge the signals obtained.

As it can be seen from Figure 2.49, from the background to the first addition there is an increase in signal intensity at 1.0 V, which would be linked to the oxidation of gold; however, with the second addition of the analyte, this peak decreases in intensity, and also for the third one, while from the fourth to the seventh there were no more variations of the signal, which is why we did not continue until the tenth addition. This led to the hypothesis that 10 minutes of irradiation were not enough to clean the electrode from paracetamol, which probably is adsorbed on the electrode surface causing the gold signal to be lost. At this point it was thought to perform the same test, however, irradiating 30 minutes between one aliquot and the other, but it was noted that one hour of irradiation was not enough to clean it.
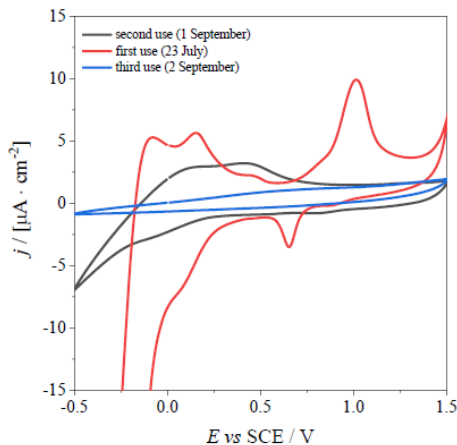
Figure 2.50 – Superimposition of three successive stabilisation CVs, which demonstrate the fouling of the electrode.

It can be seen from Figure 2.50 that from the second use of the electrode for the determination of paracetamol, the oxidation peak of gold is lost as well as that of reduction, even more for the third use. This made it clear that one hour of UV irradiation is not enough to clean the electrode. For this reason, the test of paracetamol with DPV was not continued, despite the idea was to perform these tests with 30 minutes of UV irradiation between one aliquot and the other, as it would not have been enough to clean the electrodes.

2.3.4. Ciprofloxacin.

To be able to understand if the WE could be sensitive to the presence of ciprofloxacin, 20 cm^3 of PBS at pH 4 were inserted inside the beaker, and LSVs were performed with the same parameters:

- Apply potential: 0 V
- Start potential: 0 V
- Stop potential: 1.5 V
- Scan rate: 0.1 V·s^{-1}
- Step: 0.008 V

To carry out the analyses, a solution of about 1·10^{-3} M was prepared by weighing 0.0192 g of ciprofloxacin, transferred quantitatively into a 50 cm^3 flask and making up to milliQ with water. The solution thus prepared was sonicated until the total dissolution of the salt and the flask was placed in the refrigerator.

To be able to understand if with this electrode it was possible to determine ciprofloxacin, initially 5 repetitions of cyclic voltammetries between -0.5V and 1.5V were performed to stabilize the WE, then the LSV were performed (see Figure 2.51), at first for the background, and then for three successive additions of 1 cm^3 of the previously prepared $1\cdot10^{-3}$ M ciprofloxacin solution. At that point, to be able to understand if this molecule fouls the WE, the electrodes were washed with milliQ water, and subsequently the LSV of the background and that of the third addition ($1.3\cdot10^{-4}$ M) were performed; then the electrodes were washed again, the WE was exposed to UV light for an hour; in the end the background LSV and $1.3\cdot10^{-4}$ M were repeated. Once these additions were finished, the electrode was washed with milliQ water and left under a UV lamp to clean it from any dirt.
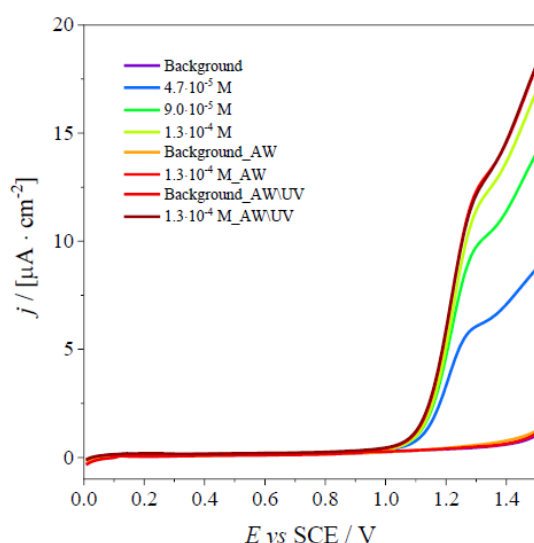
Figure 2.51 - Superimposition of LSVs performed in PBS at pH 7.4 with 3 additions of ciprofloxacin. To study the possible fouling of WE by this drug, washing with water (described in the legend with AW) and washing with both milliQ water and 1 hour of irradiation with a UV lamp was tested.

From Figure 2.51 it can be seen that at +1.25 V there is the oxidation peak of ciprofloxacin, and that this drug does not foul the electrode, as both the background and the third addition are superimposable both after washing with milliQ water and after having irradiated with the UV lamp.

Given the results obtained, it was decided to use a more sensitive technique than LSV. Square wave voltammetry (SWV) was chosen as several works have worked with this technique and it appears to be one of the best for the

determination of ciprofloxacin. Specifically, the work of Kasarla Ramakrushna Reddya was taken as reference [23].

The operating parameters used for the SWV were the following:

- Apply potential: -0.3 V
- Start potential: -0.3 V
- Stop potential: 1.5 V
- Step: 0.005 V
- Modulation amplitude: 0.05 V
- Frequency: 25 Hz

To analyse ciprofloxacin in a concentration range of $1 \cdot 10^{-6}$ M – $1 \cdot 10^{-5}$ M, the solution from which the various additions were made was the previously prepared $1 \cdot 10^{-3}$ M solution. Specifically, the stabilization of the electrode was initially performed with 5 CVs between -0.5 V and +1.5 V, and only subsequently the SWV of the background (PBS at pH 4) and of 10 consecutive additions of 20 mm^3 of the ciprofloxacin solution were performed $1 \cdot 10^{-3}$ M. To better observe the drug signal, the background subtraction was performed using the Nova function and the resulting spectrum was cut between 0.5 and 1.5 V, as shown in Figure 2.52.
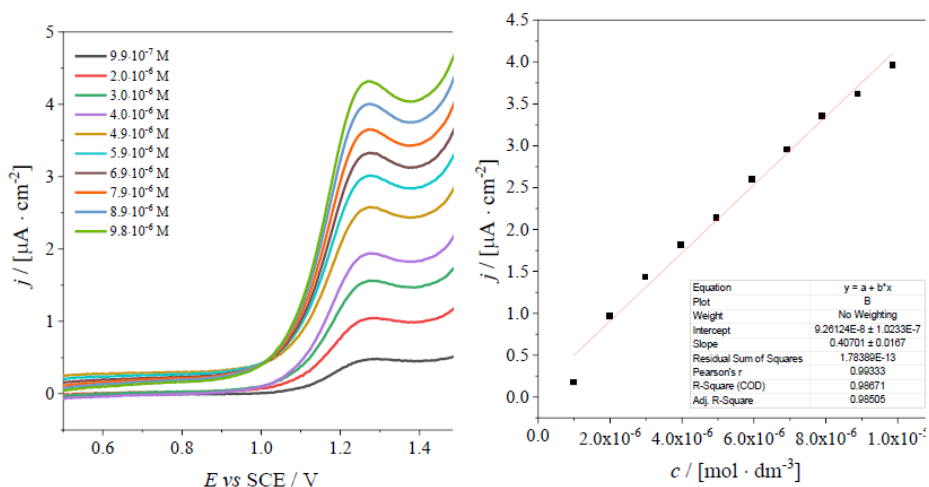
Figure 2.52 - on the left SWV overlap of the 10 ciprofloxacin additions with background subtraction, on the right the respective calibration line.

From Figure 2.52 it can be seen that the ciprofloxacin signal is at 1.25 V, and that as the concentration increases, the intensity of the signal increases. Furthermore, the first addition ($9.9 \cdot 10^{-7}$ M) has a certain height, so it was

decided to go down in concentration, analysing with the same technique the lowest concentration range, specifically between $9.9 \cdot 10^{-8}$ M and $9.1 \cdot 10^{-7}$ M.

The parameters used to set the SWV were the same as in the previous test, *i.e.*:

- Apply potential: -0.3 V
- Start potential: -0.3 V
- Stop potential: 1.5 V
- Step: 0.005 V
- Modulation amplitude: 0.05 V
- Frequency: 25 Hz

A dilution from the previously prepared ciprofloxacin solution was carried out to analyse this concentration range, so 250 mm^3 of the $1.0 \cdot 10^{-3}$ M solution was poured quantitatively in a 25 cm^3 flask and then made up to volume with milliQ water, thus obtaining a $1.0 \cdot 10^{-5}$ M solution of ciprofloxacin.

First, the stabilization of the electrode was performed, subsequently SWV of the bottom, and SWV of the 10 subsequent additions of 200 mm^3 of the $1.0 \cdot 10^{-5}$ M solution, as shown in Figure 57.
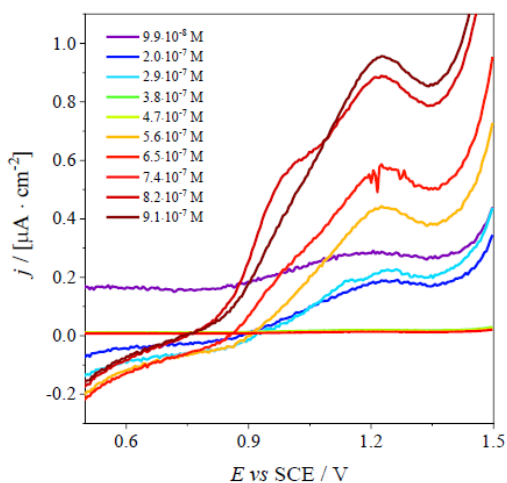
Figure 2.53 - SWV superimposition obtained from the analysis of ciprofloxacin in a concentration range between $9.9 \cdot 10^{-8}$ M and $9.1 \cdot 10^{-7}$ M.

Given the results obtained, it was decided to change the electroanalytical technique, passing to the DPV as it has lower detection limits. Then the same concentration range of the previous test was analysed also with this technique, using the following operating parameters:

- Apply potential: -0.5 V
- Start potential: -0.5 V
- Stop potential: 1.5 V
- Step: 0.005 V
- Modulation amplitude: 0.05 V
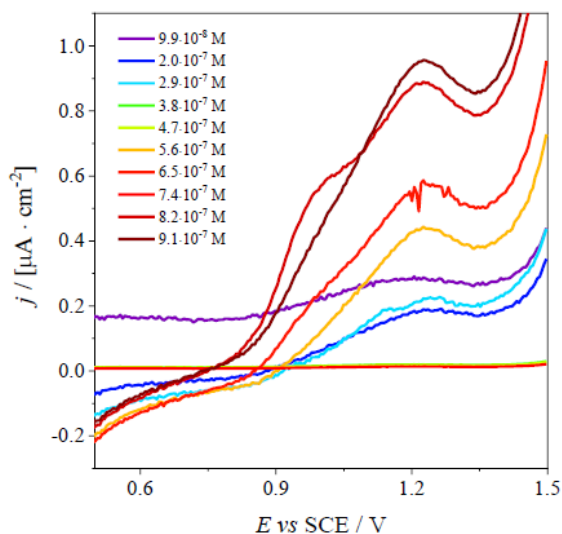- Modulation time: 0.05 s
- Interval time: 0.5 s

Figure 2.54 - DPV superimposition obtained from the analysis of ciprofloxacin in a concentration range between $9.9 \cdot 10^{-8}$ M and $9.1 \cdot 10^{-7}$ M. Compared to the range analysed by the instrument, only the potential range between 0.5 V and 1.5 V was taken into consideration in the overlap.

As it can be seen from Figure 2.54, the DPVs are very jagged, they have a high background noise, which is assumed to be also generated by the evolution of oxygen since, by setting a start potential of -0.5V, the instrument has automatically set a apply potential of -0.5V, generating a high production of bubbles inside the beaker, on the magnetic stir bar and on the three electrodes. An attempt was also made to vary the analysed potential range by varying the applied potential according to try to avoid evolution, but also working with the 0.5-1.5V potential range and therefore a consequent applied potential of 0.5V, a high bubble production.

Seen the results obtained so far, ciprofloxacin seems to be an excellent candidate for photoelectrochemical measurements, as confirmed by literature [20]. This work will be explained in Chapter 3.

2.3.5. Arsenic.

Up to now, pharmaceutical molecules have been analysed, but excellent results have not been obtained; therefore, it was decided to analyse an inorganic molecule such as arsenic, which, even though it has been regulated, it continues to present problems at environmental levels.

Also, for this molecule, the electrode was tested with LSV by making three consecutive additions of 1 cm^3 of the $1.0 \cdot 10^{-3}$ M stock solution. The stock solution was prepared by weighing 0.0492 g of As$_2$O$_3$, transferred quantitatively into a 25 cm^3 flask and brought to volume with milliQ water. Then, in a 50 cm^3 beaker, 20 cm^3 of PBS at pH 4 were inserted, the WE was stabilized with the CVs, then background LSV was performed, and then three additions of 1 cm^3 each, of the solution $1.0 \cdot 10^{-3}$ M. Also in this case, to understand the possible fouling, the background and the third addition of arsenic were tested both after washing with milliQ water and after one hour of UV irradiation.

It was decided to use an applied potential of -0.5 V as in many studies carried out in recent years, for the determination of arsenic in low concentrations it was necessary to perform preconcentration of the analyte, for example through a linear sweep anodic stripping voltammetry (LSASV), which in addition to preconcentrating the analyte on the electrode surface also performs a stripping, and through oxidation, the analyte is removed from the surface. However, before going down in concentrations, it was thought to understand through LSV whether this analyte could be analysed with these types of electrodes. The parameters for the analysis are the following:

- Apply potential: -0.5 V
- Start potential: -0.5 V
- Stop potential: 1.5 V
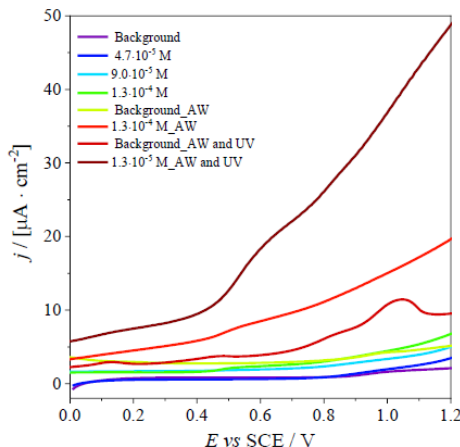- Scan rate: 0.1 V·s^{-1}
- Step: 0.008 V

Figure 2.55 - Superimposition of the LSVs performed respectively of the background (PBS at pH 4), of three consecutive additions of arsenic, and the effect on cleaning the electrode with milliQ water and with UV irradiation.

As it can be seen from Figure 2.55, in such conditions it is not possible to obtain the determination of arsenic. Reading in the literature it has been noticed that titanium dioxide has a point of zero charge (pzc) at 6.3, therefore working at a pH < pzc, titania is positively charged (as in Figure 2.56) while working at pH > pzc, titania is negatively charged [24].
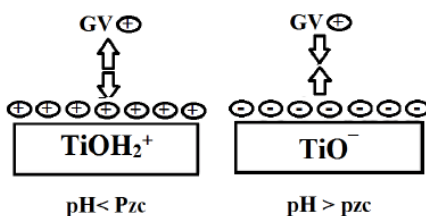
Figure 2.56 – Charge of titania as the pH of the solution varies.

Having seen this in the literature, it was decided to work at a higher pH. Initially PBS at a pH of 7.4 was tested (working with the same parameters described above and with the same quantities). This is because, at a pH of 4, titania is positively charged, the arsenic present in solution is an As (III) and therefore there is an electrostatic repulsion between these two species. In fact, from Figure 2.55 any peak is observed, which is typically around +0.2 V for this analyte. While, working at a neutral pH (slightly higher than the pzc of titania), the latter should have a negative charge and therefore be able to determine arsenic.
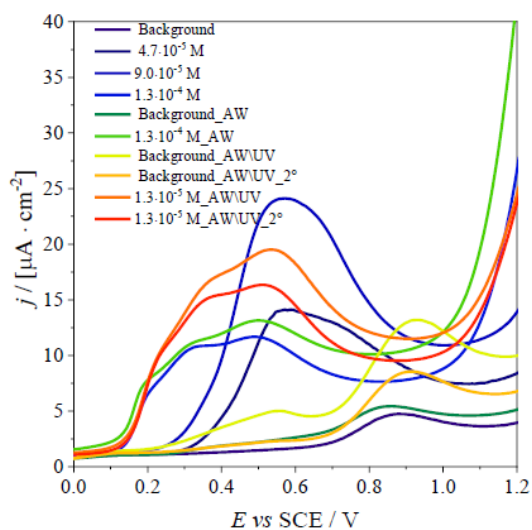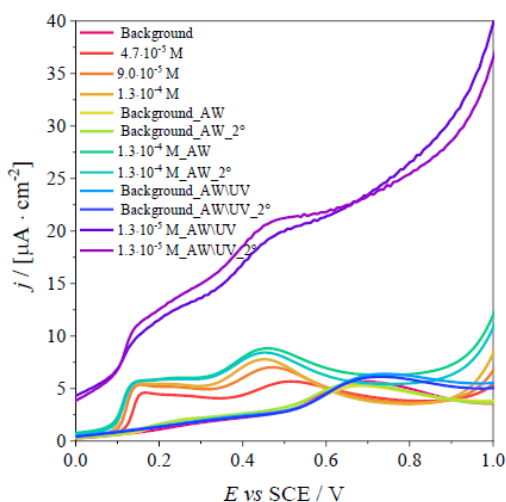
113

Figure 2.57 - Superimposition of the LSVs performed respectively of the background (PBS at pH 7.4), of three consecutive additions of arsenic, and the effect on cleaning the electrode with milliQ water and with UV irradiation.

In Figure 2.57, it is observed that with increasing arsenic concentration, there is an increase in the oxidation signal of gold, which however seems to have moved from +0.9 V for the background to about +0.5 V due to the presence of arsenic. However, before washing with water and even before irradiation with the UV lamp, an intermediate peak is observed between the arsenic oxidation peak and the gold oxidation peak, at +0.5 V, while by cleaning the electrode we note the presence of two peaks, one at about +0.2 V and the other at about +0.5 V.

It has been hypothesized that these two peaks are respectively related to arsenic and gold nanoparticles. The fact that the consecutive additions of arsenic did not point out the presence of these two peaks but a single peak at +0.5V, led to the assumption that arsenic fouls the electrode.

Washing with water seems to make the background signal return almost superimposed on the first CV performed on the PBS, as does the third addition. However, with irradiation, the signals are higher, but with the repetition of the same test the signal decreases its intensity, both for the background and for the third addition.

Looking only at the CVs related to the third addition, it would seem that ultraviolet light cleans the electrode better than cleaning it with milliQ water alone, as the signal is higher; at the same time, the background signal is also

higher, and only with the repetitions of the cyclovoltammetries it manages to lose the signal at +0.5 V, this has led to the assumption that with the UV light it cleans the electrode better but probably some radical is formed that only with a few repetitions manages to remove it from the surface.

At this point, having read the question of the pzc in the literature, it was decided to work at an even higher pH, to be sure that the titania was at a pH above its point of zero charge, and therefore to avoid electrostatic repulsion. The parameters used are the same as in the two previous tests, by changing the pH of the electrolytic solution, where the PBS was brought to a pH of 9 using a concentrated NaOH solution.

Figure 2.58 - superposition of the LSVs performed respectively of the background (PBS at pH 9), of three consecutive additions of arsenic, and the effect on cleaning the electrode with milliQ water and with UV irradiation.

From Figure 2.58, it can be seen that after performing the background LSV, which only has the gold oxidation peak at about +0.8 V, while with the presence of As, that peak is no longer noticed, but the mark appears, as in the previous test, a signal at +0.5V, which however completely disappears in the background after washing with milliQ water and also with washing with water and one hour of irradiation with the UV lamp. Working at a neutral pH, which is slightly higher than the titania pzc, there is no clear variation between the uncleaned electrode and the electrode washed with water, not even with ultraviolet light cleaning, as the baseline, while the signal height remained the same.

With these conditions, the evolution of oxygen was obtained probably because an open cell has been used and therefore, eventually, it could be possible to

change the electrolyte to avoid the formation of bubbles, or possibly work in a degassed cell. To understand if it was a problem of the applied negative potential, the system was tested at a null value, narrowing the working range so as not to stress the gold too much. Specifically, working with PBS at pH 9, the CVs of the background and of the three additions of 1 cm^3 of the stock solution were performed, using the same parameters:

- Apply potential: 0 V
- Start potential: 0 V
- Upper potential: 0.8 V
- Lower potential: -0.008 V
- Stop potential: 0 V
- Number of scans: 1
- Scan rate: 0.1 V·s^{-1}
- Step: 0.008 V
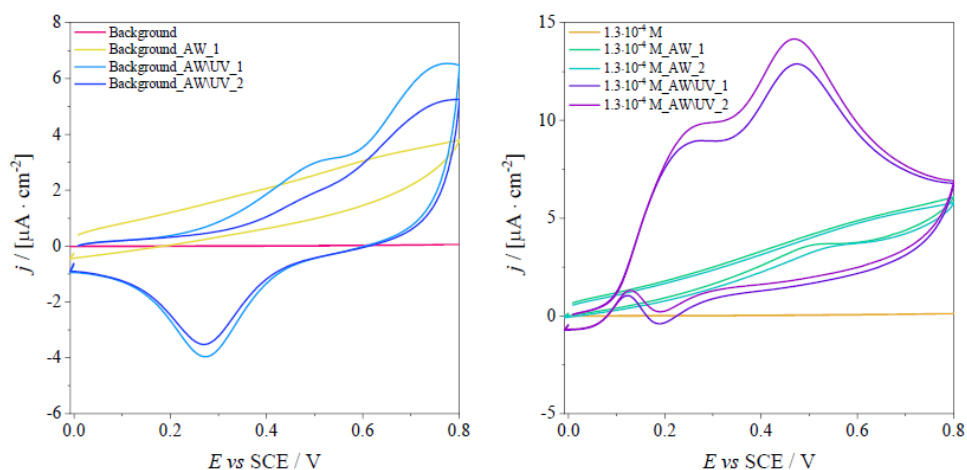
Figure 2.59 - Superimposition of the cyclovoltammetries, to the left of the background and the relative cleaning with water and UV irradiation, to the right of the third additions and the relative cleaning with water and UV irradiation.

By carrying out this test there was even less production of bubbles, but, as it can be seen from Figure 2.59, the electrode was extremely resistive, and only after irradiation it returned to its usual trend, with the oxidation peak of the gold around +0.8 V and the reduction to around +0.4 V. This electrode had also been used for all previous tests with arsenic and had never given resistance problems after cleaning an hour of irradiation with the UV lamp. This could be since working several times at high concentrations, after a while it is necessary to irradiate for a longer time, or the waiting time between one test and another

has affected the measurement. It could probably be the second hypothesis as in this test, after cleaning with the lamp, the electrode is no longer resistive. Surely, as for LSV, with the presence of arsenic, the gold peak seems to be shifted to lower potentials, in addition to the fact that the analyte itself is present in the form of a step at about 0.2 V.

2.4. Conclusions.

In this work the optimization and application of an FTO electrode modified with gold nanoparticles and titanium dioxide for the determination of emerging pollutants (diclofenac, flurbiprofen, paracetamol, ciprofloxacin, and arsenic) were studied. The best conditions for the synthesis of the working electrodes and the understanding of the best dimensions of the gold nanoparticles for the deposition on the FTO support were performed in previous works. In the first part of the work, studies on the aging of titanium dioxide sol were performed, through electroanalytical techniques (cyclovoltammetry and electrochemical impedance spectroscopy), spectrophotometric studies (UV and DLS) surface studies (AFM) and electron-hole recombination time (transient photocurrent).

Subsequently, studies were also carried out on different types of synthesized electrodes, specifically the electroanalytical responses of a working electrode with titania alone, with only gold nanoparticles (calcined and not calcined), both with gold nanoparticles and with titanium dioxide. With these comparisons it was chosen to continue with the complete working electrode, that is an FTO with deposition of 10 μm diameter gold nanoparticles, and titanium dioxide aged seven days (calcined). In the last part of the work, the focus was on the electroanalytical determinations, but above all on the possible fouling of the different types of analytes. Specifically, diclofenac was analysed using CVs and a considerable fouling of the electrode was noted, which can only be cleaned with one hour of irradiation with an ultraviolet lamp. Therefore, despite having tested pulsed techniques in low concentrations of analyte, it was not possible to carry out calibration lines due to the lack of regularity of the peaks. So, another NSAID molecule was analysed, specifically flurbiprofen, for which no information were obtained even with CVs at high analyte concentrations. At that point it was decided to change the analyte, observing the behaviour of paracetamol, which can be observed through CVs, and through DPV, but it is an analyte that can be adsorbed a lot on the electrode surface, and one hour of irradiation with a UV lamp is not enough to clean the electrode. Then ciprofloxacin was tested which, unlike the previous analytes, did not foul the electrodes, and was analysed by SWV in the concentration range $9.9 \cdot 10^{-7}$ M – $9.8 \cdot 10^{-6}$ M. In the end, an inorganic molecule, arsenic, was analysed by varying the pH of the solution as titania has a point of zero charge of 6.5, therefore CVs at different pH of the electrolytic solution and the fouling of the electrode were observed.

In conclusion, this work has given the possibility to exploit an FTO electrode based on two materials obtainable in a short time (easy synthesis) and with low

cost. Surely exploiting titanium dioxide as an electrode cover leads to numerous advantages, first photo-renewable properties, which can be an advantage for remote determinations.

As development of this work, the electrode has been employed for photoelectrochemical measurements; the results of this experimentation are shown in the following chapter (Chapter 3).

2.5. Bibliography.

[1] Commissione Europea, "Raccomandazione della Commissione, del 18 ottobre 2011, sulla definizione di nanomateriale (2011/696/UE)," vol. 2010, no. 2005, p. 3, **2011**.

[2] S. Bayda, M. Adeel, T. Tuccinardi, M. Cordani, and F. Rizzolio, The history of nanoscience and nanotechnology: From chemical-physical applications to nanomedicine, *Molecules* **2020**, vol. 25, no. 1, pp. 1–15.

[3] M. C. Daniel and D. Astruc, Gold Nanoparticles: Assembly, Supramolecular Chemistry, Quantum-Size-Related Properties, and Applications Toward Biology, Catalysis, and Nanotechnology, *Chemical Reviews* **2004**, 104, 1, 293–346.

[4] P. K. Jain, K. S. Lee, I. H. El-Sayed, and M. A. El-Sayed, Calculated absorption and scattering properties of gold nanoparticles of different size, shape, and composition: Applications in biological imaging and biomedicine, *The Journal of Physical Chemistry B* **2006**, 110, 14, 7238–7248.

[5] P. Zhao, N. Li, and D. Astruc, State of the art in gold nanoparticle synthesis, *Coordination Chemistry Reviews* **2013**, 257, 3–4, 638–665.

[6] M. Hu, J. Chen, Z.Y. Li, L. Au, G.V. Hartland, X. Li, M. Marquez, Y. Xia, Gold nanostructures: Engineering their plasmonic properties for biomedical applications, *Chemical Society Reviews* **2006**, 35, 11, 1084–1094.

[7] R. Herizchi, E. Abbasi, M. Milani, and A. Akbarzadeh, Current methods for synthesis of gold nanoparticles, *Artificial Cells, Nanomedicine, and Biotechnology* **2016**, 44, 2, 596–602.

[8] K. R. Brown, A. P. Fox, and M. J. Natan, Morphology-dependent electrochemistry of cytochrome C at Au colloid-modified SnO_2 electrodes, *Journal of the American Chemical Society* **1996**, 118, 5, 1154–1157.

[9] C. Daruich De Souza, B. Ribeiro Nogueira, and M. E. C. M. Rostelato, Review of the methodologies used in the synthesis gold nanoparticles by chemical reduction, *Journal of Alloys and Compounds* **2019**, 798, 714–740.

[10] C. M. Welch and R. G. Compton, The use of nanoparticles in electroanalysis: A review, *Analytical and Bioanalytical Chemistry* **2006**, 384, 3, 601–619.

[11] D. Dambournet, I. Belharouak, and K. Amine, "Tailored preparation methods of TiO_2 anatase, rutile, brookite: Mechanism of formation and electrochemical properties, *Chemical Materials* **2010**, 22, 3, 1173–1179.

[12] M. Mohamad, B. U. Haq, R. Ahmed, A. Shaari, N. Ali, and R. Hussain, A density functional study of structural, electronic and optical properties of titanium dioxide: Characterization of rutile, anatase and brookite polymorphs, *Materials Science in Semiconductor Processing* **2015**, 31, 405–414.

[13] M. Lazzeri, A. Vittadini, and A. Selloni, Structure and energetics of stoichiometric TiO_2 anatase surfaces, *Physical Review B - Covering Condensed Matter and Materials Physics* **2001**, 63, 15, 1554091–1554099.

[14] L. E. Oi, M. Y. Choo, H. V. Lee, H. C. Ong, S. B. A. Hamida and J. C. Juan, Recent advances of titanium dioxide (TiO_2) for green organic synthesis, *RSC Advances* **2016**, 6, 110, 108741–108754.

[15] S. C. Pillai and S. Hehir, Sol-Gel Materials for Energy, Environment and Electronic, *Springer* **2017**.

[16] B. Zhang, S. Cao, M. Du, X. Ye, Y. Wang and J. Ye, Titanium dioxide (TiO_2) mesocrystals: Synthesis, growth mechanisms and photocatalytic properties, *Catalysts* **2019**, 9, 1.

[17] G. Maino, D. Meroni, V. Pifferi and L. Falciola, Electrochemically assisted deposition of transparent, mechanically robust TiO_2 films for advanced applications, *Journal of Nanoparticle Research* **2013**, 15, 11.

[18] R. G. Compton and C. E. Banks, Understanding Voltammetry, *Oxford University*, Third Edition, **2018**.

[19] M. Hema, Y. Arasi, T. Selvi and R. Anbarasan, Titania Nanoparticles Synthesized by Sol-Gel Technique, *Chemical Science Transactions* **2012**, 2, 1, 239–245.

[20] L. Cao, Z. Li, R. Jia, L. Chen, Y. Wu and J. Di, Sensitive Photoelectrochemical Determination of Ciprofloxacin Using an Indium Tin Oxide Photoelectrode Modified with Small Gold Nanoparticles, *Analytical Letters* **2020**, 53, 9, 1472–1488.

[21] D. Tafalla and P. Salvador, Kinetic Approach to the Photocurrent Transients in Water Photoelectrolysis at n-TiO2 electrodes. Part II - Analysis of the photocurrenttime dependence, *Journal of The Electrochemical Society* **1990**, 137, 6, 1810–1815.

[22] L. Lo Presti, V. Pifferi, G. Di Liberti, G. Cappelletti, L. Falciola, G. Cerrato and M. Ceotto, Direct measurement and modeling of spontaneous charge migration across anatase-brookite nanoheterojunctions, *Journal of Materials Chemistry A* **2021**, 9, 12, 7782–7790.

[23] K. R. Reddy, P. K. Brahman, and L. Suresh, Fabrication of high-performance disposable screen-printed electrochemical sensor for ciprofloxacin sensing in biological samples, *Measurement* **2018**, 127, 175–186.

[24] S. Bendjabeur, R. Zouaghi, O. N. H. Kaabeche, and T. Sehili, Parameters Affecting Adsorption and Photocatalytic Degradation Behavior of Gentian Violet under UV Irradiation with Several Kinds of TiO_2 as a Photocatalyst, *International Journal of Chemical Reactor Engineering* **2017**, 15, 4.

3. Photoelectrochemical applications.

3.1. Introduction.

Due to their many benefits –including high stability, quick response times, ease of operation, and, most importantly, a reduction in background noise (due to the separation of the excitation source from the detected signal) when compared to electrochemical and photochemical analyses – photoelectrochemical (PEC) sensors have gained a lot of attention recently. The photoactive electrode, which is the central component of photoelectrochemical studies, needs to be carefully engineered to yield the best results [1-4].

Since titanium dioxide is known to have photocatalytic capabilities, it was one of the first materials selected for these investigations [5-11].

Unfortunately, this material has several drawbacks because the photogenerated charges recombine quickly and it only functions well in strong UV light. Numerous techniques, including morphological control, doping, sensitization using quantum dots, surface catalyst deposition and heterojunction creation, are available to address these issues. Specifically, it has been demonstrated that this last method is highly successful [9, 12-16], particularly when it comes to the creation of semiconductor-metal nanoparticle heterojunctions.

After passing across the interface, the photogenerated electrons can really stay in the nanoparticles, and the creation of a Schottky barrier serves as an effective electron trap to stop recombination. Furthermore, there is an increase in absorption in the visible range when metals like Ag and Au with localized surface plasmon resonance (LSPR) characteristics are utilized [9, 16, 17-20].

The detection of antibiotics is one area in which PEC sensors have only recently been used [2]. Up until now, systems with analyte recognition elements, such as enzymes, aptamers and molecular imprinted polymers, have been the primary methods used in this regard.

These systems have the benefit of being more selective, but they also have to deal with the difficulties of more intricate storage and synthetic processes. Rather, more reliable and straightforward systems can be constructed without the requirement for a recognition system because of the inherent interaction between the photoactive substance and the analyte.

Ciprofloxacin, a third-generation quinolone drug that is widely used in clinical medicine and livestock and poultry farming, is one of the antibiotics that PEC

detected. However, even small amounts of this drug have been found to be harmful to the environment, particularly when it comes to toxicity issues in wastewaters and surface waters. These investigations, however, are scarce and mostly based on assessments where the presence of ciprofloxacin on the photoelectrode surface, which obstructs electron transmission, is seen to cause a reduction in photocurrent (signal-off type PEC) [21-24].

Compared to a signal-on type PEC, where there is a genuine chemical reaction between the photoactive material and the analyte and consequent rise in the photocurrent signal, this sort of detection poses greater challenges for interferents.

3.1.1. Aim of this work.

Seen the promising results in the analysis of the transient photocurrent reported in chapter 2.2.9. and the results reported by Cao *et al.* [21], in this study low power light sources were used to evaluate a heterojunction made of gold nanoparticles coated with a porous titanium dioxide layer for the first time to determine ciprofloxacin using signal-on photoelectrochemical analysis. It was possible to create a reliable system with good analytical parameters and no interference issues. To completely comprehend the crucial role that the semiconductor-metal heterojunction represents, the system was compared with bare titanium dioxide.

3.2. Materials and methods.

All the details regarding reagents and instruments used during the thesis will be reported in this chapter. The reagents are listed in Table 3.1, each with the brand, CAS number and the main usage. Table 3.2 lists the instruments and the materials. The procedures section focuses on the preparation of solutions widely used during the thesis, while procedures for materials synthesis and device assembly will be discussed in more detail in the next chapters.

Table 3.1 - description of all reagents used in this work.

Name	Use	CAS number	Brand
Titanium(IV) isopropoxide	Titania synthesis	546-68-9	Sigma-Aldrich
Hydrocloric acid 37%	Titania synthesis	7647-01-0	Sigma-Aldrich
LUTENSOL ON70	Titania synthesis	-	-
Ethanol absolute ≥ 99.8%	Titania synthesis, electrode assembly	64-17-5	Sigma-Aldrich
Acetone	Electrode assembly	67-64-1	Sigma-Aldrich
2-propanol	Electrode assembly	67-63-0	Carlo Erba
Sulfuric acid, 95.0-97.0%	Electrode assembly	7664-93-9	Sigma-Aldrich
Toluene anhydrous 99.8%	Electrode assembly	108-88-3	Sigma-Aldrich
MPTMS	Electrode assembly	4420-74-0	Sigma-Aldrich
APTES	Electrode assembly	919-30-2	Sigma-Aldrich
Ciprofloxacin HCl	Analyte	86393-32-0	Sigma-Aldrich
Sodium phosphate dibasic	Electrolyte preparation (PBS)	7558-79-4	Sigma-Aldrich

Potassium phosphate monobasic	Electrolyte preparation (PBS)	7778-77-0	Fluka
Sodium perchlorate hydrate	Electrolyte	207683-20-3	Sigma-Aldrich
$K_4[Fe(CN)_6] \cdot H_2O$	Probe molecule	14459-95-1	Fluka

Table 3.2 - description of the materials and tools used.

Name	Brand
FTO	Sigma-Aldrich
Potentiostat Galvanostat [PGSTAT30]	MetrOhm
Micropipettes	Gilson
Oven	Forno MAB
UV-vis spectrophotometer [model UV-2600; 240V]	Shimadzu
N_2 [air liquid 6.0]	Alphagz 2.0a
Analytical scale [crystal 100 cal]	Gibertini
pHmeter [model 338]	AMEL instruments
DLS [Zetasizer Nano ZS]	Malvern
UV lamp [HG 500]	Jelosil
LEDs	Thorlabs
SEM [TM-1000]	HITACHI
Optical microscope	paralux

3.2.1. Preparation of the solutions.

- $NaClO_4$ 0.1 M was prepared dissolving 12.13 g of $NaClO_4$ salt in 1000 cm^3 of water. The obtained solution was stored at room temperature in transparent flasks.

- Phosphate buffer solution (PBS) was prepared dissolving 5.4124 g of Na_2HPO_3 and 1.1722 g of KH_2PO_3 in 1000 cm^3 of water. The obtained solution was conserved at 4 °C.

The final pH of those solution was measured with a pH-meter.

- $K_4[Fe(CN)_6]$ 50.5 mM was prepared dissolving 10.66 g of $K_4[Fe(CN)_6] \cdot 3H_2O$ in 500 cm^3 of milliQ water. The solution was then stored at 4 °C.

- To obtain concentration of 1, 2 and 3 mM of iron probe in the electrochemical cell containing 20 cm^3 of electrolyte solution, aliquot of 400 mm^3 of the probe solution had to be added to the cell.

Two ciprofloxacin solutions of different concentration were prepared, so that it was possible to cover the whole range of concentration needed in the electrochemical cell using the micropipettes available in the laboratory.

- Ciprofloxacin 10^{-3} M was prepared dissolving 0.0193 g of ciprofloxacin HCl salt in 50 cm^3 of water

- Ciprofloxacin 10^{-5} M was obtained by diluting the 10^{-3} M solution

Both solutions were stored at 4 °C and away from sunlight.

Electrochemical data were collected using the program Nova 2.1.2 (build 6333, Copyright © 2016, Metrohm Autolab BV), and presented using OriginPro^R. Data processing was performed with both Microsoft Excel and OriginPro^R.

3.2.2. Device assembly.

The device has been assembled through the procedure reported in Chapter 2, paragraph 2.2.14.

3.2.3. Device characterisation.

3.2.3.1. Optical microscopy and SEM imaging.

Microscopy techniques were considered to provide a fast, non-destructive way to characterize newly assembled devices. The goal was to verify that no significant differences could be observed between the different electrodes, thus proceeding with electrochemical tests knowing that the synthetic part occurred with good reproducibility.

An optical microscope was initially used, as it was already proved by previous works to be a reliable method to observe the TiO_2 layer deposited on gold microelectrodes. As shown in Figure 3.1, this technique proved to work extraordinarily well to monitor the degradation of the used electrodes: newly produced electrodes were characterized by a mostly uniform film, with only few cracks. Older electrodes lose the covering material, and only few spots remain covered.
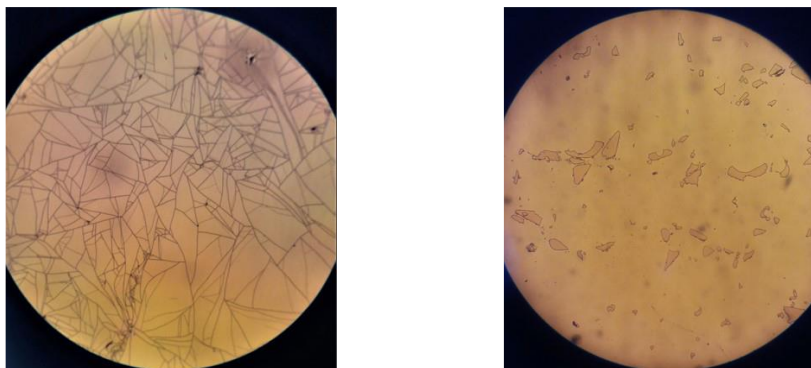
Figure 3.1 - Optical images of a freshly prepared electrode (left) and a worn-out electrode (right).

In some cases, such as the one reported in Figure 3.2, it is even possible to distinguish the part of the electrode that was immersed in solution, as it is the one that suffers most of the damage.
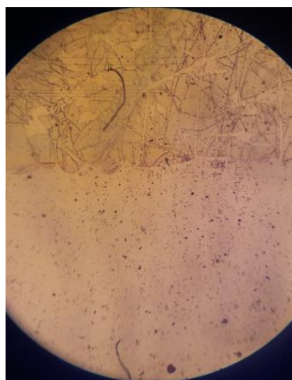
Figure 3.2 - Detail of the electrode surface. Only the lower part, with less TiO_2 cover, was immersed in solution.

It is worth noting that the picture of the damaged electrodes was mostly taken after many months of usage, sometimes under high power irradiation or high values of applied potential, and therefore the device can be considered very durable.

Another aspect that was observed is related to the synthetic procedure. As shown in Figure 3.3, the horizontally calcinated electrode often presented a strip with low TiO_2 covering, extending from one side of the electrode to the other with a width of approximately 2 mm.
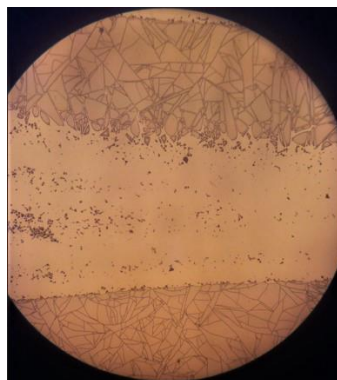
Figure 3.3 - Detail of the electrode surface. A 2 mm-wide strip without titanium dioxide cover could be observed in most synthetized electrodes.

The morphology of the deposited TiO_2 film was also highly dependent on the environmental conditions (such as temperature and humidity) at the time of both the sol preparation and the device assembly. When the conditions were not ideal, it was not possible to obtain a good layer. As shown in Figure 3.4, high temperature and low humidity are thought to cause preferential build-ups of TiO_2 deposits with high thickness, while most of the FTO surface remains uncovered.
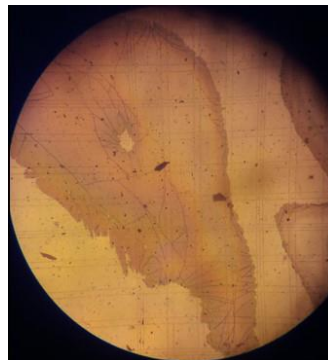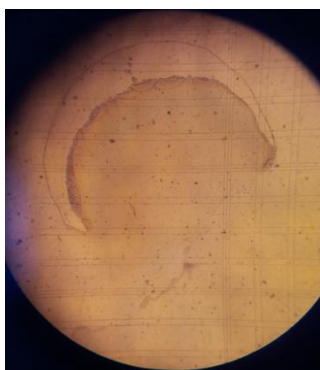
Figure 3.11 - Detail of the electrode surface. In these case, TiO_2 deposition wasn't uniform: large thick deposits could be observed, whilst the rest of the electrode surface remained uncovered.

Even though optical microscopy proved to be useful, it was limited by its maximum magnifying power. Another technique, Scanning Electronic Microscopy (SEM) was therefore used.

The obtained SEM images are reported in Figure 3.5. Figure 3.5A was taken in the same area of figure 3.3 and shows the 2 mm wide strip not covered with

titanium dioxide. The SEM image also shows the presence of thick TiO_2 deposits on the FTO surface (the darker spots). Figure 3.5B shows an area with good TiO_2 cover, with the characteristic cracks.
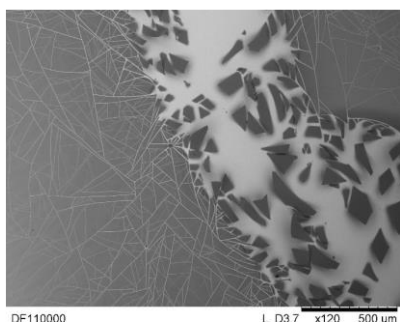
A)
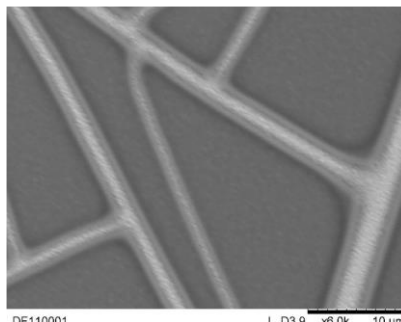
B)

Figure 3.5 - (A-B) SEM image of a horizontally-calcinated electrode: toward the center of the electrode, a large area of the FTO was not covered (white). Magnification 120x and 6000x. Thick TiO2 deposits were observable on the surface.

Most of the electrodes presented a surface morphology like the one in Figure 3.6: the titanium dioxide layer is uniformly distributed on the surface. Small cracks could be observed in the film and some titanium dioxide aggregates were also presents.
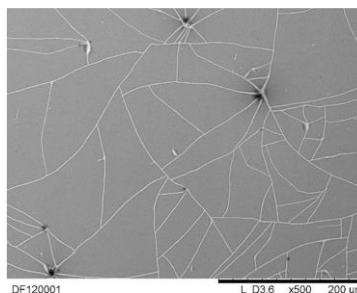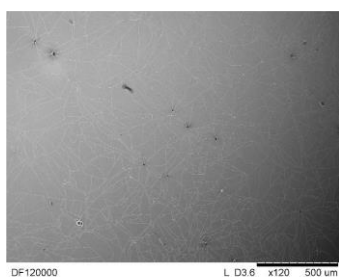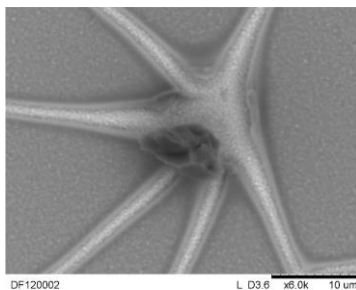
Figure 3.6 - SEM image of a hybrid electrode calcinated with the TiO$_2$ sol aged 30 days. The film is quite uniform, with some cracks on the surface. It is possible to observe some TiO$_2$ aggregates of around 10 nm. Magnification 120x, 500x and 6000x clockwise.

EDX analyses were conducted to quantify the amount of metal nanoparticles present on the electrodes and check whether their quantity was constant among different electrodes or not. Unfortunately, EDX proved to be unable to detect the element, maybe due to the low sensitivity. The spectrum in Figure 3.7 shows the presence of tin (79.1%) and silicon (0.6%), that are components of the FTO substrate and titanium (20.3%).
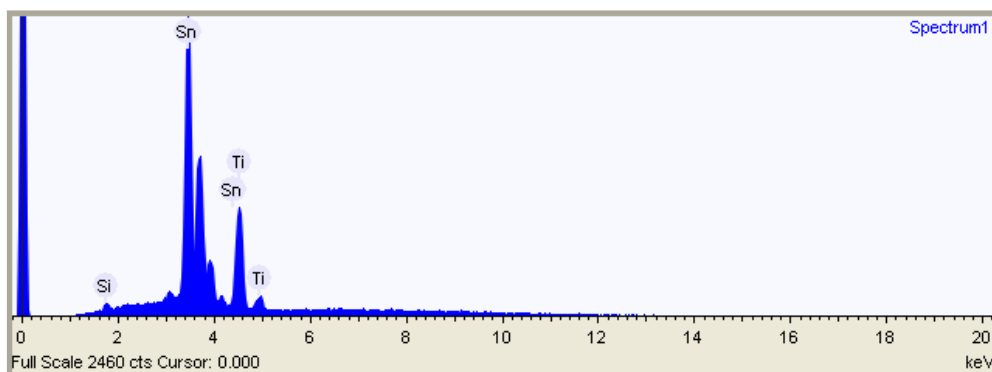
Figure 3.7 - EDX spectrum of the device. Conditions: Acquisition time: 120 s; process time: 4 s; Accelerating voltage: 15.0 kV.

3.2.3.2.   Cyclic voltammetry.

The electrochemical characterisation of the electrodes is reported in Chapter 2, paragraph 2.2.15.

3.2.3.3.   Electrochemical impedance spectroscopy.

The EIS performed on the background (NaClO₄) and in the presence of K₄[Fe(CN)₆] 3 mM has been reported and discussed in Chapter 2, paragraph 2.2.16.

In this chapter the EIS performed in the presence of ciprofloxacin: the resistance of both the TiO_2 and the hybrid electrode is higher in the darkness than with irradiation and the resistance of titanium dioxide is higher than the hybrid material (Figure 3.8).
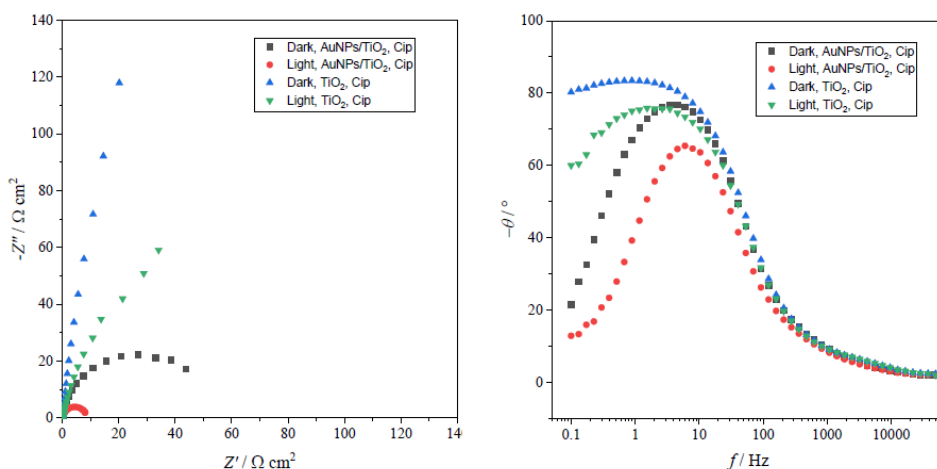

Figure 3.8 - Electrochemical Impedance Spectroscopy recorded in NaClO₄ 0.1 M solution: Nyquist plot (left) and Bode phase plot (right). Applied potential: 0.1 V; Irradiation with a 500 W 365 nm UV lamp. Ciprofloxacin concentration: 10^{-5} M.

Observing an overlay of all the previously commented plots, it is clear that, while irradiation has a great effect on both materials, the addition of ciprofloxacin only leads to significant changes with the hybrid material. The first phenomenon can be explained as the main effect of irradiation is connected to the presence of TiO_2, common in both materials. Addition of ciprofloxacin only leads to a change of resistance in the hybrid material, suggesting that gold nanoparticles have a catalytic effect towards ciprofloxacin oxidation. The AuNPs collect the photogenerated electrons generated by the interaction of the TiO_2 with the UV light, thus favouring the separation of the electron-hole pair; the holes are then free to oxidize ciprofloxacin. This result is also confirmed in paragraph 3.2.3.5, as the photocurrent of a TiO_2 electrode does not change with addition of ciprofloxacin, while that of the hybrid material-based electrode does.

3.2.3.4.   Profilometer measurements.

Profilometric analyses were performed to measure the thickness of the deposited layer. Both electrodes with bare titanium dioxide and electrodes with AuNPs and TiO_2 were analysed. The instrument has a pin that moves above the surface and it is able to see the height difference between two different points.

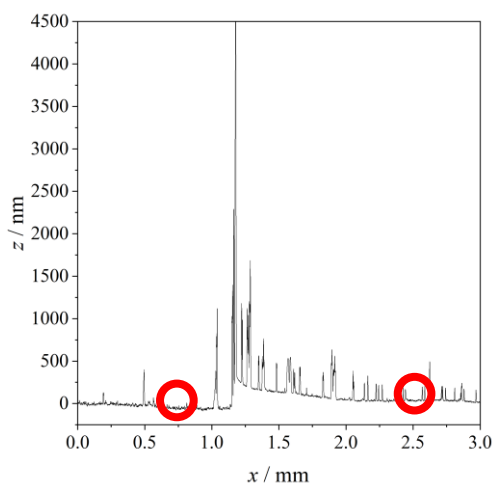The measurements were repeated three times for each sample and the electrodes analysed were calcinated at different aging times of the sol.

Figure 3.9 - Profilometric graph. The red circles are the point where the points were taken for the measurement.

In Table 3.3 the values of the thickness of different electrodes at different aging times are reported. The thickness is calculated as difference of the point where titanium dioxide is present and of the bare electrode.

Table 3.3 - Thickness values of different electrodes at different aging time of the sol.

	7 days	**14 days**	**30 days**
FTO/TiO₂ – A	(155 ± 52) nm	(55 ± 22) nm	(84 ± 25) nm
FTO/TiO₂ – B	(99 ± 19) nm	(72 ± 13) nm	(81 ± 13) nm
FTO/AuNPs/TiO₂ – A	(91 ± 10) nm	(75 ± 19) nm	(58 ± 20) nm
FTO/AuNPs/TiO₂ – B	(108 ± 31) nm	(61 ± 15) nm	(69 ± 18) nm

The first thing that can be seen is that there are no differences between the electrodes with bare titanium dioxide and the electrodes with also the AuNPs, since the latter are small (around 10 nm in diameter).

The second thing is that the TiO_2 layer aged for 7 days is thicker than the layer at 14 or 30 days of aging. This could lead to deeper pores on the surface of the titanium dioxide layer and thus to a different diffusion mechanism (in this case, linear diffusion), as already proven with CV and EIS analyses.

3.2.3.5.   Photocurrent tests.

Experimental setup.

For these tests, the electrochemical cell was positioned so that the working electrode (WE) was parallel to the UV lamp, at approximately 15 cm. It was not convenient to further decrease the distance between the lamp and the electrode, as the heat produced by the lamp could affect the measurement.

A platinum wire was used as counter electrode (CE) and a saturated calomel electrode (SCE) was used as refence electrode (RE). These were both located in the cell in a way that would not obstruct the light flux from the lamp to the WE. Unless otherwise specified, all the photocurrents shown in the following pages have been recorded applying a potential of +0.1 V (vs SCE).
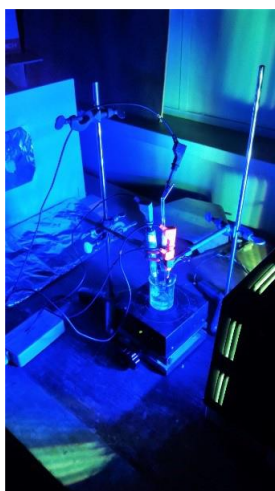
Figure 3.10 - Photograph of the experimental setup used to record the photocurrents. The WE is on the red connection, directly exposed to the irradiation source.

Magnetic stirring was maintained during the entire recording, at approximately 600 rpm. Stirring is commonly used in amperometry to facilitate contact between the electroactive species and the electrode. As shown in Figure 3.11, it affects the signal intensity and therefore it is important to keep the value steady in order to be able to compare different measurements.
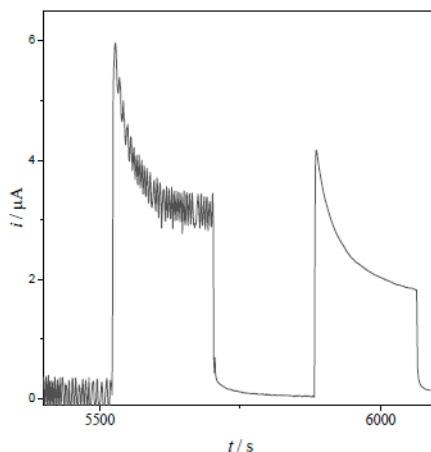

Figure 3.11 - Effect of stirring on the photocurrent signal: the first signal was recorded under stirring while the second one without stirring.

Preliminary tests with 500 W UV lamp.

First, photocurrent responses of bare FTO, TiO_2/FTO and TiO_2/AuNPs/FTO electrodes were compared to determine whether a significant improvement could be achieved thanks to the presence of gold nanoparticles.

The results, displayed in the picture below, showed that the hybrid electrode had a 3-times higher photocurrent compared to TiO_2/FTO electrode. As expected, bare FTO electrode did not show any photoelectrical response.
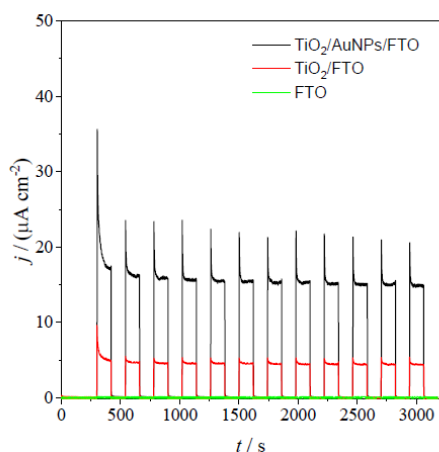
Figure 3.12 - Overlay of TiO$_2$/AuNPs/FTO, TiO$_2$/FTO and bare FTO electrode in 0.1 M NaClO$_4$. Applied potential 0.1 V.

Both TiO$_2$/FTO and TiO$_2$/AuNPs/FTO electrodes were also tested in presence of ciprofloxacin, and while the hybrid material gave a directly proportional signal with the concentration of the analyte, the signal of TiO$_2$/FTO remained unchanged. This confirmed what was previously suggested by EIS measurements in chapter 3.2.3.3.: gold nanoparticles' catalytic activity is fundamental to oxidize ciprofloxacin and record an electric signal. Also, the detected signal is higher in presence of the AuNPs because they help in collecting the photogenerated electrons, thus leaving the holes free to oxidize ciprofloxacin.
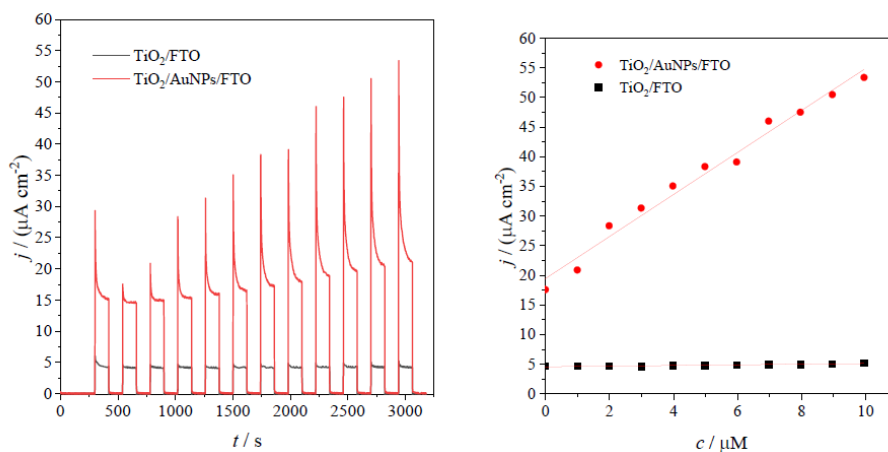
Figure 3.13 - Photoelectrical response of TiO$_2$/FTO and TiO$_2$/AuNPs/FTO in 0.1 M NaClO$_4$ and ciprofloxacin (range 10^{-6} – 10^{-5} M).

136

To verify the stability of the electrode over time, both the background photocurrent and the photocurrent in the presence of ciprofloxacin were recorded multiple times several days apart. The results, presented in Figure 3.14, show that the signal intensity only slightly decreases, and the sensitivity toward ciprofloxacin remains almost unchanged.
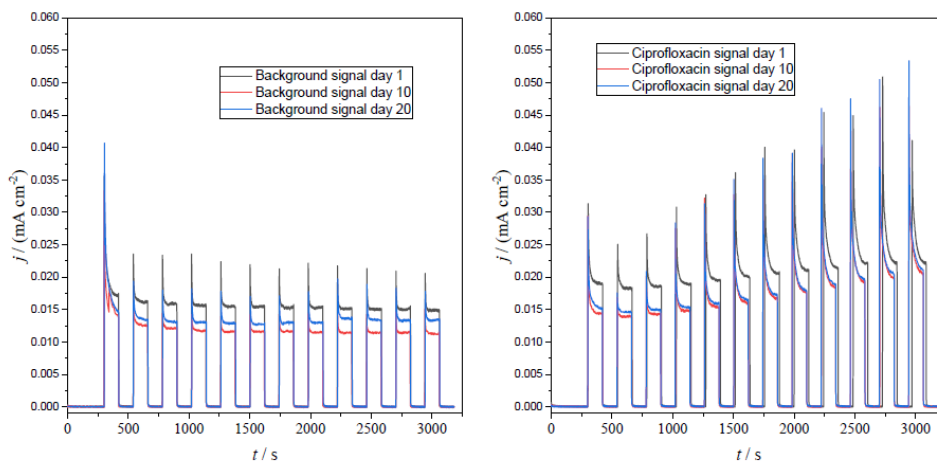

Figure 3.14 - Photocurrent signals recorded 10 days apart of the background (left) and in the presence of ciprofloxacin (right). Concentration of ciprofloxacin 1, 2, 3, 4, 5, 6, 7, 8, 9 and 10 mM.

Preliminary tests with LEDs.

As discussed before, one of the main advantages of electrochemical sensors is the possible miniaturization for on-site use. To achieve this, a better source of illumination is needed. LEDs (Light Emitting Diodes) have many advantages compared with traditional lamps: they can be easily miniaturized; they have less heat dissipation and their wavelength can be easily controlled.

The response of the electrodes was evaluated under irradiation at 3 different wavelengths: 395 nm (characteristic for the TiO_2 cover), 455 nm and 530 nm (characteristic of the AuNPs). As shown in the picture below, irradiation at 395 nm gave the most intense response, while no response was obtained at 530 nm. It was also verified that the orientation of the WE electrode (with the conductive side toward the solution or toward the light source) did not influence the signal.
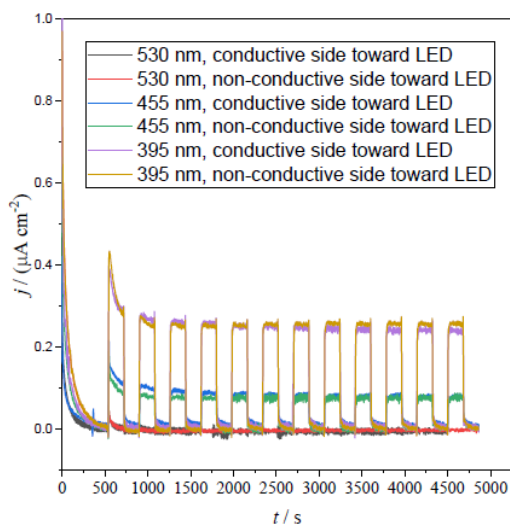
Figure 3.15 - Photoelectric response of TiO$_2$/AuNPs/FTO electrode in 0.1 M NaClO$_4$ under LED irradiation.

The signal of TiO$_2$/FTO electrode was also evaluated in the same conditions. The intensity of the signals was greatly reduced compared to the hybrid electrode. The response of TiO$_2$/FTO electrode under 395 nm LED irradiation was also tested in presence of ciprofloxacin, but as expected, there was no difference to the blank signal.

Another advantage of the LED is that the power is adjustable, therefore tests were carried out at different settings to evaluate how the photocurrent signals change with irradiating power. It is also important to note that the signal intensity was much lower than the one obtained with the 500 W lamp.
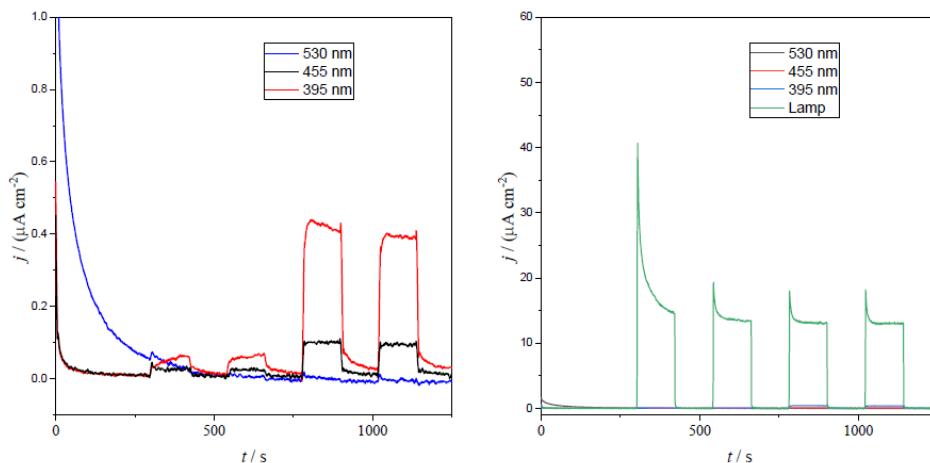
Figure 3.16 - (Left) Photoelectric response of TiO₂/AuNPs/FTO electrode in 0.1 M NaClO₄ under LED irradiation. The light source was initially set at half power for the first two measures and then at full power for the latter ones. (Right) Overlays of the signal reported on the left with the signal obtained with the 500 W lamp positioned at 15 cm from the electrode surface.

Response of the electrode at 395 nm in the presence of ciprofloxacin was evaluated in different conditions. First the LED at maximum power was used, obtaining the best result. A linear relationship was also obtained setting the LED at half power, while no signal was obtained with a less powerful light source such as a monochromator.
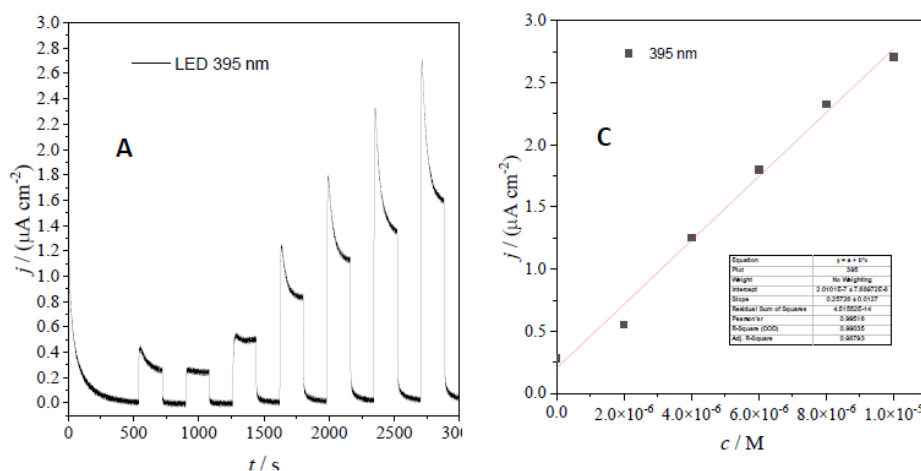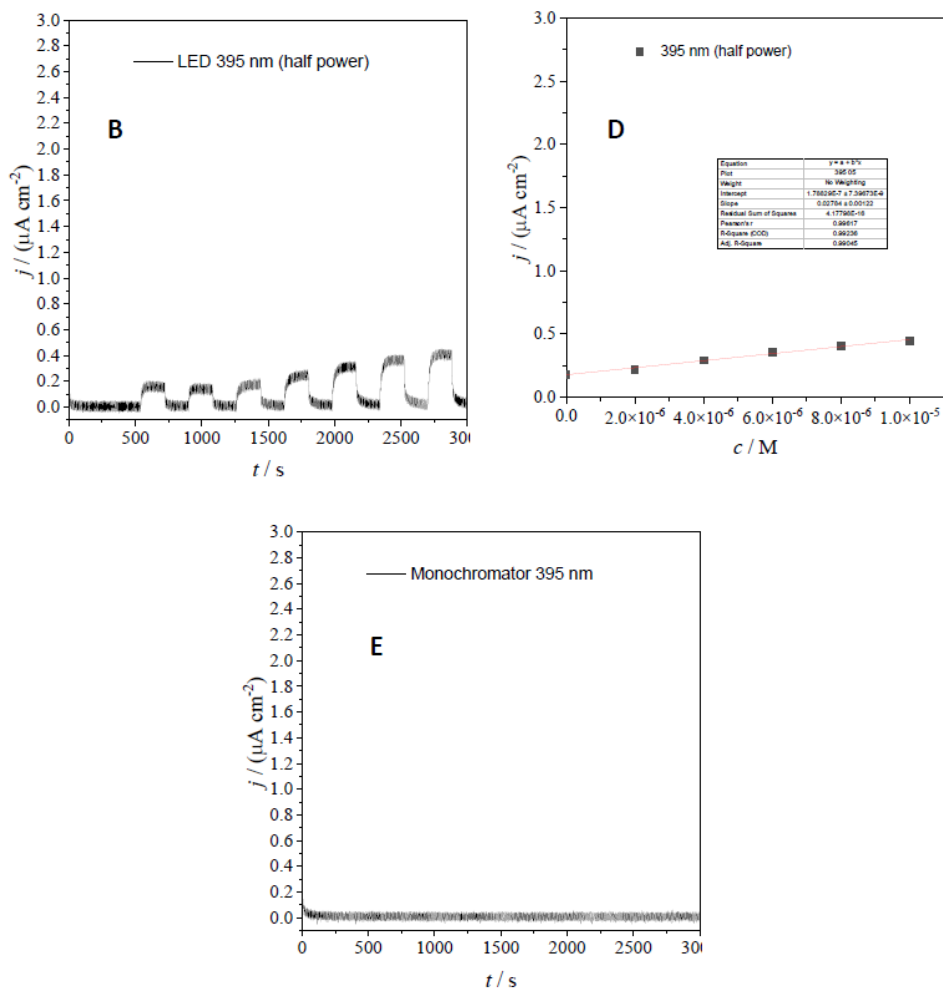
Figure 3.17 - Linear relation of the signal with ciprofloxacin concentration in the range 0-10 μM obtained with the 395 nm LED set at maximum power (A) and at half power (B), and corresponding calibration lines (C) and (D). (E) Same test conducted with a monochromator as light source.

The signal of the electrode in the presence of ciprofloxacin was also measured using the other LEDs, as reported below:
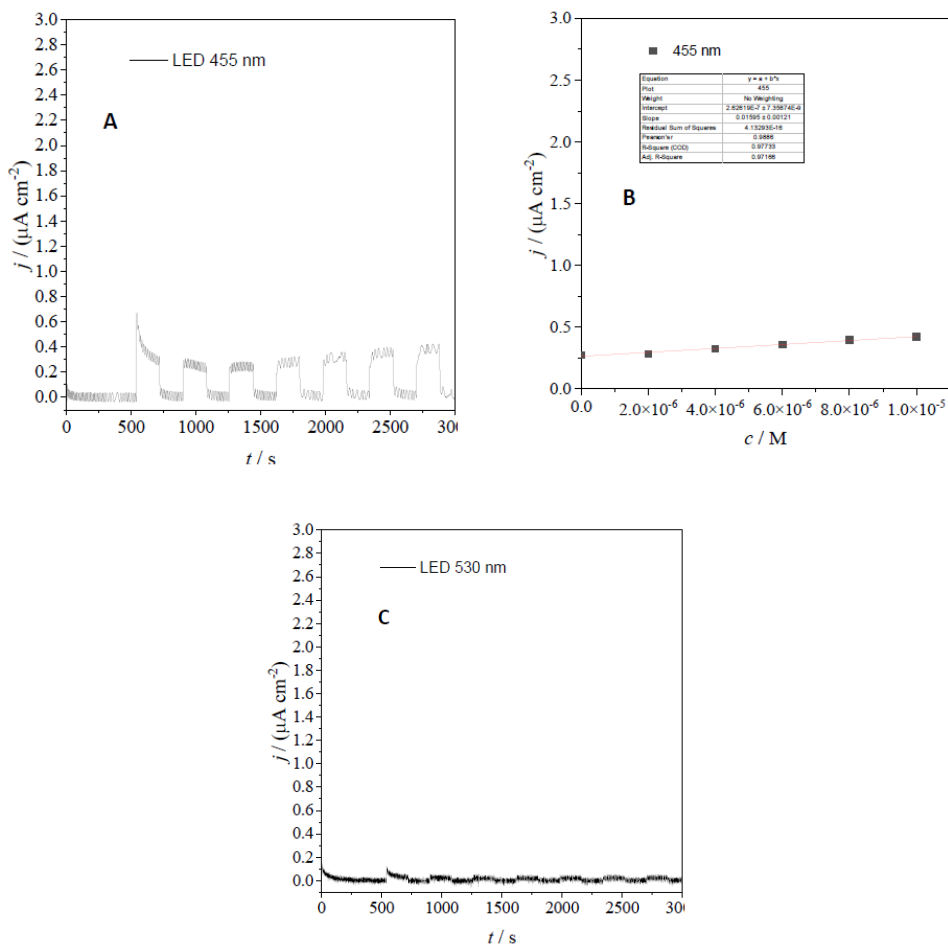
Figure 3.18 - (A) Linear relation of the signal with ciprofloxacin concentration in the range 0-10 µM obtained with the 455 nm LED and corresponding calibration lines (B). (C) Same test conducted with the 530 nm LED.

For comparison, photocurrent was also recorded using a TiO_2/FTO electrode. The graphs below are reported with the same scale of the ones previously shown. The signal does not appear to be related to the concentration of ciprofloxacin.
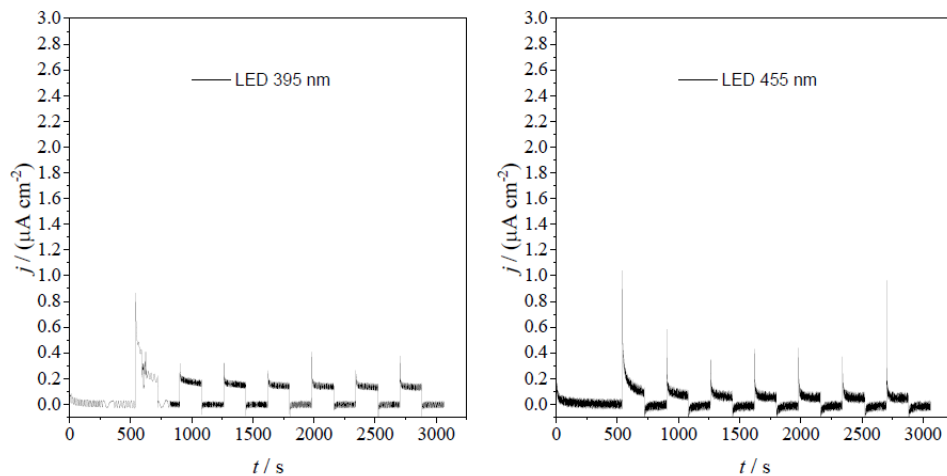
141

Figure 3.19 - Photocurrents recorded in NaClO$_4$ 0.1 M in presence of ciprofloxacin (range 0-10 μM) with a TiO$_2$/FTO electrode and different irradiation sources.

3.3. Results and discussion.

3.3.1. Ciprofloxacin determination.

Different tests were conducted to determine the Limit of Detection (LOD) of the technique and optimize the conditions.
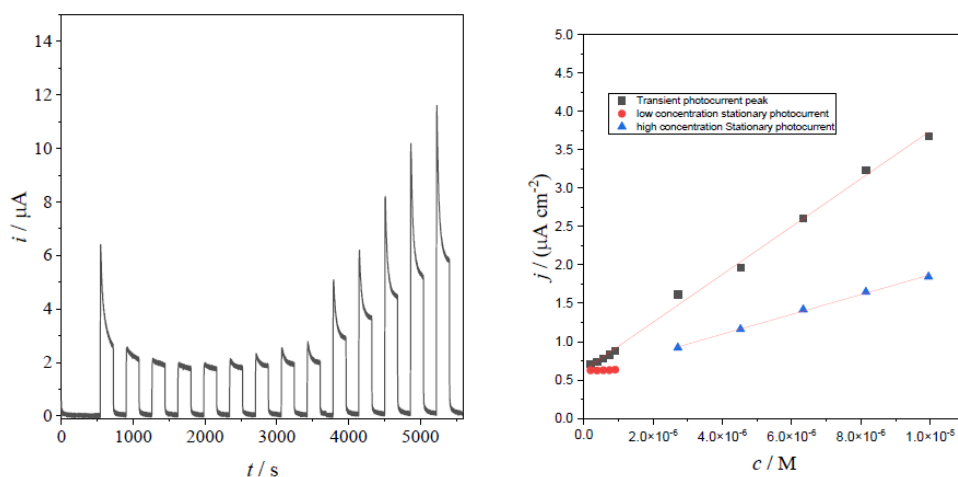

Figure 3.20 - (Left) Photocurrent recorded in NaClO$_4$ 0.1 M under 395 nm irradiation, with 5 ciprofloxacin additions in the range 0.2-1 μM and five in the range 2-10 μM. (Right) Observed linear relationship between the signals and ciprofloxacin concentration.

In the following tests, more time was given to the electrode in order to stabilize the signal under irradiation. This was necessary to obtain a low background value. It was also noted that a linear relationship with concentration was observed in the whole range if using the value of the transient photocurrent peak, while the slope is not the same if the value of the stationary photocurrent was considered. Therefore, in the following tests only the transient peak was considered.
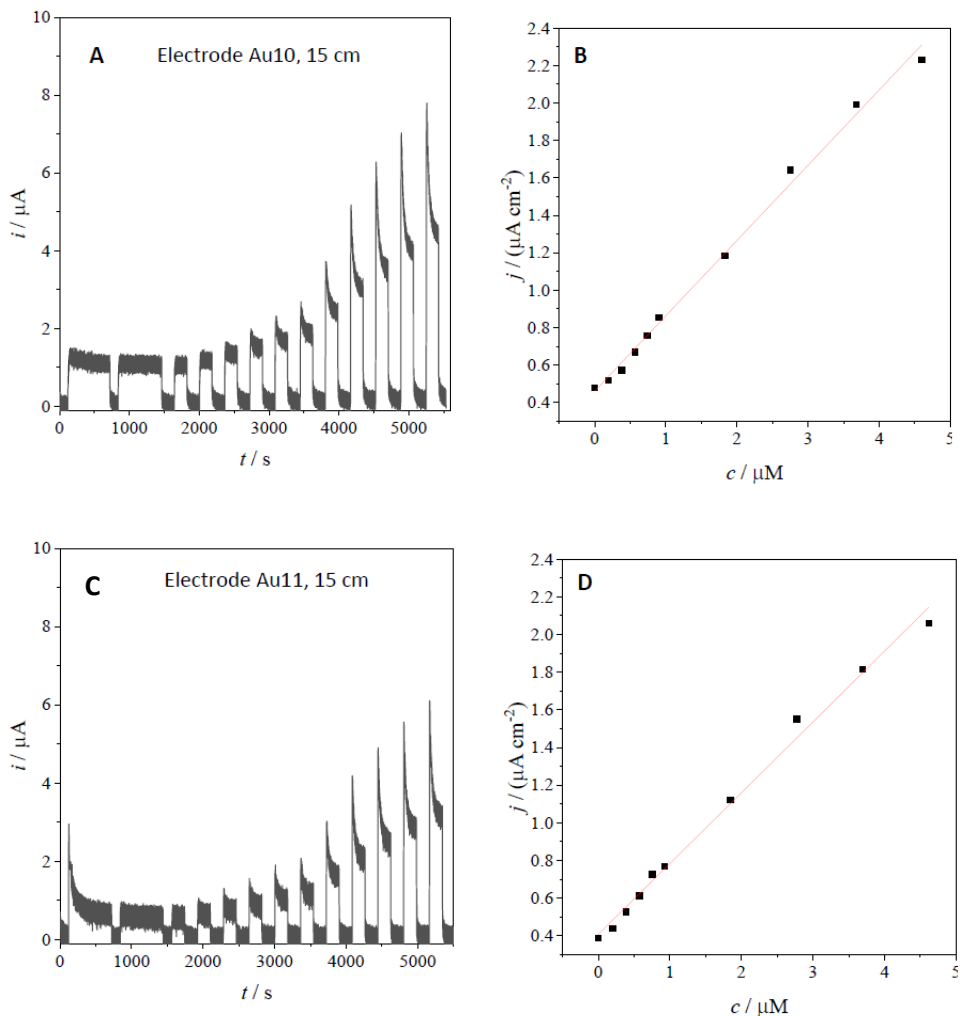
Figure 3.21 - Photocurrent recorded in NaClO₄ 0.1 M with two different electrodes (A) and (C) and corresponding calibration lines (B) and (D). Light source positioned at 15 cm. Not all the points were included in the calibration lines.

To increase the signal intensity, the distance between the electrode and the LED was also varied and it was clear that by decreasing the distance from 15 to 2 cm, the signal intensity increased a lot, as shown in the picture below.
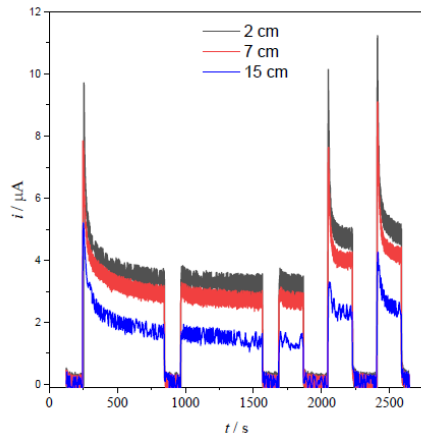
Figure 3.22 - Photocurrent recorded in NaClO$_4$ 0.1 M. The first 3 light phases were recorded with only the support electrolyte, while the other two were recorded after addition of ciprofloxacin.

The LOD was therefore recalculated with the LED at 2 cm:
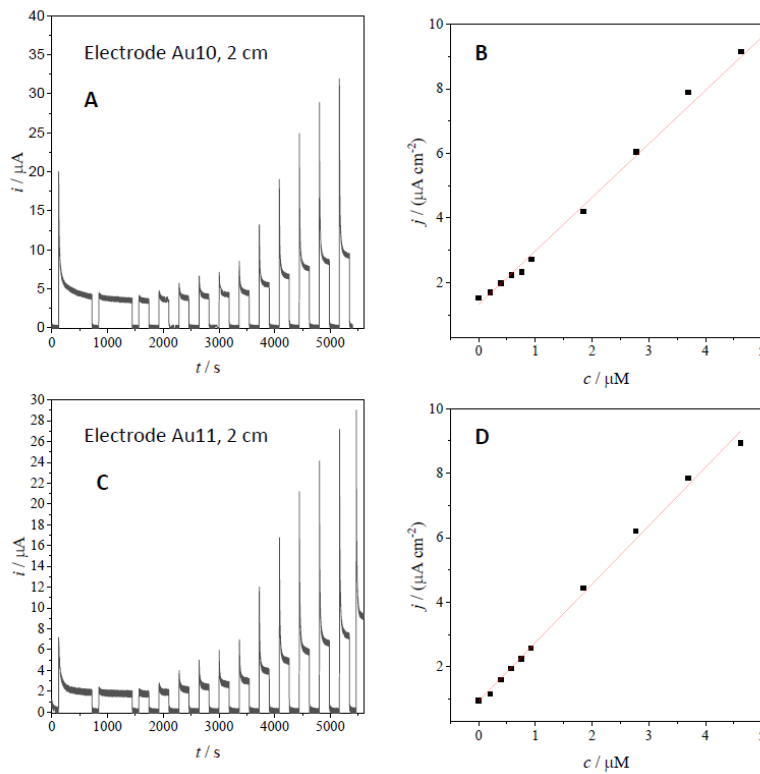

Figure 3.23 - Photocurrent recorded in NaClO$_4$ 0.1 M with two different electrodes (A) and (C) and corresponding calibration lines (B) and (D). Light source positioned at 2 cm. Not all the points were included in the calibration lines.

145

The obtained results are summarized in the following table:

Table 3.4 – Summary of the results obtained with the UV LED.

	LED at 15 cm	LED at 2 cm
Electrode Au10	(0.361 ± 0.009) µM	(0.33 ± 0.08) µM
Electrode Au11	(0.43 ± 0.01) µM	(0.32 ± 0.08) µM

Interestingly, although the position of the LED had great effect on the current signal intensity, it did not influence the LODs, which were coherent and reproducible. Using the calibration line reported in Figure 3.23 D, the mean recovery factor was also estimated to be 99.8%.

Other photocurrent tests were conducted in a different supporting electrolyte (PBS pH 7.5) and at different potential applied (0.45 V). In both cases no significant advantages were obtained. Furthermore, working at higher values of potential does expose the electrode to higher stresses that may result in irreversible damages.
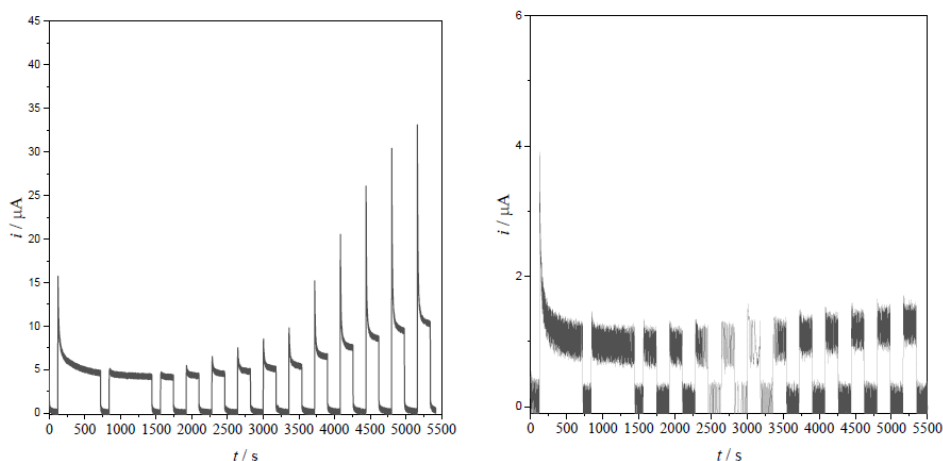

Figure 3.24 - Photocurrent tests recorded at 0.45 V in NaClO₄ solution (left) and at 0.1 V in PBS solution (right)

Shorter time windows for the dark and light phases were also tested. It did not bring any significant improvements and greatly increased the chances of human error; therefore, it was decided to continue using phases of 3 minutes each.

3.3.2. Study of the interferences.

The effect of the most common inorganic and organic interferents in surface waters was also investigated. As for inorganic ions, Na^+, Mg^{2+}, Ca^{2+}, Zn^{2+} and Fe^{3+} were selected. For each ion, two additions of 20 μL each of solution 0.1 M were performed (thus obtaining a concentration of 1 and 2 mM), leading to the following results:
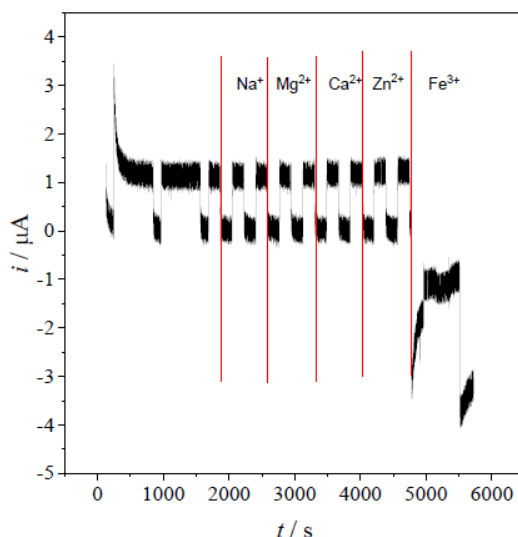
Figure 3.25 - Photocurrent recorded in NaClO₄ 0.1 M: three readings of the background, followed by two additions for each ion.

Figure 3.25 shows that only iron caused significant interference. It is important to consider that the concentration of iron in waters is generally much lower than the one used in the previous test, approximately 9×10^{-7} M. For this reason, other tests were conducted with Fe^{3+} 1 μM and as shown in Figure 3.26, in this case the presence of iron does not interfere with ciprofloxacin detection.
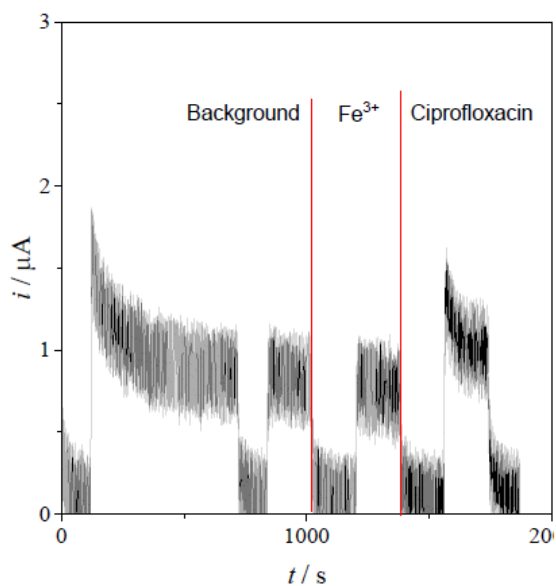
Figure 3.26 - Photocurrent recorded in NaClO$_4$ 0.1 M: readings of the background, then Fe^{3+} and ciprofloxacin 1 μM.

As for organic interferents, paracetamol, diclofenac and humic acid were tested. Paracetamol and diclofenac were added in the same concentration used for the determination of ciprofloxacin (20 μL 0.001 M), while humic acids were detected at a concentration of 0.002% - 20 ppm.
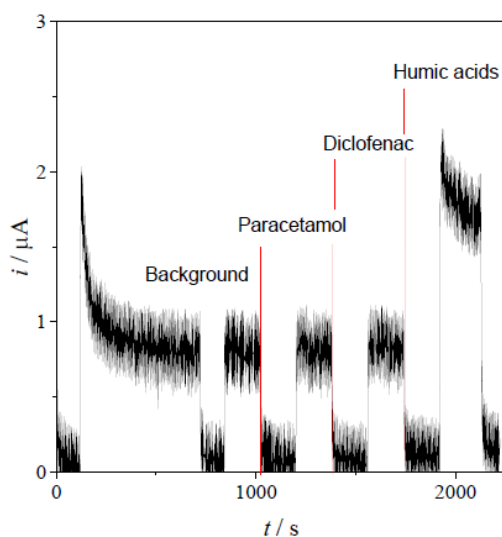

Figure 3.27 - Photocurrent recorded in NaClO$_4$ 0.1 M: readings of the background, then paracetamol, diclofenac and humic acids as described above.

Among those, as shown in Figure 3.27, only humic acids caused interference. Humic acids' concentration in surface waters vary in the range 0.1-20 ppm [25], while it is even lower in ground water averaging 1.2 mg/L (0.00012%) [26]. A test was conducted with humic acids at lower concentrations, between 0.0001% and 0.0007%, obtaining a linear relationship with the current signal.
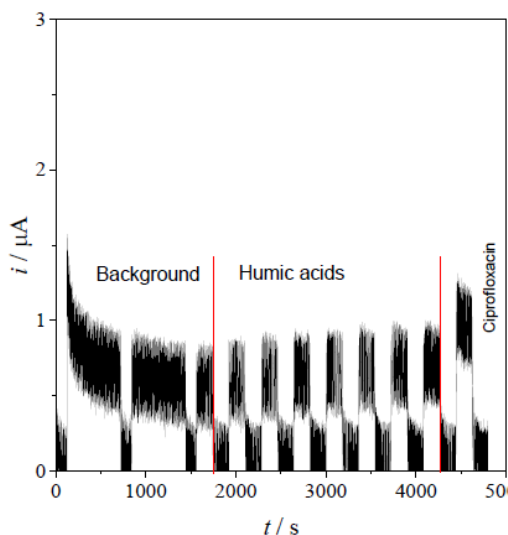

Figure 3.28 - Photocurrent recorded in NaClO4 0.1 M with consecutive additions of humic acids. Ciprofloxacin was added (1 μM) for reference at the end of the test.

These results may suggest a different application for the sensor, as it is effectively able to detect humic acids in real samples.

3.4. Conclusions.

During this thesis work, the properties of a hybrid electrode of titanium dioxide and gold nanoparticles on FTO where studied.

After a quick evaluation of the surface morphology, conducted via optical microscopy and SEM, studies of the diffusion mechanism at the electrode were performed with cyclic voltammetry. The obtained results suggest that the electrode surface is comprised of an array of microelectrodes, positioned close enough to have an overlap of their diffusion layers.

EIS measurements showed that irradiation of both TiO_2 and TiO_2/AuNPs caused a reduction in their resistance, probably due to the presence of an increased number of charge carriers: the AuNPs collect the photogenerated electrons generated by the interaction of the TiO_2 with the UV light, thus favouring the separation of the electron-hole pair; the holes are then free to oxidize ciprofloxacin. The addition of ciprofloxacin did not influence the values of resistance of bare TiO_2, but had great impact on TiO_2/AuNPs, pointing to the catalytic activity of gold nanoparticles.

This idea was confirmed by photocurrent studies, where only the hybrid material proved to have sensitivity toward ciprofloxacin. Furthermore, the photocurrent response of the hybrid material was higher than that of the semiconductor even in $NaClO_4$. This suggests that the gold layer could also achieve an increase in the material conductivity.

After testing the photocurrent response with a 500 W UV lamp, low power LEDs were also used. The hybrid material gave an excellent response under 395 nm irradiation and a signal was also observed at 455 nm. The 395 nm irradiation was also used to perform LOD studies for ciprofloxacin detection, obtaining a value of 320 nM. Interferent effects were also considered, proving the feasibility of the device.

Overall, the sensor proved to have good performances: although the detection limits of other literature work are better than the one presented in this thesis, none of them worked with low power LEDs, preferring to use high power lamps. Some of these sensors, all for transient photocurrent detection, are presented in Table 3.5.

Table 2.5 – Comparisons with the results obtained in other works.

Material	Irradiation	Potential	LOD	Reference
AuNPs/ITO	350 W Xe lamp	0.2 V	0.08 nM	[21]
g-CN/BiOCl	150 W Xe lamp	0 V	0.6 nM	[22]
Bi/BiOBr	150 W Xe lamp	0 V	16 nM	[23]
Bi/BiOCl	150 W Xe lamp	/	150 nM	[24]
TiO_2/AuNPs/FTO	2 W, 395 nm, LED	0.1 V	320 nM	This work

Overall, gold-titania nanohybrids proved to be good materials for the realization of photoelectrochemical sensors for emerging pollutants such as ciprofloxacin. To further optimize the device, it could be useful to test a material with an increased quantity of gold nanoparticles. Ideally, such material should be able to produce a signal even at irradiation of 530 nm, where gold's plasmonic band is excited. Modulating the photocurrent response of the material to move from the UV range to the visible part of the spectrum could pave the way for interesting application of the nanomaterial.

Another interesting aspect would be to test different metal nanoparticles to compare their effect on titanium dioxide and selecting the best element to improve the analytical response of the material.

3.5. Bibliography.

[1] W. W. Zhao, J. J. Xu, H. Y. Chen, Photoelectrochemical detection of metal ions, *Analyst* **2016**, 141, 4262–4271.

[2] Q. Liu, H. Zhang, H. Jiang, P. Yang, L. Luo, Q. Niu, T. You, Photoactivities regulating of inorganic semiconductors and their applications in photoelectrochemical sensors for antibiotics analysis: A systematic review, *Biosens. Bioelectron.* **2022**, 216, 114634.

[3] L. Neven, H. Barich, N. Sleegers, R. Cánovas, G. Debruyne, K. De Wael, Development of a combi-electrosensor for the detection of phenol by combining photoelectrochemistry and square wave voltammetry, *Anal. Chim. Acta* **2022**, 1206, 339732.

[4] M. Petruleviciene, J. Juodkazyte, I. Savickaja, R. Karpicz, I. Morkvenaite-Vilkonciene, A. Ramanavicius, $BiVO_4$-based coatings for non-enzymatic photoelectrochemical glucose determination, *J. Electroanal. Chem.* **2022**, 918, 116446.

[5] B. Bastug Azer, A. Gulsaran, J. R. Pennings, R. Saritas, S. Kocer, J. L. Bennett, Y. Devdas Abhang, M. A. Pope, E. Abdel-Rahman, M. Yavuz, Core–shell defective TiO_2 nanoparticles by femtosecond laser irradiation with enhanced photocatalytic performance, *J. Electroanal. Chem.* **2022**, 918, 116466.

[6] F. Bakhshandeh, S. Saha, S. Sakib, I. Zhitomirsky, L. Soleymani, TiO_2 Nanoparticles Co-Sensitized with Graphene Quantum Dots and Pyrocatechol Violet for Photoelectrochemical Detection of Cr(VI), *J. Electrochem. Soc.* **2022**, 169, 057520.

[7] H. Geng, X. Chen, L. Sun, Y. Qiao, J. Song, S. Shi, Q. Cai, $ZnCuInSe/Au/TiO_2$ sandwich nanowires-based photoelectrochemical biosensor for ultrasensitive detection of kanamycin, *Anal. Chim. Acta* **2021**, 1146, 166–173.

[8] S. Sheng, Z. Zhang, M. Wang, X. He, C. Jiang, Y. Wang, Synthesis of MIL-125(Ti) derived TiO_2 for selective photoelectrochemical sensing and photocatalytic degradation of tetracycline, *Electrochim. Acta* **2022**, 420, 140441.

[9] Z. Yang, W. Xu, B. Yan, B. Wu, J. Ma, X. Wang, B. Qiao, J. Tu, H. Pei, D. Chen, Q. Wu, Gold and Platinum Nanoparticle-Functionalized TiO2

Nanotubes for Photoelectrochemical Glucose Sensing, *ACS Omega* **2022**, 7, 2474–2483.

[10] P. Gao, H. Ma, J. Yang, D. Wu, Y. Zhang, B. Du, D. Fan, Q. Wei, Anatase TiO_2 based photoelectrochemical sensor for the sensitive determination of dopamine under visible light irradiation *New J. Chem.* **2015**, 39, 1483–1487.

[11] J. Zhao, J. Cheng, Y. Sun, J. Liu, W. Chen, Y. Xu, J. Yang, Y. Li, Carbon dots for virus detection and therapy, *Microchimica Acta* **2021**, 188.

[12] L. Shi, Y. Yin, L. C. Zhang, S. Wang, M. Sillanpää, H. Sun, Design and engineering heterojunctions for the photoelectrochemical monitoring of environmental pollutants: a review, *Appl. Catal. B* **2019**, 248, 405–422.

[13] H. Cheng, X. Wang, Z. Bai, C. Zhu, Z. Zhang, Q. Zhang, Q. Wang, H. Dong, B. Xu, Optimization of PEC and photocathodic protection performance of $TiO_2/CuInS_2$ heterojunction photoanodes *Nanotechnology* **2023**, 34, 015703.

[14] M. Zanatta, L. Calvillo, J. Zheng, G. A. Rizzi, C. Durante, G. Giallongo, D. Chirkov, L. Colazzo, C. Marega, A. Gennaro, G. Granozzi, Cu_2O/TiO_2 heterostructures on a DVD as easy&cheap photoelectrochemical sensors *Thin Solid Films* **2016**, 603, 193–201.

[15] Y. He, Z. Ren, L. Yan, J. Liu, L. A. Belfiore, J. Tang, S. Mao, Pt nanoparticles enhanced TiO_2 on ultra-violet photo-detection: Hot-electron injection effect over near-field enhancement *Appl. Surf. Sci.* **2022**, 605, 154768.

[16] M. V. Dozzi, A. Candeo, G. Marra, C. D'Andrea, G. Valentini, E. Selli, Effects of Photodeposited Gold vs Platinum Nanoparticles on N,F-Doped TiO_2 Photoactivity: A Time-Resolved Photoluminescence Investigation *J. Phys. Chem. C* **2018**, 122, 14326–14335.

[17] Y. Jiang, Q. Li, J. Yao, X. Guo, Y. Ying, X. Liu, Y. Wen, H. Yang, Y. Wu, Advanced photoelectrochemical detection of paraquat based on plasmonic metal modified photocathode material, *Appl. Surf. Sci.* **2022**, 581, 151903.

[18] S. Saha, J. Yang, S. S. M. Masouleh, G. A. Botton, L. Soleymani, Hot hole direct photoelectrochemistry of Au NPs: Interband versus Intraband hot carriers, *Electrochim. Acta* **2022**, 404, 139746.

[19] A. B. Tesler, T. Sannomiya, S. Hejazi, R. Mohammadi, N. Vogel, M. Altomare, P. Schmuki, Metallic nanoparticle-on-mirror: Multiple-band light

harvesting and efficient photocurrent generation under visible light irradiation, *Nano Energy* **2021**, 90, 106609.

[20] M. Khairy, E. M. Kamar, M. A. Mousa, Photocatalytic activity of nano-sized Ag and Au metal-doped TiO_2 embedded in rGO under visible light irradiation *Mater. Sci. Eng. B* **2022**, 286, 116023.

[21] L. Cao, Z. Li, R. Jia, L. Chen, Y. Wu, J. Di, Sensitive Photoelectrochemical Determination of Ciprofloxacin Using an Indium Tin Oxide Photoelectrode Modified with Small Gold Nanoparticles, *Anal. Lett.* **2020**, 53, 1472–1488.

[22] L. Xu, H. Li, P. Yan, J. Xia, J. Qiu, Q. Xu, S. Zhang, Graphitic carbon nitride/BiOCl composites for sensitive photoelectrochemical detection of ciprofloxacin, *J. Colloid Interface Sci.* **2016**, 483, 241–248.

[23] P. Yan, L. Xu, D. Jiang, H. Li, J. Xia, Q. Zhang, M. Hua, Photoelectrochemical monitoring of ciprofloxacin based on metallic Bi self-doping BiOBr nanocomposites, *Electrochim. Acta* **2018**, 259, 873–881.

[24] L. Xu, P. Yan, H. Li, S. Ling, J. Xia, J. Qiu, Q. Xu, H. Li, S. Yuan, Metallic Bi self-doping BiOCl composites: Synthesis and enhanced photoelectrochemical performance, *Mater. Lett.* **2017**, 196, 225–229.

[25] S. Basumallick and S. Santra, Monitoring of ppm level humic acid in surface water using ZnO–chitosan nano-composite as fluorescence probe, *Appl. Water Sci.* **2017**, 7, 1025–1031.

[26] S. Boggs, D. Livermore, and M. G. Seltz, Humic Substances in Natural Waters and Their Complexation with Trace Metals And Radionuclides: A Review, **1985**.

4. Mesoporous silica.

4.1. Introduction.

Mesoporous materials, classified by IUPAC as having a narrow distribution of pore size between 2 and 50 nm, include silica and silica-based organic–inorganic hybrids, metal oxides and carbon and organic polymers. Their open, porous structure, wide surface area, high pore volume, and adjustable mesopore dimensions have drawn a lot of interest [1-4]. The Mobil Oil Company has been developing ordered mesoporous silica for almost 20 years, and it possesses the qualities of both crystalline zeolites and amorphous silica gels [5, 6].

The manufacture of these materials and their practical applications in several domains, including catalysis [7,8], electrochemical sensors [9-15], pollutant adsorption [16-18] and molecular sieving/separation [19,20], and the aforementioned fields, have been the subject of numerous research investigations to date.

The main characteristic of mesoporous silica is the poly-condensation of the silica precursor (mainly sodium silicates and silicon alkoxides, such as tetraethoxysilane, TEOS and tetramethoxysilane, TMOS) in the presence of supramolecular assemblies or macromolecular structure-directing agents (*i.e.*, ionic or non-ionic surfactants) [1, 21-23]. Figure 1 shows the schematic process of formation of the mesoporous structure, which is revealed after removing the organic template by calcination or by solvent extraction. The experimental conditions can be controlled to tune the morphology, mesostructured type, and orientation of the material [24-28].
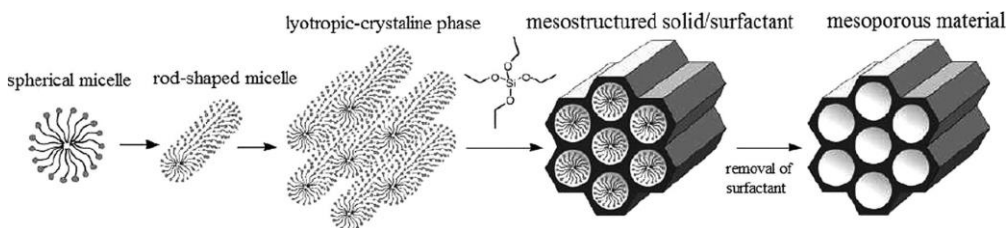

Figure 4.12 - Formation of mesoporous materials via structured-directing agents (taken from [29]).

Initially, ordered mesoporous silica films were produced at air-water [30] or water-oil [31] interfaces using the self-assembly of silica precursors with surfactant templates. Nevertheless, the most adaptable technique to date is the evaporation-induced self-assembly approach (EISA) [32]. In this method, a

homogeneous sol solution of a soluble precursor (for example, TEOS) and a surfactant (for example, cetyltrimethylammonium bromide, CTAB) prepared in a water/alcohol mixture is deposited onto a solid support. While the substrate grows, the solution covers the surface and undergoes preferential evaporation of alcohol, leading to the film formation by self-assembly condensation originating from the concentration of the surfactant and inorganic species. The coating is normally casted onto the substrate by dip-coating, spray coating or spin-coating.

Various pore structures can be obtained via EISA, including different types of 2D or 3D mesostructures. 2D structures are less stable from both a chemical and a mechanical point of view and also the access to the pore channels is more difficult, because they prefer to orient parallelly to the surface. This limits the application of these materials due to restricted accessibility and/or mass transport rates [32-34].

Another key point that makes mesoporous silica so appealing is its possible functionalisation: in literature there are a lot of examples of functionalised mesoporous silica for different purposes, such as one-step electrogeneration of amino-modified mesoporous silica films for the detection of copper (II) [45], mesoporous silica containing gold nanoparticles for the oxidation of ascorbic acid [46] or the functionalisation with (3-mercaptopropyl)trimethoxysilane (MPTMS) and AgNPs [47].

The orientation of the channels is essential to have a facilitated accessibility for the applicative purposes seen above; for these reasons, mesoporous channels vertically oriented would be the best choice, but the preparation of such vertically aligned mesoporous silica films has proven to be particularly challenging [35]. Many efforts have been made and documented in the literature to achieve this goal [36]. The following section will provide a summary of the methods that have been put forth thus far for the development of mesoporous silica thin films that exhibit vertically aligned mesopore channels normal to the underlying support.

4.1.1. Control of the mesopore orientation with EISA.

Zhao *et al.* initially reported on continuous mesoporous silica thin films with 3D-accessible pore structure.[37] Here, the mesoporous films were produced on polished silicon (110) wafers or glass sheets using the dip-coating process, which uses cationic surfactants (such gemini C_{18-3-1} or CTAB) in nonaqueous fluids under acidic conditions. The uniformity of the film thickness ranged

from 300 nm to several hundred micrometers, with pore sizes ranging from 18 to 25 Å, contingent upon the surfactant type employed as the structure-directing agent.

4.1.1.1. Use of patterned substrates.

The orientation of the substrate and the crystallographic orientation of the material grown on it are connected in epitaxial development of crystalline materials. To reduce the interfacial energy between the two materials, the epitaxial layer is produced in this manner [38]. A 2D hexagonal mesoporous silica film that is produced on a substrate experiences a significant alteration in its crystallographic orientation due to its structural anisotropy. The lattice matching of the silicatropic liquid crystal and the aligned surface micelle structure, both of which are produced by the EISA method, leads to this new orientation [38-40]. According to Miyata *et al.* [38, 39] mesoporous silica films with uniaxially aligned porous structure can be prepared efficiently on substrates having surface structural anisotropy, such as a glass substrate with rubbing-treated polyamide coatings, The flexibility of mesostructured materials is partly responsible for this effect, as it permits a relatively substantial mismatch between the periodicity of the regularly ordered surface micelles generated by adsorption on a surface and the intrinsic lattice constants of mesostructured materials.[38]

In another work, Richman *et al.* [41] have shown that vertically directed pores in honeycomb-structured films can be formed via nanoscale epitaxy on a patterned substrate. The pattern was created using the surface of cubic mesoporous films. The vertical orientation with mesochannel diameters in the range of 10–15 nm is obtained when conditions for a precise lattice match between the hexagonal and cubic films are met (*i.e.*, achievable using mixed templates or selective pore swelling).

4.1.1.2. Scanning electrochemical microscopy (SECM).

Through the use of a scanning electrochemical microscope, a microelectrode (diameter ranging from 5 to 50 µm) was precisely positioned at a close distance from the surface that needed to be modified. The sol was then locally electrolyzed in the thin layer that formed between the microelectrode and the surface to be modified. This process allowed for the deposition of micron-sized mesoporous silica spots through electrochemical assistance. [42] Under these

circumstances, it is possible to produce thin films with mesopore channels growing perpendicularly from the surface by properly arranging the working and counter electrodes (*i.e.*, guaranteeing potential-driven interfacial assembly of the surfactants).

4.1.1.3.   Electrochemically-assisted self-assembly (EASA).

Walcarius group has demonstrated that electrochemically-assisted self-assembly (EASA) may be used to efficiently create uniform mesoporous silica thin films with closely packed, hexagon-shaped, vertically aligned pore channels of 2-3 nm in diameter on a variety of conducting substrates [43, 44].

The sol−gel process involves two reactions, the hydrolysis and condensation of silica precursors, which occur simultaneously or successively. Their rates are strongly pH-dependent, the hydrolysis being fast at pH 3−4 while condensation is accelerated when increasing pH above 4 (or in ultra-acidic media (pH < 1)). Based on this knowledge, starting from a stable sol at pH 3, it is possible to electrochemically trigger a pH increase at the electrode/solution interface by the application of a suitable cathodic potential leading to polycondensation of the silica precursors and film deposition onto the electrode surface. The applied potential not only plays the role of generating the hydroxyl catalyst but also contributes to electrochemical interfacial surfactant templating (*i.e.*, CTAB) to induce the growth of the mesopore channels orthogonally to the underlying electrode support. Also in this case, the structure is kept integral after the removal of the surfactant. [44]
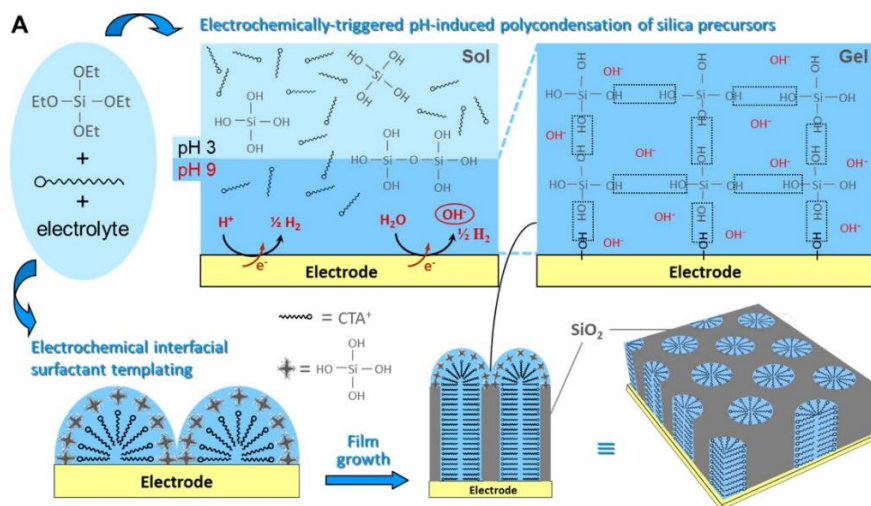

Figure 4.13 - Schematic illustration of the EASA process (taken from [44]).

Through the co-condensation of organosilane and alkoxysilane reagents [49, 50], organic groups can be homogeneously added to mesostructured silica sol-gels, although this usually has an impact on the resulting materials' physico-chemical characteristics. [51, 52] In particular, the hexagonal mesoporous structure is kept integral only up to a concentration of APTES of 10% [45].

The mesoporous structure confers to the material size-exclusion and charge-exclusion properties [53].

4.1.2. Aim of this work.

Considering the results obtained in Chapter 3, for the study of the interferences, the aim of the work is to combine the properties of vertically-aligned mesoporous silica films to have charge/size exclusion effects with the already considered photoelectrochemical properties of the hybrid material composed by AuNPs and TiO_2 layer for the determination of ciprofloxacin with a low-power light source. This work was done in collaboration of prof. Alain Walcarius and his research group at the Laboratoire de Chimie Physique et Microbiologie pour les Matériaux et l'Environnement (LCPME), a mixed research unit of Université de Lorraine et du CNRS (UMR 7564) in Villers-lès-Nancy, where I attended a four-month stage.

4.2.   Materials and methods.

All the details regarding reagents and instruments used during the work are reported in this paragraph. The reagents are listed in Table 4.1; Table 4.2 lists the instruments and the materials. The procedures section focuses on the preparation of solutions widely used during the work.

Table 4.1 - description of all reagents used in this work.

Name	Use	CAS number	Brand
Titanium(IV) isopropoxide	Titania synthesis	546-68-9	Sigma-Aldrich
Hydrocloric acid 37%	Titania synthesis	7647-01-0	Sigma-Aldrich
LUTENSOL ON70	Titania synthesis	-	-
Ethanol absolute $\geq$ 99.8%	Titania synthesis	64-17-5	Sigma-Aldrich
Acetone	Electrode assembly	67-64-1	Sigma-Aldrich
2-propanol	Electrode assembly	67-63-0	Carlo Erba
Sulfuric acid, 95.0-97.0%	Electrode assembly	7664-93-9	Sigma-Aldrich
APTES	Electrode assembly	919-30-2	Sigma-Aldrich
Tetraethoxysilane (TEOS) 98%	Mesoporous silica synthesis	78-10-4	Alfa Aesar
$NaNO_3$	Mesoporous silica synthesis	7631-99-4	Fluka
Cetyltrimethylammonium bromide (CTAB) 99%	Mesoporous silica synthesis	57-09-0	Acros
$HAuCl_4$	Electrode assembly	16961-25-4	Sigma-Aldrich
Ciprofloxacin HCl	Analyte	86393-32-0	Sigma-Aldrich
Sodium perchlorate hydrate	Electrolyte	207683-20-3	Sigma-Aldrich
$K_4[Fe(CN)_6] \cdot H_2O$	Probe molecule	14459-95-1	Fluka

Table 4.2 - description of the materials and tools used.

Name	Brand
FTO	Sigma-Aldrich
Potentiostat Galvanostat [PGSTAT30]	MetrOhm
Micropipettes	Gilson
Oven	Forno MAB
N_2 [air liquid 6.0]	Alphagz 2.0a
Analytical scale [crystal 100 cal]	Gibertini
pHmeter [model 338]	AMEL instruments
LEDs	Thorlabs
TEM [F20] field emission gun (FEG)	FEI Tecnai

4.2.1. Device assembly.

Following the work of Walcarius group [45], electro-assisted self-assembly of mesoporous silica thin films was achieved under potentiostatic conditions on fluorine-doped tin oxide (FTO) electrode. Its typical composition was 20 mL ethanol, 20 mL aqueous solution of 0.1 M $NaNO_3$ and 0.1 M HCl, to which 13.6 mmol "TEOS+APTES" and 4.35 mmol CTAB were added under stirring. TEOS alone was used to prepare pure silica films and a mixture of TEOS and APTES to get amine-functionalized deposits. When APTES was added to the sol, it was necessary to adjust the pH to 3 with concentrated HCl. The sol was aged for 2.5 h under stirring before use. The surface of the electrode was delimited by a round seal (10 mm inner diameter) on which a Teflon reservoir containing the sol was placed. A cathodic potential of −1.5 V was applied for 25 s. The electrode was then quickly removed from the solution and immediately rinsed with distilled water. The deposit was finally dried and aged overnight in an oven at 130 °C. Template extraction was achieved by immersing the film electrode in an ethanol solution containing 0.1 M HCl under moderate stirring for 5 min.

4.2.2. AuNPs electrodeposition.

Following the procedure reported by Lei *et al.* [48], gold nanoparticles were deposited starting from a $HAuCl_4$ solution 0.5 mM containing KCl 0.1 M and subjected to a potential sweep between –0.8 and +1.5 V for 15 cycles.

Titanium dioxide was deposited with the same procedure described in Chapter 2, paragraph 2.2.3.

4.2.3. TEM characterisation

TEM analyses were performed at the Department of Earth Science, University of Milan, using a FEI TECNAI F20 Field Emission Gun (FEG) transmission electron microscope. Instrument is equipped with S-Twin lens that lead a resolution of 0.24 nm. The imaging system is composed by one tv rate 626 Gatan and one slow scan 794 Gatan CCD cameras (Gatan, Peasanton, CA, United States). The system operates with an accelerating voltage of 200 kV. Investigated samples were scratched from FTO glass, then dispersed in ethanol and ultrasonicated. The suspension (~ 5 µL) was deposited on a carbon-coated Cu grid.

The sample analysed were the mesoporous silica modified with APTES after the extraction of the template and the mesoporous silica containing AuNPs.
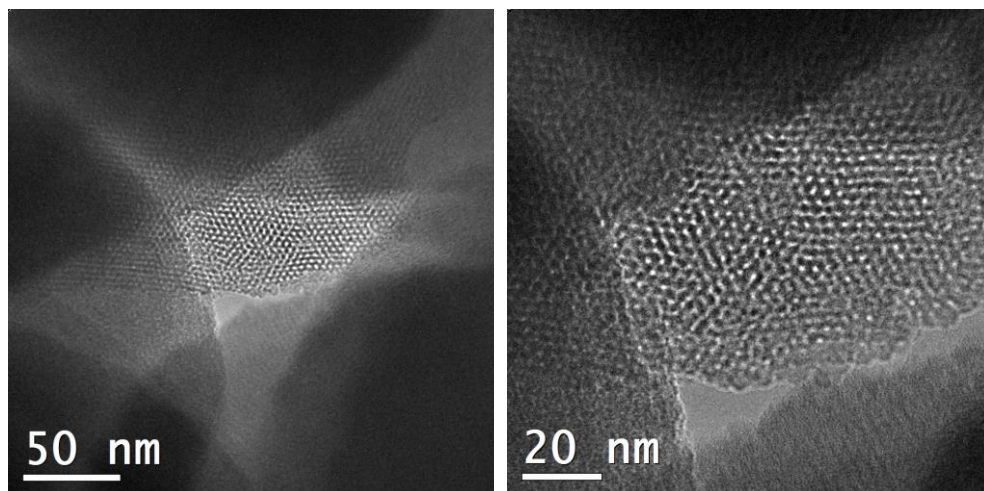

a.   b.
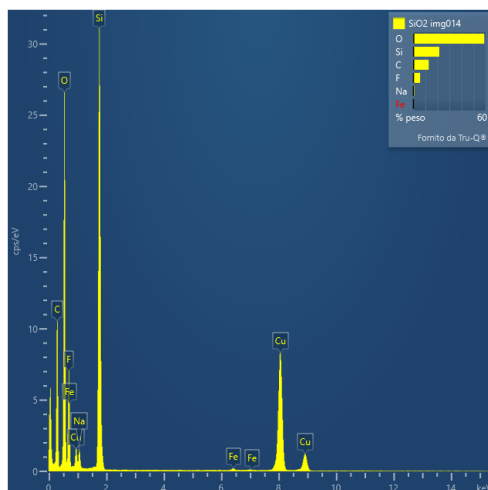
c.

Figure 4.3 – TEM images at different magnifications (a. and b.) and EDS spectrum (c.) of the amino-modified mesoporous silica.

From Figure 3a and 3b it is possible to see the typical ordered hexagonal mesoporous structure of vertically aligned mesoporous silica. EDS analysis confirms the presence of Si and O, but also of C (coming from the modification with APTES) and F (deriving from the FTO glass).
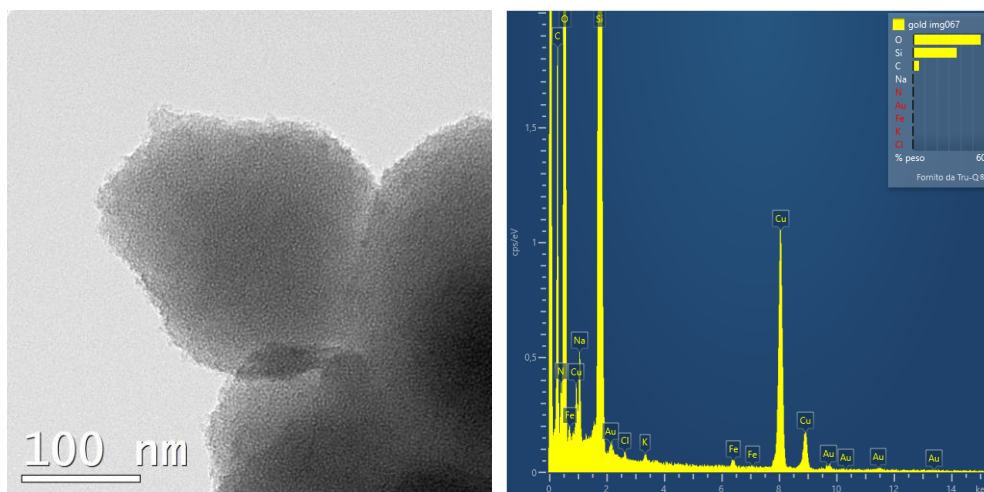
a.   b.

Figure 4.4 – TEM image (a.) and EDS spectrum (b.) of the amino-modified mesoporous silica containing gold nanoparticles.

The porous structure is still visible also after the electrodeposition of AuNPs. The latter are not visible with TEM imaging, but their presence is confirmed by EDS analysis (Figure 4b), in which some peaks related to gold are present (around 2 keV and in the region between 9.75 and 13.5 keV). Their presence is also confirmed by cyclic voltammetry and electrochemical impedance spectroscopy (see paragraph 4.2.5).

4.2.4. Cyclic voltammetry.

All the possible combinations of materials (bare mesoporous silica, mesoporous silica containing AuNPs, mesoporous silica containing AuNPs covered by TiO_2, bare titanium dioxide and mesoporous silica covered by TiO_2) were electrochemically characterised with cyclic voltammetry (CV). Cyclic voltammetries were performed in a three-electrode cell in which the reference electrode was a SCE, the counter electrode a Pt wire and the working electrode was the modified FTO glass. CVs were performed in $NaClO_4$ 0.1 M using $K[Fe(CN)_6]$ 3 mM as probe molecule.
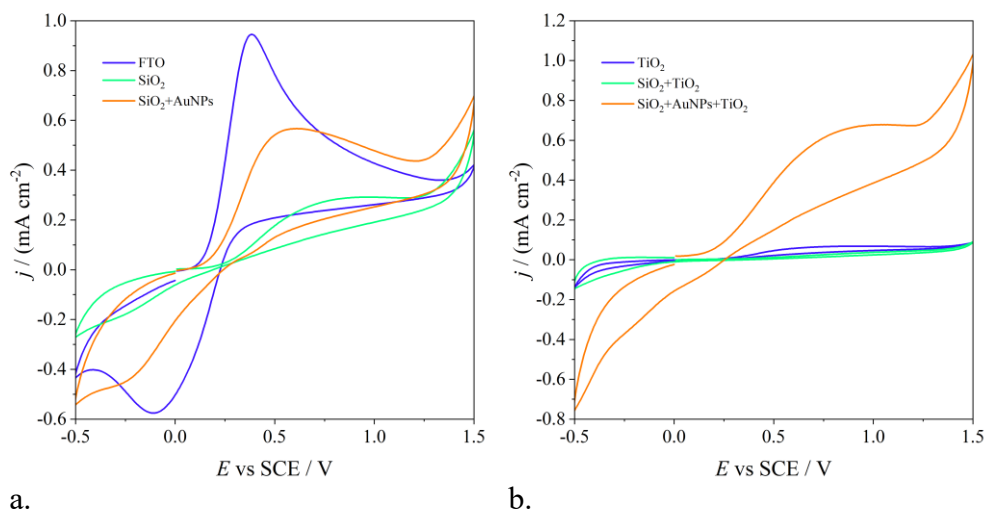

a.   b.

Figure 4.5 - Comparison of different electrodes (a. not containing TiO_2, b. containing TiO_2) in CV at a scan rate of 100 $^{mV s-1}$ using $K[Fe(CN)_6]$ 3 mM as probe molecule.

From a quick comparison showed in Figure 4.5a, it is possible to see that the signal related to the mesoporous silica, when using an anionic probe, is low: this is due to the electrostatic interactions occurring between the anionic probe

and the negative groups on the surface of the mesoporous silica. The signal increases in presence of the gold nanoparticles because they are electroactive and increase the electrochemical signal.

The same trend is visible in Figure 5b, in which the signals related to the samples not containing AuNPs are low, compared to the electrode where they are present.
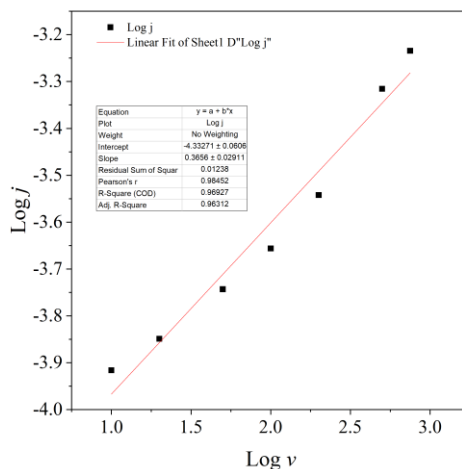
The study of the scan rate was performed on four different electrodes:

a. bare mesoporous silica
b. mesoporous silica + gold nanoparticles
c. mesoporous silica + titanium dioxide
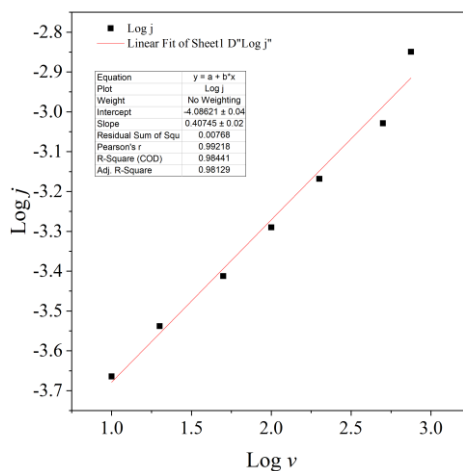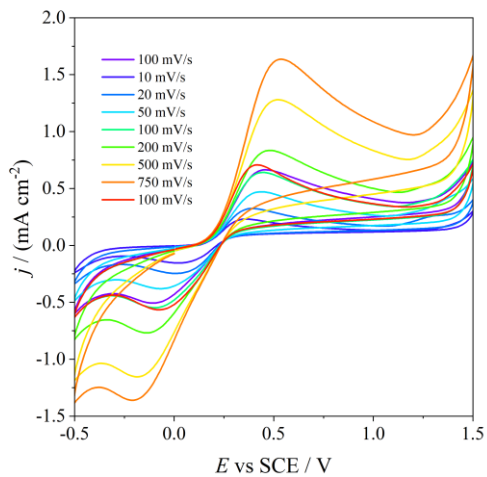d. mesoporous silica + gold nanoparticles + titanium dioxide

The superimposition of the CVs and the linear fitting of the Log j vs Log v plots are reported in the following figures.
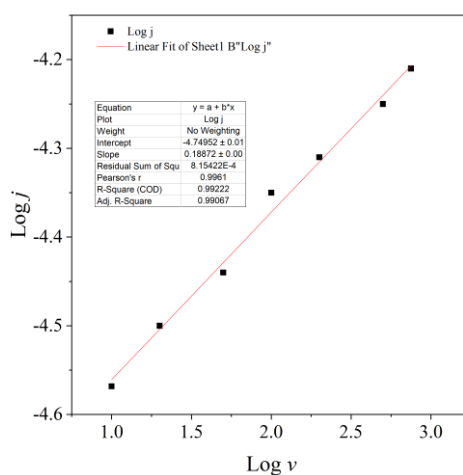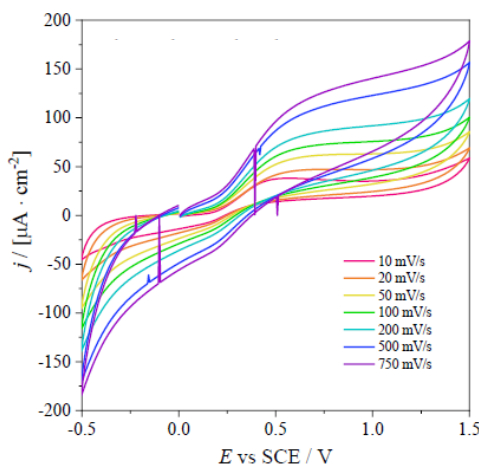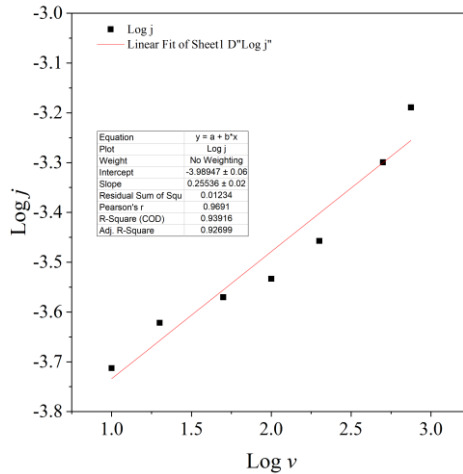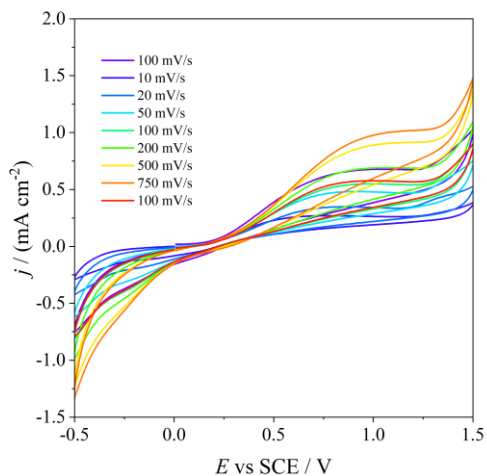

a

a'

b

b'

c

c'

d

d'

166
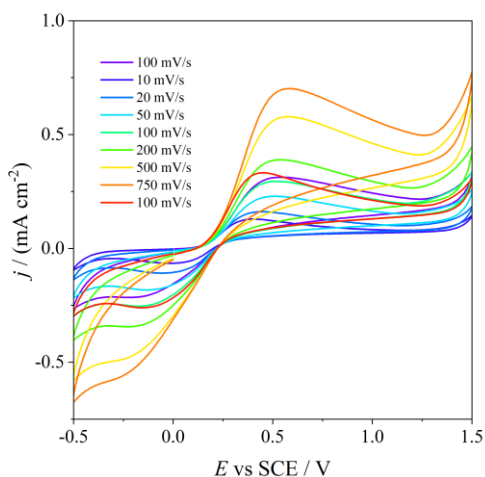
Figure 4.6 – Study of the scan rate of different electrodes (a. bare mesoporous silica, b. mesoporous silica + gold nanoparticles, c. mesoporous silica + titanium dioxide, d. mesoporous silica + gold nanoparticles + titanium dioxide) and their linear fit using K[Fe(CN)$_6$] 3 mM as probe molecule.

The values of the slope of the linear plot of Log j vs Log v are reported in the table below (Table 4.3).

Table 4.3 - Values of the slope of different electrodes.

Electrode	Slope (Log j vs Log v)	Slope (j vs $v^{0.5}$)
a. SiO$_2$	(0.366 ± 0.029)	$(1.93 \cdot 10^{-5} \pm 8.24 \cdot 10^{-7})$
b. SiO$_2$ + AuNPs	(0.407 ± 0.022)	$(4.52 \cdot 10^{-5} \pm 3.62 \cdot 10^{-6})$
c. SiO$_2$ + TiO$_2$	(0.189 ± 0.007)	$(1.17 \cdot 10^{-6} \pm 1.12 \cdot 10^{-7})$
d. SiO$_2$ + AuNPs + TiO$_2$	(0.255 ± 0.029)	$(1.74 \cdot 10^{-5} \pm 1.23 \cdot 10^{-6})$

From the description done in Chapter 1, paragraph 1.2, for the electrodes a and b (not covered by the TiO$_2$ layer), we are in presence of a linear diffusion (case 4). For the electrodes c and d (with the TiO$_2$ layer) the diffusion lines partially overlap, making the diffusion like the linear case, but not totally planar (case 3).

4.2.5. Electrochemical impedance spectroscopy.

All the possible combinations of materials (bare mesoporous silica, mesoporous silica containing AuNPs, mesoporous silica containing AuNPs covered by TiO$_2$, bare titanium dioxide and mesoporous silica covered by TiO$_2$) were electrochemically characterised with electrochemical impedance spectroscopy (EIS).

Electrochemical impedance spectroscopy was performed in a three-electrode cell in which the reference electrode was a SCE, the counter electrode a Pt wire and the working electrode was the modified FTO glass. The EIS was performed in NaClO$_4$ 0.1 M using K[Fe(CN)$_6$] 3 mM as probe molecule at +0.25 V.
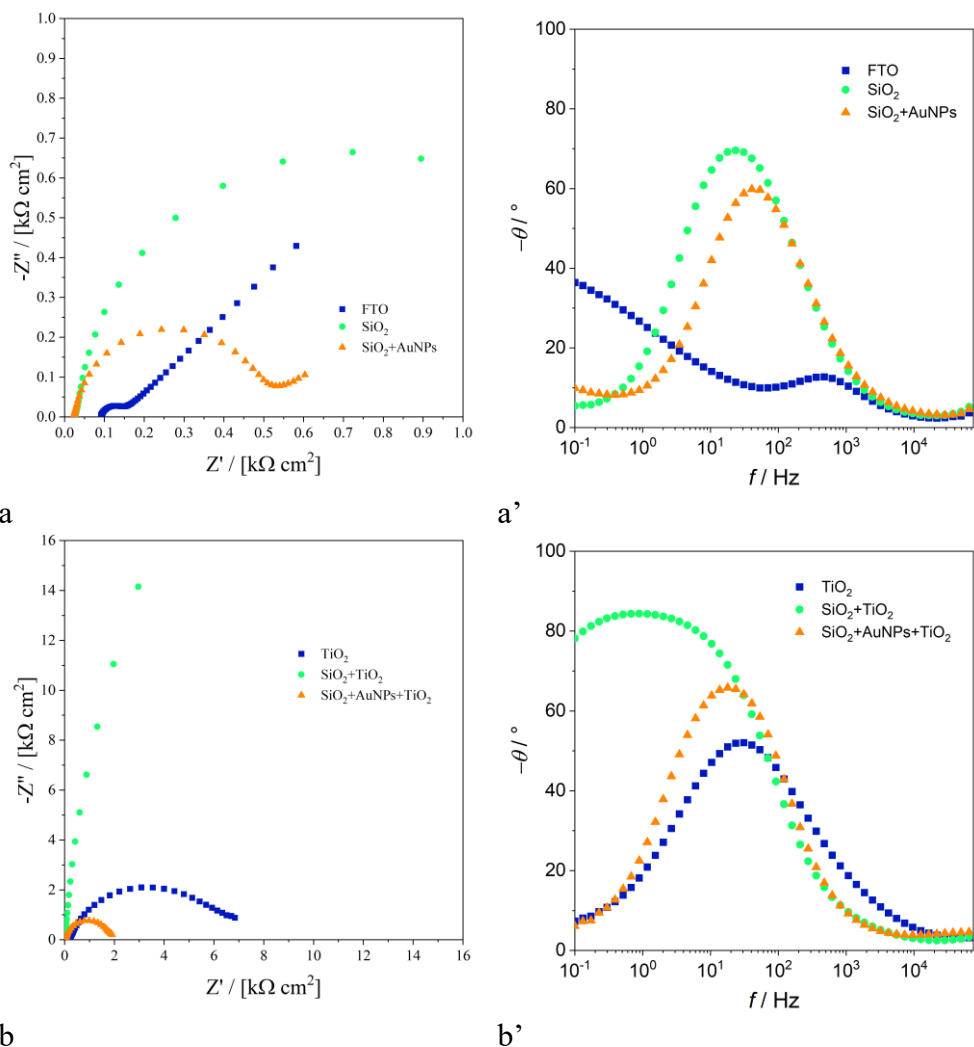
Figure 4.7 - Comparison of different electrodes (a. not containing TiO$_2$, b. containing TiO$_2$) in EIS at +0.25 V using K[Fe(CN)$_6$] 3 mM as probe molecule.

From the superimposition in Figure 4.7, it is possible to see in the Nyquist plot (Figure 7a and b) that the electrodes containing gold nanoparticles are less resistive than the electrodes that do not contain them. This is due to the lower charge transfer resistance associated with AuNPs (since they are conductive). Anyway, the surface is not totally conductive due to the presence of the mesoporous silica and, in some cases, titanium dioxide, which are an insulator and a semiconductor, respectively.

4.2.6. Photocurrent analysis.

Considering the promising results obtained in Chapter 3, it was decided to directly start the photocurrent analysis using the low-power light source, the UV LED. The samples compared were the ones containing the titanium dioxide layer.

For these tests, the electrochemical cell was positioned so that the working electrode (WE) was parallel to the UV LED, at approximately 2 cm.

A platinum wire was used as counter electrode (CE) and a saturated calomel electrode (SCE) was used as reference electrode (RE). These were both located in the cell in a way that would not obstruct the light flux from the LED to the WE. All the photocurrents shown in the following pages have been recorded applying a potential of +0.1 V.
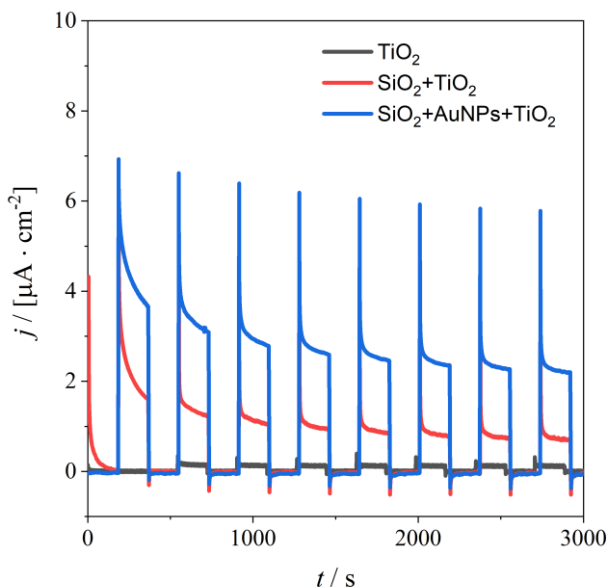

Figure 4.8 – Comparison of the electrodes containing only TiO₂ (black line), SiO₂+TiO₂ (red line) and SiO₂+AuNPs+TiO₂ in transient photocurrent experiments on the background (NaClO₄ 0.1 M) at an applied potential of +0.1 V.

Looking at Figure 4.8, it is clearly visible that the values of current density are higher for the electrode containing mesoporous silica, gold nanoparticles and titanium dioxide, as expected. However, the behaviour of the electrode made of mesoporous silica and titanium dioxide is unexpected: the values of current density are three times higher than the signal related to bare titanium dioxide. This could be led to two different phenomena: firstly, there is a higher active surface due to the combination of the SiO2 with TiO₂, (which are both

mesoporous materials). The second phenomenon is a charge stabilization coming from the interaction between SiO_2 and TiO_2. SiO_2 improves the band structure of TiO_2, [54, 55] prevents diffusion of the photogenerated charge carriers because of its insulating nature, [56] and acts as a shallow donor to capture photogenerated electrons. [55] The synergism between titanium dioxide and mesoporous silica creates a porous structure that improves the interaction of adsorbed protons with photogenerated electrons/holes in the reaction sites. [57] Furthermore, OH anions on the SiO_2 surface reduce the charge re- combination rate because they can react with photoexcited holes, producing •OH that oxidizes adsorbed molecules. [58]

4.3.   Results and discussions.

4.3.1. Determination of ciprofloxacin.

With the fine-tuned method developed for the hybrid electrode (AuNPs/TiO₂) and explained in the previous chapter, ciprofloxacin was determined in the concentration range 1-10 μM.
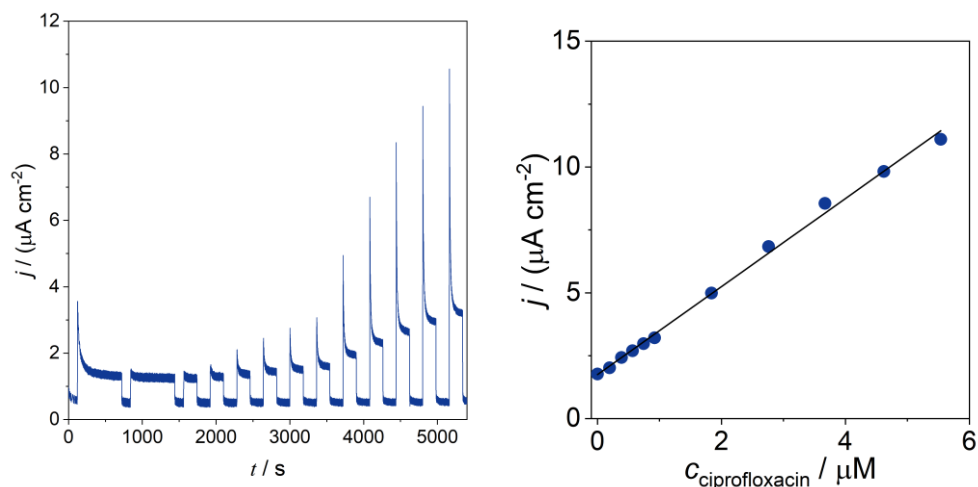

Figure 4.9 – Ciprofloxacin determination with the electrode made of $TiO_2+AuNPs+TiO_2$ in transient photocurrent experiments (on the left) in a concentration range between 1-10 μM in $NaClO_4$ 0.1 M at an applied potential of +0.1 V. On the right, the calibration line.

The calibration line was obtained several times and on different electrodes. The analytical parameters are very good: the sensitivity is (1.75±0.03) (μA cm^{-2} μM^{-1}), the limits of detection and quantification (obtained with S/N=3 and S/N=10, respectively) are (0.38±0.07) μM and (1.15±0.08) μM, respectively.

The precision of the method is very good with a low RSD % (<5%) and the trueness is also excellent, with apparent recovery factors of 99.7 %.

4.3.2. Study of the interferences.

The effect of the most common inorganic and organic interferents in surface waters was also investigated. As for inorganic ions, Na^+, Mg^{2+}, Ca^{2+}, Zn^{2+} and Fe^{3+} were selected. The concentrations of the organic and inorganic interferents are 1 μM, except humic acids, whose concentration is 20 ppm, the average concentration of this class of substances in surface water (while in groundwater the average concentration is around 1-5 ppm).
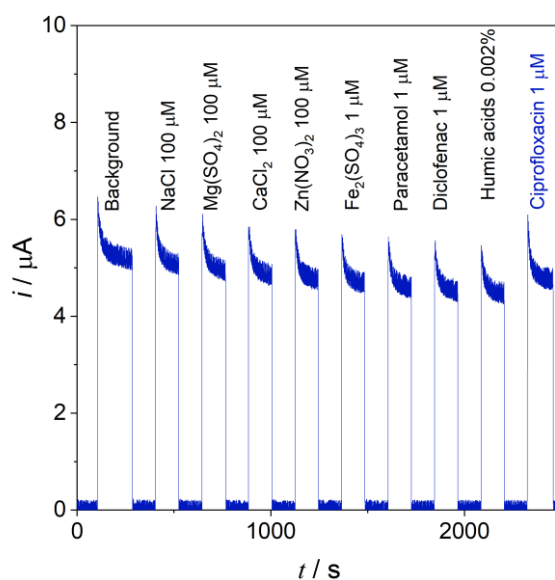

Figure 4.10 – Photocurrent recorded in NaClO₄ 0.1 M: readings of the background, then inorganic ions, paracetamol, diclofenac, and humic acids as described above.

Comparing these results with the ones obtained with the hybrid electrode (Chapter 3, paragraph 3.3.2), it is possible to see that the concentration of humic acids used in this experiment (20 ppm) does not interfere with the determination of ciprofloxacin. This did not happen when using the hybrid electrode without the mesoporous silica, meaning that mesoporous silica helps in excluding big molecules thanks to its size-exclusion effect.

The other substances do not interfere with the determination of ciprofloxacin, as already seen with the hybrid electrode.

4.4.   Conclusions.

During this work, the properties of mesoporous silica were studied. The silica was combined with gold nanoparticles and titanium dioxide to study their effects in the photoelectrochemical determination of ciprofloxacin.

The surface of mesoporous silica was studied with TEM and the presence of AuNPs was confirmed by EDS analysis. Studies of the diffusion mechanism at the electrode were performed with cyclic voltammetry and electrochemical impedance spectroscopy, also to study the charge-exclusion effect of the material.

Photocurrent studies performed on the samples containing titanium dioxide confirmed that the presence of gold nanoparticles is fundamental for the determination of ciprofloxacin and to have a good current density during the analyses. Further studies on the couple SiO_2/TiO_2 are necessary to fully understand the photoelectrochemical behaviour of this couple since the photocurrent signal is higher than the one of bare titanium dioxide.

From the study of the selectivity, mesoporous silica coupled with the heterojunction formed by gold nanoparticles and titanium dioxide provided a better result than the heterojunction alone, because of the size-exclusion effect.

4.5. Bibliography.

[1] W. Li, Q. Yue, Y. Deng and D. Zhao, Ordered Mesoporous Materials Based on Interfacial Assembly and Engineering, *Adv. Mater.* **2013**, 25, 5129–5152.

[2] A. Walcarius, Mesoporous materials and electrochemistry, *Chem. Soc. Rev.* **2013**, 42, 4098–4140.

[3] A. Walcarius, Mesoporous materials-based electrochemical sensors, *Electroanalysis*, **2015**, 27, 1303–1340.

[4] M. Etienne, L. Zhang, N. Vilà and A. Walcarius, Mesoporous Materials-Based Electrochemical Enzymatic Biosensors, *Electroanalysis*, **2015**, 27, 2028–2054.

[5] C. T. Kresge, M. E. Leonowicz, W. J. Roth, J. C. Vartuli and J. S. Beck, Ordered mesoporous molecular sieves synthesized by a liquid-crystal template mechanism, *Nature*, **1992**, 359, 710–712.

[6] J. S. Beck, J. C. Vartuli, W. J. Roth, M. E. Leonowicz, C. T. Kresge, K. D. Schmitt, C. T. W. Chu, D. H. Olson and E. W. Sheppard, A new family of mesoporous molecular sieves prepared with liquid crystal templates, *J. Am. Chem. Soc.*, **1992**, 114, 10834–10843.

[7] Q. H. Yang, J. Liu, L. Zhang and C. Li, Functionalized periodic mesoporous organosilicas for catalysis, *J. Mater. Chem.*, **2009**, 19, 1945–1955.

[8] T. Yokoi, Y. Kubota and T. Tatsumi, Amino-functionalized mesoporous silica as base catalyst and adsorbent, *Appl. Catal. A*, **2012**, 421, 14–37.

[9] B. J. Melde, B. J. Johnson and P. T. Charles, Mesoporous silicate materials in sensing, *Sensors*, **2008**, 8, 5202–5228.

[10] A. Walcarius, Electroanalytical applications of microporous zeolites and mesoporous (organo) silicas: recent trends, *Electroanalysis*, **2008**, 20, 711–738.

[11] C. Ispas, I. Sokolov and S. Andreescu, Enzyme-functionalized mesoporous silica for bioanalytical applications, *Anal. Bioanal. Chem.*, **2009**, 393, 543–554.

[12] M. Hasanzadeh, N. Shadjou, M. de la Guardia, M. Eskandani and P. Sheikhzadeh, Mesoporous silica-based materials for use in biosensors, *TrAC, Trends Anal. Chem.*, **2012**, 33, 117–129.

[13] M. Hasanzadeh, N. Shadjou, M. Eskandani and M. D. L. Guardia, Mesoporous silica-based materials for use in electrochemical enzyme nanobiosensors, *TrAC, Trends Anal. Chem.*, **2012**, 40, 106–118.

[14] M. Hasanzadeh, N. Shadjou, E. Omidinia, M. Eskandani and M. de la Guardia, Mesoporous silica materials for use in electrochemical immunosensing, *TrAC, Trends Anal. Chem.*, **2013**, 45, 93–106.

[15] H. Rao, X. Wang, X. Du and Z. Xue, Mini review: Electroanalytical sensors of mesoporous silica materials, *Anal. Lett.*, **2013**, 46, 2789–2812.

[16] A. Walcarius and L. Mercier, Mesoporous organosilica adsorbents: nanoengineered materials for removal of organic and inorganic pollutants, *J. Mater. Chem.*, **2010**, 20, 4478–4511.

[17] L. Gibson, Mesosilica materials and organic pollutant adsorption: part A removal from air, *Chem. Soc. Rev.*, **2014**, 43, 5163–5172.

[18] L. Gibson, Mesosilica materials and organic pollutant adsorption: part B removal from aqueous solution, *Chem. Soc. Rev.*, **2014**, 43, 5173–5182.

[19] A. Sayari and S. Hamoudi, Periodic mesoporous silica-based organic−inorganic nanocomposite materials, *Chem. Mater.*, **2001**, 13, 3151–3168.

[20] P. Kumar and V. V. Guliants, Periodic mesoporous organic–inorganic hybrid materials: Applications in membrane separations and adsorption, *Microporous Mesoporous Mater.*, **2010**, 132, 1–14.

[21] F. Hoffmann, M. Cornelius, J. Morell, M. Fröba, Silica-based mesoporous organic–inorganic hybrid materials, *Angew. Chem. Int. Ed.* **2006**, 45, 3216–3251.

[22] Y. Wan, D. Zhao, On the controllable soft-templating approach to mesoporous silicates, *Chem. Rev.* **2007**, 107, 2821–2860.

[23] C. Sanchez, L. Rozes, F. Ribot, C. Laberty-Robert, D. Grosso, C. Sassoye, C. Boissière, L. Nicole, "Chimie douce": A land of opportunities for the designed construction of functional inorganic and hybrid organic-inorganic nanomaterials, *C. R. Chim.* **2010**, 13, 3–39.

[24] J. L. Blin, M. Impéror-Clerc, Mechanism of self-assembly in the synthesis of silica mesoporous materials: in situ studies by X-ray and neutron scattering, *Chem. Soc. Rev.* **2013**, 42, 4071–4082.

[25] D. M. Ford, E. E. Simanek, D. F. Shantz, Engineering nanospaces: ordered mesoporous silicas as model substrates for building complex hybrid materials, *Nanotechnology* **2005**, 16, S458–475.

[26] C. Gérardin, J. Reboul, M. Bonne, B. Lebeau, Ecodesign of ordered mesoporous silica materials, *Chem. Soc. Rev.* **2013**, 42, 4217–4255.

[27] M. Linden, S. Schacht, F. Schuth, A. Steel, K. K. Unger, Recent advances in nano-and macroscale control of hexagonal, mesoporous materials, *J. Porous. Mater.* **1998**, 5, 177–193.

[28] Z. A. ALOthman, A review: fundamental aspects of silicate mesoporous materials, *Materials* **2012**, 5, 2874–2902.

[29] V Urbanova, A Walcarius, Vertically-aligned Mesoporous Silica Films, *Z. Anorg. Allg. Chem.* **2014**, 640, (3-4), 537–546.

[30] H. Yang, N. Coombs, I. Sokolov, G. A. Ozin, Free-standing and oriented mesoporous silica films grown at the air–water interface, *Nature* **1996**, 381, 589–592.

[31] S. Schacht, Q. Huo, I. G. Voigt-Martin, G. D. Stucky, F. Schuth, Oil-water interface templating of mesoporous macroscale structures, *Science* **1996**, 273, 768–771.

[32] Y. Lu, R. Ganguli, C. A. Drewien, M. T. Anderson, C. J. Brinker, W. Gong, Y. Guo, H. Soyez, B. Dunn, M. H. Huang, J. I. Zink, *Nature* **1997**, 389, 651–655.

[33] V. R. Koganti, S. E. Rankin, Synthesis of surfactant-templated silica films with orthogonally aligned hexagonal mesophase, *J. Phys. Chem. B* **2005**, 109, 3279–3283.

[34] U. H. Lee, M. H. Kim, Y. U. Kwon, Mesoporous thin films with accessible pores from surfaces, *Bull. Korean Chem. Soc.* **2006**, 27, 808–816.

[35] C. J. Brinker, D. R. Dunphy, Morphological control of surfactant-templated metal oxide films, *Curr. Opin. Colloid Interface Sci.* **2006**, 11, 126–132.

[36] U. H. Lee, M. H. Kim, Y. U. Kwon, Mesoporous thin films with accessible pores from surfaces, *Bull. Korean Chem. Soc.* **2006**, 27, 808–816.

[37] D. Zhao, P. Yang, D. I. Margolese, G. D. Stucky, Synthesis of continuous mesoporous silica thin films with three-dimensional accessible pore structures, *Chem. Commun.* **1998**, 1, 2499–2500.

[38] H. Miyata, S. Kobori, W. Kubo, M. Watanabe, K. Kuroda, Lattice matching in the epitaxial formation of mesostructured silica films, *Langmuir* **2013**, 29, 761–765.

[39] H. Miyata, W. Kubo, A. Sakai, Y. Ishida, T. Noma, M. Watanabe, A. Bendavid, P. J. Martin, Epitaxial-like growth of anisotropic mesostructure on an anisotropic surface of an oblique nanocolumnar structure, *J. Am. Chem. Soc.* **2010**, 132, 9414–9419.

[40] H. Miyata, Epitaxial growth of a surfactant-silica mesostructure on oriented polyimide films, *Microporous Mesoporous Mater.* **2007**, 101, 296–302.

[41] E. K. Richman, T. Brezesinski, S. H. Tolbert, Vertically oriented hexagonal mesoporous films formed through nanometre-scale epitaxy, *Nat. Mater.* **2008**, 7, 712–717.

[42] Y. Guillemin, M. Etienne, E. Sibottier, A. Walcarius, Microscale controlled electrogeneration of patterned mesoporous silica thin films, *Chem. Mater.* **2011**, 23, 5313–5322.

[43] A. Walcarius, E. Sibottier, M. Etienne, J. Ghanbaja, Electrochemically assisted self-assembly of mesoporous silica thin films, *Nat. Mater.* **2007**, 6, 602–608

[44] A. Goux, M. Etienne, E. Aubert, C. Lecomte, J. Ghanbaja, A. Walcarius, Oriented mesoporous silica films obtained by electro-assisted self-assembly (EASA), *Chem. Mater.* **2009**, 21, 731–741.

[45] M. Etienne, A. Goux, E. Sibottier, A. Walcarius, Oriented mesoporous organosilica films on electrode: a new class of nanomaterials for sensing, *J. Nanosci. Nanotechnol.* **2009**, 9, 2398-2406

[46] L. Ding, W. Li, Q. Sun, Y. He, Prof. B. Su, Gold nanoparticles confined in vertically aligned silica nanochannels and their electrocatalytic activity toward ascorbic acid, *Chem. Eur. J.* **2014**, 20, 12777 – 12780

[47] Fedorchuk, A.; Walcarius, A.; Laskowska, M.; Vila, N.; Kowalczyk, P.; Cpałka, K.; Laskowski, Ł., Synthesis of Vertically Aligned Porous Silica Thin Films Functionalized by Silver Ions, *Int. J. Mol. Sci.* **2021**, 22, 7505.

[48] Lei, J.; Kang, J.; Liu, J.; Wang, G. A Novel Electrochemical Sensing Strategy Based on Poly (3,4-ethylenedioxythiophene): Polystyrene Sulfonate, AuNPs, and Ag^+ for Highly Sensitive Detection of Alkaline Phosphatase, *Nanomaterials* **2022**, 12, 3392.

[49] S.L.Burk ett, S.D.Sims, and S.Mann, Synthesis of hybrid inorganic–organic mesoporous silica by co-condensation of siloxane and organosiloxane precursors, *Chem. Commun.* **1996**, 1367.

[50] D.J.Macquarrie, Direct preparation of organically modified MCM-type materials. Preparation and characterisation of arninopropyl-MCM and 2-cyanoethyl-MCM, *Chem. Commun.* **1996**, 1961.

[51] A.Walcarius and C.Delacôte, Rate of Access to the Binding Sites in Organically Modified Silicates. 3. Effect of Structure and Density of Functional Groups in Mesoporous Solids Obtained by the Co-Condensation Route, *Chem. Mater.* **2003**, 15, 4181.

[52] F. Cagnol, D. Grosso, and C. Sanchez, A general one-pot process leading to highly functionalised ordered mesoporous silica films, *Chem. Commun.* **2004**, 15, 1742.

[53] Deomila Basnig, Neus Vilá, Grégoire Herzog, Alain Walcarius, Voltammetric behaviour of cationic redox probes at mesoporous silica film electrodes, *Journal of Electroanalytical Chemistry* **2020**, 872, 113993.

[54] E. Hussain, I. Majeed, M.A. Nadeem, A. Iqbal, Y. Chen, M. Choucair, R. Jin, and M.A. Nadeem, Remarkable effect of BaO on photocatalytic H_2 evolution from water splitting via TiO_2 (P25) supported palladium nanoparticles, *J. Environ.Chem. Eng.*, **2019**, 7, 102729.

[55] W.H. Saputera, J. Rizkiana, W. Wulandari, and D. Sasongko, Role of defects on TiO_2/SiO_2 composites for boosting photocatalytic water splitting, *RSC Adv.*, **2020**, 10, 27713–27719.

[56] Y. Gong, D.P. Wang, R. Wu, S. Gazi, H.S. Soo, T. Sritharan, and Z. Chen, New insights into the photocatalytic activity of 3-D core-shell P25@silica nanocomposites: impact of mesoporous coating, *Dalton Trans.*, **2017**, 46, 4994–5002.

[57] W. Chen, M. Liu, X. Li, and L. Mao, Synthesis of 3D mesoporous g-C_3N_4 for efficient overall water splitting under a Z-scheme photocatalytic system, *Appl. Surf. Sci.*, **2020**, 512, 145782.

[58] L. Dubnová, M. Zvolská, M. Edelmannová, L. Mat ˇejová, M. Reli, H. Drobná, P. Kustrowski, K. Kocí, and L. Capek, Photocatalytic decomposition of methanol-water solution over N-La/TiO$_2$ photocatalysts, *Appl. Surf. Sci.*, **2019**, 469, 879–886.

5. Microelectrodes.

5.1. Introduction.

5.1.1. Dopamine.

Dopamine (DA), which belongs to the catecholamine family of neurotransmitters, is crucially important in humans. It is produced in adrenal glands and distinct areas of the brain (e.g., hypothalamus) and is the most abundant catecholamines involved in brain-body integration [1].

Dopamine is formed by the enzymatic decarboxylation of L-DOPA and it is used as precursor in the synthesis of the neurotransmitter's noradrenaline and adrenaline [2] (Figure 5.1). In more detail, DA molecule contains two phenolic hydroxyl groups which can be easily oxidized to dopamine-o-quinone, in other words, they have intense electrochemical activity.
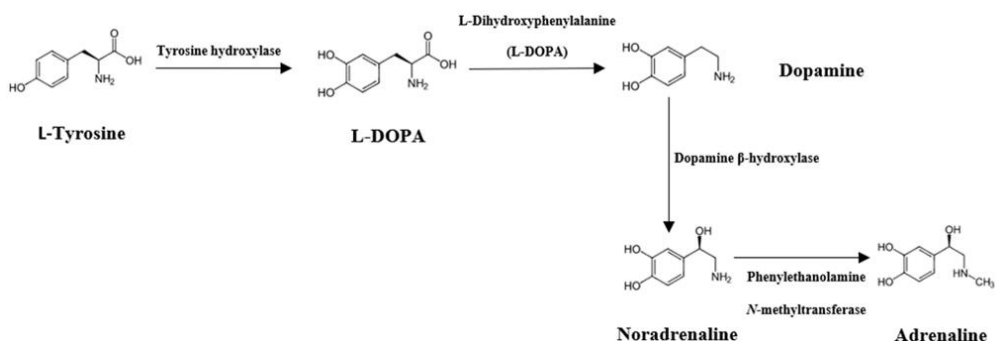

Figure 5.14 - Sequence of enzymatic reactions generating catecholamines from L-Tyrosine.

As a major and powerful neuromodulator, it affects neuronal plasticity, as well as many brain functions. Nevertheless, its function is not restricted to that: it regulates and organizes stress responses, consciousness, information flow and attention span, learning, the sleep-wake cycle, motivation, motions, and memory formation. For a healthy individual, the concentration of DA in the extracellular fluid is in the range of 0.01-1 μM [1]. Extreme abnormalities of DA levels produced in the central nervous system is linked to neurological and physiological illness. An indicator of high DA levels is cardiotoxicity, which in turn leads to rapid heart rate, hypertension as well as heart failure. By contrast, a low concentration of DA may result in some mental and physical diseases such as Parkinson's disease, schizophrenia, Alzheimer's disease and

depression [3]. Consequently, precise, and periodic diagnosis of DA in physiological fluid is recognized as important for therapeutic implications.

Dopamine itself is available as a manufactured drug for intravenous injection. It is most commonly used as a stimulant drug in the treatment of severe low blood pressure, slow heart rate, and cardiac arrest, especially in new-born infants [4].

The development of highly sensitive and selective sensors able to detect trace amount of DA in our environment and various biological fluids is very important in clinical diagnosis, monitoring treatment efficacy, disease prevention, and environmental protection, since this molecule is considered an emerging contaminant.

Many analytical approaches have been developed and employed for the determination of dopamine, among which the most-used techniques in clinical laboratories are High Performance Liquid Chromatography (HPLC), fluorescence spectrometry, capillary electrophoresis, UV-vis spectrophotometry, calorimetry, and mass spectrometry. These techniques are extremely sensitive; however, they require complex and expensive equipment, complicated pre-treatment, considerable time, skilful operators, and large volume of solvents and chemicals that possibly cause themself environmental pollution [1].

Compared with the techniques reported above, electrochemical sensors are more suitable technologies to detect neurotransmitters owing to their simple instrument operation, low cost, fast responses, linear output, low power consumption, high resolution, high repeatability, and high accuracy [5]. In addition, electrochemical techniques are based on the electrical signals generated by the Faradaic process, which makes them the best suited for the detection of DA since it is an electroactive compound that can be easily oxidized [1]; more specifically the $2e^-/2H^+$ redox reaction of dopamine under physiological conditions constitutes the basis of electroanalytical detection and currents generated may be linearly dependent on the concentration of the electroactive molecules, enabling quantification of these compounds [2].

The main limitation is the relatively large oxidation potential of direct oxidative detection on the electrode and formation of phenoxy radicals with subsequent coupling and formation of passivating polymeric film on the electrode [2]. This insulating film on the electrode surface compromises the long-term stability of the sensors. In detail, the reaction pathway of DA fouling is outlined in Figure 5.2 [6].
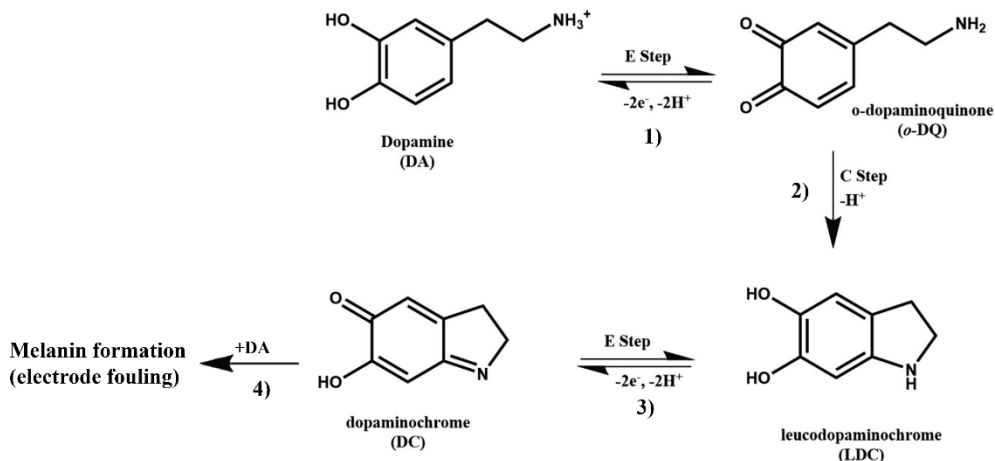
Figure 5.15 - Dopamine fouling mechanism: (1) The electrochemical oxidation of DA proceeds via a two-electron transfer forming the o-dopaminoquinone (o-DQ); (2) o-DQ undergoes an intramolecular addition when the amine is protonated, resulting in a cyclization leading leucodopaminochrome (LCD); (3) LCD undergoes a two-electron oxidation to form dopaminochrome (DC); (4) DC may polymerize to melanin on the electrode by a free radical polymerization, significantly inhibiting the surface dependent redox chemistry of DA (taken from [6]).

Another big problem that must be solved in the electrochemical detection of dopamine is the co-existence of several interfering biomolecules, such as ascorbic acid (AA), epinephrine (EP), and uric acid (UA), due to the closeness of the oxidation potentials of these compounds that results in difficulties in distinguishing the individual peak potentials [1].

In recent years, copious attempts have been made to develop devices able to overcome these limitations. Various electrode materials have been tested, including metal and carbon-based nanomaterials electrodes, modified electrodes with enzymes (biosensors), self-assembled monolayers, nanotubes, nanowires, nanoparticles, and conducting polymers films [2].

5.1.2. A new frontier in electroanalytical detection: microelectrodes.

The working electrode of an electrochemical sensor can generally be a conventional electrode or a microelectrode according to the size of the electrode. Because of the large size, traditional electrodes have some disadvantages: for example, they cannot be applied for the *in vivo* detection of substances. In fact, their sensitivity for the detection of the target analyte is

low, or it can easily change and destroy the test object and so on. But microelectrodes can effectively avoid those abovementioned downsides because of their size superiority [6]. In other words, microelectrodes are an innovative and promising force in bioanalysis and analytical chemistry, namely due to the appropriate geometric size to biological sample or natural environments. They provide the appropriate spatial resolution and they can be inserted into varying environments. Therefore, due to their microscale volumes and fast response times, microelectrodes have been applied in high performance biosensors and sensors for detecting secretory elements such as dopamine (DA).

Microelectrodes are miniaturized working electrodes with micrometre dimensions that can be made with metallic or non-metallic conductor [8], such as carbon fiber, platinum, gold, or silver ultrathin wires. In addition, over the years, different microelectrodes and microelectrodes arrays have been designed and fabricated in various geometries, which are outlined in Figure 5.3.
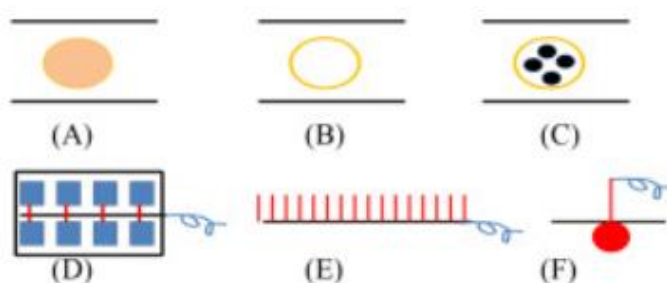

Figure 5.16 - Microelectrode types: (A) microdisk, (B) microring, (C) microring array, (D) lithographically produced microarrays, (E) microfiber array, and (F) microspheres (from Analytical Techniques in Biosciences, cap 10).

As early as the 1960s, microelectrodes were found to have extremely excellent and interesting electrochemical characteristics. In detail, three key electrochemical properties are significantly affected by the size of the electrode: (1) the mass transport regime; (2) the charging of the double layer and (3) the ohmic drop in solution.

5.1.2.1.   Mass transport regime.

Diffusion to a microelectrode differs substantially from that to a macroelectrode, including mm-size electrodes. For a simple fast electron transfer process, the application of a potential step from a value where no

current flows to one where the reaction is diffusion controlled produces different diffusion regimes.

At short times, the diffusion layer thickness δ ($\delta = \sqrt{\pi D t}$ is very thin relative to the electrode ($\delta \ll r_e$). Diffusion to and from the electrode is linear (irrespective of the electrode geometry) and the microelectrode behaves like a conventional electrode (clear peak in the voltammogram).

$$j = \frac{c^* \sqrt{D}}{\sqrt{\pi t}}$$

$$I = \frac{nFA\sqrt{Dc^2}}{\sqrt{\pi t}}$$

Eq. 5.1 *Eq. 5.2*

As time increases, the diffusion layer thickness δ becomes comparable, and then larger than the dimension of the electrode ($\delta \gg r_e$). The diffusion regime evolves from planar to spherical or convergent and yields a steady-state rate of mass transport to the electrodes (steady-state voltammograms).

$$j = D\frac{c^*}{r_e}$$

$$I = 4\pi r_e DFc^*$$

Eq. 5.3 *Eq. 5.4*

So, in contrast to the constant planar diffusion regime observed with large electrodes, a microelectrode shifts from linear to spherical diffusion [9] (Figures 5.4 and 5.5).
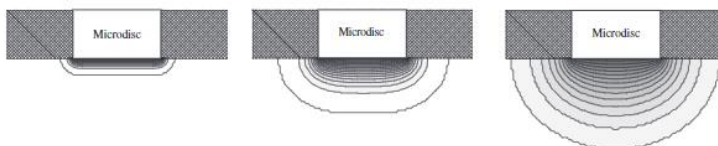

Figure 5.17 - Diffusion regimes following a potential step to a microdisc electrode. From left to right: planar diffusion at short times, transition from planar to quasi-hemispherical, and then hemispherical diffusion at long times (taken from [3]).
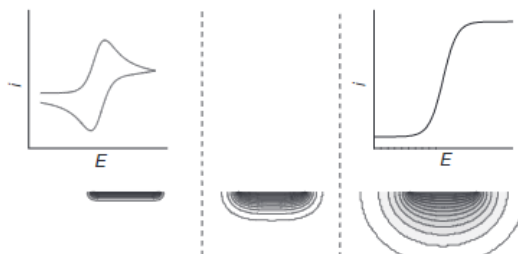

Figure 5.18 - From linear diffusion (clear peak --> I_p) to radial diffusion (steady state s --> I_{lim}) (taken from [3]).

5.1.2.2.   Double layer charging.

Because microelectrodes have a very small electroactive area, the time required to charge or discharge the double layer is very short. Hence, a great property of microelectrodes is to significantly improve the discrimination against charging current. Reliable recordings of the faradic current can be made at times shorter than those with a conventional electrode and this has opened the application of voltametric and chronoamperometric experiments to the sub-millisecond timescale [3].

5.1.2.3.   Ohmic drop.

The faradaic current flowing to microelectrodes typically ranges from a few pA to a few nA, because of their small size. On the other hand, the resistive drop is small because most of it occurs very close to the microelectrode. This is in contrast with larger electrodes, where the resistive drop continually increases with distance between the working electrode and the reference electrode. Taking these two effects into consideration, the ohmic drop due to the flow of the current in the solution is much reduced and the distortion of voltametric curves becomes negligible. Due to these properties, voltametric studies could be carried out in poorly conducting media, such as organic solvents, and even in the absence of supporting electrolyte [3].

Overall, microelectrodes offer various advantages such as high steady-state current density, high mass transfer rate, negligible ohmic drop [2], high signal-to-noise ratio, decreased double layer charging distortion, and small time constant [1].

5.1.3. Aim of this work.

The present work is focused on the characterisation and usage of photo-renewable microelectrodes based on Au and Pt, capable of restoring their initial status after UV irradiation exploiting TiO_2 photocatalytic properties.

These devices, which have been developed and optimized by professors A. Minguzzi and A. Vertova of the Applied Electrochemistry (Ap.E.) group at University of Milano, have been employed for the electroanalytical detection of dopamine. The oxidation products of dopamine form a polymeric film on the micro-disc and lead to microelectrode fouling and passivation. Thus, it has been studied the repeatability and reproducibility of the already tested cleaning

procedure (UV light irradiation of TiO_2 layer) and it has been analysed the detection of dopamine at different concentrations, to reach the lowest quantity of dopamine that can be distinguished from the blank value. Moreover, the superiority of Au microelectrode has been assessed through a comparison with the properties and performances of Pt microelectrode in the same experimental conditions. In addition, photocurrent studies have been performed to investigate the properties of TiO_2 sol subsequently at its calcination at 250 °C for 2 minutes and the capability of the device to detect dopamine after its UV activation.

5.2. Materials and methods.

In this chapter, the solutions, materials, and experimental techniques used to synthesize and characterize microelectrodes will be analysed. To allow repeatability and reproducibility, experimental details of the setups and methods used during the thesis will be reported and deeply illustrated.

The reagents used, with repetitive use, their CAS number and brand are reported in Table 5.1; Table 5.2 reports the tools and materials used.

Table 5.1 - description of all reagents used in this work.

Name	Use	CAS number	Brand
Titanium(IV) isopropoxide	Titania synthesis	546-68-9	Sigma-Aldrich
Hydrocloric acid 37%	Titania synthesis	7647-01-0	Sigma-Aldrich
LUTENSOL ON70	Titania synthesis	-	-
Ethanol absolute ≥ 99.8%	Titania synthesis, electrode assembly	64-17-5	Sigma-Aldrich
Hexaaminoruthenium (III) chloride	Probe molecule	14282-91-8	Sigma-Aldrich
Dopamine hydrochloride	Analyte	62-31-7	Sigma-Aldrich
Sodium phosphate dibasic	Electrolyte preparation (PBS)	7558-79-4	Sigma-Aldrich
Potassium phosphate monobasic	Electrolyte preparation (PBS)	7778-77-0	Fluka
Au and Pt wires	Electrode assembly	-	Good Fellow
Copper wire 0.05 cm	Electrode assembly	-	Sigma-Aldrich
Epofix resin	Electrode assembly	-	Struers
Epofix hardener	Electrode assembly	-	Struers

PTFE tubes	Electrode assembly	-	Sigma-Aldrich
Leit-C	Electrode assembly	-	Sigma-Aldrich

Table 5.2 - description of the materials and tools used.

Name	Brand
Forcipol machine	Struers
Waterproof silicon carbide paper (4000)	Struers
Polishing alumina 0.05 pm	Struers
Potentiostat Galvanostat [PGSTAT30]	MetrOhm
Micropipettes	Gilson
N_2 [air liquid 6.0]	Alphagz 2.0a
Analytical scale [crystal 100 cal]	Gibertini
pHmeter [model 338]	AMEL instruments
UV lamp [HG 500]	Jelosil

5.2.1. Preparation of solutions.

PBS (Phosphate-Buffered Saline 0.1 M, pH 7.4) has been prepared by weighing 2.7062 g of Na_2HPO_4 and 0.5861 g of KH_2PO_4 were weighed on the analytical balance and transferred quantitatively into the 0.5 dm^3 volumetric flask; subsequently, made up to volume with milliQ water. The solution has been stored in the refrigerator.

$[Ru(NH_3)_6]Cl_3$ 0.2 M: to prepare the solution of the hexaaminoruthenium (III) chloride probe, 0.6192 g of $[Ru(NH_3)_6]Cl_3$ were weighed on an analytical balance and transferred quantitatively into a 10 cm^3 volumetric flask; then made up to volume with milliQ water. After stirring the solution, the volumetric flask has been stored in the refrigerator. The probe solution was used to characterize the microelectrodes, to determine the experimental radius.

Dopamine 0.2 M: to prepare the dopamine hydrochloride solution, 0.0379 g were weighed on the analytical balance and transferred quantitatively into a small vial; then, made up to volume with 1 cm^3 of milliQ water. After shaking, the solution is ready to use (the same procedure was used to prepare dopamine solution characterized by lower concentration).

5.2.2. Synthesis of the TiO₂ sol.

The sol was synthesized following the procedure described in Chapter 2, paragraph 2.2.2.

The titania sol was stored in 3 labelled bottles and placed in a desiccator. In detail, this procedure was employed to minimize the sol contact with the moisture, because, if adsorbed, it could lead to destabilization of the suspension and to the formation of crystals characterized by different sizes and shapes. For the same reason, it is always necessary to work with clean and dry glassware.

5.2.3. Microelectrode preparation.

Another university research group patented [11] a method to assemble microelectrodes easier to handle than those made of glass. The manufacture of disk microelectrodes started with the creation of an electric contact between metal micro-wire and copper wire, using leit-C. To obtain its hardening, the leit-C was dried in oven for 10 minutes at 70 °C. Subsequently, the electric contact was insulated by inserting it in the bigger PTFE with the smaller one. The epoxy mixture was injected inside the tube, employing a syringe. More specifically, epoxy mixture has been prepared by mixing epofix resin and epofix hardener at 25:3 respectively and the solution has been blending in a clockwise sense for 1 minute, to eliminate bubbles that could lead to non-insulated electrical contact. Finally, the epoxy mixture was dried in oven for 30 minutes at 90 °C, then, after cooling, microelectrode was removed from the PTFE casing. Figure 5.6 illustrates the previous steps.
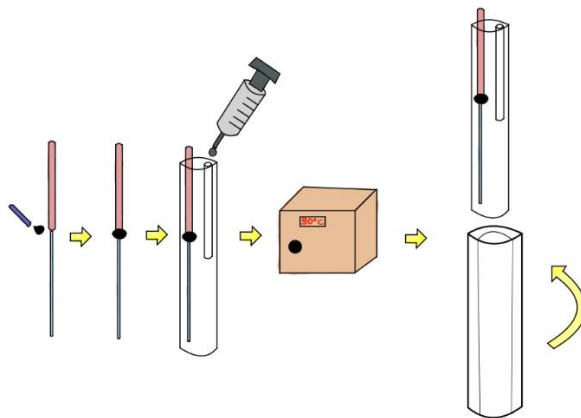

Figure 5.6 - Schematic representation of the device preparation.

The disk exposure was performed by cutting and levelling the microelectrode tip, using Forcipol machine provided with silicon carbide paper. Moreover, the micro-disk was polished on cloth with alumina 0.05 pm. Before each electrochemical characterization, the status of the microelectrode disk was checked with monocular optical microscope with three objective lenses (4X, 10X and 40X), see Figure 5.7.

Figure 5.7 - Au disk (on the left) and Pt disk (on the right) at optical microscope.

The final device was assembled following the previous reported patented procedure and the resulting micro-disk was functionalized through dip-coating in TiO_2 sol. In detail, a sort of calcination was carried out using a heating plate set at 250 °C by approaching microelectrode tip to the plate for 2 minutes, if the moisture was high, or at a major distance, heat (350 °C) and time (4 minutes) if humidity was low (Figure 5.8).
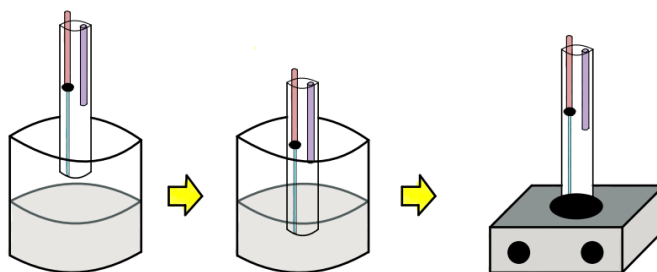

Figure 5.8 - Preparation of disk microelectrode coated with TiO_2 layer.

5.2.4. Characterisation of the microelectrode.

Microelectrode characterization has been performed in a small electrochemical cell provided with a reference electrode (RE) Ag/AgCl/KCl 1 M, platinum wire as counter electrode (CE) and Au or Pt disk microelectrode as working electrode (WE). The electroactive probe molecule used is hexaaminoruthenium (III) chloride, $[Ru(NH_3)_6]Cl_3$ 98 % purchased from Sigma-Aldrich, and it has been dissolved in 10 cm3 of PBS 0.1 M pH=7.4. In addition, the entire set-up was sparged with nitrogen to avoid the influence of

oxygen, proved by another research group, on the values of steady state current registered during cyclic voltammetry (CV) (Figure 5.9).
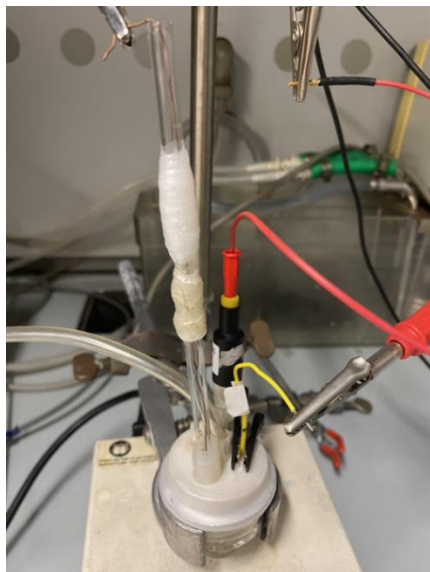

Figure 5.9 - Electrochemical setup.

As for each type of microelectrode, the first experimental step is always the disk microelectrode characterization. In detail, the scope of these experiments was based on the determination of the experimental radius of the metal micro-disk, using the following equation: $I_{SS} = 4nFDrc_{bulk}$, where:

- I_{SS} / nA is the steady state current;
- n / 1 mol_{e-} mol^{-1} is the number of exchanged electrons;
- F = 96485 C mol_{e-}^{-1} is the Faraday constant;
- $D = 5.1 \cdot 10^{-6}$ cm^2 s^{-1} is the diffusion constant;
- r / μm is the radius of the metal micro-disk;
- $c_{bulk} = 1$ mM is the concentration.

5.2.4.1. Electrochemical characterisation of the disk microelectrode without the TiO₂ layer.

Before registering each cyclic voltammetry in the presence of the electroactive probe molecule, the solution (10 cm^3 of PBS 0.1 M at pH 7.4) has always been sparged with nitrogen for 20 minutes to remove oxygen and then it is left under nitrogen atmosphere. Then, the cyclic voltammetries have been performed in PBS before and after the addition of 50 mm^3 of the probe molecule by applying

a negative potential scan from 0.1 V to -0.4 V (vs Ag/AgCl/KCl 1 M) with a scan rate of 10 mVs^{-1} (step 0.008 V) and, in detail, three or five cycles have been recorded for each voltammogram (Figure 5.10 A and B).

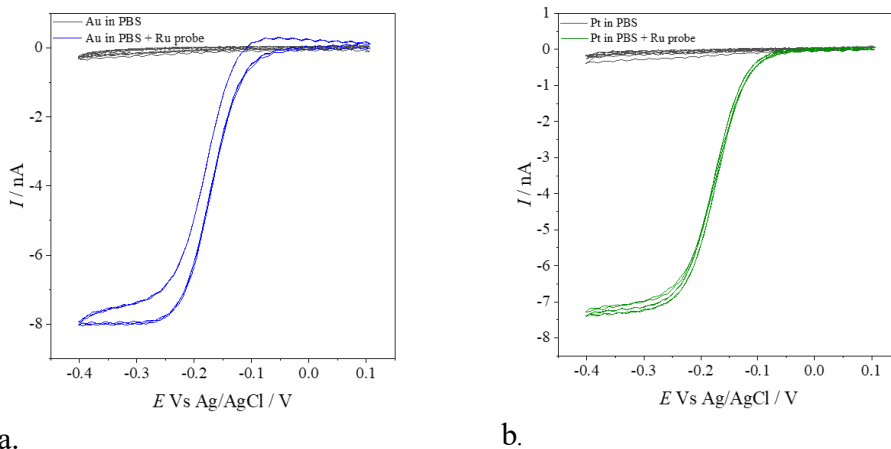a.   b.

Figure 5.10 – a. CV Au in PBS + CV Au in PBS and Ru probe (after degassing with nitrogen); b. - CV Pt in PBS + CV Pt in PBS and Ru probe (after degassing with nitrogen).

It is important to notice that the experimental radii are slightly different from the nominal one, because the experimental results obtained could be affected by systematic or gross errors, especially connected to the solution preparation and the temperature that affects diffusion coefficient of the probe molecule:

Table 5.3 - Experimental radii of disk microelectrodes.

Microelectrode	$r_{nominal}$ / μm	I_{ss} / nA	$R_{experimental}$ / μm
Au	(25 ± 2.5)	6.05	31
Pt	(25 ± 2.5)	7.0	34

5.2.4.2.   Electrochemical   characterisation   of   the   disk microelectrode with the TiO₂ layer.

Cyclic voltammetry, following the previous procedure, has been also used for the characterization of disk microelectrode coated with TiO₂ layer (a new dip-coating is required at the beginning of each new test). More specifically, the aim of this characterization was to make certain that, after dip-coating

procedure and calcination which have been checked with optical microscope (Figures 5.11 and 5.12), the electroactive molecules (dopamine) were able to diffuse through the TiO_2 layer to arrive at the micro-disk surface. In detail, it was expected a decrease of the current in comparison to the value obtained with the metal disk exposed, due to the variation of analyte diffusion regime after the coating procedure (Figures 5.13 A and B and 11).

Figure 5.11 - Cross section of Au disk microelectrode before (left) and after (right) dip-coating in TiO_2 sol.
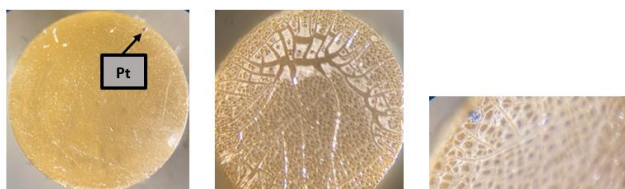
Figure 5.12 - Cross section of Au disk microelectrode before (left) and after (right) dip-coating in TiO_2 sol.
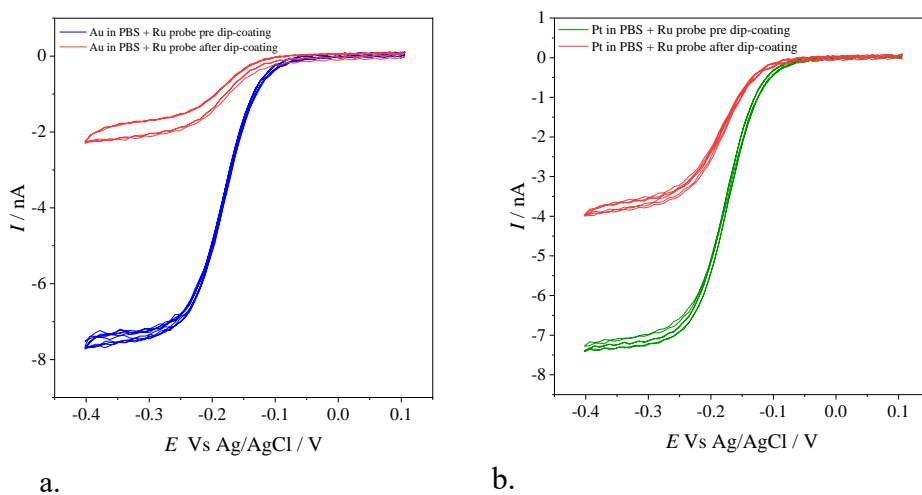

a.   b.

Figure 5.13 - a. Comparison of CVs of Au disk microelectrode polarizing at 10 mVs⁻¹ in PBS + Ru probe before (blue) and after (red) dip-coating; b. Comparison of CVs of Pt disk microelectrode polarizing at 10 mVs⁻¹ in PBS + Ru probe before (green) and after (red) dip-coating.

Analysing the analytical data reported in Figure 5.13 A and B, the blue and green CV correspond to the metal disk exposed and the red one is related to the coated metal disk employing TiO_2 sol. Hence, the observed cathodic current drop caused by the presence of the TiO_2 layer is desirable because it indicates a higher coating degree and a close contact between TiO_2 layer and metal micro-disk.

Moreover, in previous studies, different Au disk microelectrodes coated with TiO_2 layer has been developed and tested with different days from TiO_2 sol synthesis. In detail, after 12 days from TiO_2 sol synthesis the best results have been obtained, in terms of current decrease and coating (amount of TiO_2 in close contact with the micro-disk).

Once the microelectrode coating has been qualitative and quantitative checked, the device was ready to be used in the electroanalytical detection of dopamine.

5.2.5. Disk microelectrode electrochemical fouling procedure.

After the CV characterization and the qualitative evaluation of dopamine oxidation potential (performed in previous experiments), microelectrodes have been widely used for the electroanalytical detection of dopamine. It has been determined that dopamine hydrochloride sensing led to quickly deactivation of the device because, as reported and explained in the introduction part, an insulating polymer film always forms on the disk micro-sensor. In more detail, the purpose of these tests was to achieve the gradual device signal loss to examine, during the cleaning procedure, the photo-renewable properties of TiO_2 layer under UV irradiation.

Sensor deactivation has been performed exploiting the chronoamperometry approach, in which, at a constant potential, Faradaic current is measured versus time (j vs t).

For the electrochemical measurement, chronoamperometry has been performed in the same cell showed before (Figure 5.9).

First, a fresh stock solution of dopamine 0.2 M has been prepared (it was necessary to prepare a new one every day) and the entire setup (10 cm^3 of PBS 0.1 M at pH 7.4) was always sparged with nitrogen for 20 minutes and after left under nitrogen atmosphere.

In case of Au microelectrode coated with TiO_2, fouling procedure has been performed in the concentration range 0.1-1 mM (higher ranges were already analysed in previous studies), polarizing the sensor at +0.45 V (vs Ag/AgCl/KCl 1M) and, so, anodic current due to dopamine two electron transfer oxidation was monitored overtime. Under constant stirring to favour dopamine diffusion towards disk microelectrode surface, the baseline was stabilized for 100 s and then, every 100 s, 5 mm^3 of fresh dopamine stock solution were added up to 1 mM. The same experimental conditions have been used for the fouling procedure of Pt microelectrode coated with TiO_2.

Carrying out fouling at low concentration window, it was difficult, especially for Au microsensor, to observe microelectrode signal deactivation (current drop) as in case of higher ranges, so at least two (Pt) and three (Au) chronoamperometries have been registered to achieve the desirable results (after each chronoamperometry the device was washed with milliQ water).

Moreover, after the last chronoamperometry and before the cleaning test, it was important to check the presence of TiO_2 coating at the optical microscope (Figure 5.14) and by CV characterization, after degassing for 20 minutes the solution (10 cm^3 of PBS 0.1 M at pH 7.4) and adding 50 mm^3 of the Ru probe molecule. (Figure 5.15 A and B).
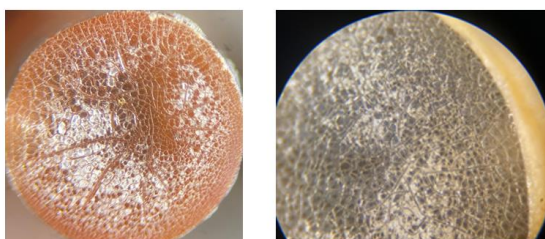

Figure 5.14 - Cross section of Au (left) and Pt (right) disk microelectrodes after fouling test with dopamine.
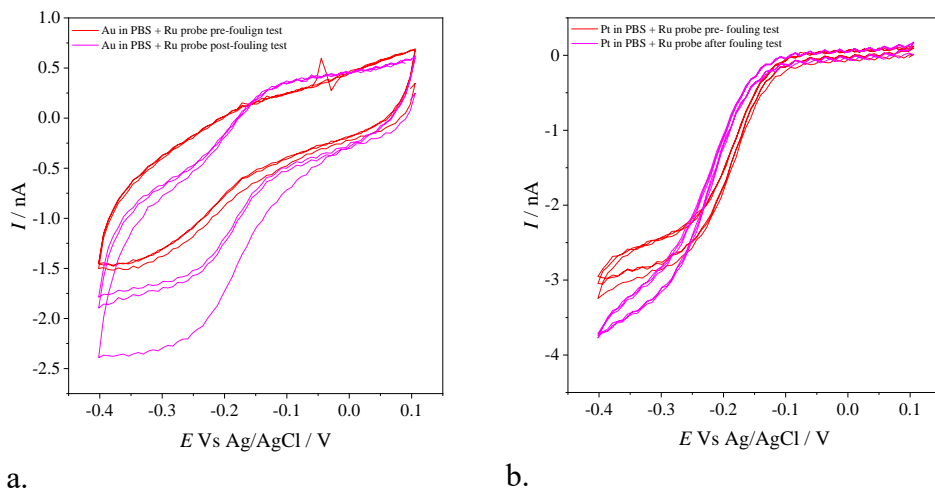
Figure 5.15 – a. Comparison of CVs Au microelectrode coated with TiO$_2$ layer in PBS + Ru probe before (red) and after (pink) fouling test; b. Comparison of CVs Pt microelectrode coated with TiO$_2$ layer in PBS + Ru probe before (red) and after (pink) fouling test.

Thus, analysing the comparison of CVs reported in Figures 5.15 A and B, it is possible to observe a slightly decrease of TiO$_2$ coating degree and an increase of cathodic current related to a higher disk microelectrode exposure in solution.

Even if the cathodic current increases of a value less than 1 nA respect to the one reached after dip-coating, the metal-disk was still coated, and this demonstrates that the reaction involved for the Ru probe molecule occur as outer sphere reaction (surface insensitive and no chemical or catalytic interactions). Then, it was possible to irradiate with UV lamp, in order to study the photocatalytic properties of TiO$_2$.

5.2.6. Disk microelectrode cleaning procedure.

As mentioned in the introduction section, TiO$_2$ has the capability to impart photo-renewable properties at the interface. In more detail, in these experiments it has been tested the behaviour of TiO$_2$ layer under UV light irradiation of a 500 W UV lamp.

After assessing the coating degree of disk microelectrode by cyclic voltammetry, disk microelectrodes coated with titanium dioxide layer were cleaned by merging them in PBS 0.1 M at pH 7.4 for a specific time (depending on the type of metal microsensor used) and at 15 cm, under UV irradiation (Figure 5.16).
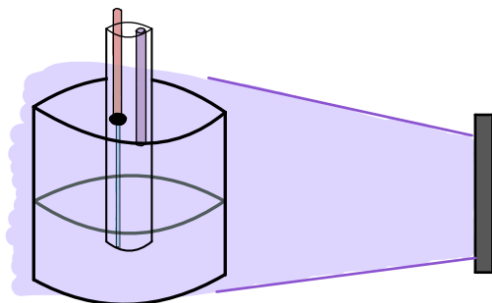
Figure 5.16 - Schematic drawing of the cleaning procedure.

Then, the cleaning degree has been checked exploiting chronoamperometry in the same concentration range (0.1-1 mM) in which device deactivation took place and employing the same experimental parameters and setup used in fouling procedure (cleaning procedure has been performed in the same day of calcination and fouling). In detail, it was expected an increase of the anodic current (*j* vs *t*) related to the dopamine oxidation.

5.2.7. Determination of the limits of detections (LODs).

Beyond the development of fouling and cleaning procedures, another main goal of this thesis is the evaluation of the detection limits, defined as the lowest quantity of the target analyte, in this case dopamine, which can be distinguished from the blank value. More specifically, LODs determination is a key parameter to adequately validate a new electroanalytical microsensor.

Hence, exploiting the same experimental condition and the electrochemical cell and electrodes employed in the previous studies, chronoamperometry technique was performed at different concentration windows.

In particular, the equation exploited for the evaluation of the detection limit is:

$$LOD = \left(\frac{\sigma_{blank}}{S}\right) \cdot 3.29$$

where:

σ_{blank} = Root-MSE (SP)

S = slope of the calibration line

Uncertainty over the LOD can be calculated using:

$$error_{LOD} = \left|\left(\frac{\sigma_{blank}}{S}\right) \cdot error\ S \cdot 3.29\right|$$

196

5.2.8. Transient photocurrent characterisation of gold microelectrode coated with titanium dioxide.

This study was performed to understand which one of the two main photo-active crystalline phases of TiO_2 (rutile (tetragonal system) or anatase (tetragonal)) is formed after pseudo-calcination at 250 °C for 2 minutes (a traditional calcination procedure is carried out for 1 hour at 400 °C with a nitrogen flow of 200 cm^3 min^{-1}), in order to exploit also the transient photocurrent as a technique to conduct electroanalytical determination and quantification of electroactive molecules and biomolecules.

In detail, in a transient photocurrent analysis, the current that flow between working electrode (WE) and counter electrode (CE) is measured when the electrochemical setup is irradiated with UV lamp or UV LED. These experiments are performed in two different conditions: "light on" and "light off." In a "light on" state, the signal j vs t increases because the excitation pulse is switched on, then the current tends to decrease up to a plateau, and, lastly, decays to the baseline when the light is off. By studying the decay over time, it is possible to derive information on the hole-electron recombination (Figure 5.17).
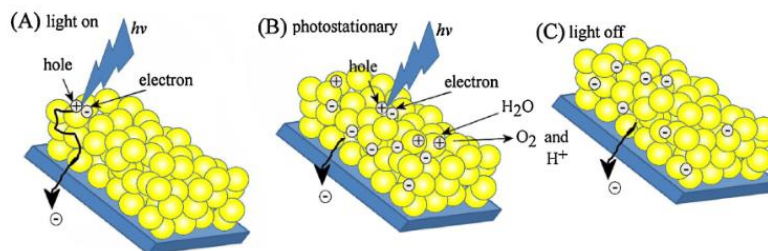

Figure 5.17 - Schematic illustration of the formation of holes and electrons upon photoexcitation of thin layer (taken from [12]).

For this work, the transient photocurrent of Au microelectrode coated with TiO_2 layer were performed. The parameters and the electrochemical cell for chronoamperometry were the same employed for fouling and cleaning tests (Au microelectrode coated with TiO_2 layer was polarized at +0.45 V (vs Ag/AgCl/KCl 1 M)).

During the 5000 s, the first 1200 s were performed to stabilize the current, and, later, 10 light-dark cycles were registered every 120 s, using UV lamp (Figure 5.18).
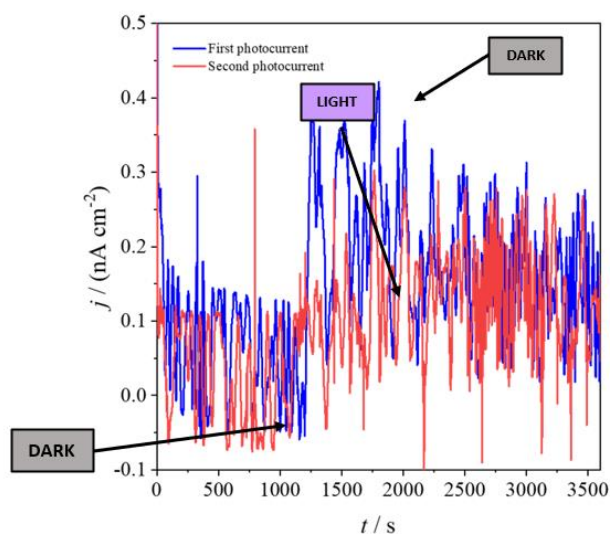
Figure 5.18 - Transient photocurrent (UV lamp) of the Au microelectrode coated with TiO$_2$.

Analysing Figure 5.18, it is difficult to see the small increase and decrease (few nA) in *j*, because of the fast hole-electron recombination process in the TiO$_2$ layer. This is due to the presence of surface defect sites (and consequently to a low crystalline quality of the material) at which the photoinduced charge recombines. Probably increasing the temperature up to 400 °C could be a good point to improve the transient photocurrent signal.

To improve the results, the transient photocurrent was performed by carrying out 10 light-dark cycles each of 120 s and 300 s, respectively (Figure 5.19).
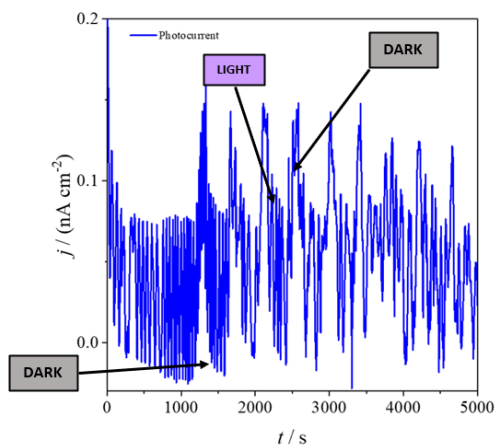

Figure 5.19 - Transient photocurrent (UV lamp) of the Au microelectrode coated with TiO$_2$.

Examining Figure 5.19, hole-electron recombination process on the surface and signal-to-noise ratio are better but still inadequate. Despite that, as it will be reported in the results and discussion section, chronoamperometry, after light-dark cycles, in the presence of dopamine was registered.

Another test under UV light was conducted using UV LED (M395L4 - 395 nm, 400 mW (Min) Mounted LED, 500 mA, purchased from Thorlabs) since they have lower thermal dissipation and better control over the radiation wavelength, but the results were very bad because the intensity of the UV light was not high enough to promote electrons to the conductive band (Figure 5.20).
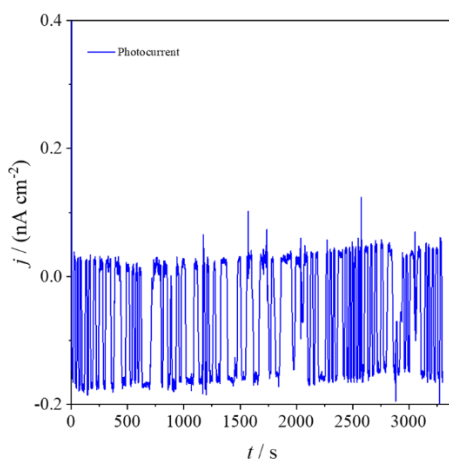

Figure 5.20 - Transient photocurrent (UV LED) of the Au microelectrode coated with TiO$_2$.

In fact, analysing Figure 5.20, the desired anodic current increase, due to the UV irradiation of the TiO$_2$ layer, is not present.

5.3.   Results and discussion.

This section reports the experimental results achieved from the experiments described in the previous part, concerning the electroanalytical detection of dopamine.

5.3.1. Destabilisation of dopamine solution.

With a view to greater environmental sustainability and savings, the stability of dopamine stock solutions was tested. In particular, this purpose was achieved before performing the real aims of the thesis, exploiting chronoamperometry technique in an electrochemical cell (a 50 cm^3 beaker) containing 20 cm^3 of PBS 0.1 M at pH 7.4 and provided with a FTO electrode

calcinated with gold nanoparticles and titanium dioxide as working electrode (WE), saturated calomel electrode (SCE) as reference electrode (RE) and a platinum wire as counter electrode (CE).

The first study was carried out using a fresh dopamine stock solution of 1 mM, prepared the day of the test, and an old dopamine stock solution of 1 mM, prepared the day before. The chronoamperometric curves shown in Figure 5.21A were registered polarizing the electrode at +0.45 V (vs Ag/AgCl/KCl 1 M) and are characterized by 15 steps, each of them corresponding to a dopamine addition of 200 mm^3 every 120 s on PBS 0.1 M at pH 7.4 (concentration window: 0.01-0.1 mM).

The second study was performed employing the same dopamine stock solution of 1 mM on two consecutive days. The chronoamperometric curves reported in Figure 5.21B were obtained using the same experimental conditions and setup of the first study.
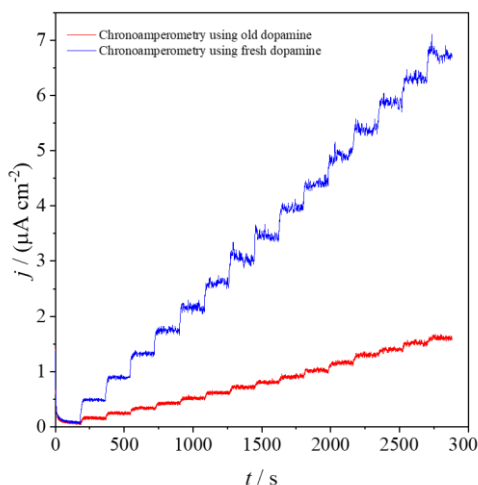

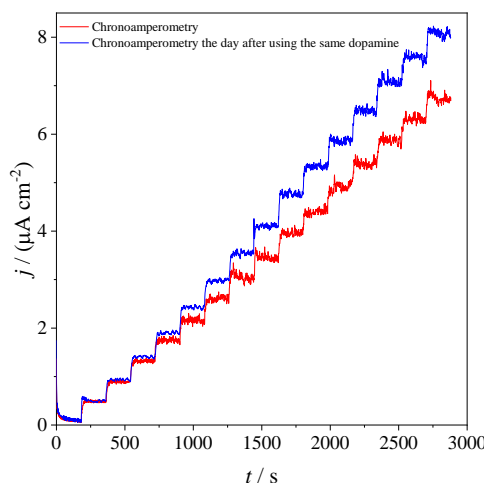Figure 5.21A - First study on the destabilization of dopamine solution.

Figure 5.21B - Second study on the destabilization of dopamine solution.

Analysing Figure 5.21A and Figure 5.21B it stands out the undeniable loss of signal repeatability.

Comparing the two signals in Figure 5.21A it is possible to see how using an old dopamine solution leads to an undeniable loss of signal repeatability. This is due to the rapid and spontaneous polymerisation of the dopamine in solution in the presence of oxygen (Figure 5.22), bringing to a stock solution characterised by different dopamine structures (monomers, dimers, oligomers, and polymers).

Looking at Figure 5.21B, it can be seen that, when using for two days in a row the same dopamine solution without cleaning the electrode, the signal related to this analysis (the blue line) is higher than the first analysis (red line). This is probably due to the formation of other dopamine structures that could be layered onto the surface of the electrode, thus leading to a higher signal in chronoamperometry.
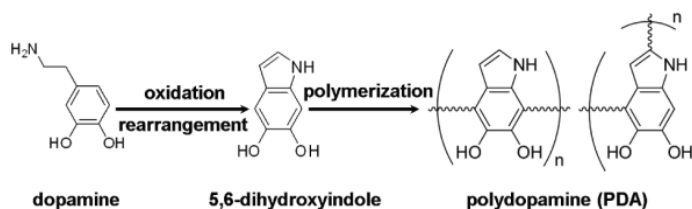

Figure 5.22 - Oxidative polymerization of dopamine (taken from [13]).

5.3.2. Electrochemical fouling procedure.

In the next paragraphs, chronoamperometric curves performed for the electroanalytical sensing of dopamine are illustrated and discussed. In detail, studies were carried out from the concentration range of 0.1-1 mM for the microelectrode and 0.01-0.1 mM for the FTO electrode. It was decided to study these ranges first because the higher ranges had already been analysed in previous tests; moreover, the interest is always to get as close as possible to the dopamine concentrations present in vivo and in the surrounding environment.

5.3.2.1. Gold disk microelectrode coated with TiO₂ layer electrochemical fouling.

After cyclic voltammetry characterization of Au disk microelectrode coated with TiO₂ layer, described in the previous part (Paragraph 5.2.4.2) and the evaluation of the potential at which dopamine oxidation occurs, its electroanalytical sensing by chronoamperometry was performed.

As already mentioned, dopamine detection leads to fouling and passivation of the metal disk microelectrode and that behaviour is ensured electrochemically by observing a decrease of anodic current related to dopamine oxidation in comparison with the initial signal recorded, due to a decrease of metal disk surface involved in the electronic transfer.

The first chronoamperometric curve, reported in Figure 5.23, was registered polarizing the microelectrode at +0.45 V (vs Ag/AgCl/KCl 1 M) and it is characterized by 10 steps, each of them corresponding to a dopamine addition of 5 mm^3 every 100 s on PBS 0.1 M at pH 7.4.
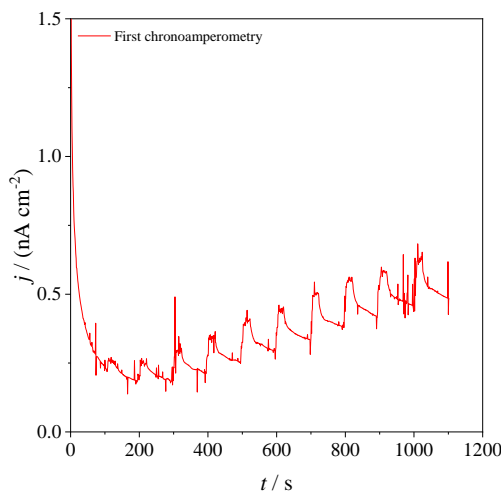

Figure 5.23 - Au disk microelectrode polarized at +0.45 V in PBS 0.1 M at pH 7.4 + 0.1-1 mM of dopamine (1st chronoamperometry).

It has been established that to be sure of microelectrode fouling, it is essential to perform at least two more chronoamperometric measurements, after washing the microelectrode tip with milliQ water. The amperometric results and their comparison are shown in Figure 5.24 A, B, C and D, respectively.
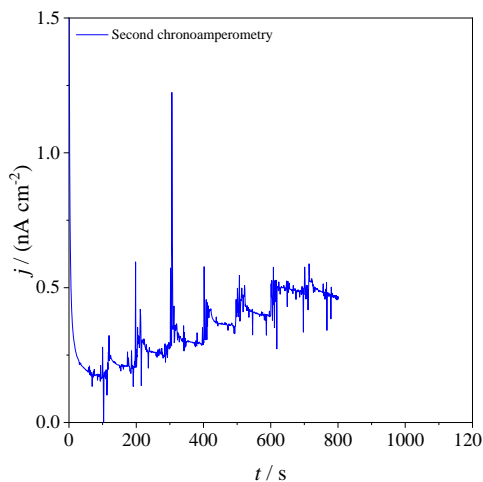
Figure 5.24 A - Au disk microelectrode polarized at 0.45 V in PBS 0.1 M pH=7.4 + 0.1-1 mM of dopamine (2nd chronoamperometry).
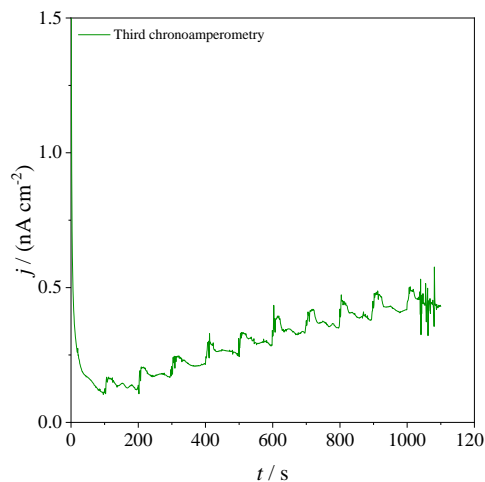

Figure 5.24 B - Au disk microelectrode polarized at 0.45 V in PBS 0.1 M pH=7.4 + 0.1-1 mM of dopamine (3rd chronoamperometry).

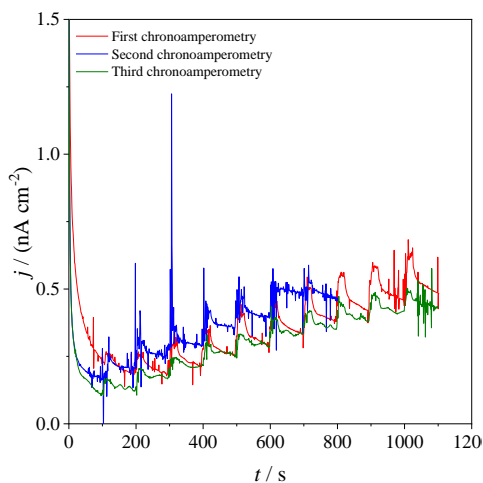*Figure 5.24 C - Comparison of chronoamperometric curves plot of Au disk microelectrode coated with TiO$_2$ layer.*
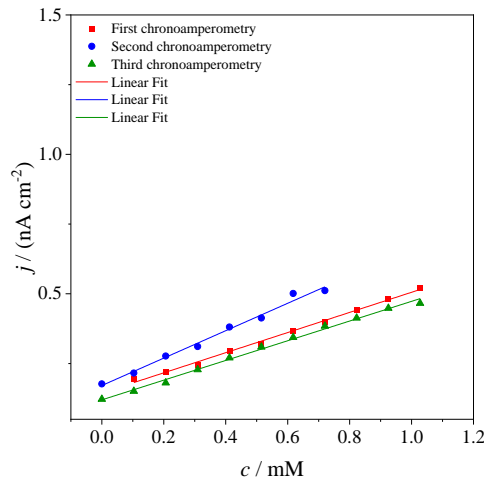

Figure 5.24 D - Comparison of the calibration plot of Au disk microelectrode coated with TiO$_2$ layer.

Considering a low concentration window, the curves *j* vs *c* obtained are characterized by high linearity up to the last dopamine addition and similar slopes (see Table 5.4).

Table 5.4 - Linear fitting.

Red Linear Fit		Blue Linear Fit		Green Linear Fit	
Equation	y = a + b*x	*Equation*	y = a + b*x	*Equation*	y = a + b*x
Intercept	$(1.4 \cdot 10^{-10} \pm 5.2 \cdot 10^{-12})$	*Intercept*	$(1.7 \cdot 10^{-10} \pm 9.5 \cdot 10^{-12})$	*Intercept*	$(1.2 \cdot 10^{-10} \pm 4.9 \cdot 10^{-12})$
Slope	$(3.6 \cdot 10^{-7} \pm 8.1 \cdot 10^{-9})$	*Slope*	$(4.9 \cdot 10^{-7} \pm 2.2 \cdot 10^{-8})$	*Slope*	$(3.5 \cdot 10^{-7} \pm 8.1 \cdot 10^{-9})$
Residual Sum of Squares	$4.6 \cdot 10^{-22}$	*Residual Sum of Squares*	$1.3 \cdot 10^{-21}$	*Residual Sum of Squares*	$6.9 \cdot 10^{-22}$
Pearson's r	0.998	*Pearson's r*	0.994	*Pearson's r*	0.998
R-Square (COD)	0.996	*R-Square (COD)*	0.99	*R-Square (COD)*	0.995
Adj. R-Square	0.995	*Adj. R-Square*	0.99	*Adj. R-Square*	0.995

So, since the chronoamperometric curves reported have not a bell shape, the fouling procedure conducted in a low concentration range results more complicated, in fact the decrease of anodic current respect to the initial one is not so easily distinguishable and evident, but fortunately present.

After fouling tests, the TiO_2 coating degree has been checked with its characterization by cyclic voltammetry.

5.3.2.2. Platinum disk microelectrode coated with TiO_2 layer electrochemical fouling.

To make a comparison with the performances of the gold disk microelectrode coated with TiO_2 layer, fouling test were carried out employing platinum microelectrode coated with TiO_2 layer. The same considerations taken into account for Au disk microelectrode coated with TiO_2 layer are also valid for Pt disk microelectrode coated with TiO_2 layer. Before using Pt microelectrode in fouling procedure, it has been characterized by cyclic voltammetry (Figure 5.13).

The first chronoamperometric curve, reported in Figure 5.25, was registered polarizing the microelectrode at +0.45 V (vs Ag/AgCl/KCl 1 M) and is characterized by 10 steps, each of them corresponding to a dopamine addition of 5 mm^3 every 100 s on PBS 0.1 M at pH 7.4.
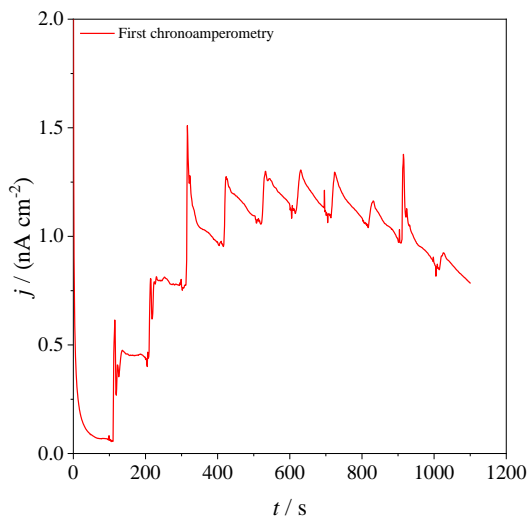
Figure 5.25 - Pt disk microelectrode polarized at +0.45 V in PBS 0.1 M at pH 7.4 + 0.1-1 mM of dopamine (1st chronoamperometry)

As for previous fouling procedure, a second chronoamperometry was registered to be sure of the microelectrode fouling (Figure 5.26).
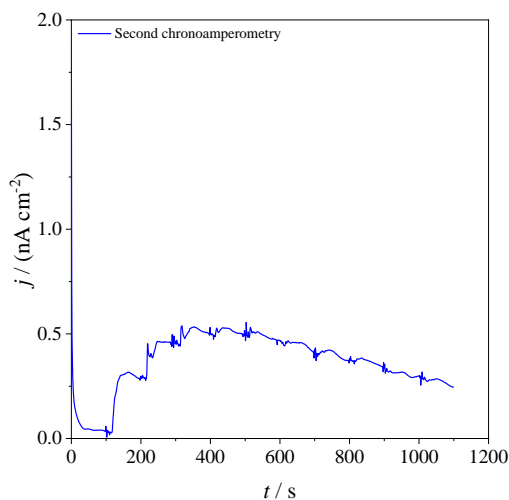

Figure 5.26 - Pt disk microelectrode polarized at 0.45 V in PBS 0.1 M at pH 7.4 + 0.1-1 mM of dopamine (2nd chronoamperometry)

In this case, as shown in the following Figure 5.27, the decrease of the signal due to dopamine addition into the PBS solution is more evident than the one observed in the previous test.
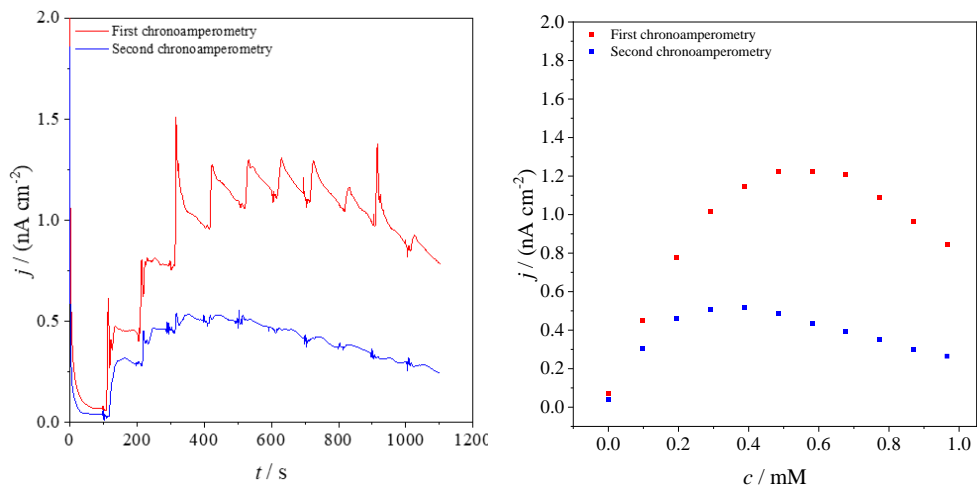
Figure 5.27 - Comparison of chronoamperometric curves and calibration plot of Au disk microelectrode coated with TiO₂ layer.

Analysing the calibration plot, the curves *j* vs *c* are characterized by a bell shape (very low linearity) typical of a microelectrode that gets increasingly soiled with each dopamine addition. This means that the Pt microelectrode coated with TiO₂ layer reaches the saturation point more quickly than the gold one and so the cleaning procedure could be more difficult. It is possible that the amount of different dopamine structures (like dimers, oligomers and polymers) that get attached to the surface of the electrode is higher, thus leading to a bigger fouling effect and a more difficult cleaning procedure.

After fouling tests, the TiO₂ coating degree has been checked with its characterization by cyclic voltammetry.

5.3.2.3. FTO electrode calcinated with AuNPs and TiO₂ layer electrochemical fouling.

To check the performances of a macroelectrode in dopamine detection, FTO electrode calcinated with Au nanoparticles and titanium dioxide layer (Au13) was employed in fouling procedure, using a lower concentration range (0.01-0.1 mM) for fouling problems.

After cyclic voltammetry characterization (Figure 5.28) performed using a three electrodes cell (a 50 cm^3 beaker) containing 20 cm^3 of PBS 0.1 M at pH 7.4, performed after UV activation for almost 8 hours to verify if the gold was still present, dopamine electroanalytical detection by chronoamperometric technique was carried out.
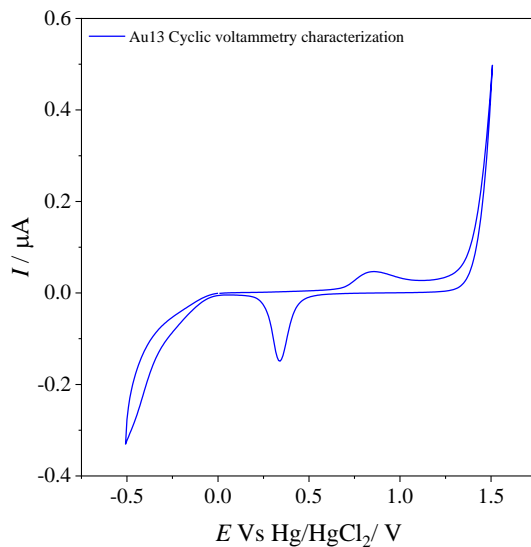
Figure 5.28 - Au13 cyclic voltammetry characterization performed in PBS 0.1 M at pH 7.4.

The first chronoamperometric curve reported in Figure 5.29 was registered polarizing the FTO electrode at +0.45 V (vs Hg/HgCl$_2$/KCl 1 M) and is characterized by 15 steps, each of them corresponding to a dopamine addition of 200 mm^3 (concentration window: 0.01-0.1 mM) every 120 s on PBS 0.1 M at pH 7.4.

Figure 5.29 - FTO electrode polarized at +0.45 V in PBS 0.1 M at pH 7.4 + 0.01-0.1 mM of dopamine (1st chronoamperometry).

Also in that case, two other chronoamperometries, reported in Figures 5.30 and 5.31 were registered to demonstrate electrode fouling.

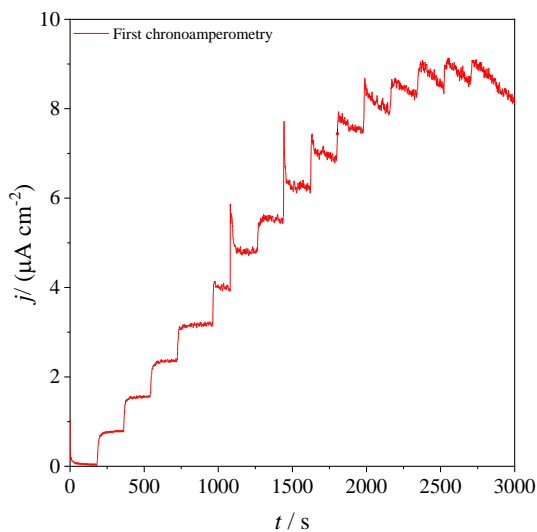In Figure 5.32, the comparison of the three chronoamperometries is shown and observing the green curve it is possible to be sure of the electrode fouling, which is demonstrated by the evident decrease of the current respect to the initial one.
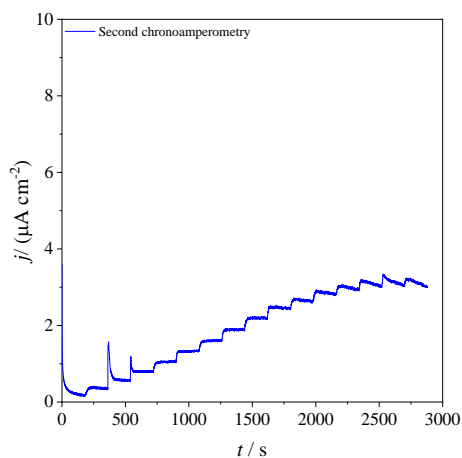

Figure 5.30 - FTO electrode polarized at +0.45 V in PBS 0.1 M at pH 7.4 + 0.01-0.1 mM of dopamine (2nd chronoamperometry).
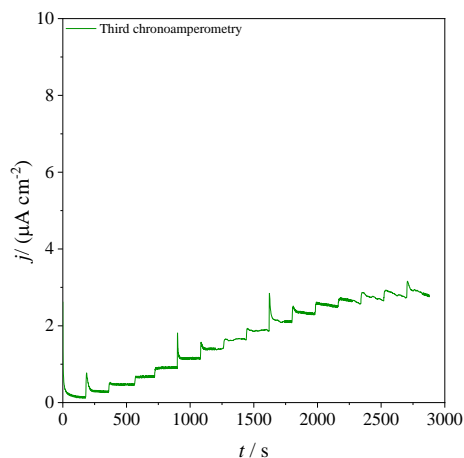
Figure 5.31 - FTO electrode polarized at +0.45 V in PBS 0.1 M at pH 7.4 + 0.01-0.1 mM of dopamine (3rd chronoamperometry)
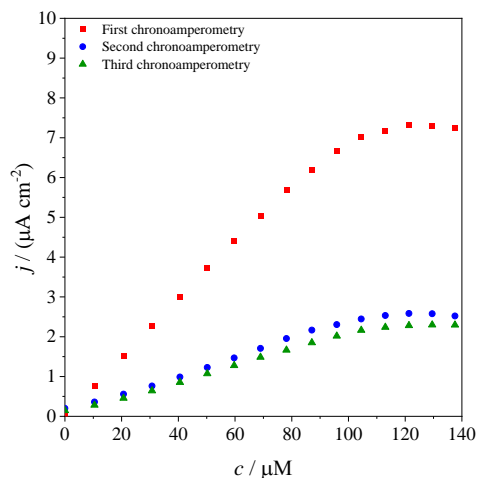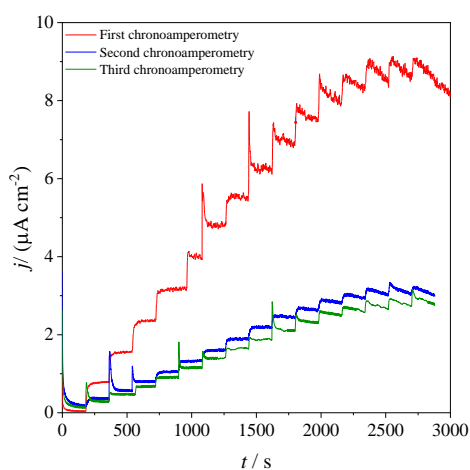

Figure 5.32 - Comparison of chronoamperometric curves and calibration plot of FTO electrode.

Looking at the calibration plot and the linear fit (reported in Figure 5.33), the curves j vs c are characterized by a good linearity except for the latest dopamine additions (see Table 5.5).
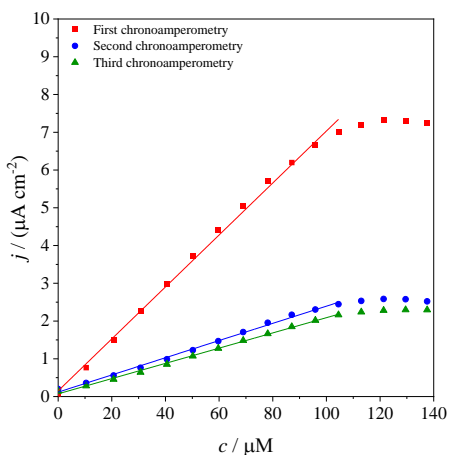
Figure 5.33 - Calibration plot.

Red Linear Fit	
Pearson's r	0.998
R-Square (COD)	0.996
Adj. R-Square	0.996
Blue Linear Fit	
Pearson's r	0.998
R-Square (COD)	0.996
Adj. R-Square	0.996
Green Linear Fit	
Pearson's r	0.999
R-Square (COD)	0.998
Adj. R-Square	0.998

Table 5.5 - Linear fitting.

As for Pt microelectrode coated with TiO_2 layer, FTO electrode calcinated with AuNPs and titanium dioxide reaches the saturation point faster than gold microelectrode in the dopamine sensing and so the cleaning procedure could be more difficult and time consuming. This behaviour could be attributed to the lower surface to volume ratio than that of the microelectrode.

5.3.3. Cleaning procedure.

After the fouling of the device, the coating degree of TiO_2 layer, except for FTO electrode, has been checked by cyclic voltammetry (the results are reported in the paragraph 5.3.2") and then, it was irradiated with UV lamp.

5.3.3.1. Gold disk microelectrode with TiO_2 layer cleaning procedure.

Gold disk microelectrode, post electroanalytical detection of dopamine, was immersed in a PBS solution inside a beaker in quartz and irradiated with UV lamp for 30 minutes.

Then, the cleaning degree has been tested by chronoamperometry in the same concentration window (0.1-1 mM) of the fouling test, to evaluate the current increment due to dopamine addition and the results were compared with the curves obtained in the microelectrode fouling.

Figure 5.34 reports the comparison between the last fouling test and the chronoamperometric curve registered after UV irradiation. In particular, the chronoamperometry was registered polarizing the microelectrode at +0.45 V (vs Ag/AgCl/KCl 1 M) and it is characterized by 10 steps, each of them corresponding to a dopamine addition of 5 mm^3 every 100 s on PBS 0.1 M at pH 7.4.
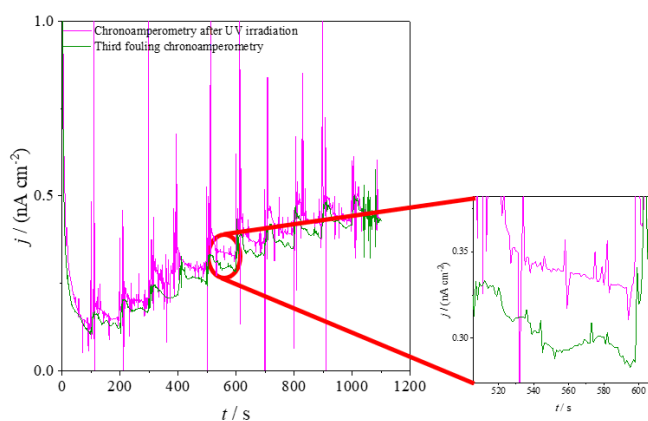
Figure 5.34 - Comparison between the last fouling test (green curve) and the chronoamperometric curve registered after a 30-minute UV irradiation (pink curve).

Thus, the comparison demonstrates that TiO$_2$ layer has conferred photo-renewable properties to the disk microelectrode. The increment of current due to dopamine addition is evident from the first j vs t peak and this means that the metal disk is clean. However, to ascertain that the active surface of the microelectrode is completely regenerated under UV light, it is necessary to compare the first fouling chronoamperometry with the chronoamperometric curve obtained after UV irradiation (Figure 5.35).

Figure 5.35 - Comparison between the first fouling test (red curve) and the chronoamperometric curve registered after 30 minutes UV irradiation (pink curve).

Observing this comparison, it is possible to establish that the signal has not been completely restored after UV irradiation and some traces of dopamine product were still anchored on the metal disk, but the currents obtained after cleaning are very close to those recorded with a completely un-cleaned microelectrode.

Furthermore, the curve *j* vs *c* obtained after irradiation is characterized by a good linearity and a slope that is very similar to the one got in the first fouling test (see Table 5.6), so TiO_2 provided photo-renewable properties to microelectrode (Figure 5.36).

Table 5.6 - Linear fitting.

Red Linear Fit	
Equation	y = a + b*x
Intercept	$(1.4 \cdot 10^{-10} \pm 5.2 \cdot 10^{-12})$
Slope	$(3.6 \cdot 10^{-7} \pm 8.1 \cdot 10^{-9})$
Residual Sum of Squares	$4.6 \cdot 10^{-22}$
Pearson's r	0.998
R-Square (COD)	0.996
Adj. R-Square	0.995
Pink Linear Fit	
Equation	y = a + b*x
Intercept	$(1.5 \cdot 10^{-10} \pm 1.4 \cdot 10^{-11})$
Slope	$(3.4 \cdot 10^{-7} \pm 2.2 \cdot 10^{-8})$
Residual Sum of Squares	$3.4 \cdot 10^{-22}$
Pearson's r	0.98
R-Square (COD)	0.97
Adj. R-Square	0.96
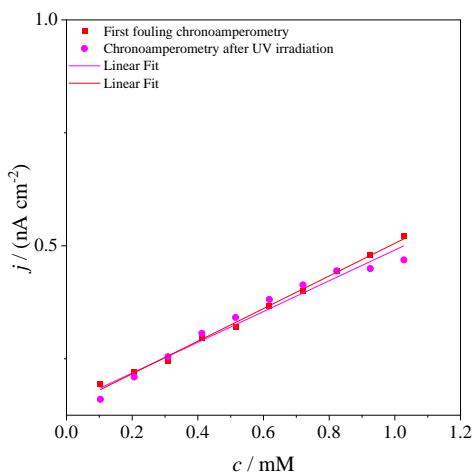
Figure 5.36 - calibration plot.

5.3.3.2. Platinum disk microelectrode coated with TiO₂ layer cleaning procedure.

The cleaning experiments here discussed are equal to the previous procedure but, in this case, it has been tested the photo-renewable properties of TiO_2 layer deposited on the platinum disk microelectrode.

First, platinum disk microelectrode, after electroanalytical detection of dopamine, was dipped in PBS solution inside a beaker in quartz and irradiated with UV lamp for 30 minutes.

Subsequently, the cleaning degree has been checked by registering a chronoamperometry in the same concentration range (0.1-1 mM) of the fouling test and the current increment due to dopamine addition in solution is compared with the curves obtained in the microelectrode fouling.

Figure 5.37 shows the comparison between the first fouling test and the chronoamperometric curve registered after UV irradiation. In detail, the chronoamperometry was registered polarizing the microelectrode at +0.45 V (vs Ag/AgCl/KCl 1 M) and it is characterized by 10 steps, each of them corresponding to a dopamine addition of 5 mm^3 every 100 s on PBS 0.1 M at pH 7.4.
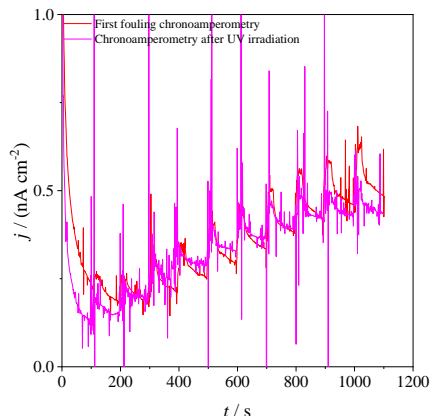

Figure 5.37 - Comparison between the first fouling test (red curve) and the chronoamperometric curve registered after 30 minutes of UV irradiation (pink curve).

The amperometric curve shape obtained is quite flat and the current increment due to dopamine addition in solution is not comparable to the ones registered in the first fouling test, therefore it is possible to assert that the cleaning procedure was not successful, and the disk microelectrode is still un-cleaned.

To improve the cleaning results, higher UV irradiation timing have been tested.

Hence, to assess if the cleaning procedure led to some evident effect, platinum disk microelectrode was irradiated using the previous procedure for two and a half hours, and the chronoamperometric result, compared with the first fouling chronoamperometry, is reported in Figure 5.38.

Figure 5.38 - Comparison between the first fouling test (red curve) and the chronoamperometric curve registered after 2 hour and a half of UV irradiation (pink curve).

By examining the comparison shown in the Figure above, the increment of current due to dopamine addition in solution is higher than the initial one with completely cleaned microelectrode, but after the fourth addition the increment of signal decreased, which means that some traces of dopamine product were still pegged to the metal disk and, so, after few additions of dopamine in the PBS solution, the fouling mechanism is more accelerated than the original one because of these traces. That result demonstrates that, thanks to TiO_2 layer, platinum microelectrodes are capable to restore their initial properties.

Seeing how the first peaks are good and the purpose is to optimize the timing of cleaning procedure, the cleaning procedure was tested after one hour (Figure 5.39) and one hour and a half (Figure 5.40) of UV irradiation.
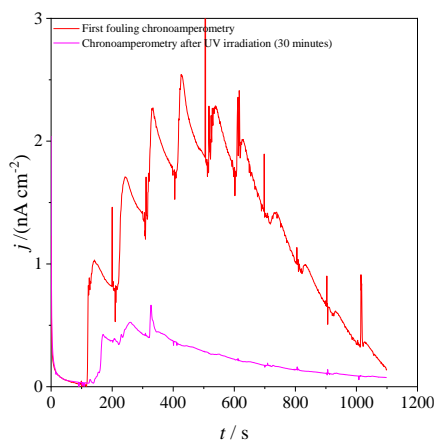
Figure 5.39 - Comparison between the first fouling test (red curve) and the chronoamperometric curve registered after 1 hour of UV irradiation (pink curve).
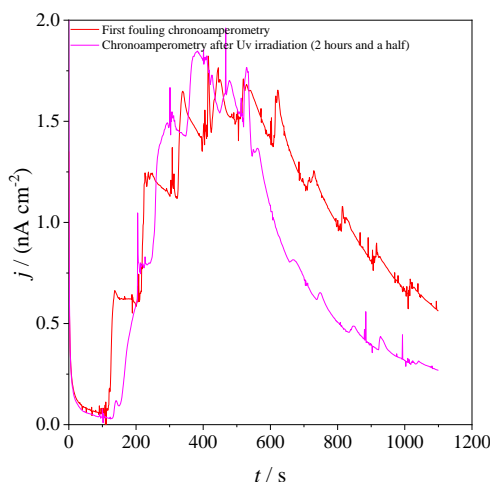

Figure 5.40 - Comparison between the first fouling test (red curve) and the chronoamperometric curve registered after 1 hour and a half of UV irradiation (pink curve).

In conclusion, the best recovery of the initial properties of the disk microelectrode has been achieved after one hour and a half of UV irradiation.

5.3.3.3. FTO electrode calcinated with AuNPs and TiO₂ layer cleaning procedure.

The cleaning procedure, here used, is the same of the previous cases and it has tested the photo-renewable properties of TiO_2 layer deposited on a FTO electrode functionalized with AuNPs.

FTO electrode, after electroanalytical detection of dopamine, was irradiated with UV lamp for 8 hours. Then, the cleaning degree has been confirmed by a chronoamperometry in the same concentration range (0.01-0.1 mM) of the fouling test and the current increment due to the addition of the electroactive molecule in solution is compared with the chronoamperometric curves obtained in the electrode fouling.

In detail, Figure 5.41 shows the comparison between the last fouling test and the chronoamperometric curve registered immediately after UV irradiation. Chronoamperometry was registered polarizing the electrode at +0.45 V (vs $Hg/HgCl_2/KCl$ 1 M) and it is characterized by 15 steps, each of them corresponding to a dopamine addition of 200 mm^3 every 120 s on PBS 0.1 M at pH 7.4.
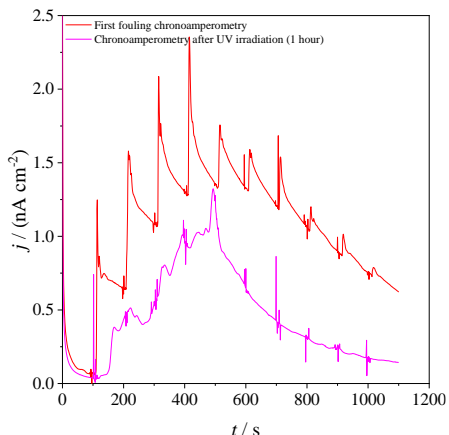
Figure 5.41 - Comparison between the last fouling test (green curve) and the chronoamperometric curve registered after 30 minutes UV irradiation (pink curve).

Thus, also in this case, the comparison shows that TiO_2 layer has conferred photo-renewable properties to the electrode. The increment of current due to dopamine addition is evident from the first *j* vs *t* peak and this means that the electrode surface is clean. Obviously, to ascertain that the electrode active surface is completely regenerated under UV light, it is necessary to compare the first fouling chronoamperometry with the chronoamperometric curves obtained after UV irradiation (Figure 5.42).

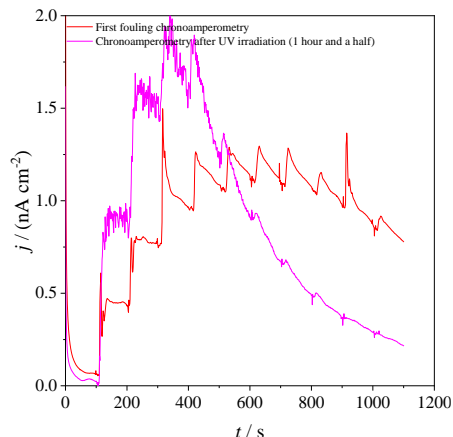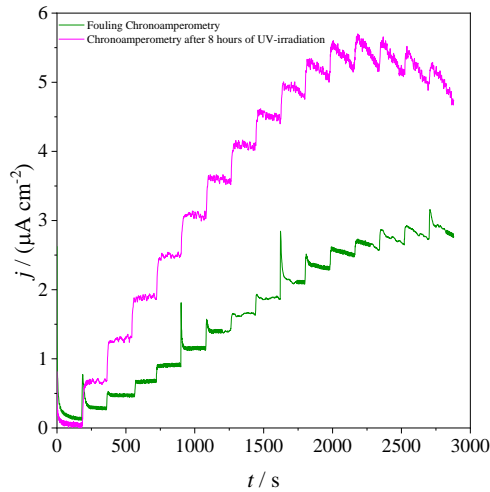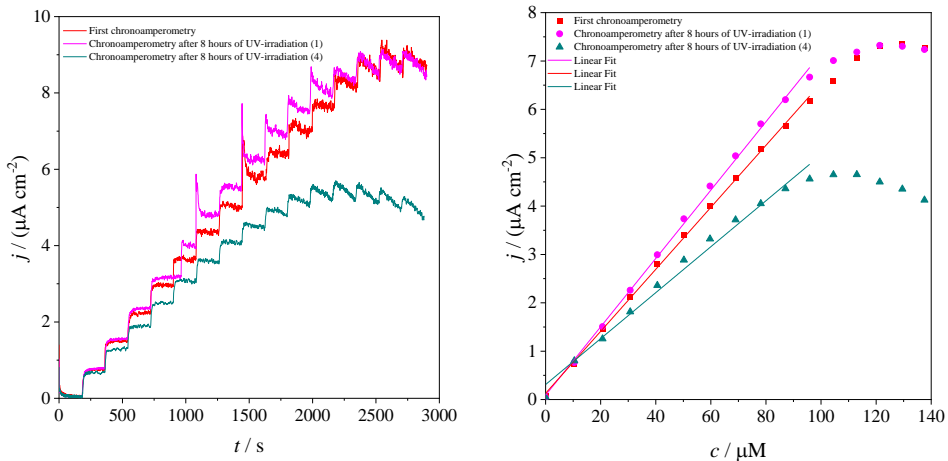*Figure 5.42 - Comparison between the first fouling test (red curve) and the chronoamperometric curve registered after first UV irradiation (pink curve) and the ones recorded after fourth UV irradiation (aqua green curve).*

Analysing this comparison, it is possible to establish that the chronoamperometric signal has been completely restored after first UV irradiation; in fact, the currents obtained after cleaning are coincident or even higher than those recorded with a completely un-cleaned microelectrode.

The plot also reports the chronoamperometric curve referred to the fourth UV irradiation, registered after four fouling cycles and the sensor signal starts to drastically decrease after the sixth dopamine addition. This means that the initial properties of the electrode are completely recovered after one fouling and cleaning procedure, but a massive use of this device leads to a progressively deterioration of the performances. In addition, the UV irradiation timing, and the geometric size of the FTO electrode are less appropriate than the microsensor to biological sample or natural environments.

Considering the linear fit (Table 5.7), as for the fouling procedure, the curves j vs c are characterised by a good linearity except for the latest dopamine additions.

Table 5.7 - Linear fits.

	Pearson's r	R-Square (COD)	Adj. R-Square
Red linear fit	0.999	0.999	0.999
Pink linear fit	0.999	0.998	0.998
Aqua linear fit	0.994	0.99	0.99

5.3.4. Superiority of gold microelectrode coated with TiO_2 layer in the fouling and cleaning procedure.

The results reported in the previous paragraphs demonstrate that the most appropriate metal for the electroanalytical detection of biomolecules that leads to device fouling and passivation, necessitating a subsequently cleaning, is gold set in the microelectrode and coated with a TiO_2 layer.

More specifically, in the monitoring of wastewater pollutants is important to fabricate sensors capable to rapidly restore its properties and to be used for consecutive and *in-situ* analyses. In this context, gold microelectrode coated with TiO_2 layer could be a more prominent candidate than platinum microelectrode coated with TiO_2, as evidenced by the fouling and cleaning plot displayed.

Microelectrodes differ from macroelectrodes (*i.e.*, FTO electrode analysed) for the fact they have an increase active surface area, same dimensions of

biomedical or biological molecules and high surface to volume ratio. In addition, microsensors are characterized by convergent diffusion instead of linear diffusion that leads to faster rate of mass transport than macroelectrodes and reduced capacitance of the double layer, which allow to overcome the diffusion limitation of the large diffusion layer [14]. These features carry to a slower deactivation of the electrode and to easier cleaning test, which is a major and most important step forward.

5.3.5. Determination of the limit of detection (LOD).

After having explored the fouling and cleaning procedure, the next purpose reached is the evaluation of the detection limits of the innovative devices used to validate them. In particular, several concentration ranges for each sensor have been analysed, until no current increment was observed.

5.3.5.1.   Gold microelectrode coated with TiO₂ layer.

To achieve this objective, in the case of the gold microelectrode coated with TiO$_2$ layer the first concentration range investigated is 0.01-0.1 mM.

Figure 5.43 reports the amperometric curve obtained and it is characterized by 10 steps, each of them corresponding to a dopamine addition of 5 mm^3 (dopamine stock solution has a concentration of 0.02 M) on PBS solution 0.1 M at pH 7.4.

Figure 5.43 - Chronoamperometric curve registered in the concentration range 0.01-0.1 mM (left) and the calibration plot (right).

The calibration plot j vs c shown on the right has high linearity, similar to the lower concentration range analysed, and leads to a detection limit of (Table 5.8):

Equation	y = a + b*x
Intercept	$(4.8 \cdot 10^{-11} \pm 3.9 \cdot 10^{-12})$
Slope	$(2.6 \cdot 10^{-6} \pm 6.8 \cdot 10^{-8})$
Residual Sum of Squares	$4.1 \cdot 10^{-22}$
Pearson's r	0.997
R-Square (COD)	0.994
Adj. R-Square	0.993
LOD/ μM	**(8.5 ± 0.2)**

Later, the concentration window 1-10 µM has been tested and also for this range the chronoamperometry is characterised by 10 steps, each of them corresponding to a dopamine addition of 10 mm^3 on PBS solution 0.1 M at pH 7.4 (Figure 5.44).

Figure 5.44 - Chronoamperometric curve registered in the concentration range 1 – 10 µM.

Figure 5.44 demonstrates that, in this concentration range, the gold microelectrode is not capable of distinguishing the electroactive biomolecule (dopamine) from the blank, so the sensor has a linearity range of $1.0\cdot10^{-3}$ to $1.0\cdot10^{-5}$ M.

5.3.5.2. Platinum microelectrode coated with TiO₂ layer.

As for gold microelectrode, the first concentration window tested is 0.01-0.1 mM and the 10 steps of chronoamperometric curve, obtained through dopamine additions of 5 mm^3 (dopamine stock solution has a concentration of 0.02 M) in 10 cm^3 of PBS 0.1 M at pH 7.4, are reported in Figure 5.45.

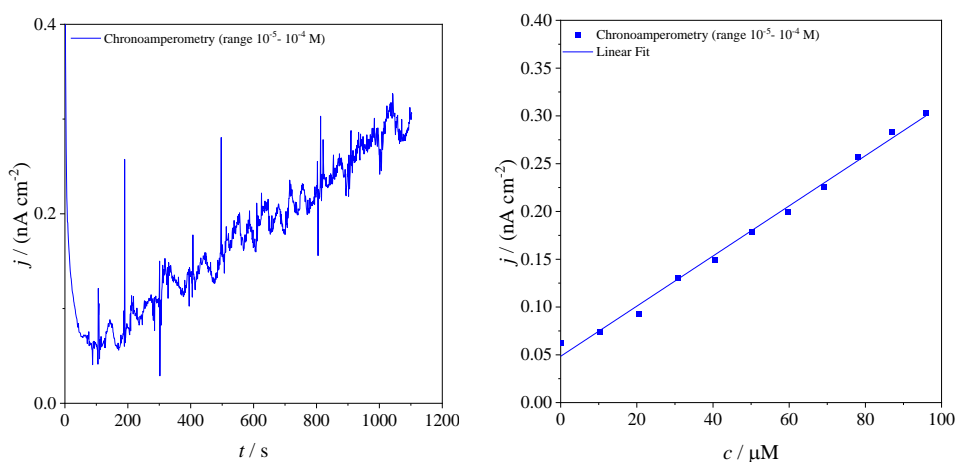*Figure 5.45 - Chronoamperometric curve registered in the concentration range 0.01-0.1 mM (left) and the calibration plot (right).*

Also in this case, the calibration plot j vs c is characterized by a very good linearity up to the last dopamine addition, but the limit of detection calculated is slightly higher than that obtained with gold microelectrode (Table 5.9):

Table 5.9 - analytical parameters.

Equation	y = a + b*x	Pearson's r	0.995
Intercept	$(8.8 \cdot 10^{-11} \pm 1.2 \cdot 10^{-11})$	R-Square (COD)	0.99
Slope	$(5.9 \cdot 10^{-6} \pm 2.1 \cdot 10^{-7})$	Adj. R-Square	0.99
Residual Sum of Squares	$3.9 \cdot 10^{-21}$	LOD/ µM	(11.5 ± 0.4)

Then, a concentration window even lower was analysed (1-10 µM) and the chronoamperometry registered is characterized by 10 steps, each of them corresponding to a dopamine addition of 10 mm^3 on PBS 0.1 M at pH 7.4 (Figure 5.46).
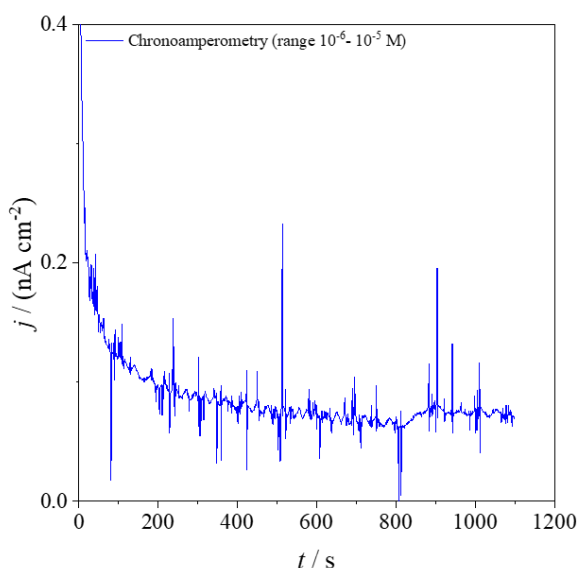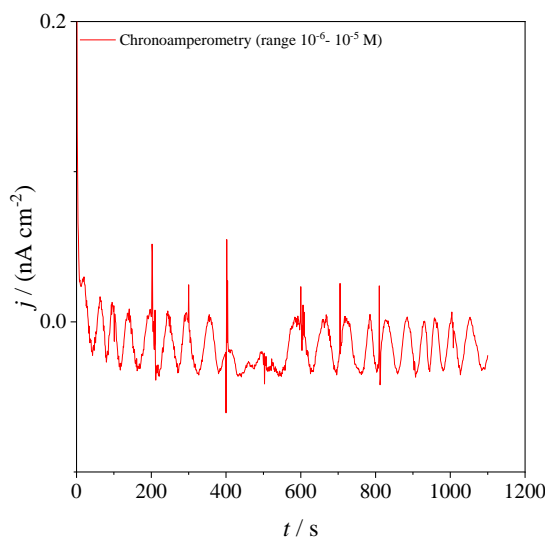

Figure 5.46 - Chronoamperometric curve registered in the concentration range 1-10 µM.

Platinum microelectrode coated with TiO_2 layer, similar to the gold one, cannot detect dopamine in a range so low and also in this case the linear range is $1.0 \cdot 10^{-3} – 1.0 \cdot 10^{-5}$ M.

5.3.5.3.   FTO electrode calcinated with AuNPs and TiO₂ layer.

Having performed the fouling procedure in the concentration range 1-10 μM, the first concentration window analysed is 1-10 μM and the chronoamperometric curve, characterized by 10 dopamine additions of 20 mm^3 (dopamine stock solution 10^{-3} M) in 20 cm^3 of PBS 0.1 M at pH 7.4 solution, is shown in Figure 5.47.
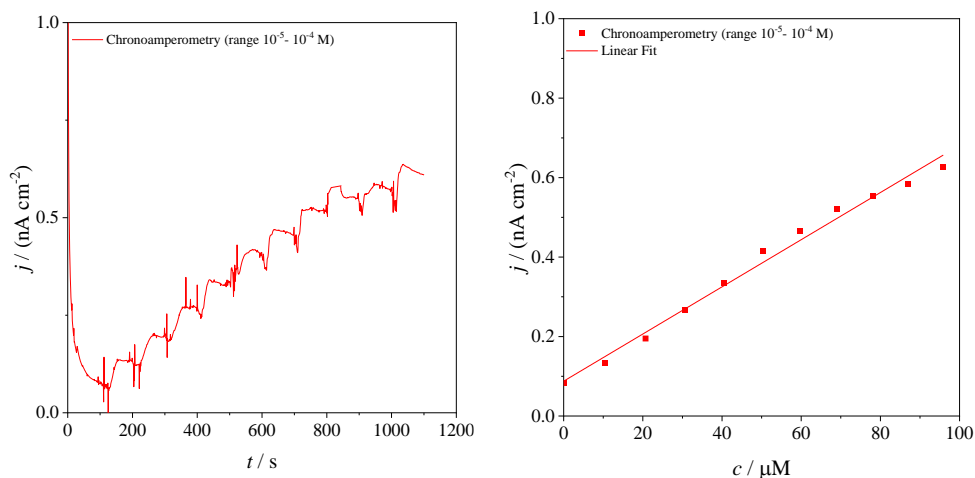

Figure 5.47 - Chronoamperometric curve registered in the concentration range 1-10 μM (left) and the calibration plot (right).

The calibration plot *j* vs *c* illustrated on the right has high linearity, greater than the lower concentration range analysed and leads to a detection limit of (Table 5.10):

Table 5.10 – Analytical parameters in the concentration range 1-10 μM.

Equation	y = a + b*x
Intercept	$(5.7 \cdot 10^{-8} \pm 7.4 \cdot 10^{-9})$
Slope	(0.077 ± 0.001)
Residual Sum of Squares	$1.5 \cdot 10^{-15}$
Pearson's r	0.999
R-Square (COD)	0.998
Adj. R-Square	0.998
LOD/ nM	**(556 ± 9)**

The higher linearity obtained highlights that the fouling procedure, in that concentration range, is more difficult and so the deactivation of the electrode is lower.

The subsequent concentration range is 0.2-1.5 μM, since the window 0.1-1 μM has not led to a current increment and the chronoamperometry obtained (Figure 5.48) is characterized by 10 steps, each of them corresponding to a dopamine addition of 40 mm^3 (dopamine stock solution 10^{-4} M) in 20 cm^3 of PBS.
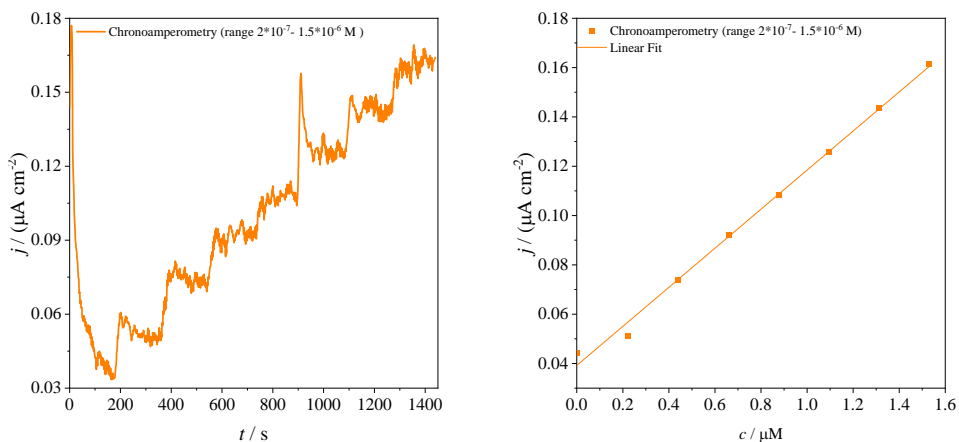
Figure 5.48 - Chronoamperometric curve registered in the concentration range 0.2-1.5 μM (left) and the calibration plot (right).

Also, in that concentration range analysed, the calibration plot *j* vs *c* is characterized by high linearity as reported in Table 5.11 and the detection limit calculated, using the equation written in paragraphs 5.2.7, is:

Table 5.11 – Analytical parameters in the concentration range 0.2-1.5 μM.

Equation	y = a + b*x
Intercept	$(4 \cdot 10^{-8} \pm 2 \cdot 10^{-9})$
Slope	(0.079 ± 0.002)
Residual Sum of Squares	$5.6 \cdot 10^{-17}$
Pearson's r	0.998
R-Square (COD)	0.996
Adj. R-Square	0.995
LOD/ nM	(126 ± 3)

Moreover, to adequately evaluate the detection limit of FTO electrode calcinated with gold nanoparticles and TiO$_2$ layer, a test in the concentration window 34-2800 nM has been carried out. In particular, the dopamine additions have been: 50 mm^3 for the first four steps, 200 mm^3 for the fifth and sixth addition and 400 mm^3 for the remaining seven addition. The chronoamperometric curve recorded is shown in Figure 5.49.
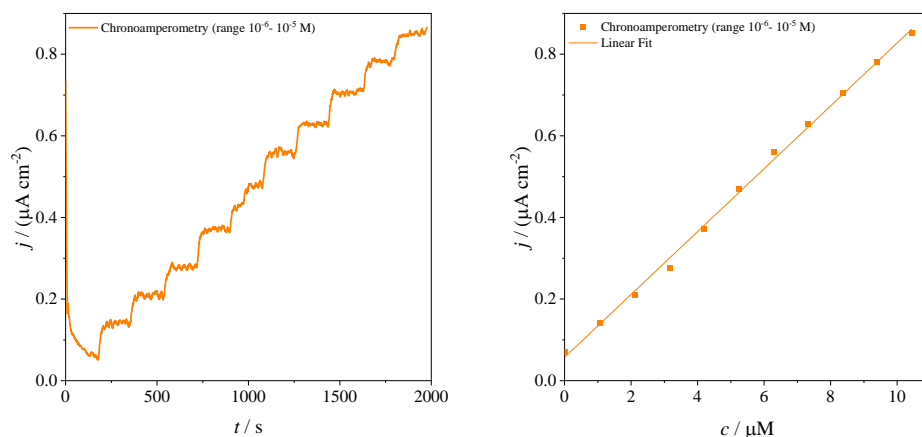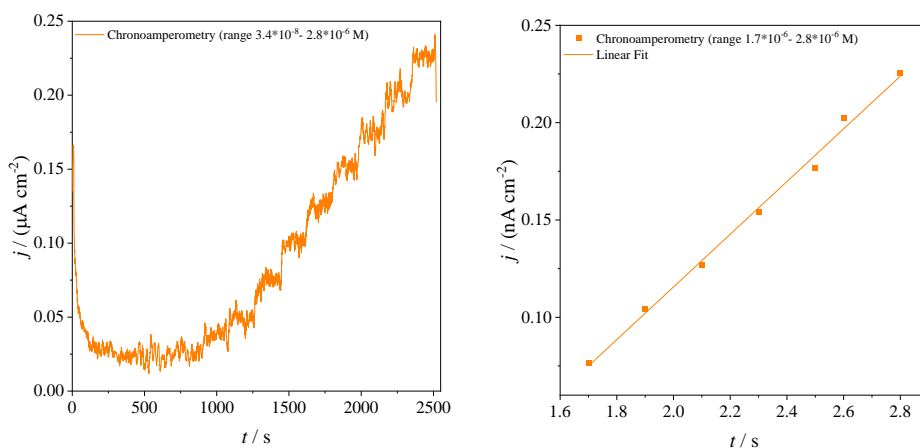

Figure 5.49 - Chronoamperometric curve registered in the concentration range 34-2800 nM (left) and the calibration plot (right).

From the graphs the first six points have been neglected and only the last seven points have been considered, due to their high linearity and distinctiveness.

So, the detection limit obtained from the calibration plot reported above is:

Table 5.12 - Analytical parameters in the concentration range 34-2800 nm.

Equation	y = a + b*x
Intercept	$(-2\cdot10^{-7} \pm 1\cdot10^{-8})$
Slope	(0.135 ± 0.004)
Residual Sum of Squares	$9.2\cdot10^{-17}$
Pearson's r	0.997
R-Square (COD)	0.995
Adj. R-Square	0.994
LOD/ nM	(104 ± 3)

5.3.6. Superiority of the FTO electrode calcinated with AuNPs nanoparticles and TiO$_2$ layer.

Analysing the values obtained, it is possible to assume that the device characterised by a detection limit which approaches mostly the dopamine concentration in human body (0.01-1 µM) and in environmental matrices (nM concentrations) is FTO electrode calcinated with gold nanoparticles and TiO$_2$ layer. In fact, from the calibration plot, conducted in the concentration range 34–2800 nM, a LOD of 104 nM was obtained. That quantity is not enough for detection in vivo, nevertheless it is an important starting point for further improvements. The result reached is due to the gold nanoparticles (AuNPs) and to their exceptional optical and electrochemical properties.

In detail, it is well known that gold nanoparticles have a greater surface area, high signal-to-noise ratio, faster mass transport to the electrode surface, high surface to volume ratio, better control, and selectivity on the analysis. These features lead, in contrast to gold bulk set in the microelectrode, to a lower quantity of dopamine that can be detected. In other word, microelectrodes seem to be a prominent material for the detection of dopamine, as underlined in the fouling and cleaning procedure, but microelectrodes have not high sensitivity to DA, there may be interference from ascorbic acid and substances in vivo and they are characterized by low sensitivity and spatiotemporal resolution; so, in order to enhanced the microelectrode characteristics, researchers have been devoted to modify microelectrode with materials which have specific functions as Nafion or metal nanoparticles. Consequently, by coupling the potential of microelectrode, before described, and the peculiarity of the nanoparticles, it will be possible to reach the natural concentrations of dopamine.

5.4. Conclusions.

In this work the optimization and electroanalytical application of photo-renewable gold and platinum microelectrodes modified with titanium dioxide were studied. In detail, the attention has been focused on the electrochemical detection of dopamine, a harmful biomolecule present both in human body and in the environment, which leads to fouling and passivation of the sensor.

Thanks to the work done, it is possible to assert that a new and potential alternative to biosensor, which have high costs and low stability, are photo-renewable metal microelectrode coated with TiO_2. It has been assessed that the most prominent material between gold and platinum is the first, and this is appreciable by observing the graphs reported in the previous section.

First, titanium dioxide photocatalytic properties in contact with metal micro-disk have been deeply investigated and the results obtained demonstrate that the best and most competitive outcome on the market in device signal restoring was achieved with TiO_2 layer in contact with gold micro-disk.

The second part of the work is based on an initial validation of the microdevice through the evaluation of the detection limit, in order to reach the lowest concentration of dopamine that can be distinguished using this transductor and, in that case, the performances of a macroelectrode functionalized with gold nanoparticles overcome those of the microelectrode (Table 4.1); thus a next challenging point, in order to exploited the properties of the microelectrode and the potentiality of the nanoparticles, is the fabrication of a microsensor modified with NPs and coated to TiO_2.

Table 5.13 - LODs

	LOD
Gold microelectrode coated with TiO_2	(8.5 ± 0.2) µM
Platinum microelectrode coated with TiO_2	(11.5 ± 0.4) µM
FTO electrode calcinated with AuNPs and TiO_2 layer	(104 ± 3) nM

Later, photocurrent studies have proven that TiO_2 layer is not totally an amorphous phase and so dopamine detection, after UV activation, can be improved in terms of analytical current increment.

Regarding the prospects of using these devices in online and in vivo monitoring, several improvements need to be developed. An important challenge is the further characterization of the TiO_2 layer on gold micro-disk

by registering X-rays diffraction spectra, to better identify the active crystalline phase.

From the electroanalytical point of view, it can be interesting the investigation of dopamine fouling and cleaning procedure using other analytical techniques, such as voltammetries.

With a view to adequately validate the device, over the repeatability, reproducibility and determination of the detection limit, other important parameters to consider are the robustness and the selectivity of the microelectrode towards possible interferents like ascorbic and uric acids, which have a similar oxidative potential.

In addition, calcination at 400 °C could be a fundamental future challenge.

So, through this work, further fundaments were laid to continue and improve the development of photo-renewable microelectrode for the electroanalytical detection of dopamine.

5.5. Bibliography.

[1] Z. Hsine, R. Mlika, N. Jaffrezic-Renault, and H. Korri-Youssoufi, Review—Recent Progress in Graphene Based Modified Electrodes for Electrochemical Detection of Dopamine, *Chemosensors* **2022**, 10, 249.

[2] K. Jackowska, and P. Krysinski, New trends in the electrochemical sensing of dopamine, *Anal Bioanal. Chem*. **2013**, 405, 3753–3771.

[3] F. B. Kamal Eddin, and Y. Wing Fen, Recent Advances in Electrochemical and Optical Sensing of Dopamine, *Sensors (Basel, Switzerland)* **2020**, 20.

[4] S. Noori, P. Friedlich, and I. Seri, Pharmacology Review, *Neoreviews* **2003**, 4, e283–e288.

[5] R. Liu, Z.-Y. Feng, L. Donghao, J. Biao, L. Yan and L.-Y. Meng, Recent trends in carbon-based microelectrodes as electrochemical sensors for neurotransmitter detection: A review. *TrAC - Trends in Analytical Chemistry* **2022**, 148.

[6] W. Harreither, R. Trouillon, P. Poulin, W. Neri, A. G. Ewing and G. Safina, Carbon nanotube fiber microelectrodes show a higher resistance to dopamine fouling, *Anal Chem* **2013**, 85, 7447–7453.

[7] C. He, M. Tao, C. Zhang, Y. He, W. Xu, Y. Lu and W. Zhu, Microelectrode-Based Electrochemical Sensing Technology for *in vivo* Detection of Dopamine: Recent Developments and Future Prospects, *Critical Reviews in Analytical Chemistry* **2022**, 52, 544–554.

[8] L. Lu, L. Liang, K. S. Teh, Y. Xie, Z. Wan and Y. Tang, The electrochemical behaviour of carbon fiber microelectrodes modified with carbon nanotubes using a two-step electroless plating/chemical vapor deposition process, *Sensors (Switzerland)* **2017**, 17.

[9] G. Denuault, M. Sosna, and K. J. Williams, *1-Classical Experiments* **2007**.

[10] G. Maino, D. Meroni, V. Pifferi and L. Falciola, Electrochemically assisted deposition of transparent, mechanically robust TiO_2 films for advanced applications, *Journal of Nanoparticle Research* **2013**, 15.

[11] A. Minguzzi, A. Vertova and S. Rondinini (**2021**), Microelectrode (Italian patent No. IT201900024193 A1). Ufficio Italiano Brevetti e Marchi.

[12] M. A. de Araújo, M. F. Gromboni, F. Marken, S. C. Parker, L. M. Peter, J. Turner, H. C. Aspinall, K. Black, L. H. Mascaro, Contrasting transient

photocurrent characteristics for thin films of vacuum-doped "grey" TiO_2 and "grey" Nb_2O_5, *Appl. Catal. B* **2018**, 237, 339–352.

[13] A. Postma and E. Tjipto, Self-polymerization of dopamine as a versatile and robust technique to prepare polymer capsules, *Chemistry of Materials* **2009**, 21, 3042–3044.

[14] R. G. Compton, E. Laborda and K. R. Ward, *Understanding voltammetry: simulation of electrode processes*, **2014**.

6. Multi-Walled Carbon Nanotubes (MWCNTs) and oligo-BT$_2$T$_4$ enantioselective electrodes.

6.1. Introduction.

Enantioselective electrodes represent an important instrument in electroanalytical chemistry, because of their ability to discriminate between different enantiomers of a chiral molecule [1]. The most important part in an enantioselective electrode is its surface, which must be modified in order to identify differences between two enantiomers [2]. Chirality is the property of a molecule not to be superimposable on its mirror image. A molecule that is not superimposable on its mirror image in three dimensions is defined as chiral. It is important to define that chirality is not a punctual property (for example belonging only to an atom) but it is a property belonging to the entire molecule. A molecule is chiral if there is no improper axis of rotation among its symmetry elements. Two molecules that are identical in all respects, except that one is a non-superimposable mirror image of the other, are called enantiomers. The main problem that makes the separation of enantiomers difficult is that they possess identical physical properties except the rotational power (identical in intensity but opposite in sign for each of them). A key point is that two enantiomers show the same chemical behavior towards non-chiral substances but a different interaction towards other chiral molecules. This is an area of particular importance, especially in the biological [3] and pharmaceutical fields, given that two enantiomers of the same drug, for example, can have completely different effects. Another example are L-amino acids, which are used in the synthesis of proteins, while some D-amino acids do not participate in the process of proteins synthesis or even generate adverse reaction to living organisms [4].

Different enantiomers of the same molecule have identical physio-chemical properties and therefore the same electrochemical behaviour, except when they interact with chiral supports; in this case, energetically different diastereomeric conditions are created. Electron transfer must occur under asymmetric conditions, for example on a chiral electrode or in a chiral medium.

Chiral electrochemical sensors can be based on chiral ionophores integrated into the ion-selective electrode membrane or on chiral effects in electrodeposited doping conducting polymers [5]. Various approaches have been employed to approach this challenge, aiming to distinguish between enantiomers of a chiral molecule [6].

A crucial strategy in this domain involves the utilization of "inherently chiral" molecular materials [7], both as electrode surface [8] and as media [9].

Chiral selectors must possess specific characteristics, including:

- The capability to differentiate between enantiomers based on substantial peak potential differences.
- Availability in both enantiomeric configurations to ensure that the initial electron transfer aligns with the desired target enantiomer, especially for preparative purposes.
- A linear dynamic range for currents, preferably with a low detection limit, enabling the integration of enantiodiscrimination with quantitative analysis and determination of enantiomeric excess.
- Broad applicability to various analytes and operating conditions/protocols.
- Reproducibility in both preparation and recognition, as well as stability.
- Ease, speed, and cost-effectiveness of preparation, low quantity requirements, and recyclability [10]. The studies carried out have explored the potential of employing both natural and synthetic chiral selectors. The latter option appears to be more promising for several reasons, such as the virtually limitless range of tailored structures and the ability to make both enantiomers of a specific selector equally accessible. In the field of electrochemistry and electrolysis, numerous attempts have been made to produce chiral enantiopure electrodes or chiral enantiopure media (utilizing synthetic selectors) to achieve enantiodiscrimination.

6.1.1. Oligo-BT$_2$T$_4$ films.

As previously mentioned, numerous efforts have been made in the field of enantioselection. An important turning point was certainly the introduction of enantioselective electrode surfaces designed according to the strategy of binary chirality, *i.e.* the development of materials in which the stereogenic element responsible for chirality coincides with the molecular moiety responsible for their specific properties. This means that both chirality and the main functional properties originate from the same element.

The "inherently chiral" films have proven to be excellent as electrode surface; in particular, thiophene-based oligomers [11], in which the chirality is given

by the torsion off the entire electroactive backbone [12]. The important and innovative aspect of these structures is that the chiroptic and enantiodiscrimination properties are closely linked to the electrochemical ones [8]. In particular, an in-depth case that will be discussed is that of the oligo-2,2'-bis(2,2'-bithiophen-5-yl)-3,3'-bibenzothiophene films, known by the acronym BT_2T_4, which are mainly made up from macrocyclic oligomers [3]. These structures have electroactive cavities of different size for a selective interaction of the analytes. The enantiopure oligo- BT_2T_4 films are obtained by oligomerization of the corresponding enantiopure monomer of BT_2T_4 (Figure 6.1) [13]. The conducting films obtained by the electro-oxidation of enantiopure (R) and (S) are constituted by oligomer of dimers (most prevalent) to pentamers (traces) [13]. The difference of the peak potential of the two enantiomers is due to the diastereomeric interactions that are formed in the electron transfer process between the film, which has an inherently chiral structure, and the chiral probe.
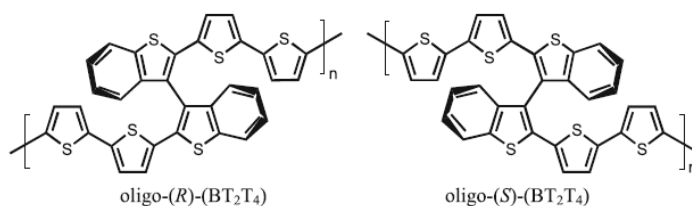

oligo-(*R*)-(BT₂T₄)   oligo-(*S*)-(BT₂T₄)

Figure 6.1 - Structure of the two enantiomers of oligo-BT₂T₄

Recent studies [12] have demonstrated the useful application of oligo-BT_2T_4 films for detecting molecules such as 3,4-dihydroxyphenylalanine (also known as DOPA, the precursor of the neurotransmitters dopamine, epinephrine, and norepinephrine, which is also used in the clinical treatment of Parkinson's disease and dopamine-responsive dystonia) or the antibiotic ofloxacin, which are molecules with complex oxidation mechanisms. It is important to underline that the ability and the "strength" of enantiodiscrimination depend on many factors. In every situation regarding the analyte to be analysed and the electrode used, it is necessary to find the ideal conditions to achieve the best possible peak separation.

6.1.2. Carbon nanotubes.

Nanomaterials have been widely used in electroanalysis because of their numerous advantages, such as high electrical conductivity, high surface area, a better signal to noise ratio and different diffusion mechanism, which lead to lower detection limits, a better affinity toward the analyte, a lower degree of interference, therefore obtaining more efficient sensors [14].

Carbon nanomaterials are very convenient for sensor design due to their excellent electrocatalytic properties. Also, the structural design of the material is very important to improve sensor efficiency. Several structures based on carbon nanomaterials are successfully used, including nanotubes, nanolayers, nano boxes, and mesoporous spheres. The most utilized carbon-based materials are graphene and its derivatives (reduced graphene oxide or graphene oxide), as well as carbon nanotubes and mesoporous carbon particles [15, 16].

Carbon nanotubes (CNTs) are 1D carbon nanomaterials with a cylindrical carbon structure. They are formed from sp^2 carbon atoms, which present an arrangement with hexagonal honeycomb lattices, the diameter of which can vary between several nanometers and many micrometers [17], like rolled-up graphene sheets. They can be divided into single-walled carbon nanotubes (SWCNTs) and multi-walled carbon nanotubes (MWCNTs), depending on the number of layers. Their surface can be functionalised to obtain better electrochemical sensors [18–20].

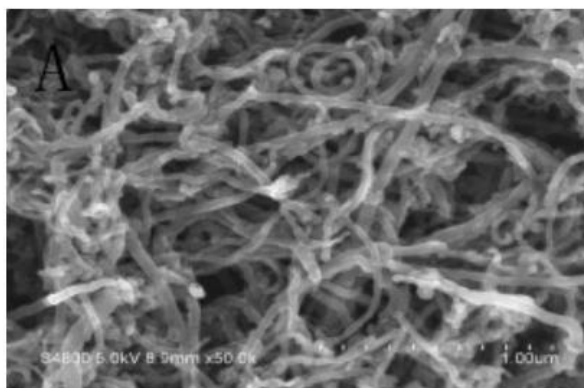*Figure 6.19 - SEM image of MWCNTs immobilized on the surface of the substrate (taken from [21]).*

Carbon nanotubes produce an increase in the speed of heterogeneous electronic transfer (Figure 6.3), to the detriment of a reduced fouling of the CNT-based electrodes [22]. The electronic properties of carbon nanotubes have the ability to mediate electron transfer reactions, furthermore the electrostatic properties

of carbon nanotubes are thought to originate from the open ends. All this makes them absolutely interesting in the development of chemical and biochemical sensors [17].
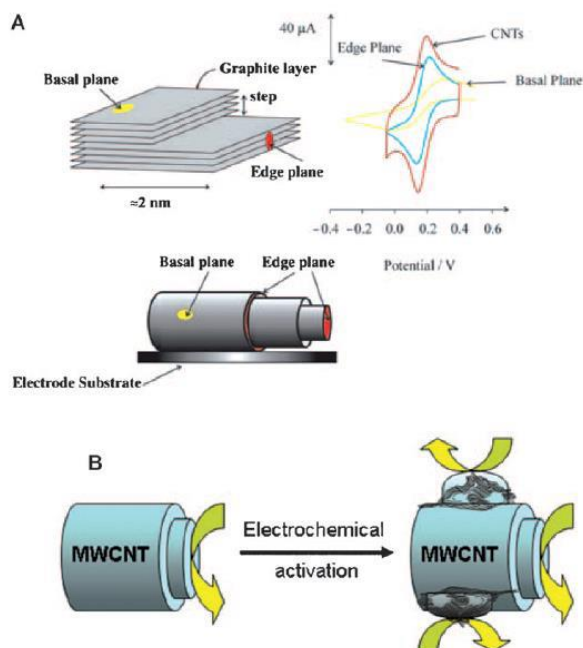

Figure 6.3 - Electrochemistry of carbon nanotubes resembles that of graphite. A) Schematic representation of a crystal of highly ordered pyrolytic graphite where the layers of graphite have an interlayer spacing of 3.35Å. This corresponds to a single MWCNT in which edge-plane-like sites are shown at the end of the tube and along the tube axis. These similarities result in identical electrochemical responses for CNT-modified electrodes when compared with the edge-plane pyrolytic graphite electrode. B) Controllable introduction of defects to MWCNT walls for enhanced heterogeneous electron transfer (taken from [22]).

It is also important to consider the chirality of CNTs: in fact, they have some chiral traits that can be investigated for specific applications. Their electronic properties are controlled by chirality, that is the angle at which the graphene sheet rolls up, thus modifying the alignment of the π orbitals [23, 24]. The angle is quantified by a chiral vector (n,m), where n and m are the (integer) numbers of hexagons traversed in the two unit-vector directions of the graphene lattice such that, when rolled up to touch the tip of the vector to its tail, the graphene would form the desired nanotube (Figure 6.4).
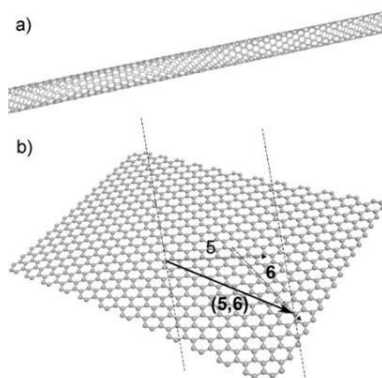
Figure 6.4 - The ideal structures of a) a single-walled nanotube and b) a graphene sheet. As an example, the chiral vectors required to roll up a(5,6) nanotube from a piece of the graphene are also illustrated (taken from [25]).

6.1.3. Aim of this work.

Seen all the characteristics and the advantages aforementioned, the aim of this work is to combine carbon nanotubes and oligo-BT_2T_4 films on an electrode surface. The modified electrodes (glassy carbon electrodes and screen printed electrodes) have been characterised with Cyclic Voltammetry (CV) and Electrochemical Impedance Spectroscopy (EIS) using at first an electrochemical achiral probe, $K_4[Fe(CN)_6]$ and then a chiral probe, N,N-dimethyl-1-ferrocenylethylamine, also considering the comparisons with the single parts (bare electrodes, electrodes with only CNTs, electrodes with only oligo-BT_2T_4 film).

6.2.   Materials and methods.

The reagents used, with repetitive use, their CAS number and brand are reported in Table 6.1; Table 6.2 reports the tools and materials used.

Table 6.1 - List of reagents.

Name	Use	CAS number	Brand
$K_4[Fe(CN)_6] \cdot H_2O$	Probe	14459-95-1	Fluka
$LiClO_4$	Electrolyte	7791-03-9	Sigma-Aldrich
$NaClO_4$	Electrolyte	7791-07-3	Sigma-Aldrich
HNO_3 65%	Cleaning	7697-37-2	Sigma-Aldrich
H_2SO_4 97%	Cleaning	7664-93-9	Sigma-Aldrich
NaOH 37%	Cleaning	1310-73-2	Sigma-Aldrich
HCl 37%	Cleaning	7647-01-0	Sigma-Aldrich
N,N Dimethylformamide > 99.8%	Preparation of MWCNTs	68-12-2	Sigma-Aldrich
Acetonitrile 99.8%	Solvent	75-05-8	Sigma-Aldrich
1-butyl-3-methylimidazolium bis(trifluoromethylsulfonyl)imide (Ionic liquid) 98%	Solvent	174899-83-3	Sigma-Aldrich
Acetone	Cleaning	67-64-1	Sigma-Aldrich
R-N,N-dimethyl-1-ferrocenylethylamine	Probe	31886-58-5	Sigma-Aldrich
S-N,N-dimethyl-1-ferrocenylethylamine	Probe	31886-58-5	Sigma-Aldrich
Tetrabutylammonium perchlorate > 99.0%	Electrolyte	1923-70-2	Sigma-Aldrich
MWCNTs > 98% purity, 6-13 nm diameter and 2.5-20 mm length	Electrode preparation	308068-56-6	Sigma-Aldrich
BT_2T_4	Electrode preparation	/	/

| Diamond synthetic nanopowder, 1 μm, 99.9% | Cleaning | 7782-40-3 | Sigma-Aldrich |

Table 6.2 - List of instruments and materials.

Name	Brand
Glassy Carbon Electrodes (GCEs)	AMEL
Screen Printed Electrodes (SPEs)	DRP-150
Potentiostat Galvanostat [PGSTAT30]	MetrOhm
Micropipettes	Gilson
Oven	Forno MAB
Ultrasonic bath - Sonorex	Bandeline
Scanning Electron Microscope (SEM) - Vega	Tescan

6.2.1. Preparation of the solutions.

$NaClO_4$ 0.1 M was prepared by dissolving 12.12 g of $NaClO_4$ salt in 1 dm^3 of milliQ water. The solution was prepared and kept at room temperature.

Tetrabutylammonium perchlorate 0.1 M was prepared by dissolving 3.42 g of tetrabutylammonium perchlorate salt in 100 cm^3 of milliQ water. The solution was prepared and kept at room temperature.

$K_4[Fe(CN)_6]$ 50.5 mM was prepared by dissolving 10.66 g of $K_4[Fe(CN)_6] \cdot H_2O$ in 500 cm^3 of milliQ water. The solution was kept in the fridge at a temperature of 4 °C This solution was used to obtain concentration of 1, 2 and 3 mM of iron probe by adding aliquots of 400 mm^3 into the electrochemical cell containing 20 cm^3 of the electrolytic solution.

N,N-dimethyl-1-ferrocenylethylamine (both R and S) 3 mM was prepared by dissolving 2.3 mg of pure N,N-dimethyl-1-ferrocenylethylamine in 3 cm^3 of acetonitrile. The solution was kept in the fridge at a temperature of 4 °C.

BT_2T_4 for electrodeposition was prepared by dissolving 1.1 mg of pure salt in 2 cm^3 of acetonitrile with an excess of $LiClO_4$ (0.3 g).

Electrochemical data were collected using the program Nova 2.1.2 (build 6333, Copyright © 2016, Metrohm Autolab BV). Data processing and presentation was performed with OriginPro[R].

6.2.2. Cleaning of the Multi-Walled Carbon Nanotubes.

The MWCNTs were cleaned according to the procedure reported in [26]: 150 mg of carbon nanotubes were weighed and stirred in 12 mL of 3:1 mixture of HNO_3/H_2SO_4 (both concentrated) for 24 hours. The product was filtered through a polyvinylidene fluoride membrane and rinsed with milliQ water until neutral pH. The filtrate was then dried in an oven for 24 hours at 80 °C. The solid was further treated in 0.1 M NaOH and sonicated for 15 minutes, then left at room temperature for 24 hours and filtered through a PVDF membrane. The final solid was then rinsed with milliQ water until neutral pH and reacidified with HCl 0.1 M. Subsequently, 1 mg of purified MWCNTs were dissolved in 2 mL of N,N-dimethylformamide > 99.8%, by sonicating for 15 min. The resulting solution was then placed in the fridge at 4 °C. The modification of the glassy carbon electrode took place by depositing 20 µL of the solution on the electrode surface, leaving it to dry at room temperature for 24 hours.

6.2.3. Electrode preparation.

The glassy carbon electrodes were cleaned before use using diamond synthetic monocrystalline nanopowder on a wet support by moving and rotating the electrode with circular movements. Then the electrodes were sonicated in milliQ water for 15 minutes and immersed in concentrated HNO_3 for few seconds.

### 6.2.4. Cyclic voltammetry characterisation.

The GC electrodes were tested before doing the depositions to find the best electrodes to use. They were tested through cyclic voltammetry (using a Pt wire as counter electrode and a Saturated Calomel Electrode as reference electrode) for the evaluation of the best-shaped signals. The analyses were performed both on the supporting electrolyte ($NaClO_4$) and on the probe molecule $[Fe(CN)_6]^{4-}/[Fe(CN)_6]^{3-}$ at different concentrations (1, 2 and 3 mM). Despite the cleaning procedure, some electrodes still presented a peak even when analysing the background; therefore, they were rejected.

At the end of the tests, the two cleanest electrodes were GC_1 and GC_2. Figures 6.5 and 6.6 show the CVs performed on these electrodes at different scan rates, both on the background (Figure 6.5) and on the 3 mM probe molecule (Figure 6.6). The tests were first performed on a wider range of

potentials, and then it was restricted to -0.75 V – +0.75 V because of the electrochemical behaviour of the oligo-BT$_2$T$_4$.
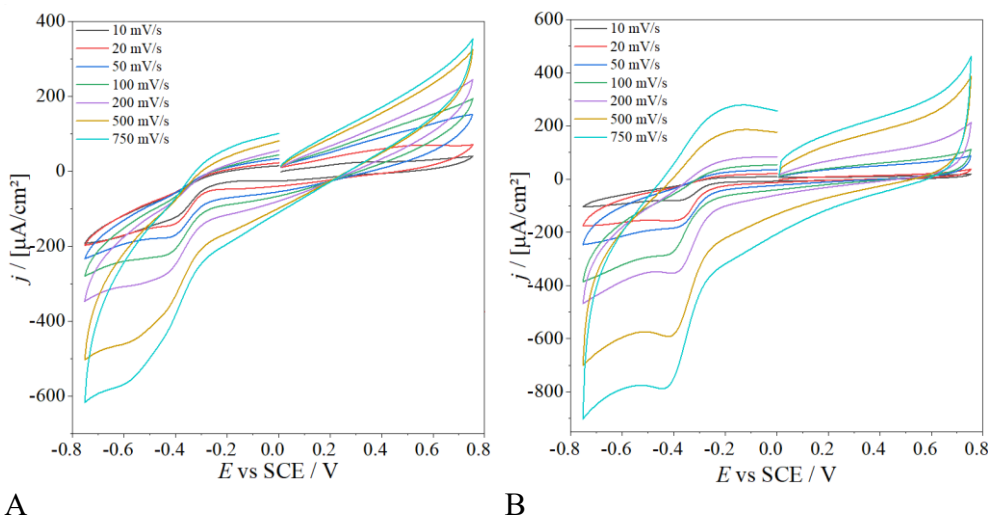
Figures 6.5- background signals at different scan rate respectively of GC_ 1 and GC_ 2.
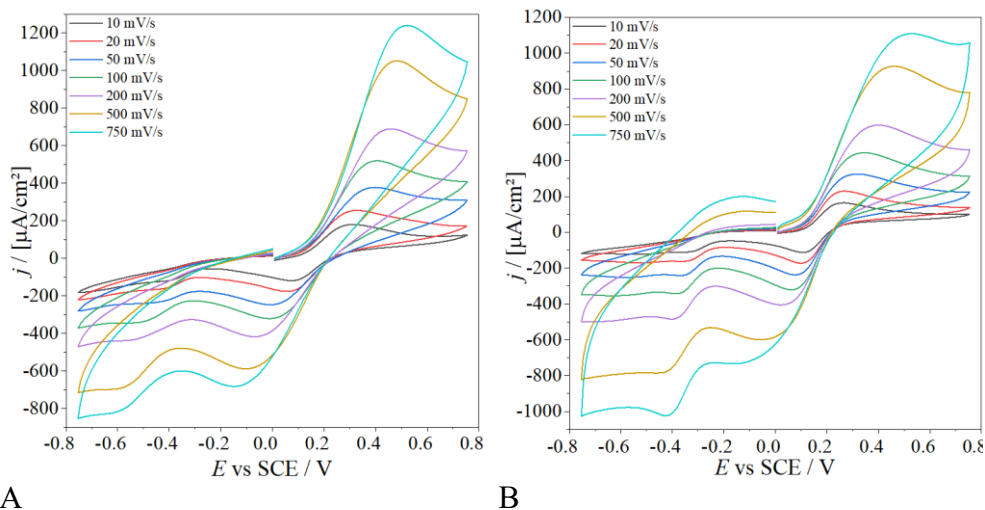
Figures 6.6: 3 mM probe signals at different scan rate respectively of GC_ 1 and GC_ 2.

The diffusion mechanism and the reversibility/irreversibility of the process was also evaluated by comparing the Log(j) vs Log(v) and J vs $v^{0.5}$.

Given the Randles–Ševčík equation for macroelectrodes (Chapter 1.2), it is possible to evaluate how current values change with the scan rate for different surface coverings. Positive deviations from the Randles–Ševčík plot can be observed with high surface coverage, while low surface coverage will lead to

uncomplete diffusion layers overlapping. Therefore, convergent diffusion will prevail, and a negative deviation will be observed.

The calculated values of $Log(j)$ vs $Log(v)$ and j vs $v^{0.5}$ for GC_1 and GC_2 are reported in Table 6.3 and Table 6.4.

Table 6.3 - Values obtained for GC_1.

Probe concentration	$Log(j)$ vs $Log(v)$	j vs $v^{0.5}$
1 mM	0.457	0.00040
2 mM	0.439	0.000764
3 mM	0.431	0.001113

Table 6.4 - Values obtained for GC_2.

Probe concentration	$Log(j)$ vs $Log(v)$	j vs $v^{0.5}$
1 mM	0.542	0.000529
2 mM	0.470	0.00082
3 mM	0.446	0.00116

Considering that the calculated values of $Log(j)$ vs $Log(v)$ are lower than the ideal value of 0.5, but not so far from it, the diffusion at the surface of the electrode is an intermediate case between convergent linear and the resulting shape in cyclic voltammetry is a pseudo-peak.

6.2.4.1. GC electrodes modified with oligo-BT₂T₄ films.

After selecting the best GC electrodes, it was possible to start modifying them with the oligo-BT_2T_4 film. At first, only the racemic mixture was electrodeposited to study the electrochemical behaviour of the film. The solution was prepared with 1 mg of pure BT_2T_4 racemate in 3 cm³ of acetonitrile and 0.3 g of $LiClO_4$ as electrolyte. The film was electrodeposited via cyclic voltammetry with 24 cycles from 0 to 1.35 V at a scan rate of 50 mV/s using a Pt wire as counter electrode and a SCE as reference electrode.

The characterisation of the modified electrode was performed in a 0.1 M $NaClO_4$ solution as electrolyte and $[Fe(CN)_6]^{4-}/[Fe(CN)_6]^{3-}$ as probe molecule.
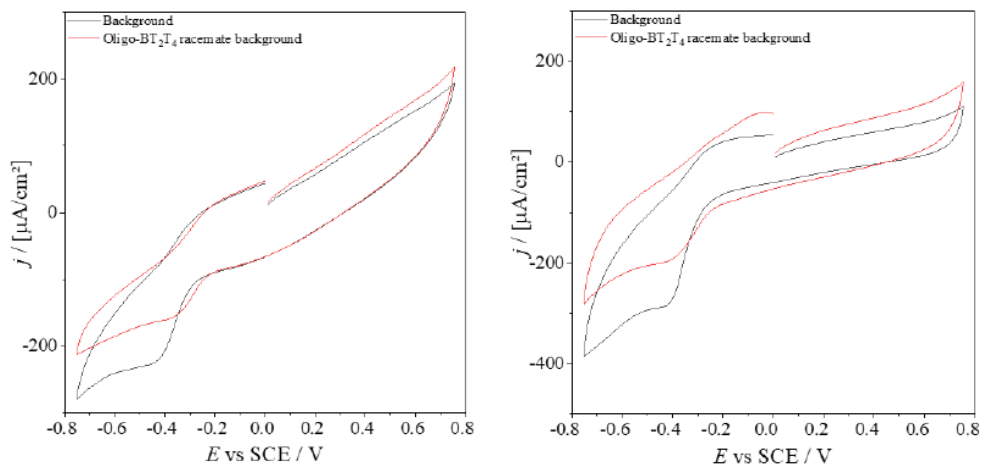
Figures 6.7 - Comparison of the background signals between the bare electrode and the electrode with the oligo-BT₂T₄ film deposited respectively of GC_ 1 and GC_ 2, at a scan rate of 100 mV/s.
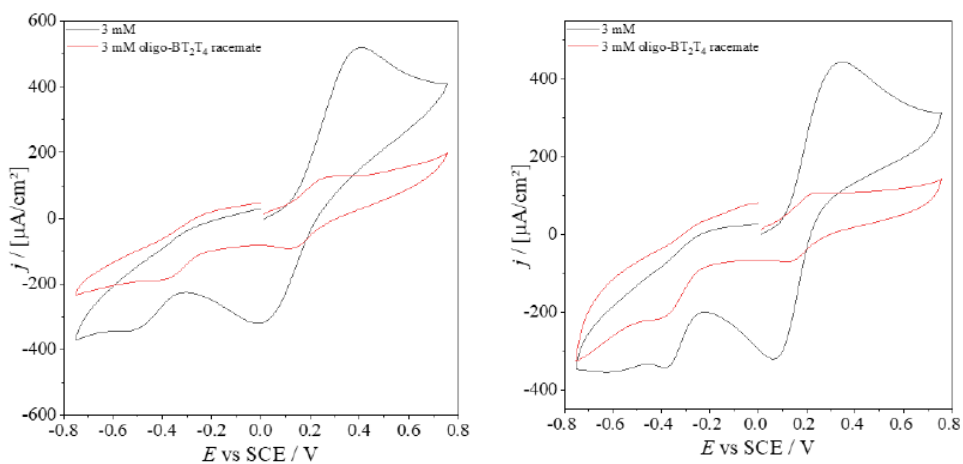
Figures 6.8 - Comparison of the 3 mM probe signals between the bare electrode and the electrode with the oligo-BT₂T₄ film deposited respectively of GC_ 1 and GC_ 2, at a scan rate of 100 mV/s.

What it is possible to see is that the probe cannot interact with the modified electrode. It can be seen from the graphs that the height of the probe peak (both in oxidation and in reduction) are almost absent when the oligo-BT$_2$T$_4$ film is present. This happens because the oligomeric film is too thick and it does not allow a good interaction between the probe molecule and the surface of the GC electrode in these working conditions.

6.2.4.2.   GC electrodes modified with MWCNTs.

The following step was the modification of the glassy carbon electrodes with the multi-walled carbon nanotubes (MWCNTs) and the comparison of the results obtained with the ones of the bare electrodes. The MWCNTs were purified according to the procedure reported in paragraph 6.2.2.

The electrodes have been modified by drop casting, depositing 20 μL of the MWCNTs solution on the electrodes surface, leaving it to dry at room temperature for 24 hours.

Studies of the electrochemical behaviour were performed on the background and on the 3 mM probe solution in cyclic voltammetry; the results are reported in Figure 6.9 and 6.10.

A   B

Figures 6.9 - Comparison of the background signals between the bare electrode and the electrode with the MWCNTs deposited respectively of GC_1 (A) and GC_2 (B), at a scan rate of 100 mV/s.

Figures 6.10 - Comparison of the 3 mM probe molecule signals between the bare electrode and the electrode with the MWCNTs deposited respectively of GC_1 and GC_2, at a scan rate of 100 mV/s.
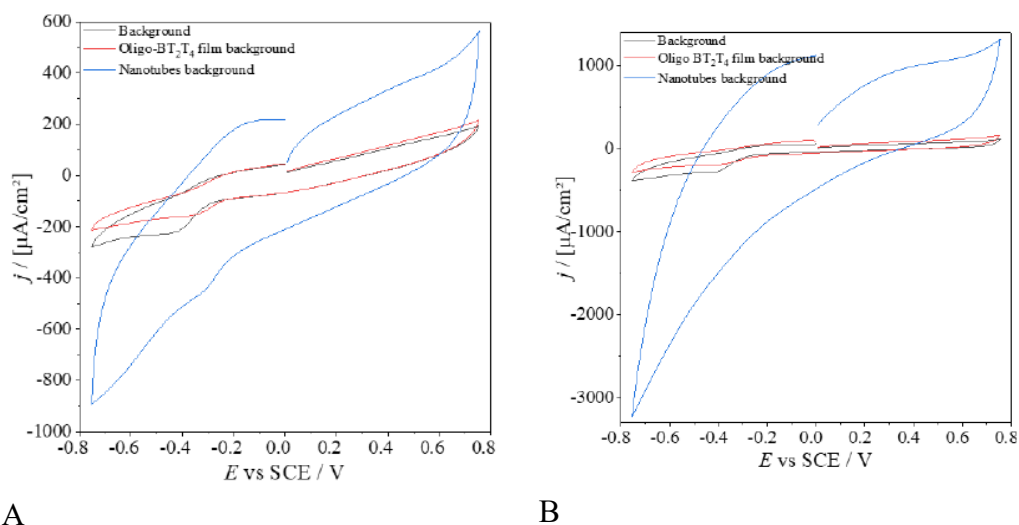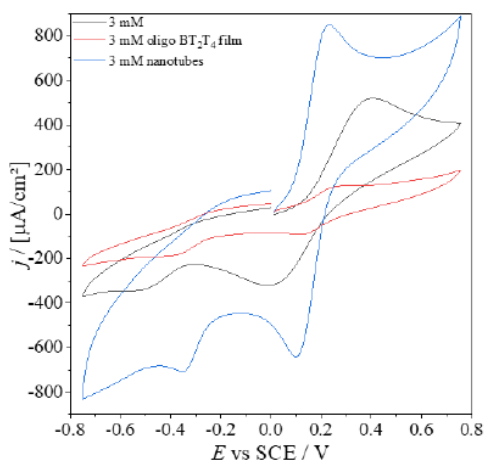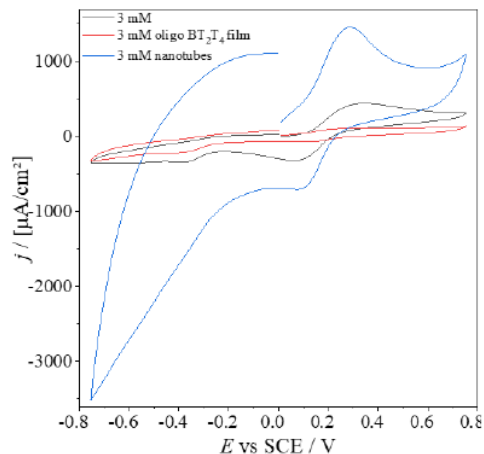
Comparing the results of the bare electrodes and of the modified electrodes, it is possible to see that the signal intensity is higher in the case of the modified electrodes, as expected. This effect appears to be more evident on GC_2 than on GC_1, which seems to have a better interaction with the MWCNTs.

Furthermore, it can also be noted that the peaks of the electrochemical probe are slightly anticipated both in terms of oxidation and reduction respect to the peaks of the bare electrode; this is probably due to thin layer diffusion [27]. This entails an advantage from an energy point of view, in addition to being able to identify the presence of carbon nanotubes even without considering the intensity of the current density signal but evaluating only the position of the peak.

In fact, nanomaterials in general, and therefore also MWCNTs, have the peculiarity of improving the diffusion of electroactive species on the active surface of the electrode [28, 29].

6.2.4.3. GC electrodes modified with MWCNTs + oligo-BT$_2$T$_4$ FILM.

Eventually, it was decided to combine both carbon nanotubes and the oligo-BT$_2$T$_4$ film on the same glassy carbon electrode to study the combined effect.

20 μL of the purified MWCNTs solution was drop casted on the surface of the GC electrode and left to dry for 24 hours. Subsequently, the oligo-BT$_2$T$_4$ film was electrodeposited from a solution of 2 mL of acetonitrile in which 1 mg of pure BT$_2$T$_4$ (racemic mixture) was dissolved using an excess of LiClO$_4$ (0.3 g) as supporting electrolyte. The film was electrodeposited in cyclic voltammetry with 24 cycles in the range 0 – 1.35 V at a scan rate of 50 mV/s, using a Pt wire as counter electrode and a SCE as reference electrode.

The modified electrode was characterized by cyclic voltammetry using NaClO$_4$ as supporting electrolyte and K$_4$[Fe(CN)$_6$] as probe molecule.
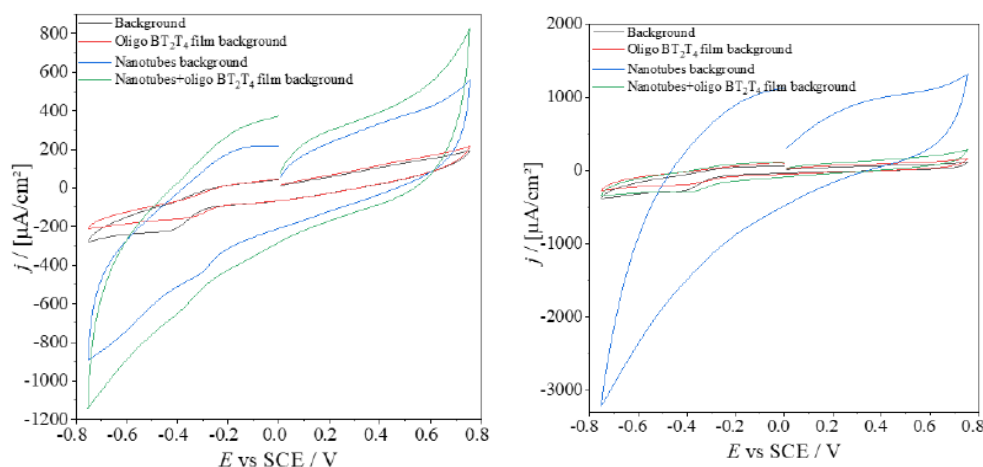
Figures 6.11 - Comparison of the background signals between the bare electrode, the electrode with the oligo-BT2T4 film deposited, the electrode with carbon nanotubes and the electrode with carbon nanotubes+oligo-BT2T4 respectively of GC_1 and GC_2, at a scan rate of 100 mV/s.
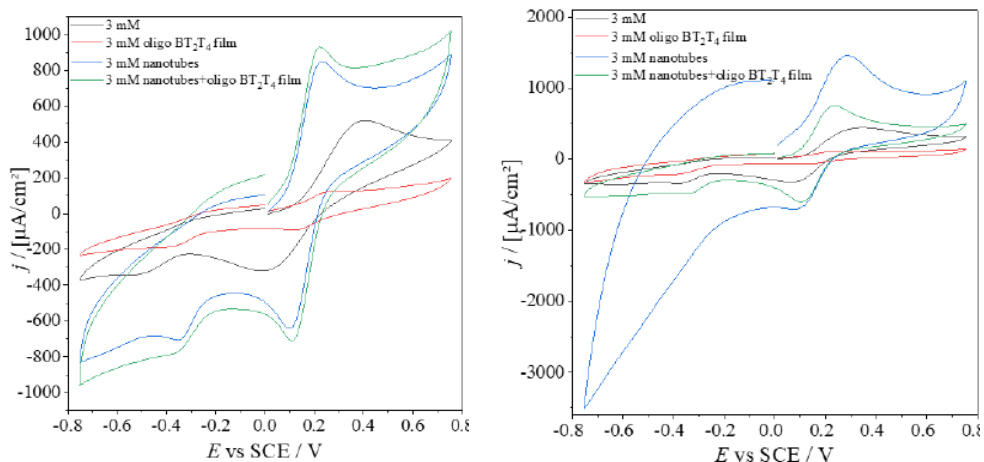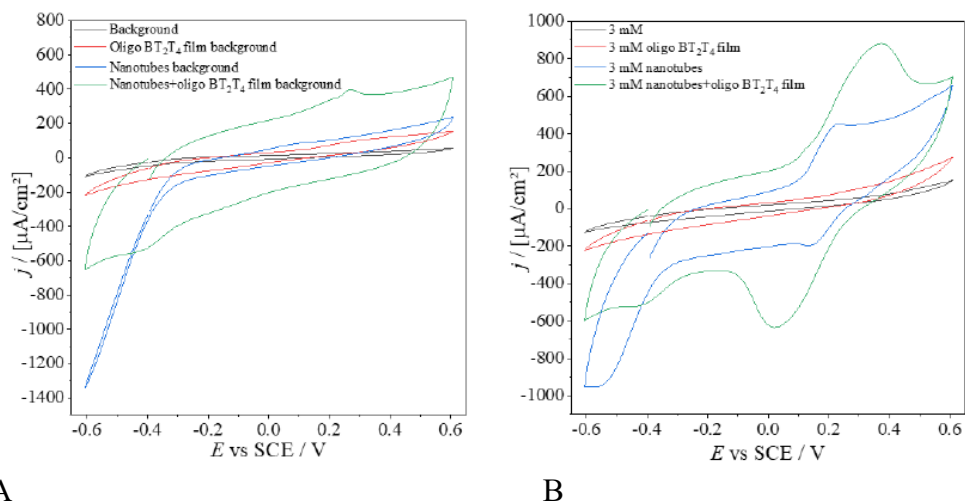
Figure 6.12- These figures show the comparison of the 3 mM $K_4[Fe(CN)_6]$ probe signals between the bare electrode, the electrode with the oligo-BT_2T_4 film deposited, the electrode with carbon nanotubes and the electrode with carbon nanotubes+oligo- BT_2T_4 film respectively of GC_1 and GC_2, at a scan rate of 100 mV s^{-1}.

The graphs show how the presence of nanotubes favours a huge increase in current density compared to the presence of only oligo-BT_2T_4 film; also, the probe peaks are much more defined. A further aspect that can be mentioned is that in the latter case, as in the case in which there is only the presence of MWCNTs, the peaks related to the electrochemical probe are slightly anticipated respect to the bare electrode (this effect is more visible on the GC_1 electrode, reported in the A figures), thus confirming the fact that carbon nanotubes can lead to oxidation peaks with potentials more shifted to the left (smaller potentials) and reduction peaks more shifted to the right (higher potentials), confirming the energy advantage due to an excellent interaction with the active surface of the glassy carbon.

6.2.4.4. SPE modified with MWCNTs+oligo-BT₂T₄ film.

Considering the results obtained with the use of a glassy carbon electrode, it was decided to simulate the same tests and the same conditions on another type of support, the screen-printed electrode (SPE), to have a comparison in terms of reproducibility. Four different situations were taken into account for the characterisation with the $K_4[Fe(CN)_6]$ probe molecule: the bare SPE, the SPE with the oligo-BT_2T_4 film, SPE+MWCNTs and SPE with both MWCNTs and the oligo-BT_2T_4 film. The amount of MWCNTs deposited on the SPE was

245

proportional to the electroactive surface area, *i.e.*, 35 μL instead of 20 μL. For the oligo-BT_2T_4 film electrodeposition, it was necessary to change the solvent for the electrodeposition, since acetonitrile could dissolve the SPE electrode. So, an ionic liquid has been used, 1-butyl-3-methylimidazolium bis(trifluoromethylsulfonyl)imide.

A   B

Figures 6.13- Comparison between the background and the 3 mM $K_4[Fe(CN)_6]$ probe signals of the bare electrode, the electrode with the oligo- BT_2T_4 film deposited, the electrode with carbon nanotubes and the electrode with carbon nanotubes+oligo-BT_2T_4 film of 4 different graphite SPEs, at 100 mV/s as scan rate.

Observing the graphs of Figure 6.13, the trend seen with the glassy carbon electrodes is confirmed, as a substantial increase in the signal intensity is achieved in the presence of the nanotubes. The difficulty of the interaction of the $K_4[Fe(CN)_6]$ probe seems to be greater in this analysis on graphite SPE compared to what happened with glassy carbons. In fact, the peaks are much less evident or practically absent (on bare electrode and electrode with only oligo- BT_2T_4). In any case it is possible to say that the results obtained with both types of electrodes are comparable and quite in line with what was expected as regards the interaction between the modified electrode and the $K_4[Fe(CN)_6]$ probe.

6.2.5. Electrochemical impedance spectroscopy (EIS) characterisation.

Electrochemical impedance spectroscopy (EIS) is an important technique that can be used for the analysis of materials and interfaces. This technique, as well as cyclic voltammetry, exploits a standard 3-electrode cell, with a Pt counter electrode, a working electrode with the material of interest and a reference electrode, generally Saturated Calomel Electrode (SCE).

The parameters for EIS experiments are reported below:

- First applied frequency: 65000 Hz

- Last applied frequency: 0.1 Hz

- Number of frequencies: 50

- Frequency step type: Logarithm

- Amplitude: 0.01 V_{RMS}

The EIS analyses were performed on the same electrodes studied in cyclic voltammetry: GC_1, GC_2 and screen-printed electrode, with no deposition, with only the oligo-BT_2T_4 film (racemate), with only MWCNTs and with both MWCNTs and oligo-BT_2T_4 film (racemate).

6.2.5.1. Glassy carbon electrodes.
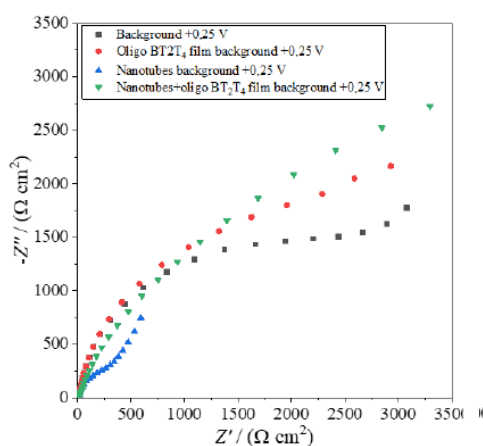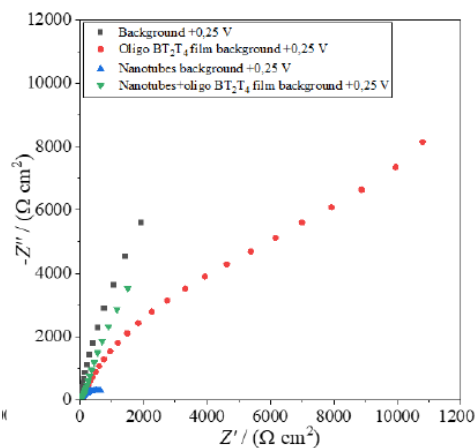
A   B
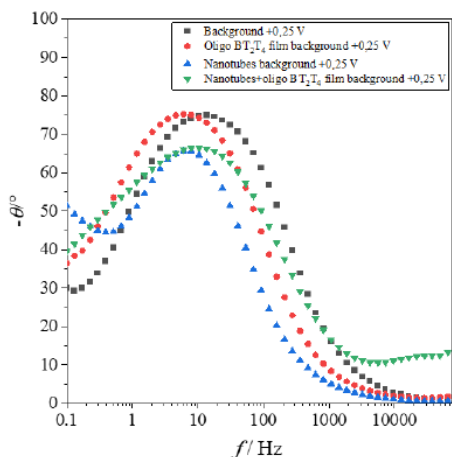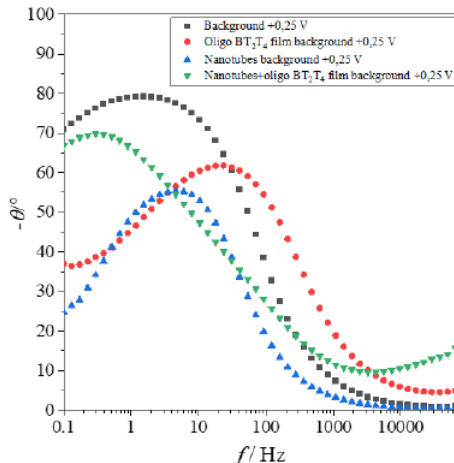
C
D

Figure 6.14 A and B - Comparison of the Nyquist plots background signals between the bare electrode, the electrode with the oligo-BT$_2$T$_4$ film (racemate), the electrode with carbon nanotubes and the electrode with carbon nanotubes+oligo-BT$_2$T$_4$ film(racemate) respectively of GC_1 (A) and GC_2 (B), at +0.25 V.

Figures 6.14 C and D - Comparison of the Bode phase plots background signals between the bare electrode, the electrode with the oligo-BT$_2$T$_4$ film (racemate), the electrode with carbon nanotubes and the electrode with carbon nanotubes+oligo-BT$_2$T$_4$ film(racemate) respectively of GC_1 (C) and GC_2 (D) at +0.25 V.

Looking at the Nyquist plots and the Bode phase plots of the background, the bare glassy carbon electrode can be considered as a capacitor; this fact is more evident on the GC_2. This is also confirmed by the Bode phase plots in which there is the maximum at about 80°, quite close to the ideal value of 90°. When, on the other hand, only carbon nanotubes are present, there is a semicircle and then a Warburg straight line at about 45°. This trend may be due to the functional groups of the nanotubes themselves. Looking at the plot of the electrode with only BT$_2$T$_4$ (racemate), it can be seen that it is more resistive than in the other cases. Considering the case in which there are carbon nanotubes+ BT$_2$T$_4$ (racemate), it is possible to see a capacitor trend but with a lower resistance than the case of the bare electrode and the electrode with only the deposited BT$_2$T$_4$ (racemate).
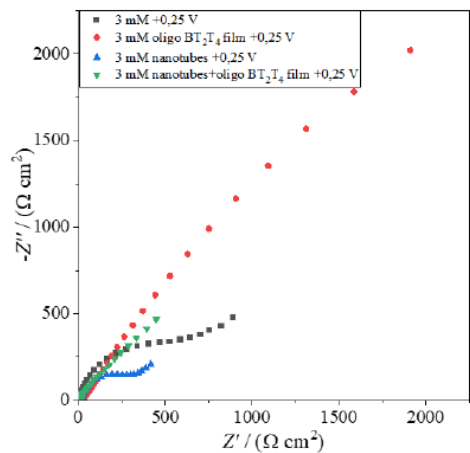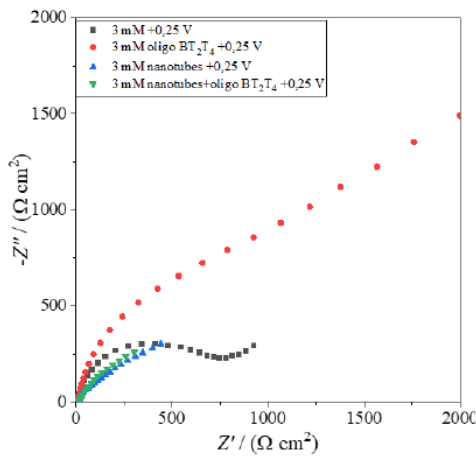
A   B
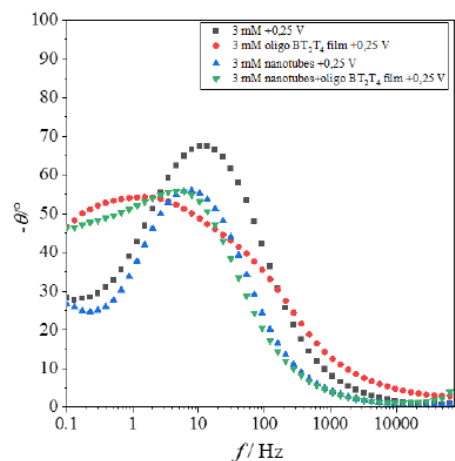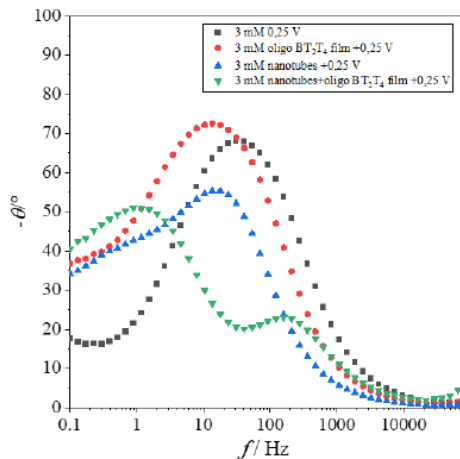
C   D

Figures 6.15 A and B - Comparison of the Nyquist plots K4[Fe(CN)6] 3 mM signals between the bare electrode, the electrode with the oligo-BT2T4 film (racemate), the electrode with carbon nanotubes and the electrode with carbon nanotubes+oligo-BT2T4 film(racemate) respectively of GC_1 and GC_2, at +0.25 V.

Figures 6.15 C and D - Comparison of the Bode phase plots K4[Fe(CN)6] 3 mM signals signals between the bare electrode, the electrode with the oligo-BT2T4 film (racemate), the electrode with carbon nanotubes and the electrode with carbon nanotubes+oligo-BT2T4 film(racemate) respectively of GC_1 and GC_2, at +0.25 V.

Considering the Nyquist plots and the Bode phase plots of the 3 mM $K_4[Fe(CN)_6]$ probe, the bare electrode can be fitted with the classic Randles circuit, in which there is a semicircle and then a Warburg-like diffusion; in the case where only carbon nanotubes are present, it is a similar but less resistive trend to charge transfer (nanotubes improve the efficiency of the charge transfer process). The case in which only the BT_2T_4 (racemate) is present is

249

certainly the most resistive as there are two semicircles. This aspect is confirmed in the GC_2 Bode phase plot in which there are 2 "humps" in the signal to indicate the presence of the double semicircle. The last case, *i.e.*, the one in which carbon nanotubes+BT$_2$T$_4$ (racemate) are present, is the one in which there is an even more conductive trend as the semicircle is very small, indicating a low resistance to charge transfer.

6.2.5.2.   Screen-printed electrodes.

The EIS characterisation on the screen-printed electrodes was carried out in the same way as the tests performed on the glassy carbon electrodes.

A

B

C

D
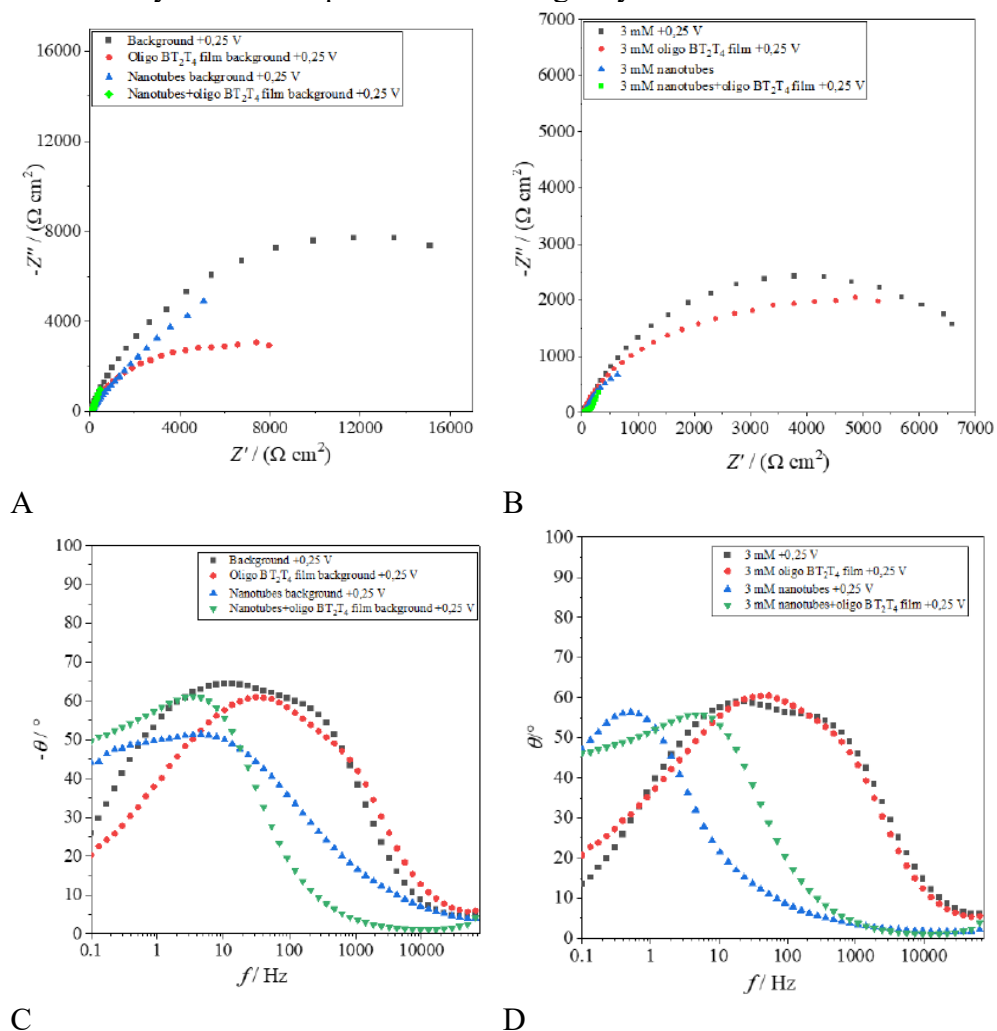
Figures 6.16 A and B - Background (Figure 4.4A) and the 3 mM K$_4$[Fe(CN)$_6$] probe (Figure 4.4B) signals comparison of the Nyquist plots between the bare electrode, the electrode with

In this case, the Nyquist plots and the Bode phase plots have a slightly different trend compared to the previous cases as different electrode supports are being evaluated. Furthermore, the screen-printed electrodes are not "perfect", *i.e.*, they have some defects due to the printing of the ink. This leads to trends, especially in the Bode phase plots, which are certainly different, with different oscillations, compared to glassy carbon electrode.

Evaluating the plots in more detail, there are two semicircles in the Nyquist plot of the bare electrode; this has been confirmed by the double "hump" present in the Bode phase. Also, when the oligo-BT$_2$T$_4$ film is present, there are two semicircles both in the background and with the probe. The particularity is a lower resistivity of BT$_2$T$_4$ film than the one found on the glassy carbon electrodes. This could indicate a better intrinsic interaction of BT$_2$T$_4$ on this type of electrodes, probably due to the occurrence of π-π interactions. On the other hand, in the case in which only carbon nanotubes or carbon nanotubes+BT$_2$T$_4$ are present, there is a small semicircle to indicate a lower resistance to electron transfer (as expected) and then a capacitive type of trend. More specifically, it can be noted that the last case, the one in which there are carbon nanotubes+BT$_2$T$_4$, is the one with the lowest impedance value and therefore the one with the lowest resistance. In general, the trend of the EIS measurements (both Nyquist plots and Bode phase plots) is compatible for the two different types of electrodes used. The graphs are coherent to each other and in line with the corresponding cyclic voltammetries (reported in paragraph 6.2.4.4). The most interesting thing to note is the better interaction that seems to exist between the BT$_2$T$_4$ and the graphite screen-printed electrodes compared to the glassy carbon ones, even if the comparison is difficult to make as the solvents used in the electrodeposition are different.

6.3. Chiral characterisation.

To exploit the real advantages of the oligo-BT$_2$T$_4$ film, it was necessary to start depositing the two enantiomers of BT$_2$T$_4$, *i.e.*, (R)-oligo-BT$_2$T$_4$ and (S)-oligo-BT$_2$T$_4$. It was therefore necessary to change the working conditions and move to the ideal ones already studied by Sannicolò *et al.* [8].

First, it was necessary to work with only few mL of the solution instead of 20 mL, so it was necessary to change the configuration of the cell.
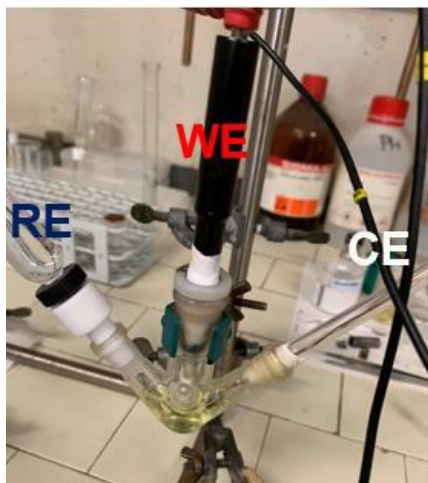
Figure 6.17 - Cell and experimental set-up used in the chiral tests.

As Figure 6.17 shows, the cell has three outputs in which the counter electrode (a Pt wire) and the reference electrode (SCE or Ag/AgCl) on the outside and the working electrode in the central part of the cell were inserted.

In this second phase of the work, the electrochemical probe used for the characterization was a chiral probe, N,N-dimethyl-1-ferrocenylethylamine (both R and S enantiomers, Figure 6.18). To use it in the best conditions, it was necessary to change the electrolyte from sodium perchlorate to tetrabutylammonium perchlorate; a change of solvent from water to acetonitrile was also necessary.
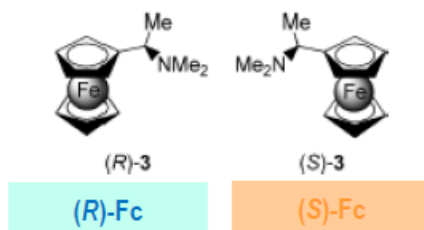
Figure 6.18 - The two enantiomers of N,N-dimethyl-1-ferrocenylethylamine probe.

To have enantiodiscrimination, it is necessary to create a diastereoisomeric environment. To achieve this result, there are possible combinations between chiral probes and the enantiopure chiral film. So, it is possible to use the R and S enantiomers of the probe on the R-BT_2T_4 film (or with the S-BT_2T_4 film, but there will be an inversion of the position of the peaks). Otherwise, it is possible to test only one enantiomer of the probe (R or S) on two different electrodes with R and S enantiomers of the oligo-BT_2T_4 film (Table 6.5)

Table 6.5 - Four possibilities to obtain a diastereomeric environment.

Chiral probe (N,N-dimethyl-1-ferrocenylethylamine)	Chiral oligo-BT_2T_4 film
R and S	R
R and S	S
R	R and S
S	R and S

In fact, in this section only one enantiomer of the chiral film was used to test the R and S enantiomers of the probe (first part) and then only the S probe was tested, electrodepositing the R and S films in two different trials (second part). To carry out the following tests, it was decided to continue with the glassy carbon electrode that has given the most efficient responses in terms of current, which is the one who seemed to have a better interaction with the probe, even when modified with carbon nanotubes and the oligo-BT_2T_4 film. For these reasons, the glassy carbon electrode chosen for these tests was GC_2.

The final part of this work was the application of this enantiopure system on screen printed electrodes to have a disposable sensor.

6.3.1. GC modified with R-BT_2T_4 films on R and S chiral probes.

As a first attempt, it was decided to create a diastereoisomeric environment by using the R enantiomer of the oligo-BT_2T_4 film and evaluating the two chiral probes R and S of the N,N-dimethyl-1-ferrocenylethylamine. Four different types of tests were carried out using the R and S enantiomers of the chiral probe by electrodepositing the oligo-BT_2T_4 film on GC_2 electrode. First, it was

decided to deposit once again the racemate of the oligo-BT$_2$T$_4$ film, as described in paragraph 6.2.4.1, to verify that the signals of the two enantiomers are equal in peak potential (Figure 6.19). The characterisation tests were performed at a scan rate of 50 mV/s from 0 to 0.7 V with N,N-dimethyl-1-ferrocenylethylamine 3 mM, both for probe R and S.
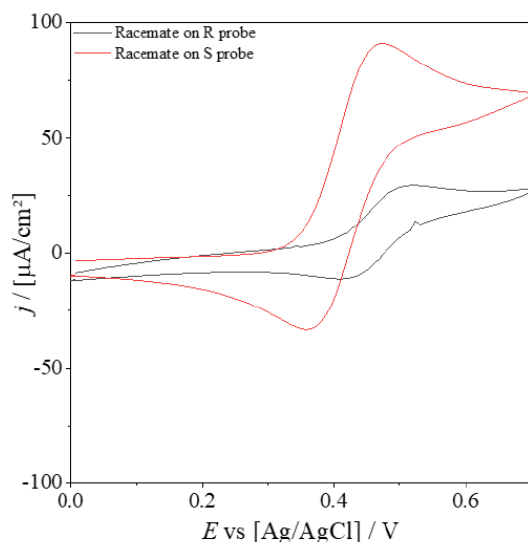
Figure 6.19 - GC_2 modified with the racemate oligo-BT$_2$T$_4$ film to test R and S enantiomers of the probe.

Looking at this figure, it is possible to understand that the obtained trend does not reflect what expected. The two signals of the R and S probes were supposed to be overlapped, but there is a slight shift to the right of the signal related to the R probe, even though it is not possible to talk about "peak separation" in this case (the difference in potential between the two peaks is too low). Furthermore, the intensities and shapes of the two signals are different: the CV related to the R probe appears to be a step, and the CV related to the S probe looks more like a peak. This indicates a non-identical diffusion in the two different tests. What can be hypothesized is a different electrodeposition of the oligo-BT$_2$T$_4$ film due to small differences on the surface of the glassy carbon electrode.

The second test was carried out by depositing only the carbon nanotubes on the glassy carbon electrode, by drop casting (20 µL). This test was used for the evaluation of a possible enantiodiscrimination effect exclusively due to the carbon nanotubes (Figure 6.20). The characterisation tests were performed at

a scan rate of 50 mV/s from 0 to 0.7 V with N,N-dimethyl-1-ferrocenylethylamine 3 mM, both for probe R and S.

Figure 6.20 - GC_2 modified with carbon nanotubes, test with R and S chiral probe 3 mM.

In this case, the trend is very particular, because it shows that carbon nanotubes have chiral elements that could lead to enantioselection, but also something different happens in the reported CVs. It seems that carbon nanotubes have a different trend on the two probes in terms of electrochemical reversibility of the signals. In fact, it can be seen that for the R probe, the oxidation peak is shifted to higher potentials, but the reduction peak is shifted to lower potentials, as well as having a different signal shape, compared to the one obtained with the S probe. In this case, it is not possible to talk about a real enantioselection, but surely there is a different interaction of the carbon nanotubes with the two different chiral probes.

The third test was carried out by first depositing the carbon nanotubes on the glassy carbon electrode in the same way, then, after waiting for 24 hours, the racemate oligo-BT_2T_4 film was electrodeposited. This test was necessary to have a comparison with the following ones, in which the electrode was modified with carbon nanotubes and the enantiopure oligo-BT_2T_4 film (Figure 6.21).

The characterisation tests were performed at a scan rate of 50 mV/s from 0 to 0.7 with R and S N,N-dimethyl-1-ferrocenyletylamine 3 mM.

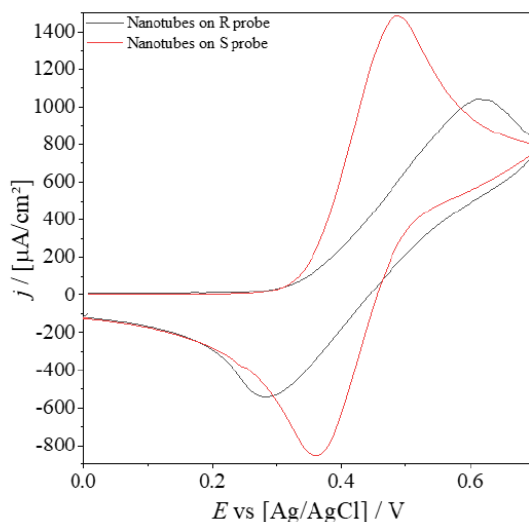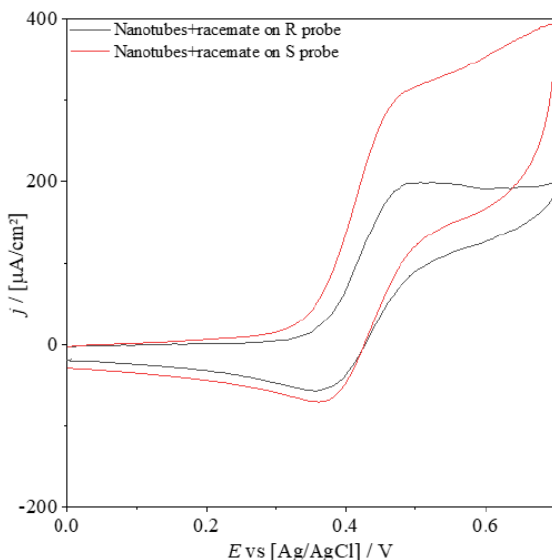*Figure 6.21 - GC_2 modified with carbon nanotubes+oligo-BT$_2$T$_4$ film racemate, test with R and S chiral probe 3 mM.*

In this case, the trend shown in the graph is similar to the expected one. Indeed, despite the presence of the carbon nanotubes, the racemate oligo-BT$_2$T$_4$ film should in theory guarantee overlapping signals between the two enantiomers, since a diastereoisomeric environment is not created.

The fourth test was carried out by first depositing the carbon nanotubes on the glassy carbon electrode as previously explained, then, after waiting for 24 hours, the enantiopure R-oligo-BT$_2$T$_4$ film was electrodeposited with 24 cycles at a scan rate of 50 mV/s. The characterisation tests were performed at a scan rate of 50 mV/s from 0 to 0.7 V with both R and S enantiomers of the chiral probe at a concentration of 3 mM (Figure 6.22).
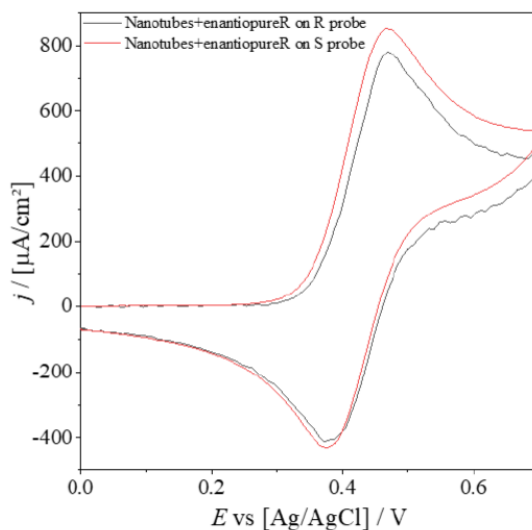
Figure 6.22 - GC_2 modified with carbon nanotubes+R-oligo-BT$_2$T$_4$ film, test with R and S chiral probe 3 mM.

In this case, a separation of the peaks was expected, due to the diastereoisomeric environment, but this does not happen. The peaks related to the two enantiomers of the probe are perfectly superimposable. This may be caused by the rearrangement of the enantiopure film on the carbon nanotubes that is not ideal to give a perfect diastereoisomeric environment and therefore fails to give enantioselection.

In Figure 6.23, all these tests are reported together, but separated according to the enantiomeric probe used. This test was used to evaluate the possible displacement of the peaks of the probe itself based on the type of electrode modification performed.

It is important to underline that these combinations of electrode type, electrode modification, probe used and operating conditions had never been tested all together, so it was possible to get a rough idea about the possible trend, but not an absolute certainty.
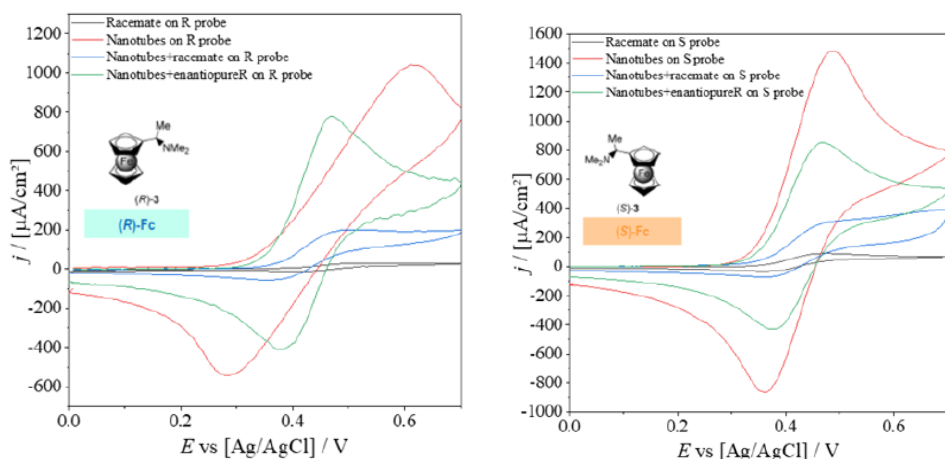
Figure 6.23 A and B - GC_2 modified with BT₂T₄ racemate, carbon nanotubes, carbon nanotubes+BT₂T₄ racemate and carbon nanotubes+R-oligo-BT₂T₄. Figure 29A (left) shows all tests on probe R, Figure 29B (right) shows all tests on S chiral probe, at a scan rate of 50 mV/s.

These graphs are useful as they allow to confirm the fact that the carbon nanotubes improve the signal intensity (as happens for the $K_4[Fe(CN)_6]$ probe). Furthermore, it is interesting to note how the signals of the tests for the racemate oligo-BT₂T₄ and for the enantiopure oligo-BT₂T₄ have a different trend. The signals of enantiopure oligo-BT₂T₄ (on nanotubes) is more intense and has a peak shape, the signal for the racemate oligo-BT₂T₄ (on nanotubes) is less intense and has a step signal. This could indicate a different type of diffusion at the electrode surface depending on the type of oligo-BT₂T₄ used. What also can be seen from these graphs is that any modification of the electrode in these oligo-BT₂T₄ electrodeposition conditions (24 cycles at 50 mV/s) does not lead to a shift in the position of the peaks, apart from the anomaly recorded with respect to the modified electrode only with carbon nanotubes, in which there appears to be an electrochemical reversibility change. What can be said from the analysis of the previous graphs is that the electrodeposition conditions used (also considering the presence of the nanotubes) are not ideal for having an enantioselection on this type of electrode. So, it was therefore necessary to change the deposition conditions of oligo-BT₂T₄ to verify a possible enantioselection ability.

6.3.2. GC modified with R-BT$_2$T$_4$ and S-BT$_2$T$_4$ on S chiral probe.

As concluded in the previous section, the conditions used to achieve enantiodiscrimination have not led to results, so it was necessary to change the conditions. A further aspect to consider is that the available quantity of N,N-dimethyl-1-ferrocenylethylamine chiral probes R and S is very limited as they are substances with a high economic value. In this phase, therefore, it was decided to reach the diastereoisomeric environment in a different way compared to what happened previously. It was decided to use a single chiral probe, the S enantiomer, and to carry out tests with enantiopure R-oligo-BT$_2$T$_4$ and S-oligo-BT$_2$T$_4$ (considering Table 5, this is the last case). From a practical point of view, this changes nothing, even though a separation of the peaks due to a diastereoisomeric interaction is still expected. It was decided to start by electrodepositing the oligo-BT$_2$T$_4$ film with 24 cycles at a scan rate of 50 mV/s. The diastereoisomeric environment was created by depositing both R-oligo-BT$_2$T$_4$ and S-oligo-BT$_2$T$_4$ (after drop casting the carbon nanotubes) for S probe analysis (Figure 6.24). The characterisation tests were performed at a scan rate of 50 mV/s from 0 to 0.6 V with N,N-dimethyl-1-ferrocenylethylamine 3 mM, for probe S, by using both enantiomers of oligo-BT$_2$T$_4$.
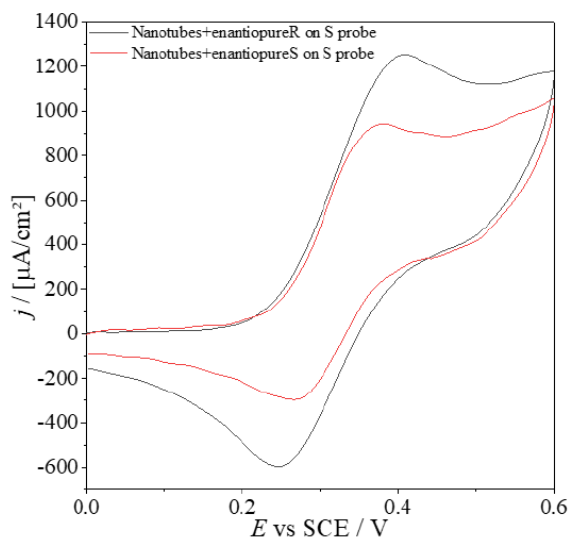
Figure 6.24 - GC_2 modified with carbon nanotubes+R-BT$_2$T$_4$ and S-BT$_2$T$_4$ enantiopure to test S chiral probe.

In this situation the two signals are practically superimposed. In reality, a very small separation is noted, in the order of tens of mV, which however is too low to be considered a "a good enantiomeric separation" because it may also be

due to other random factors. In general, therefore, it can be said that these conditions of deposition of the chiral film on carbon nanotubes do not lead to enantioselection.

Subsequently, it was decided to test another electrodeposition condition, in which the film was electrodeposited with 36 scan cycles at a scan rate of 50 mV/s. The way of creating the diastereomeric environment was the same as before, so both R-oligo-BT$_2$T$_4$ and S-oligo-BT$_2$T$_4$ were deposited to evaluate the S probe.

The characterisation tests were performed at a scan rate of 50 mV/s from 0 to 0.6 V on a S probe concentration of 3 mM (Figure 6.25).

Figure 6.25 - GC_2 modified with carbon nanotubes+R-BT$_2$T$_4$ and S-BT$_2$T$_4$ enantiopure to test S chiral probe.

The signals, in particular the position of the peaks, must be considered superimposed. It is not possible to talk about enantioselection in this case, even if some interesting aspects can be discussed. The shape of the two signals is very different from each other and this is unexpected. It seems to be a different diffusion of the species at the electrode. The electrode modified with carbon nanotubes+R-oligo-BT$_2$T$_4$ has a peak signal and with a much higher intensity than the signal related to the electrode modified with nanotubes and S-oligo-BT$_2$T$_4$, which has a step-like signal and lower intensity.

Despite this, what can be noticed is the absence of enantiodiscrimination, which was the aim of these tests. The electrodeposition conditions used in this experiment were not effective.

For these electrodeposition conditions, it was decided to carry out an electrochemical impedance spectroscopy test. In detail, Nyquist plot and Bode phase plot were constructed both for the tests with carbon nanotubes+R-oligo-BT_2T_4 and for carbon nanotubes+S-oligo-BT_2T_4.

The potentials tested were +0.2 V, where the reaction has not taken place yet, and at +0.4 V, where the reaction is taking place. These points were chosen both for Nyquist plots and Bode phase plots (Figure 6.26).
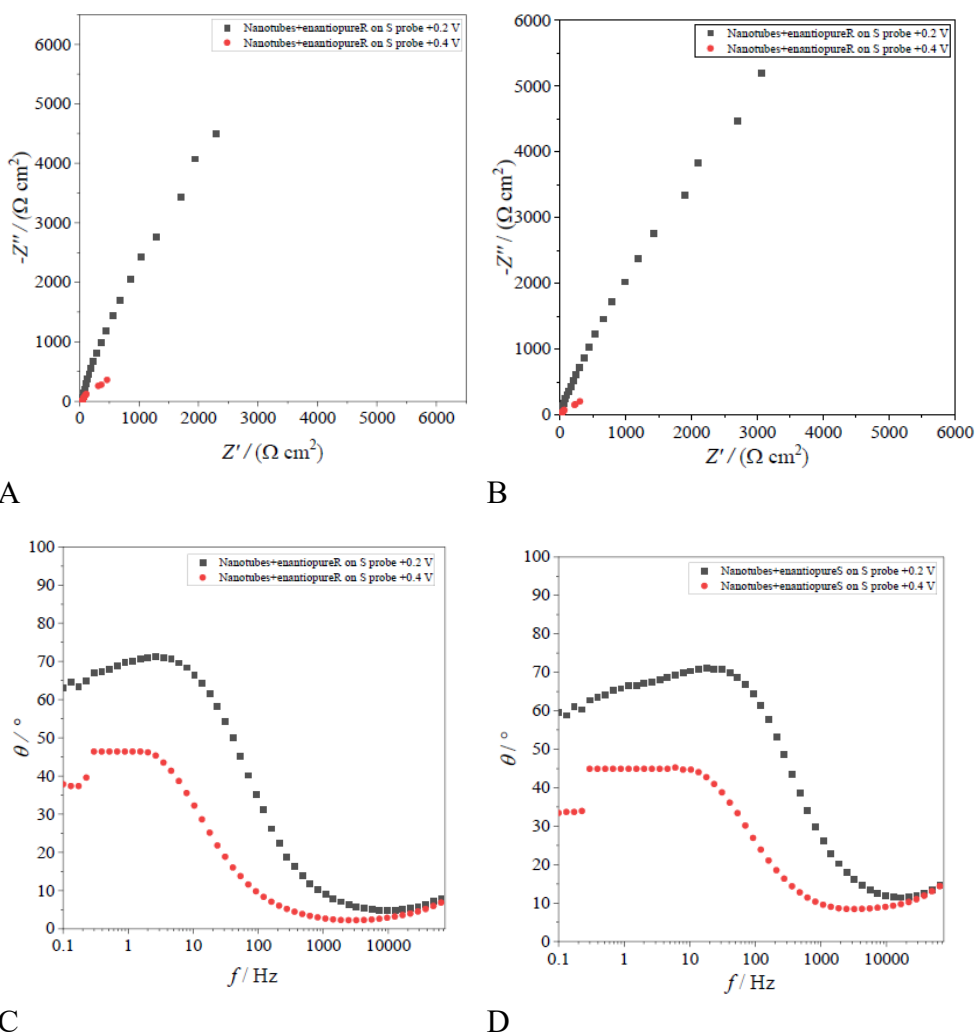
Figure 6.26 A and B – Comparison of the Nyquist plots of carbon nanotubes+R-BT$_2$T$_4$ (left) and nanotubes+ S-BT$_2$T$_4$ (right) GC_2 signals on probe S at +0.2 V and +0.4 V.

Figure 6.26 C and D – Comparison of the Bode phase plot of carbon nanotubes+R-BT$_2$T$_4$ (left) and nanotubes+S-BT$_2$T$_4$ (right) GC_2 signals on probe S at +0.2 V and +0.4 V.

The graphs show how at +0.2 V the trend is capacitive, as expected, considering that, at this potential, the reaction has not occurred yet. This trend is found both for the Nyquist plot and the Bode phase plot (peak around 75°, close to the one of an ideal capacitor) and both for the electrode modified with carbon nanotubes+R-oligo-BT$_2$T$_4$ and carbon nanotubes+S-oligo-BT$_2$T$_4$.

At +0.4 V, the trend is different, as at this potential the reaction occurs. In the Nyquist plots it seems that the resistance to electronic transfer is very low and that a Warburg-type diffusion is reached immediately. This trend must be confirmed with further experiments, but it would indicate an excellent interaction between the modified electrode and the S chiral probe. Also, in the Bode phase plot, the peak is lower working at +0.4 V (less than 50°) than at +0.2 V, indicating that there is no longer a capacitive-type trend, but there is a redox reaction.

Another condition was subsequently tested for comparison with the previous ones. It was decided to carry out another deposition of the oligo-BT$_2$T$_4$ film with 72 scan cycles at a scan rate of 200 mV/s. The way of creating the diastereomeric environment was the same as before, so both R oligo-BT$_2$T$_4$ and S-oligo-BT$_2$T$_4$ were deposited to evaluate the S probe. The characterisation tests were performed at a scan rate of 50 mV/s from 0 to 0.6 V with a S probe concentration of 3 mM (Figure 6.27).
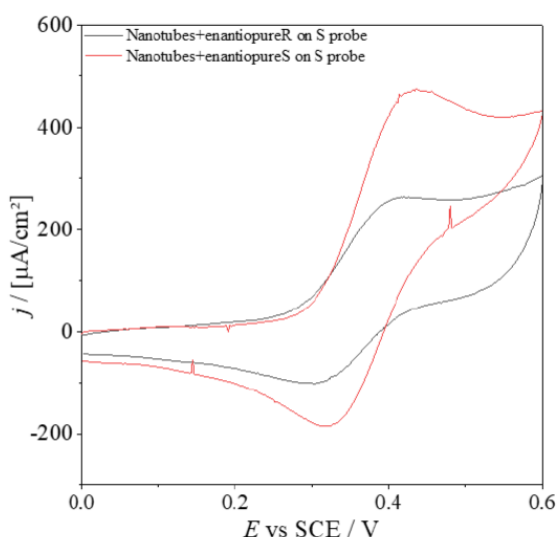
Figure 6.27 - GC_2 modified with carbon nanotubes+R-BT$_2$T$_4$ and S-BT$_2$T$_4$ enantiopure to test S probe.

From this test it can be seen that this method of electrodeposition on the carbon nanotubes is not effective for obtaining a differentiation of the peaks. In fact, the peaks related to the carbon nanotubes+R-oligo-BT$_2$T$_4$ film and carbon nanotubes+S-oligo-BT$_2$T$_4$ film are overlapping, thus indicating a non-enantioselection.

Seeing that also these electrodeposition conditions are not the best ones for having enantiodiscrimination, it was decided to try with new conditions; so, the enantiopure oligo-BT$_2$T$_4$ film was deposited with 36 scan cycles at a scan rate of 200 mV/s from 0 to +1.35 V. The diastereoisomeric environment was creating by depositing both R-oligo-BT$_2$T$_4$ and S-oligo-BT$_2$T$_4$ and characterised using only the S probe.

Before testing the probe with this new deposition method in the presence of carbon nanotubes, it was decided to electrodeposit the enantiopure films on the bare glassy carbon electrode (with 36 scan cycles at 200 mV/S). This test was necessary to verify that BT$_2$T$_4$ gave enantioselection at least "individually" and that there were no intrinsic problems related to it. The characterisation tests were performed at a scan rate of 50 mV/s from 0 to +1.2 V on with a concentration of S probe of 3 mM (Figure 6.28).

263
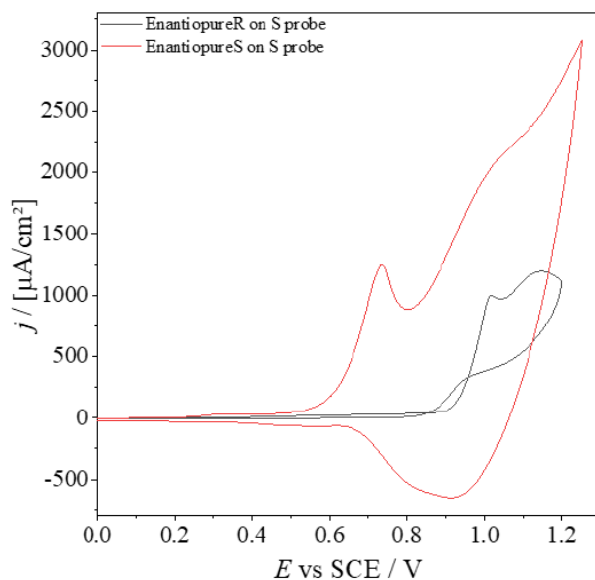
Figure 6.28 - GC_2 modified with R-BT$_2$T$_4$ and S-BT$_2$T$_4$ enantiopure to test S probe.

The peak separation predicted by theory has finally been confirmed by this test. The separation is large (about 300 mV), suggesting a good interaction of the two enantiopure films on the glassy carbon support.

At this point it was possible to deposit the R- and S-oligo-BT$_2$T$_4$ film on the carbon nanotubes deposited on the glassy carbon electrode with the same conditions (36 cycles at 200 mV/s from 0 to +1.35 V). The characterisation tests were performed at a scan rate of 50 mV/s from 0 to +1.2 V on with a concentration of S probe of 3 mM (Figure 6.29).
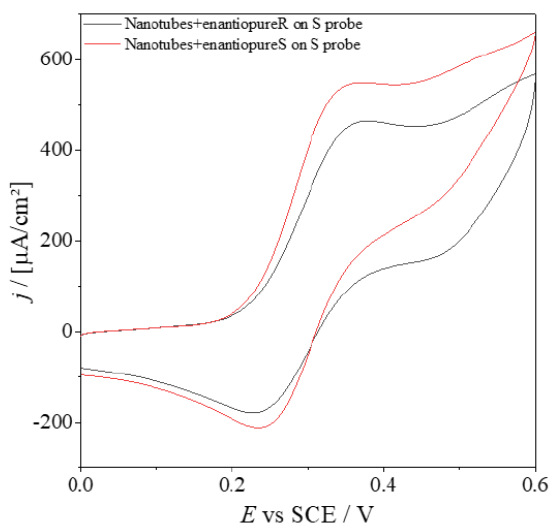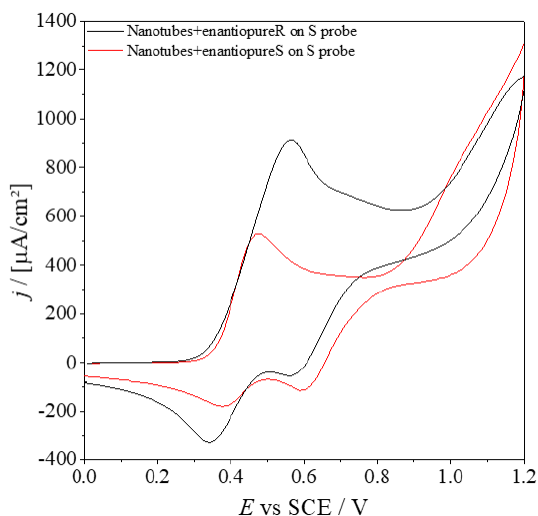
Figure 6.29 - GC_2 modified with carbon nanotubes+R-BT$_2$T$_4$ and S-BT$_2$T$_4$ enantiopure to test S probe.

Unlike the previous cases in which the peaks had always been overlapped, in this case we have a "separation", even if different from what was expected. In fact, is not possible to speak of a "classical" enantioselection, as the peaks are not shifted to the right or to the left, there seems to be a change in the electrochemical reversibility of the signal. The presence of the enantiopure R (with the nanotubes) shifts the oxidation peak to the right but the reduction one to the left with respect to the enantiopure S signal (with the nanotubes). This result is certainly surprising and unexpected.

The tests were repeated on a new carbon nanotubes+oligo- BT$_2$T$_4$ film (both R and S) deposition analysing the S probe to confirm the results showed before (Figure 6.30).

265
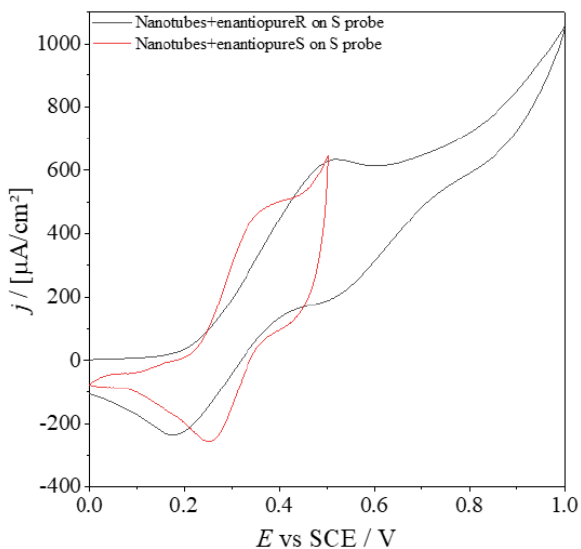
Figure 6.30 - GC_2 modified with carbon nanotubes+R-BT$_2$T$_4$ and S-BT$_2$T$_4$ enantiopure to test S probe.

This second test also confirmed the same trend obtained before. There is always a "non-classical" enantioselection, as once again there seems to be a change in electrochemical reversibility depending on the type of electrodeposited enantiopure oligo-BT$_2$T$_4$ film. The signal related to the R-oligo-BT$_2$T$_4$ film appears to be electrochemically "more irreversible" than that of the S-oligo-BT$_2$T$_4$ film. In any case, it is sure that a different interaction between the carbon nanotubes+R-oligo-BT$_2$T$_4$ film and carbon nanotubes+ S-oligo-BT$_2$T$_4$ film with the S probe in this deposition conditions.

One thing to consider in these tests is that the "strength" of enantioselection is certainly lower in the presence of nanotubes, as the peaks are closer when there are the carbon nanotubes than when they are absent. Another important aspect, however, is also to consider the displacement of the enantiopure R and enantiopure S peaks in the presence and in the absence of carbon nanotubes (Figure 6.31).
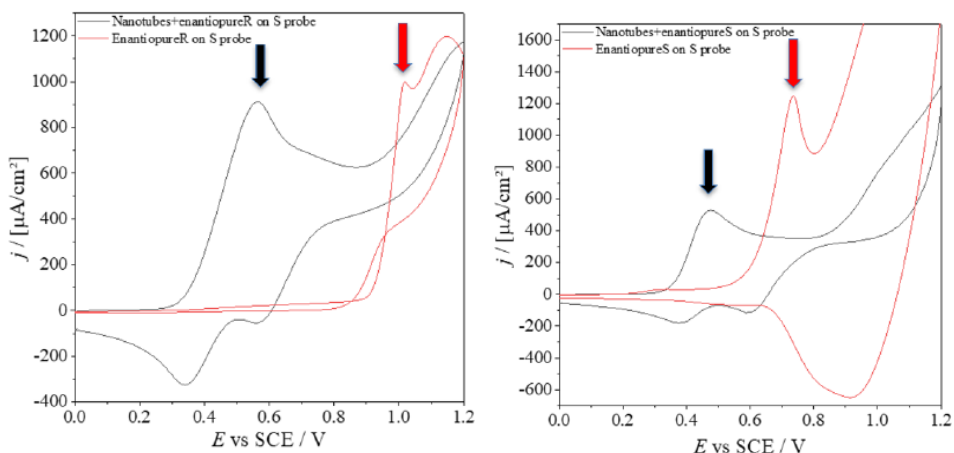
Figure 6.31 - The displacement of the enantiopure R (A) and enantiopure S (B) peaks in the presence and in the absence of carbon nanotubes.

As it can be seen in the figures above, the presence of carbon nanotubes causes a shift of the peaks to lower potentials in a conspicuous manner. The peak related to enantiopure R (on probe S), in the presence of carbon nanotubes, is anticipated by about 500 mV, and the one of enantiopure S (on S probe), in the presence of carbon nanotubes, is anticipated by about 300 mV. This aspect is fundamental because it means that the carbon nanotubes catalyse the reaction, which therefore takes place with a considerable energy advantage. This effect has also been verified in other works in literature, so this further reinforces the goodness of the results obtained (even if the enantioseparation was done by current and not by potential, as in this case) [2]. Another important consideration is the different chemical reversibility in the presence or absence of MWCNTs. It can be seen that, in their absence, there is no return peak, and the signal is therefore chemically irreversible, whereas with nanotubes the signal also has a reduction peak (return) and therefore chemical reversibility is maintained, as shown in Figure 6.31.

This test carried out by electrodepositing the oligo-BT_2T_4 film with 36 cycles at scan rate of 200 mV/s on the carbon nanotubes is effective for enantioselection, albeit with particular characteristics, unlike what happened previously. This is a key step in this experimental work, as it certifies what was expected when the work started.

In summary, the focal points of this experiment are:

- Enantiomeric peak separation is less effective in the presence of carbon nanotubes.
- The carbon nanotubes seem to catalyse the reaction (both R and S enantiopure), as they cause an important shift (hundreds of mV) of the peaks of the S probe to lower and therefore more advantageous potentials.
- The chemical reversibility is maintained only in the presence of the nanotubes. The only presence of R-BT$_2$T$_4$ or S-BT$_2$T$_4$ is not sufficient to have a return peak.

It is important to remember again that these points are only valid in these specific conditions. Other deposition conditions were also tested to confirm the results obtained in this phase.

6.3.3. SEM images.

To understand the morphology of the surface of the electrode, SEM imaging was performed on a flat glassy carbon electrode.

At first, carbon nanotubes alone were analysed at the scanning electron microscope. The amount of carbon nanotubes deposited on its surface was proportional to the deposition performed on a traditional glassy carbon electrode. The following images were obtained:

a) 1000x   b) 5000x

SEM HV: 20.0 kV	SEM MAG: 10.00 kx		
View field: 27.7 µm	Det: SE	5 µm	
SEM MAG: 10.00 kx	Date(m/d/y): 07/10/23		ISM@University o

SEM HV: 20.0 kV	SEM MAG: 15.0 kx		
View field: 18.4 µm	Det: SE	5 µm	
SEM MAG: 15.0 kx	Date(m/d/y): 07/10/23		ISM@University o
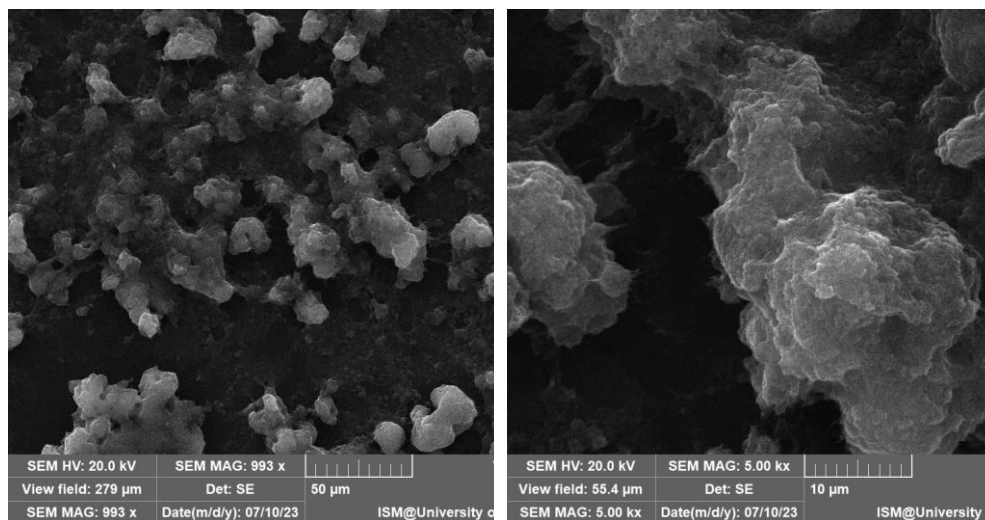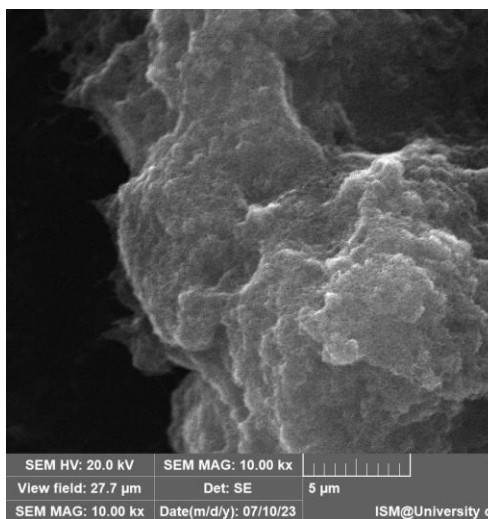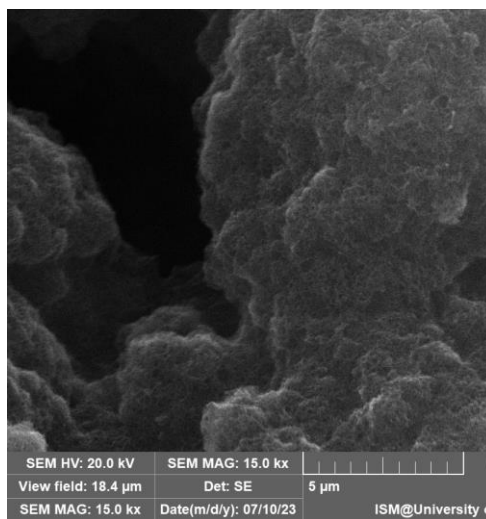
c) 10000x   d) 15000x

Figure 6.32 – SEM images of the multi-walled carbon nanotubes deposited on the flat glassy carbon electrode at different magnifications.

To understand how the oligo-BT$_2$T$_4$ electrodeposition works on the carbon nanotubes, SEM imaging was performed on a flat glassy carbon electrode on which carbon nanotubes were deposited as described before. The oligo-BT$_2$T$_4$ was electrodeposited at a scan rate of 50 mV/s for 24 cycles between 0 and +1.3 V using acetonitrile as solvent for the monomer and LiClO$_4$ as electrolyte. The images obtained are the following:

SEM HV: 20.0 kV	SEM MAG: 4.98 kx		VE
View field: 55.6 µm	Det: SE	10 µm	
SEM MAG: 4.98 kx	Date(m/d/y): 07/10/23		ISM@University of

SEM HV: 20.0 kV	SEM MAG: 9.98 kx		VE
View field: 27.7 µm	Det: SE	5 µm	
SEM MAG: 9.98 kx	Date(m/d/y): 07/10/23		ISM@University of E

a) 5000x   b) 10000x

SEM HV: 15.0 kV	SEM MAG: 4.99 kx		V
View field: 55.4 µm	Det: SE	10 µm	
SEM MAG: 4.99 kx	Date(m/d/y): 07/10/23	ISM@University of	

SEM HV: 20.0 kV	SEM MAG: 9.99 kx		V
View field: 27.7 µm	Det: SE	5 µm	
SEM MAG: 9.99 kx	Date(m/d/y): 07/10/23	ISM@University of	

c) 5000x   d) 10000x

Figure 6.33 – SEM images of the oligo-BT$_2$T$_4$ deposited onto the multi-walled carbon nanotubes: a) R-oligo- BT$_2$T$_4$ at 5000x, b) R-oligo- BT$_2$T$_4$ at 10000x, c) S-oligo- BT$_2$T$_4$ at 5000x, d) S-oligo- BT$_2$T$_4$ at 10000x.

From the images in Figure 6.33, it is possible to see that the electropolymerisation of the S enantiomer is not as regular as the one of the R enantiomer. This is probably due to a different interaction between the multi-walled carbon nanotubes and the S-oligo-BT$_2$T$_4$ film.

6.4.   Conclusions.

The initial goal of this work was to evaluate the interaction with (chiral) probes of carbon nanotube modified electrodes by combining this effect with an additional modification due to BT_2T_4. This "double" type of electrode modification had never been tested and therefore there were no guidelines in the literature. It was also difficult to implement an operational plan for how to proceed. Initially, it was chosen to work with a non-chiral probe, $K_4[Fe(CN)_6]$, to evaluate the morphological interaction between the modified electrode and the probe itself.

In this first phase, the results established that the oligomeric film of BT_2T_4 (used as a racemate in this phase) has difficulties in interacting with the $K_4[Fe(CN)_6]$ probe. In fact, the signals in cyclic voltammetry were often low in intensity and probe peaks were almost imperceptible at times. This effect was also confirmed by EIS measurements, which revealed a high resistivity of the film. Probably this effect is due more to physical than chemical reasons, in fact the film may be too thick to have a good interaction with $K_4[Fe(CN)_6]$. However, the situation changed considerably when the carbon nanotube solution was deposited via drop-casting before the BT_2T_4 film. In this case the electrical conductivity increased considerably, and the cyclic voltammetry signals were much improved both in shape (the probe peak signals are clearly visible) and in intensity. It can therefore be confirmed that nanotubes have an improving effect on BT_2T_4, at least in these operating conditions, *i.e.* aqueous environment and $K_4[Fe(CN)_6]$ as probe molecule. For the second part of the work, it was decided to use a chiral probe and change the solvent from water to acetonitrile (to reach the ideal enantioseparation conditions of BT_2T_4) to evaluate the enantiodiscrimination action of these modified electrodes more specifically with carbon nanotubes and enantiopure BT_2T_4. The results of the experiments in this phase demonstrate that enantioselection can be achieved only in some cases, under particular electrodeposition conditions of the BT_2T_4 film. The key point of this second part of the work is that it cannot be considered a "classical enantioselection"; in fact, it is more a matter of an electrochemical reversibility change since when the oxidation peak is shifted towards higher potentials, the reduction one is shifted to lower potentials. This aspect was unexpected and certainly surprising. The only electrodeposition conditions that have brought about this effect are those in which the film has been deposited with 36 cycles at 200 mV/s.

There is another very important consideration to make in this regard. It was noted that the presence of carbon nanotubes causes the probe peaks of N,N-

dimethyl-1-ferrocenylethylamine to drop to much lower potentials than enantiopure BT$_2$T$_4$ alone. This shift is several hundred mV (about 300-400 mV). This means that the nanotubes catalyse the reaction, causing a very significant energy advantage.

Furthermore, the presence of carbon nanotubes, together with BT$_2$T$_4$, causes the signals to be chemically reversible, *i.e.*, with a return (reduction) peak present. This does not happen in the case of using only enantiopure BT$_2$T$_4$ alone. Obviously, these considerations are valid only in these specific operating and electrodeposition conditions.

In the future, it will be important to understand why some electrodeposition conditions on nanotubes partially maintain the chiral properties of the film and others do not. It will be essential to find and improve the operating conditions for these modified electrodes. This can perhaps be done by studying at a morphological level how the BT$_2$T$_4$ film is arranged on the carbon nanotubes and understanding how they interact with each other both at a physical and chemical level, as well as understanding how BT$_2$T$_4$ is rearranged when carbon nanotubes are present on electrode. The most innovative and surprising point of this thesis work is probably the catalytic effect that nanotubes possess when combined with BT$_2$T$_4$ (compared to BT$_2$T$_4$ only). This aspect will certainly be studied in future works at a kinetic level to understand the reason for this trend. The final goal could then be to use these modified electrodes, when all the aspects that are still not 100% clear will be developed, for the study of new chiral analytes, exploiting all the possible advantages previously discussed.

6.5.   Bibliography.

[1] S. Arnaboldi, M. Magni, and P. R. Mussini, Enantioselective selectors for chiral electrochemistry and electroanalysis: Stereogenic elements and enantioselection performance, *Current Opinion in Electrochemistry* **2018**, 8, 60–72.

[2] D. Guo, Y. Huang, C. Chen, Y. Chen, and Y. Fu, A sensing interface for recognition of tryptophan enantiomers based on porous cluster-like nanocomposite films, *New Journal of Chemistry* **2014**, 38, 5880–5885.

[3] S. Arnaboldi, T. Benincori, R. Cirilli, W. Kutner, M. Magni, P. R. Mussini, K. Noworyta and F. Sannicolò, Inherently chiral electrodes: The tool for chiral voltammetry, *Chem Sci* **2015**, 6, 1706–1711.

[4] Xu, J., Q. Wang, C. Xuan, Q. Xia, X. Lin and Y. Fu, Chiral Recognition of Tryptophan Enantiomers Based on β-Cyclodextrin-platinum Nanoparticles/Graphene Nanohybrids Modified Electrode, *Electroanalysis* **2016**, 28, 868–873.

[5] M. Trojanowicz, Enantioselective electrochemical sensors and biosensors: A minireview, *Electrochemistry Communications* **2014**, 38, 47–52.

[6] A. Berthod, Chiral recognition mechanisms, *Anal Chem* **2006**, 78, 2093–2099.

[7] D. Pasini, and A. Nitti, Recent Advances in Sensing Using Atropoisomeric Molecular Receptors. *Chirality* **2016**, 28, 116–123.

[8] F. Sannicolò, S. Arnaboldi, T. Benincori, V. Bonometti, R. Cirilli, L. Dunsch, W. Kutner, G. Longhi, P. R. Mussini, M. Panigati, M. Pierini and S. Rizzo, Potential-driven chirality manifestations and impressive enantioselectivity by inherently chiral electroactive organic films, *Angewandte Chemie - International Edition* **2014**, 53, 2623–2627.

[9] S. Rizzo, S. Arnaboldi, V. Mihali, R. Cirilli, A. Forni, A. Gennaro, A. Ahmed Isse, M. Pierini, P. R. Mussini, F. Sannicolò, "Inherently Chiral" Ionic-Liquid Media: Effective Chiral Electroanalysis on Achiral Electrodes. *Angewandte Chemie - International Edition* **2017**, 56, 2079–2082.

[10] S. Arnaboldi, M. Magni and P. R. Mussini, Enantioselective selectors for chiral electrochemistry and electroanalysis: Stereogenic elements and enantioselection performance. *Current Opinion in Electrochemistry* **2018**, 8, 60–72.

[11] Sannicolò, F. S. Rizzo, T. Benincori, W. Kutner, K. Noworyta, J. W. Sobczak, V. Bonometti, L. Falciola, P. R. Mussini, M. Pierini, An effective multipurpose building block for 3Delectropolymerisation: 2,2′-Bis(2,2′-bithiophene-5-yl)-3,3′-bithianaphthene, *Electrochimica Acta* **2010**, 55, 8352–8364.

[12] S. Arnaboldi, T. Benincori, R. Cirilli, S. Grecchi, L. Santagostini, F. Sannicolò and P. R. Mussini, "Inherently chiral" thiophene-based electrodes at work: a screening of enantioselection ability toward a series of pharmaceutically relevant phenolic or catecholic amino acids, amino esters, and amine, *Anal Bioanal Chem* **2016**, 408, 7243–7254.

[13] Sannicolò, F., P. R. Mussini, T. Benincori, R. Cirilli, S. Abbate, S. Arnaboldi, S. Casolo, E. Castiglioni, G. Longhi, R. Martinazzo, M. Panigati, M. Pappini, E. Quartapelle Procopio, S. Rizzo, Inherently chiral macrocyclic oligothiophenes: Easily accessible electrosensitive cavities with outstanding enantioselection performances, *Chemistry- A European Journal* **2014**, 20, 15298–15302.

[14] R. G. Compton and C. E. Banks, Understanding Voltammetry, *Worldscientific (Europe)*, **2018**.

[15] J. Mittal, S. Osheen, A. Gupta, R. Kumar, Carbon nanomaterials in agriculture, *Nanosci. Sustain. Agric* **2019**, 153–170.

[16] B.R. Adhikari, M. Govindhan, A. Chen, Carbon nanomaterials based electrochemical sensors/biosensors for the sensitive detection of pharmaceutical and biological compounds, *Sensors* **2015**, 15, 22490–22508.

[17] S. Laschi, E. Bulukin, I. Palchetti, C. Cristea and M. Mascini, Disposable electrodes modified with multi-wall carbon nanotubes for biosensor applications, *IRBM* **2008**, 29, 202–207.

[18] M. Zhu, J. Chen, L. Huang, R. Ye, J. Xu, Y. F. Han, Covalently grafting cobalt porphyrin onto carbon nanotubes for efficient CO_2 electroreduction, *Angew. Chemie Int. Ed.* **2019**, 58, 6595–6599.

[19] J. Xie, J. Ye, F. Pan, X. Sun, K. Ni, H. Yuan, X. Wang, N. Shu, C. Chen, Y. Zhu, Incorporating Flexibility into Stiffness: Self-Grown Carbon Nanotubes in Melamine Sponges Enable A Lithium-Metal-Anode Capacity of 15 mA h cm^{-2} Cyclable at 15 mA cm^{-2}, *Adv. Mater.* **2019**, 31, 1–7.

[20] Y. Wu, X. Tao, Y. Qing, H. Xu, F. Yang, S. Luo, C. Tian, M. Liu, X. Lu, Cr-doped FeNi–P nanoparticles encapsulated into N-doped carbon nanotube as

a robust bifunctional catalyst for efficient overall water splitting, *Adv. Mater.* **2019**, 31, 1–9.

[21] C. Zhang, G. Wang, Y. Ji, M. Liu, Y. Feng, Z. Zhang and B. Fang, Enhancement in analytical hydrazine based on gold nanoparticles deposited on ZnO-MWCNTs films, *Sens Actuators B Chem* **2010**, 150, 247–253.

[22] M. Pumera, The electrochemistry of carbon nanotubes: Fundamentals and applications, *Chemistry - A European Journal* **2009**, 15, 4970–4978.

[23] T. W. Odom, J.-L. Huang, P. Kim and C. M. Lieber, Atomic structure and electronic properties of single-walled carbon nanotubes, *Nature* **1998**, 391, 62-64.

[24] T. W. Odom, J.-L. Huang, P. Kim and C. M. Lieber, Structure and Electronic Properties of Carbon Nanotubes, *Journal of Physical Chemistry B* **2000**, 104, 2794–2809.

[25] W. Yang, K. R. Ratinac, S. P. Ringer, P. Thordarson, J. J. Gooding and F. Braet, Carbon nanomaterials in biosensors: Should you use nanotubes or graphene, *Angewandte Chemie - International Edition* **2010**, 49, 2114–2138.

[26] V. Pifferi, G. Cappelletti, C. Di Bari and D. Meroni, Multi-Walled Carbon Nanotubes (MWCNTs) modified electrodes: Effect of purification and functionalization on the electroanalytical performances, *Electrochim Acta* **2014**, 146, 403–410.

[27] Q. Cao, Z. Shao, D. K. Hensley, N. V. Lavrik and B. J. Venton, Influence of Geometry on Thin Layer and Diffusion Processes at Carbon Electrodes, *Langmuir* **2021**, 37, 2667–2676.

[28] B. J. Sanghavi, O. S. Wolfbeis, T. Hirsch and N. S. Swami, Nanomaterial-based electrochemical sensing of neurological drugs and neurotransmitters, *Microchimica Acta* **2015**, 182, 1–41.

[29] C. Zhu, G. Yang, H. Li, D. Du, and Y. Lin, Electrochemical sensors and biosensors based on nanomaterials and nanostructures, *Analytical Chemistry* **2015**, 87, 230–249.

7. Conclusions.

This PhD thesis project was focused on the study of titanium dioxide and enantioselective materials for electroanalytical sensors. The applications of such devices were verified to be the most various ones, from environmental to medical fields. The systems investigated were composed mainly by three big families of materials: semiconductors, metal nanoparticles and enantiomeric polymers, in different conformations and combinations. For each material, a preliminary electrochemical characterization allowed to effectively verify the presence of the components and their behaviour. Then, they were applied for electroanalytical purposes to test their performances in the determination of target analytes.

Concerning titanium dioxide, the first purpose was to exploit the photoelectrochemical properties of titanium dioxide to photo-renew the surface of the electrode. This was done by studying its behaviour during time, to see if the aging time influences its electrochemical performances. The electrochemical and photoelectrochemical characterisation showed that the best results were obtained after seven days of sol aging. After coupling titanium dioxide with gold nanoparticles, the system was tested for the determination of some emerging contaminants (like diclofenac and paracetamol) to exploit its photo-renewable properties.

Considering the results obtained during the photoelectrochemical characterisation, it was decided to test the hybrid electrode composed of gold nanoparticles and titanium dioxide in photoelectroanalytical measurements, also using low-power light sources, like LEDs. The electrode was thus tested for the determination of ciprofloxacin, another emerging contaminant and showed good analytical results (good limit of detection, good sensitivity) also at low concentrations and at low applied potentials. The study of the possible organic and inorganic interferents also showed good selectivity toward the selected analyte, even if high concentrations of humic acids (20 ppm, average concentrations of this substance in surface water) gave interferences.

To try to solve this problem, the aforementioned hybrid system was coupled with a layer of vertically aligned mesoporous silica, to have a size- ad charge-exclusion effect. The system was also (photo)electrochemically characterised, and it also showed good responses in the determination of ciprofloxacin. In this case, high concentrations of humic acids did not interfere with the determination of ciprofloxacin, leading to better results and making this system ready for online and on-site applications.

Titanium dioxide was tested again for its photo-renewable properties onto a different support, gold disk microelectrodes, for the determination of dopamine. Even though the titanium dioxide layer was not totally in its crystalline phase, it showed good results in restoring the surface of the electrode after its fouling with dopamine.

Lastly, for the first time, multi-walled carbon nanotubes were coupled with oligo-BT$_2$T$_4$, an inherently chiral polymer, to get the best performances from both materials: good electrochemical signal from carbon nanotubes and enantioselectivity due to the presence of enantiopure oligo-BT$_2$T$_4$. The electrode was electrochemically characterised both with a non-chiral probe to study the diffusion at the surface of the electrode and with a chiral probe to study its enantioselective properties. The results showed that the oxidation reaction of the probe occur at lower potentials when coupling the oligo-BT$_2$T$_4$ with carbon nanotubes, the latter having a catalytic effect on the enantioselective oligomer. This paves the way for further studies and applications in both environmental and pharmaceutical fields.

8. Appendix.

8.1. Abbreviations and acronyms.

SCE: saturated calomel electrode

RE: reference electrode

WE: working electrode

CE: counter electrode

BT2T4: 2,2'-bis(2,2'-bithiophen-5-yl)-3,3'-bibenzothiophene

CV: cyclic voltammetry

EIS: electrochemical impedance spectroscopy

CNT: carbon nanotube

MWCNT: multi-walled carbon nanotube

GCE: glassy carbon electrode

SPE: screen printed electrode

FTO: fluorine-doped tin oxide

AFM: atomic force microscopy

DLS: dynamic light scattering

SEM: scanning electron microscopy

TEM: transmission electron microscopy

CIP: ciprofloxacin

8.2. Analytical parameters.

All the analytical parameters were determined according to the IUPAC protocols.

- Limit of detection: inferior limit of concentration where the analyte can be distinguished from the blank.

$LoD = \frac{3.29 \cdot \sigma_{blank}}{S}$, where S, indicating the method calibration sensitivity, is the slope of the linear calibration plot, and σ_{blank} is the blank standard deviation. When no blank signal could be detected, σ_{blank} was estimated by the standard deviation of 10 repeated scans on the same solution of the lowest available standard.

- Limit of quantification: inferior limit of analyte concentration measured with an acceptable precision and accuracy level.

$LoQ = \frac{10 \cdot \sigma_{blank}}{S}$, where S, indicating the method calibration sensitivity, is the slope of the linear calibration plot, and σ_{blank} is the blank standard deviation. When no blank signal could be detected, σ_{blank} was estimated by the standard deviation of 10 repeated scans on the same solution of the lowest available standard.

- Relative standard deviation: absolute value of the coefficient of variation.

$RSD\% = \frac{\sigma_{blank}}{\bar{x}}$, where σ_{blank} is the blank standard deviation, estimated by the standard deviation of 10 repeated scans on the same solution of the lowest available standard, and $\bar{x}$ is the average value, calculated on the 10 repeated scans.

- Apparent recovery factor: observed value, x_{obs}, derived from an analytical procedure by means of a calibration graph divided by reference value, x_{ref}, indicating the trueness of the method (higher trueness when close to 100%)
$RF = \frac{x_{obs}}{x_{ref}} \cdot 100$,

8.3.   Analytical techniques.

8.3.1. Cyclic Voltammetry (CV).

In this technique, the potential of a working electrode is varied linearly with time until a step potential, where the potential ramp is inverted, and the resulting current is measured. This method allows characterizing the electrodes, in terms of capacitance, surface area, diffusion coefficient of the analyte, rate determining steps and reversibility.

Electrode capacitance C can be calculated varying the scan rate without the presence of the analyte, from the slope of the plot Δi vs scan rate, derived from the equation $\frac{i_a - i_c}{2} = Cv$. In more details, a fixed voltage value is chosen, in which no Faradaic currents are present. The related anodic (i_a) and cathodic (i_c) capacitive current are read. Then, $\frac{i_a - i_c}{2}$ is calculated and plotted against the voltage scan rate. From the slope of the relative curve capacitance values are derived.

When the analyte is present and is electroactive, several calculations could be done in order to understand the mechanism of diffusion of the probe towards the electrode and the electrochemical reversibility or irreversibility of the reaction. In more details, if the plot i_p **vs** $v^{0.5}$, obtained by Randles-Sevcik equation: $i_P = 0.4463 nFAc \left(\frac{nFvD}{RT}\right)^{0.5}$, (where i_p is the peak current, n the number of electrons transferred in the redox event, A the electrode area, F the Faraday constant, D the diffusion coefficient, c the bulk concentration and v the scan rate), is linear, the rate determining step is the diffusion of the analyte to the electrode. On the other hand, if the peak current is proportional to the scan rate the rate determining step is the absorption of the analyte on the electrode. Moreover, the slope of the Randles-Sevcik plot can give information about the diffusion coefficient of the analyte and the surface area of the electrode.

Information about the diffusion mechanism can be obtained also from the slope of the $\ln(i_p)$ vs $\ln(v)$ plot, since the perfect planar diffusional behaviour gives a slope of 0.5.

A detailed description of the technique can be found in many dedicated books (Bard & Faulkner, 2001; Bard, 2007; C. M. A. Brett & Oliveira Brett, 1993; R. G. Compton, C. E. Banks, 2011).

8.3.2. Electrochemical Impedance Spectroscopy (EIS).

This technique measures the impedance (Z) of a system over a range of frequencies as a result of the perturbation of an applied potential or current. In this thesis, only the applied potential was employed to characterize electrodes. Impedance data can be presented using two types of plot: complex plane or Nyquist plot, the imaginary part of impedance (Z'') vs the real part (Z'), and the Bode plots: |Z| vs frequency or phase angle vs frequency. Moreover, from the fitting of impedance data, information about the morphology of the electrode surface and the electrical properties can be obtained, after the choice of the electrical circuit corresponding to the electrochemical system.

In the equivalent circuit, capacitance and resistance can be found in series or in parallel and in different combinations. In more details, CPE (instead of normal capacitance, C) is defined as constant phase element. $CPE = [(Ci\omega)^{\alpha}]^{-1}$, is modelled as pure capacitor in the case of $\alpha=1$ or as non-ideal capacitor, due to the porosity and non-homogeneity of the surface, for $0.5 < \alpha < 1$. Other parameters than can be found in an equivalent circuit are the diffusional resistance R_W and the diffusional time constant τ of the Open Warburg Element, resulting from the equation $Z_W = RWcth[(\tau i\omega)^{\alpha}](\tau i\omega)^{-\alpha}$, where $\alpha < 0.5$.

Basically, the measurement consists in applying an oscillating voltage and recording the corresponding current values. The data is then processed mathematically to give three representations:

- The Nyquist plot, in which the data are plotted in a Z' vs -Z" graph. Z' is considered as the "real part" and is related to the resistance, while -Z" represents the "imaginary part", related to the capacity. Each point is a frequency value, which increases moving from right to left in the graph.

- Bode module plot, which uses the natural logarithm of |Z| on the y-axis versus the natural logarithm of the frequency value as the x-axis.

- Bode phase plot, which uses the phase value on the y-axis and the logarithm of the frequency of the x-axis.

In a classical Nyquist plot, it is possible to observe a semicircle and a line, as shown in Figure 8.1.
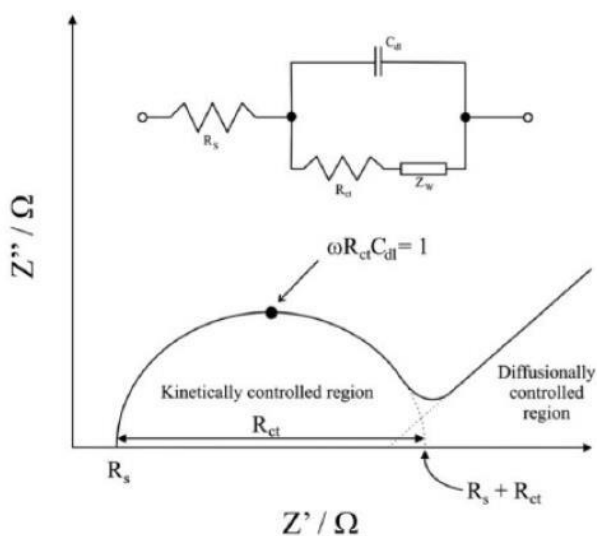
Figure 8.1 - A typical representation of the impedance spectrum (Bard, A. J. , F. L. R. Electrochemical methods: fundamentals and applications (Wiley, 2001)).

As it can be seen in Figure 8.1, depending on the area of the graph that is being observed, there is a region with greater kinetic control (semicircle) or greater diffusive control (straight line). In particular, the resistance value can be obtained from the radius of the semicircle of the Nyquist plot (or even from the peak in a Bode phase plot). On the other hand, the line is related to mass transfer. If the slope of this straight line is 45°, it is called "Warburg resistance". This slope value can be read on the y-axis of the Bode phase plot and is equal to 90° for a pure capacitor.

A detailed description of the technique can be found in many dedicated books (Bard, 2007; Orazem & Tribollet, 2008).

8.3.3. Transient photocurrent.

When a semiconductor is irradiated with a higher energy than its band gap, the generation of electron-hole pairs is promoted. Two processes can occur, the first being the recombination of holes and electrons and the second being the trapping of the charge carriers and the subsequent reaction with electron donors or acceptors absorbed on the surface.

The resulting photocurrent shape is characterized by spikes and overshoots, that can be interpreted as evidence that a recombination process is occurring. For example, considering Figure 8.2, when light is turned on at $t = 0$ s, an immediate photocurrent signal can be observed due to the separation of electron-hole pairs. For an n-type photoanode, electrons move to the external circuit while holes move towards the interface with the solution.

The presence of holes on the surface causes a flow of electrons towards them (*i.e.*, a negative current) and recombination occurs. This phenomenon leads to a photocurrent decay.

After some time, a steady state is reached in which the rate at which holes reach the interface is exactly balanced by the rate at which they are consumed by charge transfer and recombination, and therefore the photocurrent becomes constant and equal to the current passing across the semiconductor/electrolyte interface.

When, after approximately 10 s, light is switched off, a negative overshoot can be observed. This is because the hole flux to the interface is immediately interrupted, while the electron flux continue until all the excess holes are consumed by recombination or charge transfer.

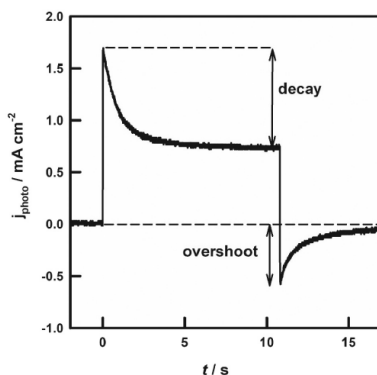*Figure 8.2 - Transient photocurrent response of an α-Fe$_2$O$_3$ electrode showing the typical decay and overshoot interpreted as evidence of surface electron-hole recombination. Note that the "decay" is significantly larger than the "overshoot".*

Overall, the net current density measured at any time is equal to the sum of the positive hole current density and the negative recombination current density, as reported in the equation below and shown in Figure 8.3.

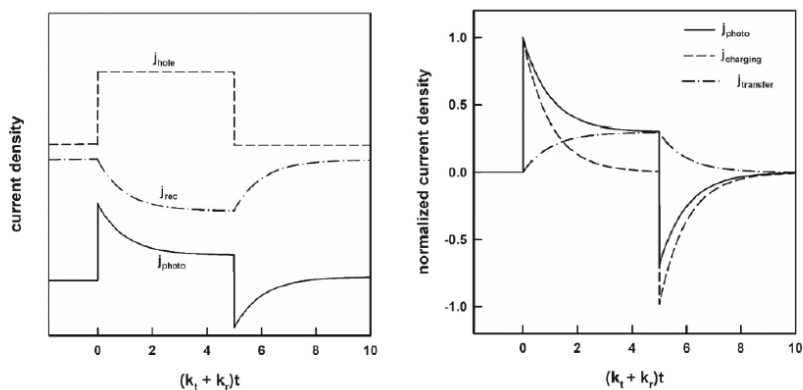$$J_{photocurrent}(t) = J_{hole} + J_{recombination} = J_{charging} + J_{transfer}$$

Figure 8.3 - Deconvolution of the photocurrent into contributions from hole and electron current densities (left) and charge transfer and charging/discharging of the space charge capacitance (right).

As both the decay and the overshoot are a measure of electron-hole recombination processes, their magnitude should be equal. This is not always the case, especially when high power irradiation is used, as other factor must be considered.

One explanation is that another phenomenon must be considered for the initial photocurrent decay: the buildup of holes at the interface can modify the potential distribution across the semiconductor-electrolyte junction, increasing the potential drop across the Helmholtz layer (ΔV_H) and decreasing the potential drop across the space charge region ($\Delta\phi_{SCR}$).

It is worth noting that those potential values are related, as the applied potential relative to the flat band potential is equal to the sum of the potential drops across the space charge region and the Helmholtz region and any increase in ΔV_H due to the build-up of charge must be matched by a corresponding decrease in band bending and hence of the photocurrent. This phenomenon is called "light-induced band edge unpinning" (L. M. Peter, A. B. Walker, T. Bein, A. G. Hufnagel, and I. Kondofersky, Interpretation of photocurrent transients at semiconductor electrodes: Effects of band-edge unpinning, *J. Electroanal. Chem.* **2020**, 872, 114234).

284

It is known that, in extreme cases at high band bending, the photocurrent may decay when the light is switched on but not show any overshoot when the light is switched off. The presence of light-induced band edge unpinning has a peculiar effect on the photocurrent shape, as shown in Figure 8.4.
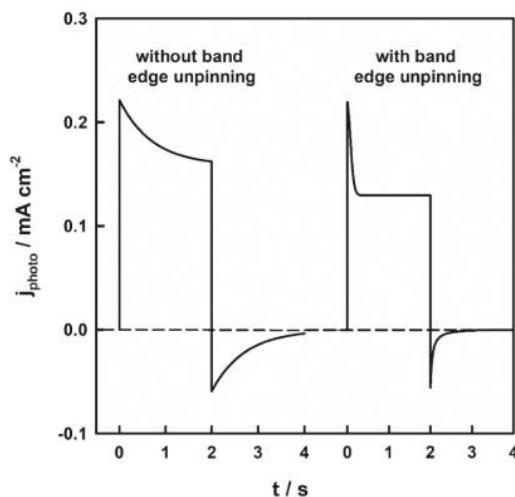

Figure 8.4 - Photocurrent transients calculated with and without band edge unpinning. With band edge unpinning, the difference in magnitude between the decay and the overshoot is due to additional suppression of the photocurrent. This is due to a potential drop across the space charge region, which accelerates both recombination and charge transfer.

Usage of a rough or nanostructured electrode leads to increased Helmholtz capacitance and decreased surface hole concentration per unit area. Both will reduce the extent of band edge unpinning under illumination.

Furthermore, the reduction in the width of the space charge region caused by band edge unpinning under illumination decreases the flux of holes to the surface. This leads to a reduction of the steady state photocurrent.

8.3.4. Other voltammetric or amperometric techniques.

This is the list of all the employed electrochemical techniques with a brief description. A detailed description of all the techniques can be found in many dedicated books (Bard & Faulkner, 2001; Bard, 2007; C. M. A. Brett & Oliveira Brett, 1993) and it is out of the scope of this Thesis:

- Linear Sweep Voltammetry (LSV): the potential of a working electrode is varied linearly with time and the resulting current is measured.

- Linear Sweep Anodic Stripping Voltammetry (LSAdSV): preconcentration deposition is performed before LSV stripping.
- Differential Pulse Voltammetry (DPV): a series of regular voltage pulses is superimposed on the potential linear sweep and the current is measured before and after the imposed pulse; the difference of the two measurements (differential measurement) is plotted against the voltage.
- Chronoamperometry: the potential is maintained at a chosen value and the resulting current is measured during time.

8.3.5. Scanning Electronic Microscopy (SEM).

Scanning Electronic Microscopy can provide information on surface topography, crystalline structure, chemical composition of a sample. This technique is non-destructive and can achieve high magnification. It works by directing an incident beam of electrons on the sample and studying the various signals from the specimen that can be collected and used to form images.

As shown in Figure 8.5, different signal can be collected. Among those:

- Secondary electrons are low energy electrons that are expelled from the sample due to a collision with the incident beam. They have low energies (typically below 50 eV) and are used to create high resolution images. They mainly give topological information.
- Backscattered electrons are the incident electrons that get scattered by atom nuclei in the specimen. They are used to get compositional information, as the scattering is related to the atomic mass of the nuclei.

It is also possible to combine the SEM analysis with an Energy Dispersive X-ray Analysis (EDX). Overall, SEM-EDX allows to achieve detailed information of the atomic composition of the sample. The incident electrons are used to expel a core electron of the sample atom. This leaves a hole and an electron from a higher orbital can occupy it. Moving from a high energy orbital to a low energy orbital, the electron emits an X-ray. The energy value of the X-ray, connected to the energy difference between orbitals, is characteristic for each element.
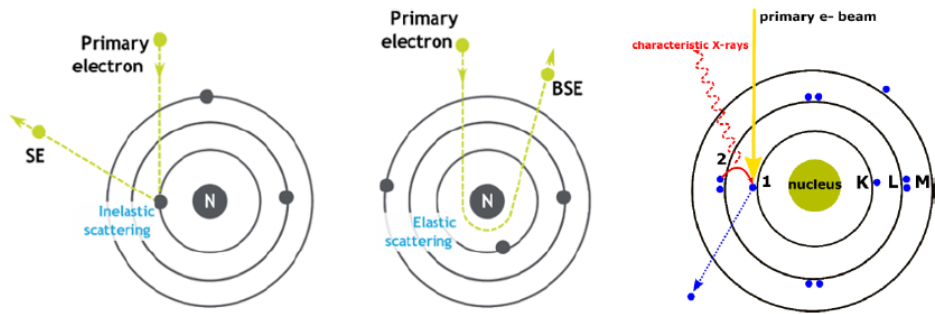
Figure 8.5 - Representation of the signals that can be obtained by the interaction of an incident electron beam and the sample (A) [from AZO Materials / azom.com].

8.4. List of Papers and Communications produced during the PhD period.

Papers:

D. Fumagalli, <u>S. Comis</u>, V. Pifferi, L. Falciola, "Gold Nanoparticles-Titania Heterojunction: Photoelectrochemical Detection of Ciprofloxacin", *ChemElectroChem* **2023**, 8, e202201136, DOI: 10.1002/celc.202201136.

Communications:

The presenting author is underlined.

Workshop of the Gruppo Interdivisionale Sensori that will be held in Rome on December 13th-15th with the title: **Metal-titania heterojunctions for photoelectrochemical analysis of emerging pollutants** (<u>Daniele Fumagalli</u>, Elisabetta Inico, Cesare Borroni, Silvia Comis, Valentina Pifferi and Luigi Falciola) – oral contribution.

Workshop of the Gruppo Interdivisionale Sensori that will be held in Rome on December 13th-15th with the title: **Electrochemical sensor based on Multi-Walled Carbon Nanotubes (MWCNTs) and BT$_2$T$_4$ oligomers for enantiomeric discrimination** (<u>Luigi Falciola</u>, Silvia Comis, Sara Grecchi, Daniele Crespi, Valentina Pifferi Tiziana Benincori, Serena Arnaboldi and Patrizia Mussini) – poster contribution.

22nd Merck Young Chemists' Symposium (MYCS) held in Rimini on November 13th–15th with the title: **Photoelectrochemical detection of ciprofloxacin using a mesoporous silica/AuNPs/TiO$_2$ hybrid electrode**. (<u>Silvia Comis</u>, Valentina Pifferi, Alain Walcarius and Luigi Falciola) – oral contribution.

XXX Congresso della Divisione di Chimica Analitica della Società Chimica Italiana held in Vasto on September 17th–21st 2023 with the title: **AuNPs+TiO$_2$ hybrid electrodes for the photoelectrochemical detection of ciprofloxacin** (<u>Silvia Comis</u>, Daniele Fumagalli, Mariangela Longhi, Valentina Pifferi, Luigi Falciola) – oral contribution.

XXX Congresso della Divisione di Chimica Analitica della Società Chimica Italiana held in Vasto on September 17th–21st 2023 with the title: **Study of electrochemical sensors based on Multi-Walled Carbon Nanotubes (MWCNTs) and BT$_2$T$_4$ oligomers for enantiomeric discrimination** (<u>Silvia Comis</u>, Sara Grecchi, Daniele Fumagalli, Daniele Crespi, Valentina Pifferi,

Tiziana Benincori, Serena Arnaboldi, Patrizia Mussini and Luigi Falciola) – poster contribution.

74th ISE annual meeting held in Lyon on September 3rd – 8th 2023 with the title: **Photoelectrochemical detection of ciprofloxacin using AuNPs+TiO$_2$ hybrid electrodes** (Silvia Comis, Daniele Fumagalli, Mariangela Longhi, Valentina Pifferi, Luigi Falciola) – oral contribution.

74th ISE annual meeting held in Lyon on September 3rd–8th 2023 with the title: **Photoelectrochemical analysis: the role of titania-based heterojunctions** (Valentina Pifferi, Daniele Fumagalli, Silvia Comis and Luigi Falciola) – oral contribution.

74th ISE annual meeting held in Lyon on September 3rd–8th 2023 with the title: **Electrochemical sensors based on Multi-Walled Carbon Nanotubes (MWCNTs) and BT$_2$T$_4$ oligomers for enantiomeric discrimination** (Silvia Comis, Sara Grecchi, Daniele Fumagalli, Daniele Crespi, Valentina Pifferi, Tiziana Benincori, Serena Arnaboldi, Patrizia Mussini and Luigi Falciola) – poster contribution.

73rd ISE annual meeting held online on September 12th–16th 2022 with the title: **Gold Nanoparticles and Titania hybrid systems for the photoelectrochemical detection of ciprofloxacin** (Silvia Comis, Daniele Fumagalli, Livia Nicolucci, Valentina Pifferi, Mariangela Longhi and Luigi Falciola) – oral contribution.

73rd ISE annual meeting held online on September 12th–16th 2022 with the title: **Photo-renewability of Au microelectrodes covered with a layer of TiO$_2$ used for the detection of dopamine** (Nicole Ceribelli, Silvia Comis, Alessandro Minguzzi, Alberto Vertova, Valentina Pifferi and Luigi Falciola) – poster contribution.

Giornate dell'Elettrochimica Italiana (GEI) held in Orvieto (TR) on September 11th–15th, 2022, with the title: **AuNPs + TiO$_2$ hybrid systems for the photoelectrochemical detection of ciprofloxacin** (Silvia Comis, Daniele Fumagalli, Livia Nicolucci, Valentina Pifferi, Mariangela Longhi and Luigi Falciola) – oral contribution.

Giornate dell'Elettrochimica Italiana (GEI) held in Orvieto (TR) on September 11th–15th, 2022, with the title: **Study of the photo-renewable properties of a Au microelectrode covered with TiO$_2$ for the detection of dopamine** (Nicole Ceribelli, Silvia Comis, Alessandro Minguzzi, Alberto Vertova, Valentina Pifferi and Luigi Falciola) – poster contribution.

Regional Meeting of the International Society of Electrochemistry (ISE) held in Prague (Czech Republic) on August 13th-20th 2022 with the title: **Photoelectrochemical detection of ciprofloxacin using (AuNPs + TiO₂) hybrid systems** (Silvia Comis, Daniele Fumagalli, Livia Nicolucci, Valentina Pifferi, Mariangela Longhi and Luigi Falciola) – oral contribution.

Faraday Discussion: Next Generation Nanoelectrochemistry held online on November 29th– December 1st 2021, with the title: **Study of the aging of TiO₂ sol for electrochemical sensors for the determination of emerging contaminants** (Silvia Comis, Livia Nicolucci, Valentina Pifferi, Mariangela Longhi, Francesco Orsini and Luigi Falciola) – poster contribution.

XXVII Congresso nazionale della Società Chimica Italiana (SCI) held online on September 14th – 23rd 2021 with the title: **Determination of emerging contaminants with electrochemical sensors based on titania nanoporous films: effect of sol aging on their electrochemical performances** (Silvia Comis, Livia Nicolucci, Valentina Pifferi, Mariangela Longhi and Luigi Falciola) – oral contribution.

72nd Annual Meeting of the International Society of Electrochemistry, August 29th- September 3rd, 2021, held in Jeju Island, Korea and online with the title: **Effect of Sol Aging on Electrochemical Performances of Titania Nanoporous Surfaces for Analytical Applications** (Silvia Comis, Livia Nicolucci, Valentina Pifferi, Mariangela Longhi and Luigi Falciola) – oral contribution.